ACCELERATOR-BASED PRODUCTION OF HIGH SPECIFIC ACTIVITY RADIONUCLIDES FOR RADIOPHARMACEUTICAL APPLICATIONS

A Dissertation

Presented to

the Faculty of the Graduate School

at the University of Missouri-Columbia

In Partial Fulfillment

of the Requirements for the Degree

Doctor of Philosophy

By

MATTHEW DAVID GOTT

Dr. Silvia S. Jurisson, Dissertation Advisor

Dr. Cathy S. Cutler, Co-Advisor

JULY 2015

The undersigned, appointed by the dean of the Graduate School, have examined the dissertation entitled

ACCELERATOR-BASED PRODUCTION OF HIGH SPECIFIC ACTIVITY RADIONUCLIDES FOR RADIOPHARMACEUTICAL APPLICATIONS

presented by Matthew David Gott, a candidate for the degree of Doctor of Philosophy, and hereby certify that, in their opinion, it is worthy of acceptance.

Dr. Silvia S. Jurisson

Dr. Cathy S. Cutler

Dr. C. Michael Greenlief

Dr. J. David Robertson

DEDICATION

This dissertation is dedicated to my wonderful parents, David and Cathy.

You have always been my greatest supporters and encouraged me every step of the way.

None of this would have been possible without you.

ACKNOWLEDGMENTS

I would like to thank Dr. C. Michael Greenlief and Dr. J. David Roberston for serving on my committee and providing advice throughout this process.

I would like to thank all of my collaborators who provided assistance and guidance throughout this project. Dr. Donald Wycoff, Dr. Anthony Degraffenreid, and Yutian Feng were instrumental in the arsenic production work. Dr. Alan Ketring, Dr. John Lydon, Mary Embree, Stacy Wilder, Alex Saale, Melissa Evans-Blumer, and the staff at the University of Missouri Research Reactor provided support and ideas for experimental work throughout this dissertation. Dr. Michael Fassbender, Dr. Beau Ballard, and the members of the C-IIAC group at Los Alamos National Laboratory provided assistance and guidance with the experimental work for the W/Re separation method. Dr. D. Scott Wilbur, Dr. Ethan Balkin, Bennett Smith, and the members of the accelerator group at the University of Washington provided assistance and ideas for the experimental work for the osmium, tungsten, and germanium targetry. Dr. Suzanne Smith, Chris Cullen, and the members of the MIRP group at Brookhaven National Laboratory provided assistance and guidance with the experimental work for the osmium, tungsten, and arsenide irradiations and separations. Lauren Radford, Kimberly Reining, Dr. David Rotsch, Dr. Dustin Demoin, and Dr. Jurisson's research group provided help throughout the project by providing ideas, support, training, and revising presentations and publications.

TABLE OF CONTENTS

ACKNOWLEDGMENTS ii

TABLE OF CONTENTS iii

LIST OF FIGURES viii

LIST OF TABLES xii

ACADEMIC ABSTRACT xvii

Chapter 1: Introduction 1

1.1 Basics of Radiopharmaceuticals 1

1.2 Modes of Radioactive Decay Commonly Used for Radiopharmaceutical Drugs 2

1.2.1 Alpha Decay 3

1.2.2 Beta Decay 5

1.2.3 Positron Emission 8

1.2.4 Isomeric Transition and Electron Capture (Gamma Emitters) 10

1.3 Isotope Production 13

1.3.1 Production of Radionuclides in Reactors 15

1.3.2 Production of Radionuclides in an Accelerator 16

1.3.3 Basics of Targetry 17

1.3.4 Basics of Separation 18

Chapter 2: Production of ^{186}Re 21

2.1 ^{186}Re Production *via* Proton Bombardment of Osmium Targets 22

2.1.1 Materials and Methods 22

2.1.2 Results and Discussion 29

2.1.3 Conclusions 39

2.1.4 Future Studies 39

2.2 ^{186}Re Production *via* Proton Bombardment of Tungsten Targets 40

2.2.1 Materials and Methods 40

2.2.2 Results and Discussion 50

2.2.3 Conclusions 73

2.2.4 Future Studies 74

Chapter 3: Production of ^{72,77}As 75

3.1 Production of ^{72}As from the Decay of Accelerator Produced ^{72}Se 75

3.1.1 Materials and Methods 76

3.1.2 Results and Discussion 83

3.1.3 Conclusions 88

3.1.4 Future Studies 89

3.2 Production of ^{77}As from the Decay of Reactor Produced ^{77}Ge 90

3.2.1 Materials and Methods 90

3.2.2 Results and Discussion 97

3.2.3 Conclusions 104

3.2.4 Future Studies 105

Chapter 4: Production of Other Radiopharmaceutical Isotopes 107

4.1 Production of ^{44,44m}Sc *via* Proton Bombardment of $CaCO_3$ 107

4.1.1 Methods and Materials..... 107

4.1.2 Results and Discussion 111

4.1.3 Conclusions..... 114

4.1.4 Future Studies 114

4.2 Production of ^{99m}Tc via Proton and Deuteron Bombardment of MoS_2 115

4.2.1 Methods and Materials..... 115

4.2.2 Results and Discussion 118

4.2.3 Conclusions..... 123

4.2.4 Future Studies 123

REFERENCES 124

Appendix A: Production Calculations 134

A.1 Discussion of Target Cross Sections..... 134

A.1.1 Proton Bombardment of Osmium via ^{nat}Os(p, x) reactions 135

A.1.2 Proton Bombardment of Tungsten via ^{nat}W(p, xn)Re reactions 136

A.1.3 Alpha Bombardment of Germanium via ^{nat}Ge(a, x) reactions..... 138

A.1.4 Proton Bombardment of Arsenic via ^{75}As(p, 4n)^{72}Se reactions..... 139

A.1.5 Proton Bombardment of Calcium via ^{nat}Ca(p, xn)Sc reactions..... 140

A.1.6 Proton Bombardment of Molybdenum via ^{nat}Mo(p, xn) reactions 141

A.1.7 Deuteron Bombardment of Molybdenum via ^{nat}Mo(d, xn) reactions 143

A.2 SRIM Calculations for Targets 145

A.2.1 Osmium Metal Target 147

A.2.2 Osmium Disulfide Target 149

A.2.3 Tungsten Metal Target 151

A.2.4 Tungsten Disulfide Target 153

A.2.5 Germanium Target 155

A.2.6 Calcium Carbonate Target 157

A.2.7 Molybdenum Disulfide Target (Proton Bombardment) 159

A.2.8 Molybdenum Disulfide Target (Deuteron Bombardment) 161

A.3 Theoretical Qualification and Quantification of Activation Products 163

A.3.1 Natural Abundance Osmium Targets 164

A.3.2 Natural Abundance Tungsten Targets 166

A.3.3 Natural Abundance Germanium Metal Target 168

A.3.4 Natural Abundance Calcium Carbonate Targets 170

A.3.5 Natural Abundance Molybdenum Disulfide Targets 171

A.4 Steady State Thermal Analysis of Irradiated Targets 174

A.4.1 Osmium Metal Target at MURR 177

A.4.2 Osmium Disulfide Target at MURR 178

A.4.3 Osmium Metal Target at BNL 179

A.4.4 Tungsten Metal Target at MURR 180

A.4.5 Tungsten Disulfide Target at MURR 181

A.4.6 Tungsten Metal Target at BNL 182

A.4.7 Germanium Metal Target at UW 183

A.4.8 Calcium Carbonate Target at MURR 184

A.4.9 Molybdenum Disulfide Target at MURR (Proton Bombardment) 185

A.4.10 Molybdenum Disulfide Target at MURR (Deuteron Bombardment) 186

Appendix B: Considerations in the Target Assembly Design 187

B.1 Determination of Target Assembly Materials 187

B.2 Design of the Target Assembly 188

B.3 Failed Target (Case Study #1) 190

B.4 Failed Targets (Case Study #2) 193

B.5 Conclusion 194

Appendix C: Data from Batch Studies 195

Appendix D: Data from Column Chromatography Studies 203

VITA 213

LIST OF FIGURES

Figure 1.2.1. ^{223}Ra decay scheme 5

Figure 1.2.2. [^{90}Y]-ibritumomab tiuxetan (Zevalin®) 7

Figure 1.2.3. [^{153}Sm]-lexidronam pentasodium (Quadramet®) 8

Figure 1.2.4. ^{18}F-2-fluoro-2-deoxyglucose 9

Figure 1.2.5. (left) ^{99m}Tc-exametazine, the d,l isomer (right) meso isomer impurity 12

Figure 1.3.1. Examples of a research reactor (left) and medical cyclotron (right) used for radionuclide production. 14

Figure 1.3.2. Schematic of ^{99}Mo/^{99m}Tc generator 20

Figure 2.1.1. Osmium Distillation Setup 26

Figure 2.1.2. (left) Aluminum backing used for target irradiations (right) 13 mm pellet die used to prepare pressed targets 27

Figure 2.1.3. Raman spectrum of annealed OsS_2 sample 30

Figure 2.1.4. Crystal diffraction spectrum of annealed OsS_2 with comparison to literature peaks 31

Figure 2.1.5. (a) OsS_2 pressed directly into backing (b) pressed pellet of OsS_2 which is transferred to target backing 33

Figure 2.1.6. TENDL-2014 theoretical cross section data for ^{189}Os(p,α)^{186}Re reaction . 36

Figure 2.1.7. (left) osmium foil inside machined well in target backing (right) bolted, sealed target 37

Figure 2.2.1. Pressed $^{nat}WO_3$ disc in tungsten alloy backing (post-sintering) 51

Figure 2.2.2. SEM images of $^{nat}WO_3$ sample prior to sintering (left) and after sintering (right) 51

Figure 2.2.3. Pressed disc of tungsten disulfide 52

Figure 2.2.4 Rhenium K_d as a function of contact time on AG 1-X8. (n=6) 57

Figure 2.2.5 Rhenium K_d as a function of time and temperature. (n=6) 58

Figure 2.2.6. First-order adsorption rate kinetics as a function of time and temperature (n=6) 59

Figure 2.2.7 Linear regression of the reduced adsorption rate constant *k/A* as a function of inverse temperature (n=6)..... 60

Figure 2.2.8. Linear regression of ln ($K_d \cdot \rho_s$) as a function of inverse temperature (n=6) 61

Figure 2.2.9. Rhenium K_d at various acid and base concentrations. (n=6) 62

Figure 2.2.10. Rhenium K_d as a function of total ionic strength *I*. (n=6) 63

Figure 2.2.11. Tungsten K_d at various base concentrations. (n=6) 64

Figure 2.2.12. Rhenium/Tungsten separation factors at various base concentrations. (n=6)..... 65

Figure 2.2.13. Rhenium Adsorption Behavior on TEVA resin (n=6) 67

Figure 2.2.14. Rhenium and Tungsten Adsorption Behavior on AnaLig (n=6) 68

Figure 2.2.15. Separation of rhenium and tungsten using AnaLig resin 69

Figure 3.1.1. Ethylene bis(stearamide) 82

Figure 3.1.2. Distribution coefficient for selenate, selenite, and arsenate as a function of pH (n = 6; the error bars are included)..... 84

Figure 3.1.3. (left) sintered Ge pellet (right) annealed Ge mass 87

Figure 3.2.1. Distribution coefficient for arsenate and germanate on acidic alumina. (n=6; error bars included) 98

Figure 3.2.2. Distribution coefficient for arsenate and germanate on silica. (n=6; error bars included)..... 98

Figure 3.2.3. Distribution coefficient for arsenate and germanate on zirconium oxide. (n=6; error bars included) 99

Figure 3.2.4. Elution profile for HCl adjusted Ge sample. (n = 3) 100

Figure 3.2.5. Elution profile for HNO_3 adjusted Ge sample. (n = 3)..... 101

Figure 3.2.6. Elution profile for H_3PO_4 adjusted Ge sample. (n = 3) 101

Figure 3.2.7. Column chromatography of Ge-77/As-77 sample. The eluent was changed from methanol to deionized water at 20 mL to recover the Ge target material. (n=6; example graph)..... 103

Figure 3.2.8. Ge-77 and As-77 retention on zirconium oxide resin. Volumes: 1-50 methanol, 50-70 pH 11, and 70-90 pH 13. 104

Figure 4.2.1. Thick MoS_2 pellet pressed using the pellet die..... 119

Figure A.1.1. TENDL-2014 theoretical cross sections for select reactions on ^{189}Os 136

Figure A.1.2. Previously reported cross section data for the $^{186}W(p, n)^{186}Re$ reaction . 137

Figure A.1.3. Previously reported cross section data for $^{181-186}Re$ production on a natural W target..... 138

Figure A.1.4. Theoretical cross section for the production of $^{72,73}Se$ via alpha bombardment of enriched ^{70}Ge..... 139

Figure A.1.5. Literature cross section data for select proton bombardment reactions on $^{75}As^{37}$..... 140

Figure A.1.6. Literature cross section data for proton bombardment of $^{44}CaCO_3$ targets 141

Figure A.1.7. Literature cross sections for technetium radioisotopes production via proton bombardment of natural molybdenum 142

Figure A.1.8. Literature cross sections for other radioisotopes production via proton bombardment of natural molybdenum compared to ^{99m}Tc..... 143

Figure A.1.9. Literature cross section for the production of ^{99}Mo via deuteron bombardment of natural molybdenum..... 144

Figure A.2.1. Stopping power as a function of proton energy for the proton bombardment of an osmium target 148

Figure A.2.2. Stopping power as a function of proton energy for the proton bombardment of an osmium disulfide target 150

Figure A.2.3. Stopping power as a function of proton energy for the proton bombardment of a tungsten target..... 152

Figure A.2.4. Stopping power as a function of proton energy for the proton bombardment of a tungsten disulfide target..... 154

Figure A.2.5. Stopping power as a function of alpha energy for the alpha bombardment of a germanium target 156

Figure A.2.6. Stopping power as a function of proton energy for the proton bombardment of a calcium carbonate target 158

Figure A.2.7. Stopping power as a function of proton energy for the proton bombardment of a molybdenum disulfide target 160

Figure A.2.8. Stopping power as a function of deuteron energy for the deuteron bombardment of a molybdenum disulfide target 162

Figure A.4.1. Illustration of an axisymmetric modeled target region. (left) cross section of an example target (right) axisymmetric region used for the thermal analysis..... 174

Figure A.4.2. Illustration of map faced meshing with edge sizing 175

Figure A.4.3. Steady state thermal analysis of osmium metal target irradiated at MURR 177

Figure A.4.4. Steady state thermal analysis of osmium disulfide target irradiated at MURR..... 178

Figure A.4.5. Steady state thermal analysis of osmium metal target irradiated at BNL 179

Figure A.4.6. Steady state thermal analysis of tungsten metal target irradiated at MURR 180

Figure A.4.7. Steady state thermal analysis of tungsten disulfide target irradiated at MURR..... 181

Figure A.4.8. Steady state thermal analysis of tungsten metal target irradiated at BNL 182

Figure A.4.9. Steady state thermal analysis of germanium metal target irradiated at UW 183

Figure A.4.10. Steady state thermal analysis of calcium carbonate target irradiated at MURR..... 184

Figure A.4.11. Steady state thermal analysis of molybdenum disulfide target irradiated at MURR..... 185

Figure A.4.12. Steady state thermal analysis of molybdenum disulfide target irradiated at MURR..... 186

Figure B.2.1. Solid-state target port for MURR GE PETtrace Cyclotron 189

Figure B.2.2. Target specifications used to produce targets at MURR 190

Figure B.3.1. (Left) empty aluminum backing (Middle) OsS_2 pressed into aluminum backing (Right) Target coated with Kapton foil epoxyed to the surface..... 191

Figure B.3.2. OsS_2 target with burnt foil and wet target material..... 191

Figure B.3.3. (A) Represents the kapton foil being able to dissipate heat through the aluminum backing. (B) Represents the OsS_2 target which was not able to dissipate heat and burned through 192

LIST OF TABLES

Table 1.1.1 Modes of Radioactive Decay Commonly Used in Radiopharmaceutical Drugs[12] 3

Table 2.1.1. Identified iridium and rhenium isotopes produced from a 46 mg $^{nat}OsS_2$ target with their half-lives, utilized gamma energies, and produced activities at the end of bombardment. 33

Table 2.1.2. Comparison of theoretical and experimental production rates for the $^{nat}OsS_2$ target irradiated at MURR 34

Table 2.1.3. Percentage of rhenium and iridium isotopes found in each aqueous and organic layer, and on the alumina column using the OsS_2 sample quantified in Table 2.1.1..... 35

Table 2.1.4. Identified iridium, rhenium, and osmium isotopes produced from an 8.5g ^{nat}Os metal target with their half-lives, utilized gamma energies, and produced activities at the end of bombardment. 37

Table 2.1.5. Comparison of theoretical and experimental production rates for the ^{nat}Os metal target irradiated at BNL 38

Table 2.2.1. Rhenium and tungsten tracer information (per sample)..... 45

Table 2.2.2. Activities of identified rhenium isotopes at the end of bombardment, 581 mg $^{nat}WS_2$ target, 11 MeV protons, 10 μAh 53

Table 2.2.3. Comparison of theoretical and experimental production rates for the $^{nat}WS_2$ target irradiated at MURR 54

Table 2.2.4. Activities of identified rhenium isotopes at the end of bombardment, 139 mg $^{nat}WS_2$ target, 14 MeV protons, 10 μAh 54

Table 2.2.5. Comparison of theoretical and experimental production rates for the $^{nat}WS_2$ target irradiated at MURR 55

Table 2.2.6. Comparison of natural abundance tungsten to purchased enriched ^{186}W and the resulted effect to rhenium isotope production rates 55

Table 2.2.7. Thermodynamic characteristics of Re adsorption on AG 1-X8 resin 62

Table 2.2.8. Retention volumes based on K_d. Calculation assumes 1.0 cm^3 bed of resin.66

Table 2.2.9. Tungsten target irradiations at BNL and their respective irradiation parameters 70

Table 2.2.10. Rhenium isotope activities at end of bombardment for tungsten targets irradiated at BLIP 70

Table 2.2.11. Comparison of theoretical and experimental production rates for the ^{nat}W metal target irradiated at BNL 71

Table 2.2.11. ^{nat}W irradiation data extrapolated to enriched ^{186}W 71

Table 3.1.1. Evaluated selenium and arsenic isotopes and their associated gamma emissions 78

Table 3.1.2. Experimental yield of $^{72,73,75}Se$ from As target and comparison to theoretical yield 85

Table 3.2.1. Evaluated germanium and arsenic isotopes and their associated gammas .. 92

Table 4.1.1. Scandium isotopes produced from a 127.8 mg $CaCO_3$ target with their half-lives, utilized gamma energies, and produced activities at the end of bombardment 112

Table 4.1.2. Comparison of theoretical and experimental production rates for the $^{nat}CaCO_3$ target irradiated at MURR 113

Table 4.2.1. Activities of identified technetium isotopes at the end of bombardment, 102.3 mg $^{nat}MoS_2$ target, 16 MeV protons, 10 μAh 119

Table 4.2.2. Comparison of theoretical and experimental production rates for the $^{nat}MoS_2$ target irradiated at MURR 120

Table 4.2.3. Activities of identified molybdenum and technetium isotopes at the end of bombardment, 284.5 mg $^{nat}MoS_2$ target, 8.5 MeV deuterons, 10 μAh 120

Table A.2.1. Target materials and the intended irradiation parameters including the desired entry and exit projectile energy, the desired thickness, and the thickness to fully stop the projectile 146

Table A.2.2. SRIM calculated stopping power for the proton bombardment of osmium metal 147

Table A.2.3. SRIM calculated stopping power for the proton bombardment of osmium disulfide 149

Table A.2.4. SRIM calculated stopping power for the proton bombardment of tungsten metal 151

Table A.2.5. SRIM calculated stopping power for the proton bombardment of tungsten disulfide 153

Table A.2.6. SRIM calculated stopping power for the alpha particle bombardment of germanium metal 155

Table A.2.7. SRIM calculated stopping power for the proton bombardment of calcium carbonate 157

Table A.2.8. SRIM calculated stopping power for the proton bombardment of molybdenum disulfide 159

Table A.2.9. SRIM calculated stopping power for deuteron bombardment of molybdenum disulfide 161

Table A.3.1. Potential nuclides produced via proton bombardment of a natural abundance osmium target..... 164

Table A.3.2. Theoretical cross sections and calculated activities for the proton bombardment of natural abundance osmium targets 166

Table A.3.3. Literature cross sections and calculated activities for the proton bombardment of natural abundance tungsten disulfide targets at MURR 167

Table A.3.4. Literature cross sections and calculated activities for the proton bombardment of a natural abundance tungsten metal targets at BNL 168

Table A.3.5. Potential nuclides produced via proton bombardment of a natural germanium target 169

Table A.3.6. Theoretical cross sections and calculated activities for the alpha particle bombardment of a natural abundance germanium metal target at UW 170

Table A.3.7. Theoretical cross section and activities for the proton bombardment of a natural abundance calcium carbonate target at MURR 171

Table A.3.8. Literature cross sections and calculated activities for the proton bombardment of a natural abundance molybdenum disulfide target at MURR 173

Table A.3.9. Literature cross section and calculated activities for the deuteron bombardment of a natural abundance molybdenum disulfide target at MURR 173

Table A.4.1. Experimental conditions used for steady state thermal analysis of an osmium metal target..... 177

Table A.4.2. Experimental conditions used for steady state thermal analysis of an osmium disulfide target..... 178

Table A.4.3. Experimental conditions used for steady state thermal analysis of an osmium metal target..... 179

Table A.4.4. Experimental conditions used for steady state thermal analysis of a tungsten metal target..... 180

Table A.4.5. Experimental conditions used for steady state thermal analysis of a tungsten disulfide target 181

Table A.4.6. Experimental conditions used for steady state thermal analysis of a tungsten metal target..... 182

Table A.4.7. Experimental conditions used for steady state thermal analysis of a germanium metal target 183

Table A.4.8. Experimental conditions used for steady state thermal analysis of a calcium carbonate target..... 184

Table A.4.9. Experimental conditions used for steady state thermal analysis of a molybdenum disulfide target 185

Table A.4.10. Experimental conditions used for steady state thermal analysis of a molybdenum disulfide target 186

Table C.1 Rhenium Contact Kinetics Study on AG 1-X8 Resin..... 195

Table C.2 Rhenium Isothermal Kinetics Study on AG 1-X8 Resin 195

Table C.3 Rhenium Adsorption Behavior on AG 1-X8 in Aqueous Media..... 196

Table C.4 Rhenium Adsorption Behavior on AG 1-X8 with Varied Tungsten Concentrations 196

Table C.5 Tungsten Adsorption Behavior on AG 1-X8 in Aqueous Media..... 197

Table C.6 Rhenium and Tungsten Adsorption Behavior on TEVA in Aqueous Media 197

Table C.7 Rhenium Contact Kinetics Study on AnaLig..... 197

Table C.8 Rhenium Isothermal Kinetics Study on AnaLig 198

Table C.9 Rhenium and Tungsten Absorption Behavior on AnaLig in Aqueous Media 198

Table C.10 Arsenate Adsorption Behavior on AG 1-X8 in Aqueous Media 198

Table C.11 Selenate Adsorption Behavior on AG 1-X8 in Aqueous Media..... 199

Table C.12 Selenite Adsorption Behavior on AG 1-X8 in Aqueous Media..... 199

Table C.13 Arsenic Adsorption Behavior on Alumina in Various Media..... 199

Table C.14 Arsenic Adsorption Behavior on Silica in Various Media..... 200

Table C.15 Arsenic Adsorption Behavior on HZO in Various Media..... 200

Table C.16 Arsenic Adsorption Behavior on AG 1-X8 in Various Media 200

Table C.17 Germanium Adsorption Behavior on Alumina in Various Media 201

Table C.18 Germanium Adsorption Behavior on Silica in Various Media 201

Table C.19 Germanium Adsorption Behavior on HZO in Various Media 201

Table C.20 Germanium Adsorption Behavior on AG 1-X8 in Various Media 202

Table C.21 Arsenic Contact Kinetics Study on HZO 202

Table C.22 Germanium Contact Kinetics Study on Silica 202

Table D.1 Separation of Rhenium and Tungsten on a 4 mL AG 1-X8 Column 203

Table D.2 Separation of Rhenium and Tungsten on a 2 mL AG 1-X8 Column 203

Table D.3 Separation of Rhenium and Tungsten on a 0.5 g AnaLig Column with H_2O Eluent 204

Table D.4 Separation of Rhenium and Tungsten on a 0.5 g AnaLig Column with NaCl Eluent 205

Table D.5 Separation of Rhenium and Tungsten on a 0.5 g AnaLig Column with HNO_3 Eluent 206

Table D.6 Separation of Arsenic and Germanium on a Single 1 mL Silica Column 207

Table D.7 Separation of Arsenic and Germanium on Dual 1 mL Silica Column 208

Table D.8.1 Tandem Loading of Arsenic and Germanium on Silica and HZO 209

Table D.8.2 Separated Washing and Elution of Silica Column 209

Table D.8.3 Separated Washing and Elution of HZO Column 210

Table D.8.4 Residual Activity Remaining on the Columns 210

Table D.9.1 Stock Solution Adjusted with HCl 211

Table D.9.2 Stock Solution Adjusted with H_3PO_4 211

Table D.9.3 Stock Solution Adjusted with HNO_3 212

Table D.10 Separation of Scandium and Calcium on a 50 mg DGA Column 212

ACADEMIC ABSTRACT

The continued progress of nuclear medicine is dependent on the availability of high specific activity (HSA) radionuclides. As cancer incidence rates continue to climb, research into improving existing methods and development of new radionuclides is critical to meet future demands. In this research, various production pathways were evaluated and processing methods developed to produce HSA radionuclides for imaging and therapy. ^{99m}Tc is used in over 80% of all nuclear medicine studies. In this research, a novel target material was used to directly produce ^{99m}Tc from ^{100}Mo. With the extensive use of ^{99m}Tc-based imaging agents, therapeutic rhenium analogues are highly desirable. ^{186}Re has favorable nuclear properties for therapy, but is hindered by its current reactor production pathway, which results in a low specific activity product. This research evaluated several accelerator-based production pathways bombarding W and Os targets to make HSA ^{186}Re. By making ^{186}Re available for therapy, drug systems utilizing a ^{99m}Tc/^{186}Re diagnostic/therapeutic isotope pair can be developed. Another diagnostic/therapeutic pair of interest in this research is ^{72}As/^{77}As. ^{72}As is a positron emitting radionuclide with attractive nuclear properties. It has a relatively long half-life compared to most PET radionuclides enabling imaging using slower localizing targeting vectors such as antibodies and proteins. ^{77}As is a β^- emitting radionuclide, which can be used for therapy. Several accelerator-based production pathways are being evaluated and are demonstrating production methods to make HSA ^{72}As and ^{77}As clinically available. ^{44}Sc is another PET radionuclide of interest. Irradiations were performed to demonstrate the production of ^{44}Sc using Ca- and Ti-based targets. As treatments advance and new

radiopharmaceuticals are designed, research focused on isotope production is critical to the continued growth and success of the nuclear medicine field.

Chapter 1: Introduction

1.1 Basics of Radiopharmaceuticals

The use of radionuclides in medicine began when George de Hevesy used ^{210}Pb and ^{210}Bi to study the metabolism of bismuth in rabbits in 1924, thus establishing the tracer principle[1]. Today, it has grown into an expansive medical modality with over 37 million nuclear medicine procedures being performed every year[2]. Diagnostic imaging accounts for 95% of the nuclear medicine procedures performed with the rest being used for therapeutic applications. Radiopharmaceuticals usually have minimal pharmacological effects, since they are administered at tracer quantities. Depending on their target, radionuclides are used either in ionic form, chelated in an appropriate complex, or labeled to appropriate molecules[1,3,4]. Radiopharmaceuticals are typically injected intravenously. Once in the body, they circulate in the blood stream and eventually accumulate at the targeted site and clear from the rest of the body. Diagnostic radionuclides emit gamma rays (or annihilation photons resulting from positron emission), which are detected by an external detector; the origin of emission can be determined from the trajectory, which allows the target site to be imaged[5]. Therapeutic radionuclides deliver a large dose of ionizing radiation, which damages the DNA within a target cell causing cell death[6]. Cancer cells are rapidly dividing and cannot repair the damage quickly enough resulting in cell destruction. Damage is minimized to surrounding healthy tissues, which can repair their DNA quickly enough if not excessively damaged[7]. Ideally, a diagnostic/therapeutic paired pharmaceutical could be utilized. The diagnostic

radiopharmaceutical is used first to image the cancer site with a low dose radiotracer and calculate the optimized dose. Next, the same pharmaceutical, now with therapeutic radionuclide, is used to deliver strong ionizing radiation to kill the target cells with minimal toxicity to normal tissues.

1.2 Modes of Radioactive Decay Commonly Used for Radiopharmaceutical Drugs

Thousands of radionuclides exist but only a select few have the desired nuclear and chemical properties to be utilized as medical radionuclides. Easily the most important characteristic of the radionuclide is its nuclear decay properties. The process by which the radionuclide decays determines its medical application. Radionuclides are unstable because they contain either too many protons or too many neutrons in their nucleus. If this imbalance is greater than the nuclear forces holding the nucleus together, the nucleus will decay and emit radiation in the form of energetic photons and charged particles in order to become stable[8]. Radionuclides that give off energetic photon emissions are well suited to imaging, while radionuclides whose decay results in the emission of charged particles are well suited to therapeutic applications. Photons of the right energy easily penetrate through body tissue and create significantly fewer ionization events along their path compared to charged particles; this reduces the effect to healthy tissues and allows for a smaller dose to visualize the targeted cells[9]. Charged particles deliver a large, therapeutic dose of ionizing radiation to the targeted disease cells while minimizing damage to the surrounding healthy tissues[9]. It is important to select the type of decay and energy most appropriate for the intended target. Alpha particles deliver a large dose of

radiation over short ranges (up to 100 μm) while beta particles distribute a smaller dose of radiation over a larger range (up to 1500 μm)[10,11]. Table 1.1 summarizes the types of radioactive decay commonly used in radiopharmaceutical drugs and their intended applications.

Table 1.1.1 Modes of Radioactive Decay Commonly Used in Radiopharmaceutical Drugs[12]

Decay Mode:	Decay Scheme:	Application:	Examples:
Alpha Decay	${}^{A}_{Z}X \rightarrow {}^{A-4}_{Z-2}Y + {}^{4}_{2}He$	Therapy	^{223}Ra, ^{225}Ac
Beta Decay	${}^{A}_{Z}X \rightarrow {}_{Z+1}{}^{A}Y + {}^{0}_{-1}e + \bar{\upsilon}$	Therapy	^{186,188}Re, ^{131}I, ^{90}Y, ^{153}Sm
Positron Emission	${}^{A}_{Z}X \rightarrow {}_{Z-1}{}^{A}Y + {}^{0}_{+1}e + \upsilon$ ${}^{0}_{+1}e + {}^{0}_{-1}e \rightarrow 2\gamma$	Imaging	^{18}F, ^{15}O, ^{11}C, ^{67}Ge, ^{82}Rb
Electron Capture	${}^{A}_{Z}X + {}^{0}_{-1}e \rightarrow {}_{Z-1}{}^{A}Y + \gamma + \upsilon$	Imaging	^{67}Ga, ^{111}In, ^{123}I, ^{201}Tl
Isomeric Transition	${}^{A}_{Z}X^{*} \rightarrow {}^{A}_{Z}X + \gamma$	Imaging	^{99m}Tc

1.2.1 Alpha Decay

Alpha decay is characteristic of high mass radioactive nuclei (predominant with A ≥ 210). In alpha decay, the equivalent of a helium nucleus, $^{4}He^{2+}$, is ejected from the parent nucleus in order to achieve a more stable proton-to-neutron ratio. The daughter nucleus may still be unstable and can further decay to achieve a more stable conformation. Alpha particles are highly energetic with kinetic energies typically ranging between 4 – 9 MeV, and due to their relatively large size and high charge-to-mass ratio, they readily interact with surrounding matter and frequently create ionization events along their path[9,11]. Alpha particles are the most ionizing, natural source of radiation occurring at a rate of approximately one ionization for every angstrom traveled. This high linear energy transfer translates into the alpha particle being very destructive in

a biological system over a very short range (up to 100 μm). For this reason, a targeting vector is typically necessary to localize the radiopharmaceutical at the target site to destroy the diseased cells and minimize the damage to healthy cells. With the continued improvement of drug delivery systems, targeted alpha therapy is a growing field within radiopharmaceuticals with heavy interest in ^{225}Ac, ^{211}At, and ^{223}Ra[10].

To date, ^{223}Ra ($t_{1/2}$ = 11.43 d, 5.176 MeV α (51.6%), 269.5 keV γ (13.9%)) is the only alpha emitting radionuclide approved by the United States Food and Drug Administration (FDA) for clinical use (Xofigo ®); a solution of $^{223}RaCl_2$ is injected intravenously to treat patients with castration-resistant prostate cancer with symptomatic bone metastases and no known visceral metastatic disease[13]. Due to the chemical similarity of the alkaline earth metals, $^{223}Ra^{2+}$ will function as a Ca^{2+} mimic; it complexes with the bone mineral hydroxyapatite at sites of actively growing bone, which occurs at an accelerated rate within metastatic bone tissue[13,14]. As mentioned previously, heavy nuclei decaying by alpha particle emission commonly undergo several decays prior to reaching a stable isotope. Radium-223 and its daughters decay and eject four alpha particles and two beta particles before ending at ^{207}Pb (Figure 1.2.1); this delivers a large dose of ionizing radiation over a short range (<10 cell diameters), damaging the DNA of cells within the targeted range, and ultimately killing the metastatic cells[13].

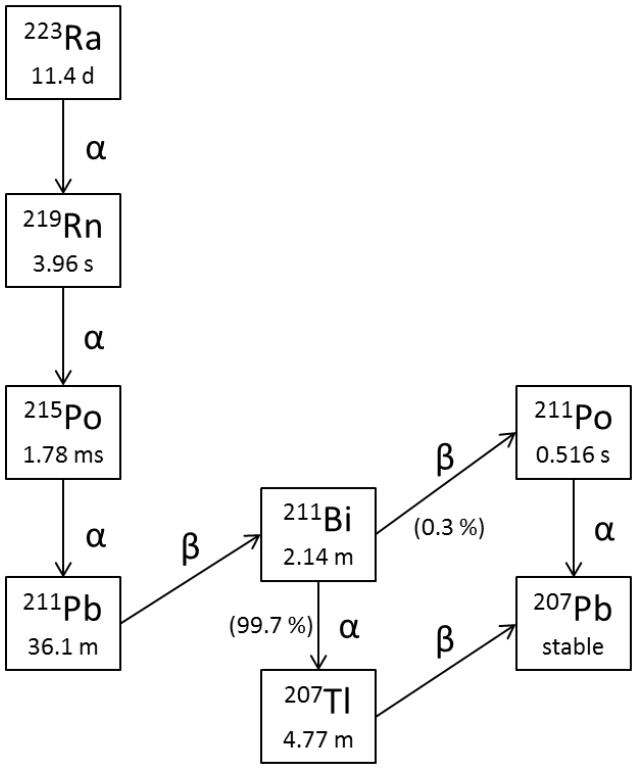

Figure 1.2.1. ^{223}Ra decay scheme

1.2.2 Beta Decay

There are several types of beta decay, but the generic term beta decay is usually associated with beta minus (β^-) decay; this type of beta decay is observed with neutron-rich isotopes. In beta decay, a neutron is converted into a proton to achieve a more stable proton-to-neutron ratio; an energetic electron (beta particle) is ejected during the process as well as an antineutrino and possibly gamma rays[15]. The ejected electron is significantly lighter than an alpha particle (~8000 times) and less likely to interact with surrounding matter; this lower linear energy transfer leads beta particles to have a significantly larger range than alpha particles (up to 1500 μm)[16]. For this reason, beta emitters find applications to larger tumor sizes than alpha particles[12]. Several targeted

therapies with beta emitters are currently in use. Some interesting examples are [^{131}I]-sodium iodide (HICON^{TM}), which is used to treat hyperthyroidism and certain types of thyroid carcinoma, [^{90}Y]-ibritumomab tiuxetan (Zevalin®), which is used to treat non-Hodgkin's lymphoma, and [^{153}Sm]-lexidronam pentasodium (Quadramet®), which is used to alleviate the pain associated with bone metastases[17–19].

[^{131}I]-sodium iodide ($t_{1/2}$ = 8.03 d, 0.182 MeV β^- (100%)) is an interesting case because it is one of the few radiopharmaceuticals administered orally. Similar to ^{223}Ra, this drug takes advantage of the body's natural transport pathways to localize the drug. Iodide-131 is selectively taken up by the thyroid, which typically maintains an iodide concentration ≥ 25x the concentration found in the plasma. The uptake of ^{131}I is affected by the concentration of stable iodide in the biological system[17]. For this reason, it is common practice to put the patient on a low iodine diet prior to treatment to maximize the uptake. In hyperthyroidism, the thyroid glands are overactive; the radiation dose is used to kill a portion of these overactive cells to reduce the thyroid activity to normal working level[17].

[^{90}Y]-ibritumomab tiuxetan is an interesting case because it was the first radioimmunotherapy drug to be approved by the FDA[18]. Radioimmunotherapy is a form of radiotherapy where the radionuclide has been bound to a monoclonal antibody. The monoclonal antibody acts as the targeting vector, which carries the radionuclide to a specific antigen within the body. For this treatment, ^{90}Y ($t_{1/2}$ = 64.053 h, 0.934 MeV β^- (100%)) is carried to the antigen CD20, which is found on the surface of lymphocytes, including cancer cells associated with B-Cell non-Hodgkin's lymphoma[18]. It is necessary to use a sufficiently long-lived radionuclide such as ^{90}Y because of the slow localization

times for the monoclonal antibodies. Once localized, the ^{90}Y can deliver the ionizing radiation to destroy the cancer cells[18].

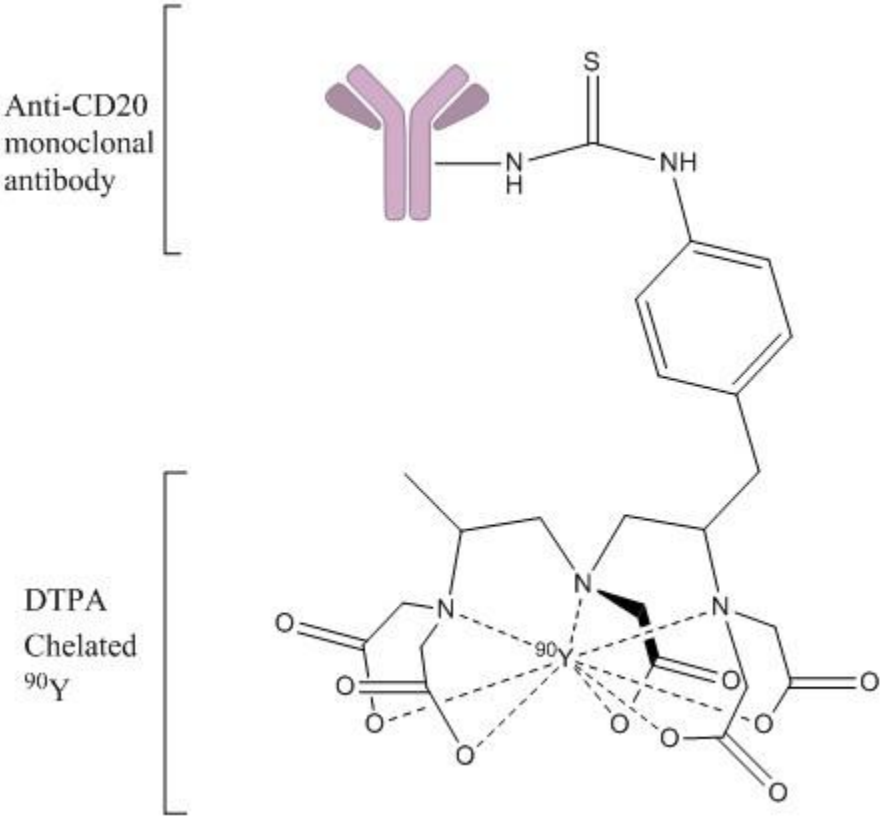

Figure 1.2.2. [^{90}Y]-ibritumomab tiuxetan (Zevalin®)

[^{153}Sm]-lexidronam pentasodium is an interesting case because the actual reaction mechanism of the drug is not fully understood. It is known that [^{153}Sm]-lexidronam will preferentially accumulate at the site of osteoblastic lesions over healthy bone (5:1 ratio). In a similar manner to radium, it is believed to be concentrating at the site of actively growing bone associated with hydroxyapatite. ^{153}Sm is a beta emitter ($t_{1/2}$ = 46.284 h, 0.224 MeV β^- (100%)) and once localized, can deliver ionizing radiation to kill the metastatic cancer cells[19].

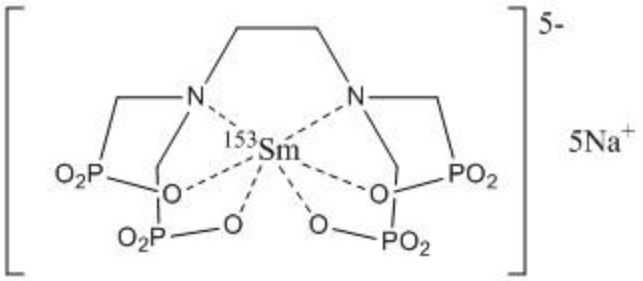

Figure 1.2.3. [^{153}Sm]-lexidronam pentasodium (Quadramet®)

1.2.3 Positron Emission

Positron emission (β^+) is another form of beta decay exhibited by proton-rich radionuclides. Instead of ejecting an electron, a particle with the same mass but positively charged called the positron is released. In this decay process, a proton is converted into a neutron with the ejection of a positron as well as a neutrino and possibly gamma rays[15]. A unique attribute of a positron is its interaction with surrounding matter; it will deposit most of its energy along its path interacting with surrounding matter, and ultimately, it collides with an electron and they annihilate. In this annihilation event, the particles are converted into two 511 keV photons, which are emitted approximately 180° apart from one another[12]. This unique emission of photons have allowed for the development of an imaging technique known as Positron Emission Tomography (PET)[12].

PET uses an imager consisting of circular array of scintillation detectors, which have been optimized for 511 keV photons. For the instrument to record a radiation event, both photons must be registered simultaneously at detectors ~180° separated; this is known as coincidence. The coincidence events are used to pinpoint the source of the emission to reconstruct an image of tumor site[20]. To minimize distortion and image blur, selecting

radionuclides that emit positrons with low kinetic energy are more ideal since the positrons will travel a shorter distance prior to their annihilation[20].

Most positron emitters currently in use are short-lived, non-metals such as ^{18}F ($t_{1/2}$ = 109.8 m), ^{11}C ($t_{1/2}$ = 20.4 m), ^{15}O ($t_{1/2}$ = 2.04 m), and ^{13}N ($t_{1/2}$ = 10.0 m). These isotopes have been used in many capacities but ^{18}F-2-fluoro-2-deoxyglucose ([^{18}F]FDG) is the long standing workhorse of PET imaging[12,20].

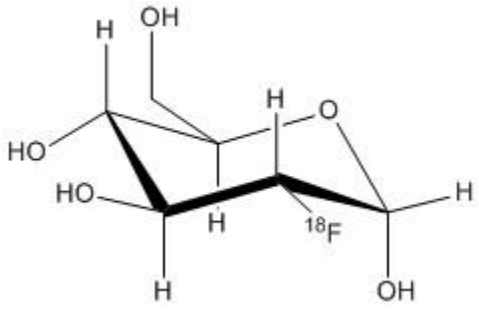

Figure 1.2.4. ^{18}F-2-fluoro-2-deoxyglucose

[^{18}F]FDG is a commercially available analog of glucose that is utilized to index glucose metabolism. [^{18}F]FDG is injected intravenously and acts similarly to glucose; it is transported from the blood to active tissues that are metabolizing glucose[20]. Once inside the tissue, it is phosphorylated to FDG-6-phosphate; this FDG-6-phopshate remains in the tissues because it cannot undergo glycolysis. The 2' hydroxyl group in normal glucose is necessary for glycolysis, but [^{18}F]FDG does not contain the hydroxyl group until the fluorine-18 decays to oxygen-18; once the fluorine decays to oxygen, the hydroxyl group is formed and the molecule becomes glucose-6-phosphate, glycolysis can then proceed as normal[20]. Typically PET studies with [^{18}F]FDG require the patient to be injected with the drug and wait an hour to allow the sugar to distribute into the tissues of the organs that

utilize glucose (heart, lungs, brain, and kidneys). During this time, movement is minimized to reduce the amount of glucose transported to the muscles. The patient is the placed into the PET scanner for a series of scans. The image gives a good indication of the glucose distribution in the body and in the brain[20].

1.2.4 Isomeric Transition and Electron Capture (Gamma Emitters)

Single Photon Emission Computed Tomography (SPECT) is the other major diagnostic imaging modality. SPECT uses characteristic gamma-rays from the decay of a radionuclide, which are detected by a large, mobile NaI scintillation detector. The detector is rotated around the patient and takes a series of 2D images which are reconstructed by a computer to create the 3D image[5]. The detector consists of group of NaI crystals, a collimator, and an array of photomultiplier tubes. The collimator only permits gamma rays traveling directly at the crystals to be detected, which provide a clearer, sharper image. The photomultiplier tubes amplify the signal received by the crystal, which is then output to a computer. The data is reconstructed by a computer to construct the image[5]. Two primary radiation decay schemes are utilized for SPECT, isomeric transition and electron capture.

1.2.4.1 Isomeric Transition

It is very common for a gamma emission to occur following other nuclear decay. The nucleus is in an excited state following the decay and emits a gamma ray to lose energy and reach a lower energy state[21]. Isomeric transition is a special excited nuclear state, referred to as the metastable state; this metastable nucleus has a measurable, significantly longer half-life compared to the excited state following other nuclear decay[21]. A well-

known example of a metastable radionuclide is ^{99m}Tc. Technetium-99m is the most commonly used radionuclide in nuclear medicine; it is used in more than 80% of all nuclear medicine procedures performed each year[2,12].

The success of ^{99m}Tc is due to its favorable nuclear properties; it has a single photon emission at 140.5 keV, which is fairly optimal for penetrating the body and easily being collimated in the NaI detector. Additionally, it has a short half-life of 6.004 h, making its use safe as an outpatient procedure. To date, seventeen ^{99m}Tc-bassed radiopharmaceuticals have been approved for use by the FDA; they are utilized for a variety of applications such as imaging brain function[22], evaluating myocardial perfusion[23], and determining renal function[24].

An interesting example of a ^{99m}Tc-based radiopharmaceutical is the brain imaging agent [^{99m}Tc]-exametazine (Ceretec^{TM}). The active drug, [^{99m}Tc]-exametazine, crosses the blood brain barrier and can be utilized to image blood flow to the different regions of the brain. Abnormal or reduced blood flow has been observed in patients with epilepsy, dementia, schizophrenia, Alzheimer's, and strokes[25]. Until recently the chelator, exametazine, was known by its chemical name hexamethylpropyleneamineoxime (HMPAO). The structure of HMPAO is what makes this drug interesting; there is a mixture of three stereoisomers present in the kit formulation (Figure 1.2.5). There is racemic mixture of the d,l enantiomers and a meso form present. All forms of [^{99m}Tc]-HMPAO are uncharged and lipophilic, which allow them to pass through the blood brain barrier, but the d,l enantiomers are unstable and form hydrophilic species and cannot pass through the blood brain barrier[25]. For this reason, the drug must be prepared just before injection to maximize the portion of the drug able to cross the blood brain barrier.

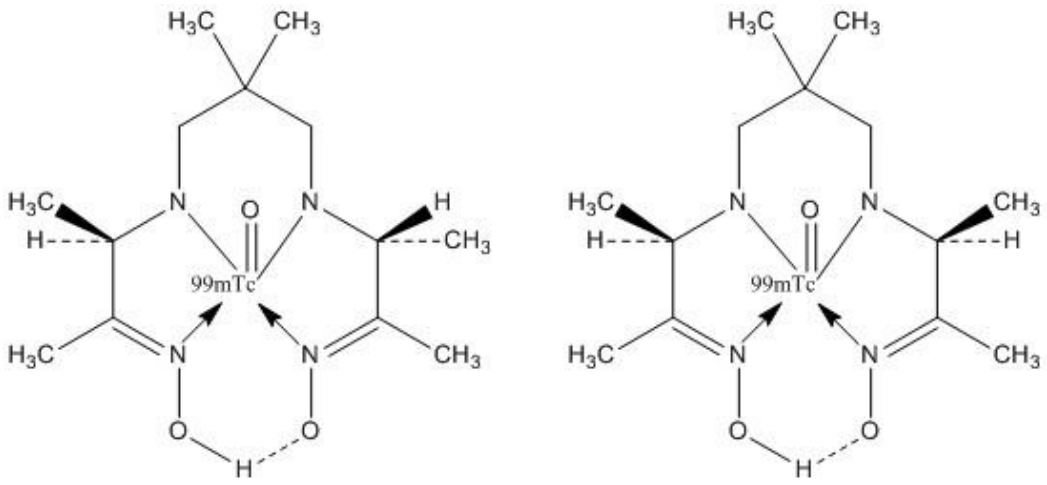

Figure 1.2.5. (left) ^{99m}Tc-exametazine, the d,l isomer (right) meso isomer impurity

1.2.4.2 Electron Capture

Electron capture is a unique form of beta decay observed in proton-rich radionuclides that have too small of an energy difference between the parent radionuclide and the potential decay daughter to decay by positron emission. For positron emission to occur, an energy gap of ≥ 1.022 MeV is required. So instead of emitting a positron, a proton captures an inner orbital electron, converting the proton to a neutron as well as emitting a neutrino and energetic photons (gamma rays)[15]. Since a proton and electron are combined, the nuclide is transmutated into a new element while remaining neutrally charged, but due to the missing inner electron, the atom is now in an excited state. Eventually, an outer shell electron will drop down and fill the gap from the missing electron; this electron is moving from a higher energy state and will emit an x-ray or Auger electron during this process. Additionally, the nucleus is left in an energetic state and may release a gamma ray to relax to a lower energy state. Several radionuclides that decay by electron capture have found use as diagnostic imaging agents. One of the most notable is ^{111}In, which has

found a variety of uses with five FDA approved radiopharmaceuticals[26]. The chemistry of indium (predominantly In(III)) and the favorable nuclear properties ($t_{1/2}$ = 2.80 d, 171.3 keV (90.7%) and 245.4 keV (94.1%) γ-rays) have led to its frequent use.

An interesting application is [^{111}In]-pentetreotide (OctreoScan^{TM}); this drug is a radiolabeled analogue of the peptide ocetreotide used to visualize neuroendocrine tumors. Octreotide is a synthetic peptide, which mimics the naturally-occurring peptide somatostatin. Somatostatin plays an important role in regulating several organ systems; it can inhibit the release of growth hormone, insulin, glucogen and thyrotropin-stimulating hormone. Within these organ systems, there are somatostatin receptors on the various tissue cells. Additionally, tumors growing from these tissues will exhibit a high density of somatostatin receptors as well[27]. Somatostatin has a very short biological half-life (~2 minutes) making it unusable for radiolabelling. [^{111}In]-pentetreotide has a significantly longer biological half-life (~ 6 hours). The patient can be scanned at 24, 48, and possibly 72 hours after injection to get a clear picture of the location and extent of the disease.

1.3 Isotope Production

With the continual growth of nuclear medicine, the field of isotope production is ever evolving to keep pace with the demand. This field traces its beginnings to 1919 when Ernest Rutherford first demonstrated the transmutation of one element into another. In his experiment, he bombarded nitrogen gas with alpha particles from a sample of radioactive polonium; this interaction created oxygen while releasing a proton at the same time[28]. He performed several other experiments to continue to understand the nature of

neutron reactions, but one thing became apparent and that is natural sources of ionizing radiation were not energetic enough and particle emissions occurred too infrequently to completely study nuclear reactivity. Several scientists began devising ways to accelerate atomic nuclei. Cockcroft and Walton developed an accelerator in 1927 using a high-voltage transformer with a voltage multiplier to bombard lithium with alpha particles, demonstrating the ability to produce accelerated nuclei[29], but the real breakthrough came in 1931. Ernest Lawrence and his graduate student, Stanley Livingston, constructed the first cyclotron which was able to accelerate protons to 80 keV. He built several increasingly larger and more powerful cyclotrons, which made it possible to produce a wide array of radioactive nuclides[30]. In the 1940s, the use of nuclear reactors made it possible to produce an even wider array of radionuclides by neutron capture[31]. Skipping forward to today, a large number of radioactive nuclides are produced on a routine basis using both nuclear reactors and particle accelerators.

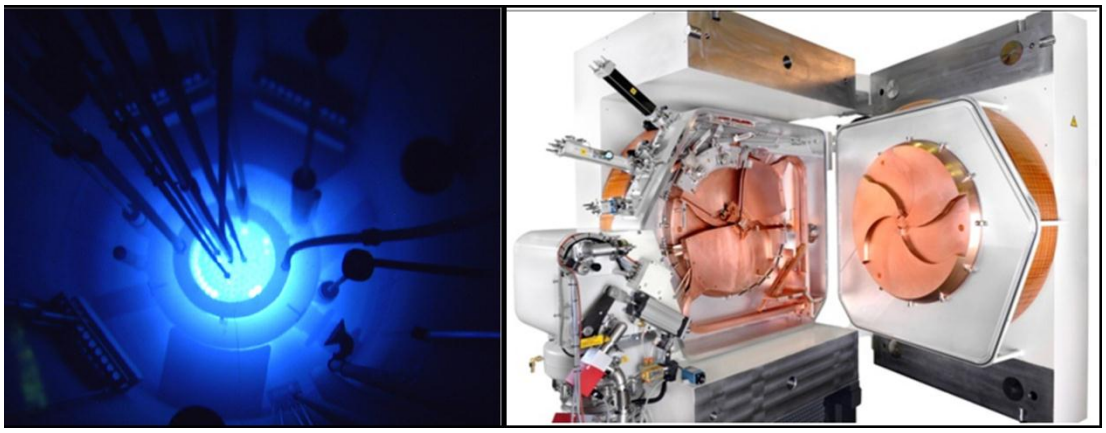

Figure 1.3.1. Examples of a research reactor (left) and medical cyclotron (right) used for radionuclide production.

1.3.1 Production of Radionuclides in Reactors

The fuel of most nuclear reactors is enriched ^{235}U, which is a fissionable material. Upon bombardment with a neutron, ^{236}U is created via the $^{235}U(n, \gamma)^{236}U$ reaction, which quickly fissions (splits) into two smaller Z nuclides and ejects 2.5 neutrons on average[32]. These neutrons further interact with other ^{235}U atoms to create a sustained nuclear chain reaction. Within the core of a nuclear reactor, a massive amount of neutrons are being emitted at any given moment; this enormous number of neutrons is referred to as neutron flux; this neutron flux is used to produce neutron-rich radionuclides[32]. Targets are typically introduced to the neutron flux either by placing the target within a station inside the core assembly, within the reflector pool in the immediate vicinity of the core, or the neutron flux is allowed to "shine" to a location outside of the reactor and bombard the target[32].

There are three main reaction pathways used to produce radionuclides using a nuclear reactor. The most common method is direct production by the (n, γ) reaction on a natural or isotopically enriched target; products of this reaction type are of low specific activity since the produced isotope is the same element as the target material. An example of this would be the production of ^{186}Re via the $^{185}Re(n, \gamma)^{186}Re$ reaction[31]. In this scenario, there is no ability to separate the target and the product since they are the same element. The second method is the production of a parent radionuclide by the (n, γ) reaction, which then beta decays to the isotope of interest. Since the daughter is a different element than the parent, it is possible to separate the product and the target material resulting in a product of high specific activity. An example of this would be the production of ^{188}Re. Rhenium-188 is available from a $^{188}W/^{188}Re$ generator system[31].

The ^{188}W parent is produced in a nuclear reactor by double neutron capture on enriched ^{186}W. Since the daughter is a different element than the parent, it is possible to separate them resulting in a high specific activity product. The third method is by fission of highly enriched ^{235}U (~93% enrichment). The fission products can be isolated from the target and are of high specific activity. For example, ^{99}Mo is currently exclusively made as a product of ^{235}U fission (~6% product) and is used to produce a $^{99}Mo/^{99m}Tc$ generator. In this scenario, both the parent and the daughter are of high specific activity enabling the use of a small generator column, which allows the daughter to be eluted in a small volume[31].

1.3.2 Production of Radionuclides in an Accelerator

In a small medical cyclotron such as the PETtrace at MURR, a tungsten wire filament is utilized to ionize diatomic hydrogen gas (H_2) thus creating H^+ and H^- ions. The H^- ions are selectively accelerated using electromagnetically charged copper dees, which accelerate the ions outward from the center. At the exit of the cyclotron, the beam passes through a stripper foil which removes the electrons and creates the desired H^+ ion. In the electromagnetic field, this ionization change allows the beam of particles to be directed out of the cyclotron. The beam is then directed toward the target using steering magnets and a collimator[33]. Accelerators/cyclotrons produce a beam of positively charged particles ($^1H^+$, $^2H^+$, $^3He^{2+}$, or $^4He^{2+}$) leading to proton-rich radionuclides. For isotope production, accelerators are used to bombard the target material with charged particles over a wide range of energies (up to hundreds MeV). The energy of the incoming particles is important to the observed nuclear reaction. Highly energized particles are more likely to cause the emission of multiple subatomic particles. Since these reactions

involve the conversion of one element to another, the products of accelerator production are commonly of high specific activity. An interesting example involving the energetics of the incoming particle is the production of ^{186}Re. To displace a neutron via the ^{186}W(p, n)^{186}Re reaction, the proton optimally needs to be accelerated to ~10 MeV[34] while displacing multiple subatomic particles via the ^{192}Os(p, α3n)^{186}Re requires a proton at ~24 MeV, which is quite a significant increase in energy[35].

1.3.3 Basics of Targetry

Target composition is incredibly important when producing isotopes. Physically the target is usually a powder, pressed disc, foil, or electrodeposited surface and, though not common with metals, liquid or gas targets are used with non-metal isotope production. The pure metal is frequently used since it provides the highest density of target atoms. Additionally, the metal usually has the highest thermal conductivity and melting point, which provides the most stable target form. Compounds may be used instead; this often occurs when the bare metal characteristics are not safe to be used in the harsh conditions present inside a reactor or accelerator. For example, lutetium oxide, Lu_2O_3, or ytterbium oxide, Yb_2O_3, is used to produce ^{177}Lu to reduce the risk to the reactor during irradiation; this is because lutetium and ytterbium metal are slightly unstable to oxidation in air under standard conditions and burn at higher temperatures to produce their respective oxides[36]. Compounds may also be used to simplify the post-irradiation processing of the target. For example, tungsten oxide, WO_3, may be used in place of tungsten metal since it helps to simplify the post-irradiation dissolution process[31].

Another important consideration is target geometry. In a reactor, the target material is typically completely surrounded by the neutron flux and thus the target geometry is not as important. Conversely, an accelerator uses a directional beam of charged particles so the target must be designed to optimize the nuclear interactions. As the charged particles pass through the target, they deposit energy along their path. If the energy drops below the threshold for the desired reaction, unwanted reactions could occur; this is prevented if the target is prepared to the correct thickness. For example, the production of ^{72}Se via the ^{75}As(p, 4n)^{72}Se reaction occurs optimally with proton energies of 50 MeV, but as the proton energies drop to 35 MeV the (p, 3n) reaction to produce ^{73}Se is favored which decreases the specific activity of the ^{72}Se product[37].

One of the most important concerns in producing radionuclides for radiopharmaceutical applications is specific activity, which is the relative abundance of a radioactive isotope to all isotopes of the same element in a given sample. In many applications, it can be critical to have the high abundance of radioactive atoms or the treatment could be ineffective. For example, radiolabeling tumor-specific antibodies or receptor-specific vectors requires high specific activity because of the limited target sites available to the drug[38]. Conversely, radiopharmaceuticals intended for pain palliation associated with bone metastases can be lower specific activity since there are a large number of targeting sites[38].

1.3.4 Basics of Separation

For isotope production, it is important to develop a rapid, robust separation method to minimize the loss of product during processing and provide a high purity product. For

this reason, most separation procedures for isotope production involve quickly dissolving the target (commonly under heating) followed by some sort of chromatographic separation. Frequently used techniques are ion exchange chromatography, extraction chromatography, liquid-liquid extraction, and precipitation; it is also common for a process to use multiple steps incorporating several techniques.

The production of a $^{99}Mo/^{99m}Tc$ generator is a great example combining ion exchange and extraction chromatography. Molybdenum's oxo chemistry allows it to be easily separated from uranium and the other fission products. One of the major sources of ^{99}Mo is AECL/Nordion (Canada) which uses Al-clad U/Al-alloy targets. The targets are then dissolved in hot nitric acid. The nitrate solution is added to an alumina (Al_2O_3) column. The column is washed with additional nitric acid which allows the uranium and other fission products to elute from the column while molybdate (MoO_4^{2-}) remains bound. Sodium hydroxide is then used to elute the now purified ^{99}Mo, which is then shipped to processing facilities for further purification and generator production. The ^{99}Mo solution is loaded on a Dowex-1 anion exchange column, which is washed with concentrated HCl to remove any remaining impurities. The ^{99}Mo is then pH adjusted to form ammonium molybdate, $(NH_4)_6Mo_7O_{24}$, and eluted from the column using dilute HCl. Alumina is used to form the generator, which adsorbs ^{99}Mo as the molybdate ion. The column has a significantly higher affinity for molybdate than pertechnetate ($^{99m}TcO_4^-$) which is eluted from the column with sterile saline (0.9% NaCl)[39].

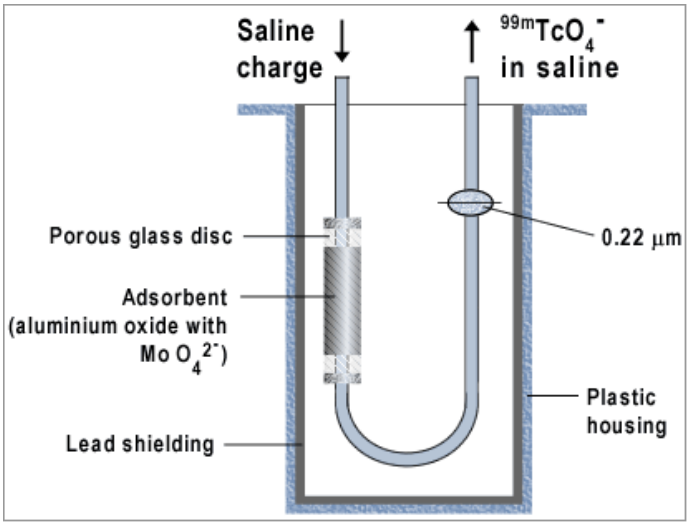

Figure 1.3.2. Schematic of $^{99}Mo/^{99m}Tc$ generator

Another interesting example is a proposed method for the purification of ^{67}Cu. Copper-67 can be produced in a reactor by the $^{67}Zn(n,p)^{67}Cu$ reaction or at an accelerator by the $^{68}Zn(p,2n)^{67}Cu$ reaction. Separation of the tracer quantity of copper from the macroscale zinc is important in preparing a radiopharmaceutical product. The interesting aspect of this production application is the electrolytic separation method[40]. Spontaneous electrodeposition of copper onto platinum electrodes occurs without application of external electromotive force. The overall reduction potential within the cell is a strong enough driving force; the only additions to the cell are sulfate and nitrate ions. A separation factor greater than $1x10^7$ was achieved from gram amounts of zinc with tracer copper in 30 minutes[40].

Chapter 2: Production of ^{186}Re

With the extensive use of ^{99m}Tc-based imaging agents, therapeutic rhenium analogues are highly desirable[12,41,42]. Rhenium-186 emits therapeutic β^- particles with a maximum energy of 1.07 MeV, allowing for a targeted tissue range of 3.6 mm. Additionally, its low abundance γ-ray emission of 137.2 keV (9.42%) allows for *in vivo* tracking of radiolabeled compounds and dosimetry calculations. With a longer half-life of 3.718 days, synthesis and shipment of ^{186}Re-based radiopharmaceuticals is not geographically constrained.

Rhenium-186 can be produced either in a reactor or in an accelerator. Currently, ^{186}Re is produced in a reactor *via* the ^{185}Re(n,γ) reaction resulting in low specific activity, which limits its therapeutic applications[43,44]. Production in an accelerator, such as the PETtrace at the University of Missouri Research Reactor (MURR), can theoretically provide a specific activity of 34,600 Ci*mmol^{-1} Re, which represents a 62 fold increase over reactor-produced ^{186}Re. Previously reported studies on accelerator-based production of ^{186}Re primarily used tungsten targets[34,45–49] while osmium target studies were limited[35]. Additional publications report the use of osmium targets to produce platinum and iridium isotopes[50–53]. Production of clinical activities of ^{186}Re necessitates the use of thick, isotopically-enriched tungsten or osmium targets; the current target preparation methods do not meet this need.

The overall purpose of the project is to develop a robust method for producing HSA ^{186}Re. It is expected the resultant method will enable better clinical use of ^{186}Re. The use

of ^{186}Re provides a great opportunity to make therapeutic analogues of existing ^{99m}Tc diagnostic agents since these group VII metals have similar chemical properties. The diagnostic/imaging pair would make it possible to image the tumor site with low radiation dose to determine the optimal therapeutic dose to maximize targeted cell destruction and minimal toxicity.

Several accelerator-based production pathways that bombarded tungsten and osmium targets with protons and deuterons were evaluated for producing HSA ^{186}Re. The evaluated reaction pathways were: ^{186}W(p ,n)^{186}Re, ^{186}W(d, 2n)^{186}Re, ^{189}Os(p, α)^{186}Re, and ^{192}Os(p, α3n)^{186}Re. Studies focused on target design to determine the optimal production rate with the highest radionuclidic purity and yield. Proton bombardment of tungsten and osmium were studied at MU. Proton bombardment of osmium was additionally studied at the University of Washington (UW) and Brookhaven National Laboratory (BNL). Due to deuteron energy requirements the ^{186}W(d, 2n)^{186}Re reaction was studied by collaborators at UW. Proton bombardment of tungsten was also performed at Los Alamos National Laboratory (LANL) that provided rhenium for separation studies.

2.1 ^{186}Re Production *via* Proton Bombardment of Osmium Targets

2.1.1 Materials and Methods

All reagents and sodium hydrosulfide were purchased from Fisher Scientific (Pittsburgh, PA). Osmium metal powder (99.95% metals basis) was purchased from Alfa Aesar (Ward Hill, MA). Fused osmium metal targets (99.9% metals basis) were purchased

from Princeton Scientific, Corp. (Easton, PA). Acidic alumina was purchased from Sigma Aldrich (St. Louis, MO). Sep-paks (alumina, silica, and cation exchange) were purchased from Waters (Tauton, MA). Poly-prep chromatography columns (0.8 cm ID; 10 mL reservoir) and Glass Econo-Columns (1.0 cm ID; 10 mL reservoir) were purchased from Bio-Rad (Hercules, CA). 20 mL HDPE scintillation vials with polyethylene caps (referred to as poly collection vials) were purchased from Fisher Scientific. Aluminum metal backings were prepared on-site (both at MU and BNL) to designed specifications using 6061 grade aluminum purchased from McMaster-Carr (Elmhurst, IL) and Yarde Metals (Hauppague, NY). Commercial food-grade aluminum foil was purchased from a local market. Araldite 2011 epoxy adhesive was purchased from Freeman Supply (Avon, OH). All reagents and materials were used as received without any further purification. All water used was purified on-site (deionized water fed into a Millipore system to > 18 MΩ·cm).

2.1.1.1 Instrumentation

Raman spectroscopy was performed by Bennett Smith at UW using an Action SepctroPro 500i spectragraph with a Princeton L-N2 cooled Si detector, a 532 nm laser light source from Coherent Compass powered to 850 μW, and a collection time of 150 seconds. Powder x-ray diffraction was performed by Bennett Smith at UW using a Bruker D8 Discover with a general area detector diffraction (GADD) system, using Cu-K alpha (1.5418 Å) x-rays and a collection time of 100 seconds. Elemental sulfur analysis was performed by Atlantic Microlab, Inc. (Norcross, Ga).

Proton irradiations at MURR were performed using a GE PETtrace 800 cyclotron with dual particle capabilities with energies up to 16.5 MeV for protons and 8.5 MeV for deuterons and with currents up to 80 microamps. Proton irradiations at BNL were performed at the Brookhaven Linac Isotope Producer (BLIP). BLIP is a linear accelerator capable of proton energies up to 200 MeV and currents up to 115 microamps. Neutron irradiations were performed using the 10 MW light-water moderated reactor at MURR, which uses a flux-trap design to produce a neutron flux up to $4.5 \cdot 10^{14}$ $n \cdot cm^{-2} \cdot s^{-1}$.

Radiochemical assays at MURR for ^{186,188,189}Re, ^{186,187,188,189,190}Ir were performed by γ-ray spectrometry using a Canberra Model GC2018S HPGe detector system (60.5 mm diameter, 30.5 mm length) at a sample distance of 5 mm from the window. The detector has a FWHM at 1.33 MeV of 1.8 keV. Spectral analyses were performed with Canberra Model 9600 multichannel analyzer. All samples were counted for at least 600 seconds and decay corrected to the time correlating to the end of target bombardment. The detector dead time was kept to less than 10 % for all samples.

Radiochemical assays at BNL for ^{186,188,189}Re, ^{186,187,188,189,190}Ir, and ^{185,191}Os were determined by γ-ray spectroscopy using an HPGe detector system. The detector was an Ortec Model GMX-18190-P HPGe detector system with a relative efficiency of 13.4% at 1.33 MeV. The detector diameter was 48.2 mm, detector length was 45.5 mm, and the distance from the window was 3 mm. The detector's specified FWHM at 1.33 MeV was 1.76 keV. Spectrum analyses were performed by an Ortec DSPEC Jr. 2.0 multichannel analyzer. All samples were counted for at least 1200 seconds and decay corrected to the time correlating to the end of target bombardment. The detector dead time was kept to less than 10 % for all samples.

2.1.1.2 Synthesis and Characterization of Osmium Disulfide at MU

Osmium metal (~100 mg) was dissolved in the distillation impinger using 10-15 mL of 12% NaOCl with gentle heating (45° C) to oxidize the osmium to osmium tetroxide, OsO_4 (Figure 2.1.1). *Caution! Do not perform osmium distillation outside of a hood or glove box. The potential release of osmium tetroxide can pose a significant health risk to the operator.* Once the sample was fully dissolved, the temperature was increased to 90° C to distill osmium tetroxide under argon gas flow. Osmium was captured as potassium perosmate, $K_2[OsO_4(OH)_2]$, in a second impinger containing 5-10 mL of a 25% w/v KOH solution. Distillation is complete when the NaOCl solution is colorless. The potassium perosmate solution was transferred to a centrifuge tube and an additional 5-10 mL of 25% w/v KOH was added to ensure the sample was highly basic. Sodium hydrosulfide (5-10 mL of 10% w/v) was then added to the potassium perosmate solution; osmium disulfide precipitates immediately as a black solid. Osmium disulfide was serially washed with several aliquots of water and acetone by agitating the sample, centrifuging to separate precipitate and supernatant, and decanting the supernatant. Osmium disulfide was then annealed at 575° C for three hours in a tube furnace and allowed to slowly cool to room temperature; all high temperature work was performed under argon gas flow to prevent osmium interaction with atmospheric oxygen. Osmium disulfide was characterized by Raman spectrometry, x-ray diffraction, and elemental sulfur analysis.

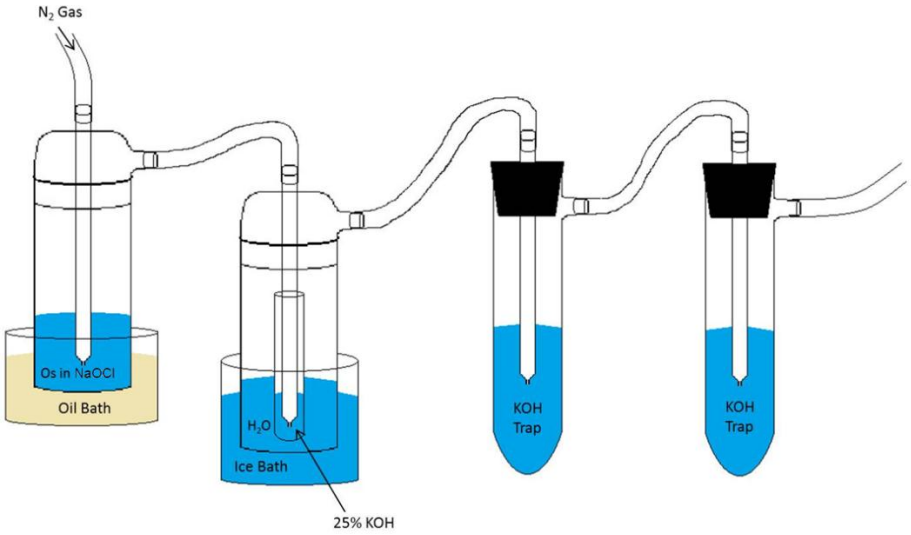

Figure 2.1.1. Osmium Distillation Setup

2.1.1.3 OsS_2 Target Preparation and Irradiation at MU

Using a hydraulic press, OsS_2 was either pressed directly into an aluminum-metal backing or pressed using a 13 mm die to form a pellet and transferred to aluminum backing (Figure 2.1.2). The osmium disulfide pellet was smooth and firmly packed at a pressure of 13.8 MPa. The target was sealed in the backing using 16 µm thick aluminum foil, which was epoxied in place. The epoxy was allowed to cure for a minimum of 15 hours per the manufacturer's specifications. The osmium disulfide targets were irradiated at MURR for 1 hour with a 10 µA current of 16 MeV protons. High vacuum was used on the target face while the back side of the target was water cooled to dissipate heat from the proton beam.

Figure 2.1.2. (left) Aluminum backing used for target irradiations (right) 13 mm pellet die used to prepare pressed targets

2.1.1.4 OsS_2 Dissolution and Separation at MU

The osmium disulfide material was mechanically separated from the target body and dissolved in 5-10 mL of 12% NaOCl with gentle heating (45° C). Once the material was dissolved, NaOH was added to the solution to increase the pH to ≥ 14. A small aliquot of this solution was collected to determine activation products produced and relative abundances. Liquid-liquid extraction was performed using 10 mL of methyl ethyl ketone (MEK) as the organic media. The aqueous layer turned black upon agitation and heat was generated. The layers were collected in separate scintillation vials. Additional impurities were removed from the rhenium product by extraction of the initial MEK solution with an additional 10 mL of 1 M NaOH. Similarly, additional rhenium was recovered from the first aqueous layer by extraction with an additional 10 mL aliquot of MEK. All aliquots were collected in separate poly collection vials. Both MEK layers were then passed through a MEK-conditioned alumina column to further purify the

isolated rhenium product. All samples were analyzed by γ-spectroscopy using an HPGe detector to identify and quantify the activation products produced.

2.1.1.5 Further Optimization of OsS_2 Separation/Purification Method at MU

To profile the osmium separation, an osmium radiotracer sample was prepared. Osmium metal (10 mg) was irradiated in the reactor at MURR to produce Os-191 ($t_{1/2}$ = 15.4 d; γ = 129.4 keV (26.5%)) as a radiotracer. Once irradiated, osmium metal was converted to OsS_2 by the previously described method. The tracer was added to a cyclotron-irradiated target and the dissolution method performed as described with one exception; instead of purifying the MEK aliquots with an alumina column, various (alumina, silica, and cation exchange) sep-paks were tested to determine which chromatographic material most effectively separated osmium and iridium impurities from the rhenium product. For each chromatographic material, A 3 mL aliquot of the first MEK extraction was passed through the sep-pak and then 7 mL of fresh methanol was passed through to wash the column and recover any remaining rhenium. The entire sample was collected into a single poly collection vial and counted by gamma spectroscopy using an HPGe.

2.1.1.6 Os Metal Target Preparation and Irradiation at BNL

Fused Os metal targets were purchased from a commercial source for these irradiations. The target dimensions were measured using calibrated calipers to ensure accurate measurements. An insert was then cut into the backing of the aluminum target can to accommodate the sized Os target. The target can, target, and bolts were all placed into a glove box and pumped down under helium gas. The target was assembled and bolted securely shut under helium gas flow. The target was then removed from the glove box,

wiped down, and tested for helium gas leak. The sealed target was then irradiated for 30 minutes with an average current of 30 μA of 30 MeV protons (entry energy into target).

2.1.1.7 Os Metal Target Dissolution at BNL

Post irradiation, the osmium target assembly was transferred into a hot cell at the target processing laboratory (TPL) due to the dose. The target can was opened and the Os disc was transferred to a 500 mL Erlenmeyer flask for dissolution. The flask was connected to an inlet for nitrogen gas and an outlet to a second Erlenmeyer flask containing 200 mL of 25% w/v KOH to prevent any volatilized OsO_4 from escaping into the hot cell or adjacent hot cells. 200 mL of 12% NaOCl was added to the dissolution flask, the system closed, and gas flow initiated over the solution. A mechanical stir bar was added to agitate the solution and to mechanically abrade the surface of the disc. Gentle heating (45° C) was used to increase the rate of dissolution. Once the target had fully dissolved, 30 μL aliquots of both the dissolution solution and KOH trap were pipetted into a clean poly counting vial, diluted to 3 mL for the correct counting geometry, and counted on an HPGe detector to qualify and quantify the radioisotopes produced during the irradiation.

2.1.2 Results and Discussion

2.1.2.1 OsS_2 Synthesis and Characterization

The production of OsS_2 was successfully achieved in high yield (93 ± 13 %; n = 3) by reacting potassium perosmate with sodium hydrosulfide under basic conditions. Several variables affected the overall yield. During the washing/centrifugation steps, fine particulate OsS_2 did not always fully settle with centrifugation, which increased the loss of material during decanting. Increasing the centrifugation time to minimize this effect

helped, but some loss was still noted in most washes. Additionally, transferring between containers during the synthesis, washing, and annealing steps led to material loss. Static interaction with the walls of the tube furnace also caused sample loss. The overall yield was still considered quite high. The final product is a dark grey – black powder.

Raman spectroscopic analysis of the sample showed an intense peak at 354 cm^{-1} and a small peak at 393 cm^{-1}, which is consistent with the literature[54]. The weak peak out near 900 cm^{-1} could be associated with the Os – S bonding. The Raman spectrum for OsO_4 shows sharp peaks at 335 and 965 cm^{-1} and a weak, broad peak at 954 cm^{-1} and it is possible there is a similar peak in the 900 cm^{-1} range for Os-S bonding. The spectrum is shown in Figure 2.1.3 and has been normalized to the intensity of the 354 cm^{-1} peak.

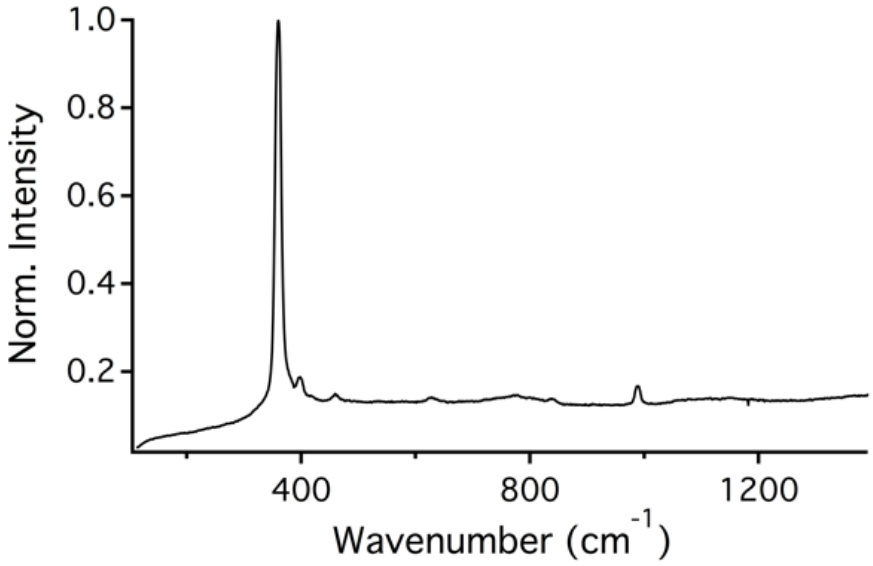

Figure 2.1.3. Raman spectrum of annealed OsS_2 sample

Powder x-ray diffraction analysis of OsS_2 prior to annealing was not possible because it was an amorphous solid. Annealing the sample allowed reorganization of the solid as the sample slowly cooled to room temperature. The dryness of the argon gas was very

critical; any water present during the annealing process could be trapped in the crystal lattice. This trapped moisture created problems with outgassing during sample irradiation. To prevent this issue, a Drierite column was added to the system prior to the argon entering the tube furnace. The anhydrous, crystalline OsS_2 is a face-centered cubic structure[55]. A sample of the annealed material was analyzed by powder x-ray diffraction and compared to a literature source (Figure 2.1.4). The diffraction pattern for the annealed sample matched the literature spectrum well and the experimental unit cell dimension (a = 5.627 Å) closely matched the literature value (a = 5.619 Å)[55].

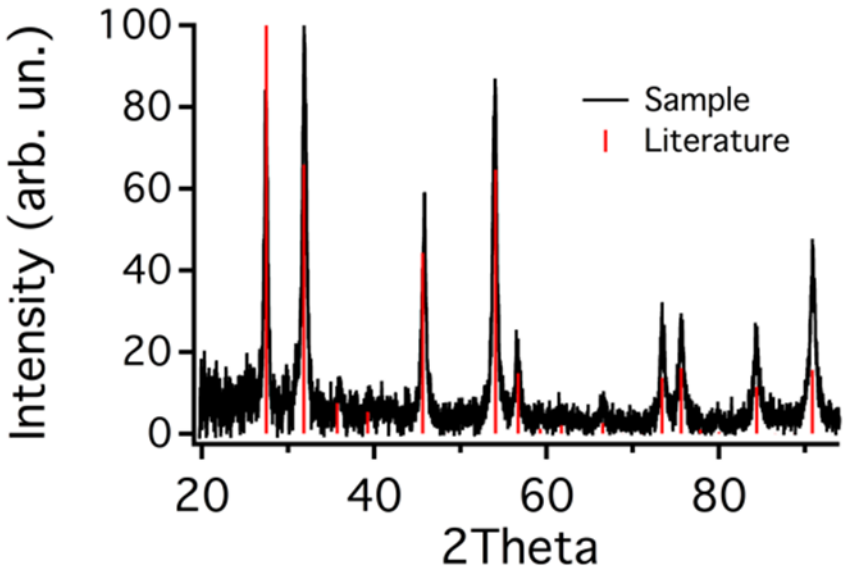

Figure 2.1.4. Crystal diffraction spectrum of annealed OsS_2 with comparison to literature peaks

Additionally, a sample of the annealed osmium disulfide was sent to an independent lab for elemental sulfur analysis. The expected value was 25.2% sulfur; the result obtained from the sample sent to the independent lab was 25.12% sulfur. With the results of the

Raman, XRD, and elemental analysis studies, osmium disulfide was determined to be well characterized and ready for use in target irradiations.

2.1.2.2 OsS_2 Target Preparation and Irradiation at MU

SRIM-2008 software[56] was used to calculate the theoretical proton stopping power for the OsS_2 targets to determine the proton entry energy and exit energy within the target (Appendix A.2.2). A proton energy of 16 MeV was chosen for this study to maximize ^{186}Re production (Appendix A.1.1).

Osmium metal formed, brittle chalky pellets even at high pressure (41.4 MPa), while osmium disulfide formed smooth, firmly-packed pellets at a significantly lower pressure (13.8 MPa). Pressed OsS_2 targets are illustrated in Figure 2.1.5a and 2.15b. It was determined that the best method to prepare the pressed pellet targets was to directly press the target material into the backing; less material was lost during pressing since material loss can occur in the pellet die and while transferring from the pellet die to the backing. Additionally, air gaps between the pressed pellet and the wall of the aluminum backing have caused problems with some of the transferred pellets (Appendix B). Once the target design was determined, irradiation runs were performed to produce ^{186}Re. Determination of activation products and their activities was performed by gamma spectroscopy on an HPGe detector.

Figure 2.1.5. (a) OsS_2 pressed directly into backing (b) pressed pellet of OsS_2 which is transferred to target backing

Thin $^{nat}OsS_2$ targets were irradiated for 1 hour with a 10 μA current of 16 MeV protons, and analyzed for radiorhenium. Under these irradiation conditions, rhenium isotopes were produced in nanocurie quantities while iridium isotopes were produced in microcurie quantities (Table 2.1.1). Also, there were no detectable quantities of radioactive osmium isotopes formed while irradiating with 16 MeV protons.

Table 2.1.1. Identified iridium and rhenium isotopes produced from a 46 mg $^{nat}OsS_2$ target with their half-lives, utilized gamma energies, and produced activities at the end of bombardment.

Isotope	$t_{1/2}$	Gamma Energy (Intensity)	Activity (All aliquots)
^{186}Ir	16.64 h	137 (23%), 297 (8.6%)	3.00 μCi
^{187}Ir	10.5 h	912 (4.3%)	143. μCi
^{188}Ir	1.72 d	155 (30%), 1210 (6.9%)	10.0 μCi
^{189}Ir	13.2 d	245 (6%)	9.00 μCi
^{190}Ir	11.8 d	187 (52%)	1.34 μCi
^{186}Re	3.718 d	137 (9.47%)	2.20 nCi
^{188}Re	17.004 h	155 (15.61%)	0.78 nCi
^{189}Re	24 h	216 (5.5%)	6.58 nCi

The production rate observed experimentally was compared to the theoretical production rate calculated using data from the TENDL-2014 database (Table 2.1.2). For several isotopes including the isotope of interest, ^{186}Re, only a small fraction of the expected

isotope was produced. A few isotopes including ^{187,189,190}Ir and ^{189}Re more closely matched their theoretical production rates. Interestingly, a significant quantity of ^{186}Ir was produced when the theoretical data from TENDL-2014 suggested that the cross section would be zero at 16 MeV.

Table 2.1.2. Comparison of theoretical and experimental production rates for the $^{nat}OsS_2$ target irradiated at MURR

Isotope	Production Rate ($\mu Ci \cdot \mu Ah^{-1} \cdot g^{-1}$)		Percentage of Theoretical Produced
	Theoretical	Experimental	
^{186}Ir	0.00	6.45	N/A
^{187}Ir	755.62	307.47	40.69
^{188}Ir	267.11	21.50	8.05
^{189}Ir	57.23	19.35	33.82
^{190}Ir	3.47	2.88	83.14
^{186}Re	0.16	0.005	3.01
^{188}Re	0.008	0.002	20.12
^{189}Re	0.38	0.014	3.72

2.1.2.3 OsS_2 Target Dissolution and Separation at MU

Osmium disulfide typically dissolves in 12% NaOCl though a significant difference in reactivity is noted between the hydrated and anhydrous form of osmium disulfide. The hydrated form readily dissolves in NaOCl and HNO_3 while the anhydrous will only very slowly dissolve in both of these solvents even with heating. The liquid-liquid extraction method quickly isolates rhenium from greater than 98% of the produced iridium isotopes (Table 2.1.2). It is important to allow sufficient time (2-3 minutes) after mixing the layers for them to properly settle and separate. Additionally, the elution of the aqueous layer must be performed at a slow flow rate (1-2 mL / minute) to prevent the aqueous solution from beading on the glass, leaving a fraction of the aqueous solution with the organic solution.

Table 2.1.3. Percentage of rhenium and iridium isotopes found in each aqueous and organic layer, and on the alumina column using the OsS_2 sample quantified in Table 2.1.1.

Layer	Rhenium Isotopes	Iridium Isotopes
Aqueous 1	0%	83.32%
Aqueous 2	0%	14.51%
Organic 1	100%	0.04%
Organic 2	0%	2.06%
Column	0%	0.08%

2.1.2.3 Further Optimization of OsS_2 Separation/Purification Method at MU

A small sample of osmium metal was irradiated in the reactor at MURR to produce a radioosmium tracer. The reactor-irradiated osmium sample was dissolved and distilled as previously described; ≥ 99.9% of the osmium was removed from the NaOCl solution during the distillation. The osmium metal was then converted to the disulfide by the previously described method and then combined with the cyclotron-irradiated osmium disulfide sample for processing. It was observed that ≥ 89% of the osmium was separated from the rhenium during the liquid-liquid extraction method. The majority of the transferred osmium was in the second MEK extracted aliquot. The first MEK layer was divided into aliquots and passed through alumina, silica, and cation exchange sep-paks to further purify the rhenium product. The alumina and the silica were able to remove ~83% of the residual osmium transferred with the rhenium while the cation exchange removed ~95%. The cation exchange sep-pak will be utilized in future studies as a secondary clean-up column. The results of this study indicate it is necessary to distill the sample first to remove the bulk osmium from the sample prior to the liquid-liquid extraction method to better purify the final Re product. The nearly quantitative removal of osmium during distillation will ensure high purity rhenium product while simultaneously recovering osmium for reuse in further production of OsS_2.

2.1.2.4 Osmium Metal Target at BNL

Data obtained from the TENDL-2014 theoretical cross section database suggests the optimal proton energy for this reaction would be ~23-24 MeV, which represents a theoretical cross section ~19x higher than observed for the reaction at 16 MeV (Figure 2.1.6)[57,58]. For this reason, an irradiation of a thick osmium metal target was performed at BNL. SRIM-2008 software[56] was used to calculate theoretical proton stopping power for the osmium metal targets to determine the proton entry energy and exit energy within the target (Appendix A.2.1). A proton energy range of 20 – 26 MeV was chosen for this study to maximize ^{186}Re production (Appendix A.1.1). The targets were prepared to the necessary thickness to achieve this energy deposition.

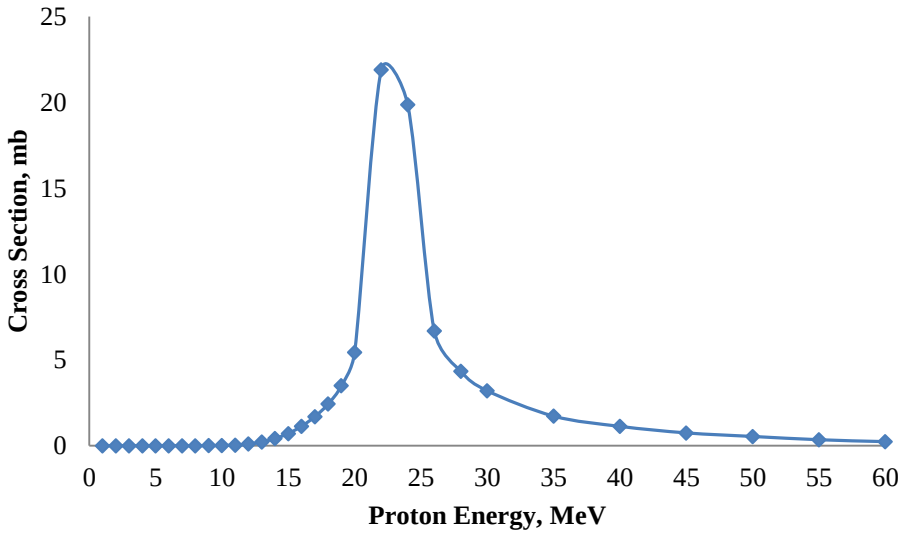

Figure 2.1.6. TENDL-2014 theoretical cross section data for ^{189}Os(p,α)^{186}Re reaction

The thick Os target (Figure 2.1.7) at BNL was irradiated for 30 minutes with an average current of 30 μA depositing a range of protons from 9-30 MeV (completely encompassing the ideal production range). Under these irradiation conditions, osmium

isotopes were produced in microcurie quantities while rhenium and iridium isotopes were produced in millicurie quantities (Table 2.1.3).

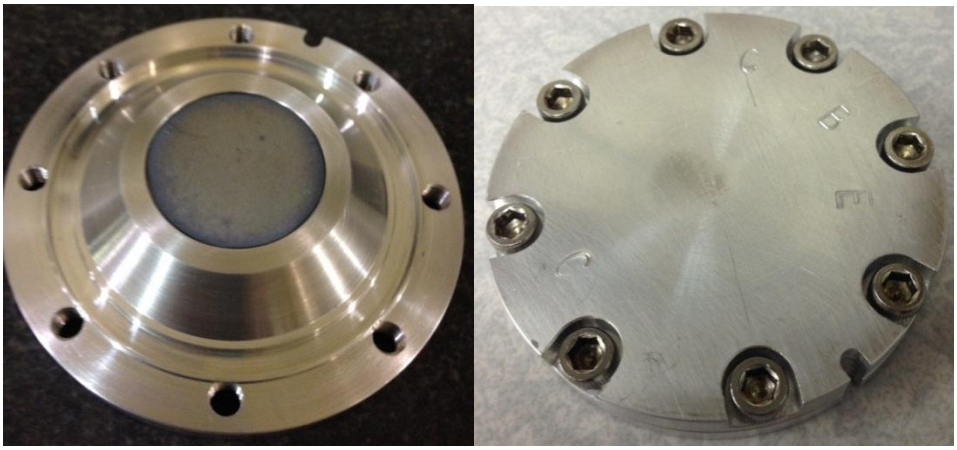

Figure 2.1.7. (left) osmium foil inside machined well in target backing (right) bolted, sealed target

Table 2.1.4. Identified iridium, rhenium, and osmium isotopes produced from an 8.5g ^{nat}Os metal target with their half-lives, utilized gamma energies, and produced activities at the end of bombardment.

Isotope	$t_{1/2}$	Gamma Energy (Intensity)	Activity
^{186}Ir	16.64 h	137 (23%), 297 (8.6%)	28.3 mCi
^{187}Ir	10.5 h	912 (4.3%)	169 mCi
^{188}Ir	1.72 d	155 (30%), 1210 (6.9%)	33.1 mCi
^{189}Ir	13.2 d	245 (6%)	4.47 mCi
^{190}Ir	11.8 d	187 (52%)	4.96 mCi
^{192}Ir	73.83 d	317 (82.86%)	35.2 µCi
^{186}Re	3.718 d	137 (9.47%)	273 µCi
^{188}Re	17.004 h	155 (15.61%)	26.1 mCi
^{189}Re	24 h	216 (5.5%)	5.00 mCi
^{185}Os	93.6 d	646 (78%)	22.7 µCi
^{191}Os	15.4 d	129 (26.5%)	179 µCi

The target was dissolved in the hot cell at the TPL. The target took a total of 45 hours to fully dissolve. The vast majority of the osmium activity remained in the dissolution

solution (85.8%) with only a small portion carried over to the trap solution. Aliquots were taken from the dissolution flask and the KOH trap flask to determine overall production rates.

The production rate observed experimentally was compared to the theoretical production rate calculated using data from the TENDL-2014 database (Table 2.1.2). For most isotopes, the experimental production rate was in good agreement with the theoretical production rate. Interestingly, a great excess of ^{188}Re was determined to be present. The isobars ^{188}Ir and ^{188}Re share the same gamma emission though ^{188}Ir has a few unique gamma emissions. Calculations were performed to determine the ^{188}Re activity from excess activity observed at a shared gamma emission compared to a uniquely ^{188}Ir gamma emission; there was some uncertainty inherit in this calculation, which could have led to overestimated activity in the product. Additionally, some of the assumptions made for the theoretical calculations could have led to an underestimate of the production rate.

Table 2.1.5. Comparison of theoretical and experimental production rates for the ^{nat}Os metal target irradiated at BNL

Isotope	Production Rate ($\mu Ci \cdot \mu Ah^{-1} \cdot g^{-1}$)		Percentage of Theoretical Produced
	Theoretical	Experimental	
^{186}Ir	226.02	221.97	98.20
^{187}Ir	1004.10	1325.49	132.01
^{188}Ir	343.14	259.61	75.66
^{189}Ir	31.70	35.06	110.61
^{190}Ir	55.76	38.90	69.77
^{192}Ir	0.82	0.28	33.85
^{186}Re	1.13	0.943	83.62
^{188}Re	1.81	21.06	1164.64
^{189}Re	4.93	0.00	0.00
^{185}Os	0.001	0.000	0.00
^{191}Os	3.82	1.404	36.74

2.1.3 Conclusions

The distillation of osmium as osmium tetroxide from NaOCl was demonstrated to be quantitative with ≥ 99.9% osmium recovered. The osmium was recovered in KOH and easily converted to OsS_2 with the addition of NaHS. A significant difference in the stability and chemical reactivity of OsS_2 was noted prior to and post sintering at high temperature. Annealing the OsS_2 resulted in a more thermal stable and chemically resistant product. The annealed material was characterized using several analytical techniques.

Accelerator-based irradiations of $^{nat}OsS_2$ and ^{nat}Os metal targets established the feasibility of producing rhenium *via* the $^{nat}Os(p, \alpha xn)Re$ reaction. The production rates at MURR (16 MeV) and BNL (30 MeV) demonstrated that higher proton energies are necessary to increase the production of rhenium isotopes. The production of unwanted iridium isotopes was significant in both cases and presents a dose issue for this production rate.

A rapid liquid-liquid extraction method isolated rhenium from the bulk of the iridium and osmium following irradiation. Distillation of the bulk osmium is necessary to effectively remove it as a contaminant from the rhenium product. A clean up column provides an additional step to remove unwanted osmium and iridium.

2.1.4 Future Studies

No future studies are planned for Os-based production at this point in time. The production of excessive iridium byproducts creates a dose issue for clinical scale production of ^{186}Re making this reaction pathway less appealing. Efforts will be directed towards W-based targetry.

2.2 ^{186}Re Production *via* Proton Bombardment of Tungsten Targets

2.2.1 Materials and Methods

All reagents, tungsten metal, tungsten trioxide, and sodium hydrosulfide were purchased from Fisher Scientific (Pittsburgh, PA) and Acros Organics (Geel, Belgium). Tungsten disulfide and sodium tungstate were purchased from Alfa Aesar (Ward Hill, MA). Enriched $^{186}WO_3$ was purchased from Oak Ridge National Laboratory, Oak Ridge, Tennessee. AG 1-X8 anion exchange resin and Glass Econo-Columns (1.0 cm ID; 10 mL reservoir), and Poly-Prep Columns (0.8 cm ID; 10 mL reservoir) were purchased from Bio-Rad (Hercules, CA). TEVA anion exchange resin was purchased from Eichrom Technologies (Lisle, IL). AnaLig Re-02 PS extraction chromatography resin was purchased from IBC Advanced Technologies (American Fork, UT). 20 mL HDPE scintillation vials with polyethylene caps (referred to as poly collection vials) were purchased from Fisher Scientific. 1 mL HDPE counting vials (referred to as poly counting vials) were prepared on-site at MURR using HDPE "Finathene 5203" beads from Fina Chemicals (Brussels, Belgium). Aluminum metal backings and thick beam degraders were prepared on-site (both at MURR and BNL) to designed specifications using 6061 grade aluminum purchased from McMaster-Carr (Elmhurst, IL) and Yarde Metals (Hauppague, NY). Commercial food-grade aluminum foil was purchased from a local market. Araldite 2011 epoxy adhesive was purchased from Freeman Supply (Avon, OH). All reagents and materials were used as received without any further purification. All water used was purified on-site (deionized water fed into a Millipore system to > 18 MΩ·cm).

2.2.1.1 Instrumentation

Scanning electron microscopy was performed using a FEI Quanta 600 FEG Extended Vacuum Scanning Electron Microscope. The system was utilized in high vacuum mode ($< 6 \cdot 10^{-4}$ Pa) with the accelerating voltage set to 10 kV. Images were collected using an Everhardt-Thornley detector.

All irradiations were performed at MURR using a GE PETtrace 800 cyclotron with dual particle capabilities with energies up to 16.5 MeV for protons and 8.5 MeV for deuterons and currents up to 80 microamps. Throughout these experiments, the beam was collimated to a 10 mm diameter aperture. Proton irradiations at BNL were performed at the Brookhaven Linac Isotope Producer (BLIP). BLIP is a linear accelerator capable of proton energies up to 200 MeV and currents up to 115 microamps.

Radiochemical assays at MURR for ^{181,182,182m,183,184,186,188}Re, and ^{187}W were performed by γ-ray spectrometry using a Canberra Model GC2018S HPGe detector system (60.5 mm diameter, 30.5 mm length) at a sample distance of 5 mm from the window. The detector has a FWHM at 1.33 MeV of 1.8 keV. Spectral analyses were performed with a Canberra Model 9600 multichannel analyzer. All samples were counted for at least 600 seconds and decay corrected to the time correlating to the end of target bombardment. The detector dead time was kept to less than 10 % for all samples.

Radiochemical assays at BNL for ^{181,182,182m,183,184,186}Re and ^{187}W were determined by γ-ray spectroscopy using an HPGe detector system. The detector was an Ortec Model GMX-18190-P HPGe detector system with a relative efficiency of 13.4% at 1.33 MeV. The detector diameter was 48.2 mm, detector length was 45.5 mm, and the distance from

the window was 3 mm. The detector's specified FWHM at 1.33 MeV was 1.76 keV. Spectral analyses were performed by an Ortec DSPEC Jr. 2.0 multichannel analyzer. All samples were counted for at least 1200 seconds and decay corrected to the time correlating to the end of target bombardment. The detector dead time was kept to less than 10 % for all samples.

Radiochemical assays at LANL for ^{183,184g}Re were determined by γ-ray spectrometry using an EG&G Ortec Model GMX-35200-S HPGe detector system with a relative efficiency at 1333 keV of 20%. The detector diameter was 50.0 mm, detector length 53.5 mm, window thickness 0.5 mm, and outer dead-layer thickness 0.3 μm. The detector's warranted FWHM at 1333 keV was 2.35 keV. Spectrum analyses were carried out with a Canberra Model 35-Plus multichannel analyzer. All samples were counted for 300 seconds and decay corrected to the time correlating to the end of target bombardment. The detector dead time was kept to less than 10 % for all samples.

2.2.1.2 WO_3 Target Preparation Studies at MU

Using a hydraulic press, tungsten trioxide was pressed at various pressures into titanium metal backings (6.9-41.4 MPa) to prepare a smooth, stable WO_3 target. After the initial tests, three WO_3 targets were prepared by pressing at 6.9 MPa and imaged using scanning electron microscopy (SEM). The targets were then sintered at 1080° C for 6 hours under atmospheric conditions in a muffle furnace. The targets were re-imaged using SEM to visualize any structural changes to the targets.

2.2.1.3 WS_2 Target Preparation and Irradiation at MU

Two WS_2 targets were prepared using a hydraulic press to directly press the material into an aluminum metal backing. Both materials formed firmly-packed, smooth pellets at 13.8 MPa. Each target was then sealed in the backing using 16 µm thick aluminum foil, which was epoxied in place. The epoxy was allowed to cure for a minimum of 15 hours per the manufacturer's specifications. The targets were irradiated at MURR using 11 or 14 MeV protons degraded from 16 MeV using aluminum degraders. A stack of thin Al foils were used to degrade the beam to 14 MeV, while a single thick Al degrader was used to degrade the beam to 11 MeV. SRIM 2008 software[56] was used to calculate theoretical proton stopping power for the aluminum degraders and the WS_2 targets to determine the necessary thickness of the degraders and calculate the energy deposited in each target. A proton energy range of 7 – 16 MeV was chosen for this study to maximize ^{186}Re production (Appendix A.1.2). The targets were prepared to the necessary thickness to achieve this energy deposition. Both targets were irradiated for a total of 10 µAh. High vacuum was used on the target face while the back side of the target was water cooled to dissipate heat from the charged particle beam.

2.2.1.4 WS_2 Target Dissolution and Activation Product Analysis at MU

Following irradiation in the cyclotron, the aluminum foil was mechanically removed from the target backing and the irradiated WS_2 was transferred to a clean poly collection vial. Ten milliliters of 30% H_2O_2 was added to the vial and gently heated (60° C) to dissolve WS_2. A magnetic stir bar was used to provide stirring. Once the sample was

fully dissolved, the entire sample was analyzed by gamma spectroscopy using an HPGe detector to qualify and quantify the produced radioisotopes.

2.2.1.5 Synthesis and Characterization of Tungsten Disulfide at MU

To define a method for the recovery and reuse of WS_2, studies evaluating the production of tungsten disulfide were performed. Approximately 100 mg of sodium tungstate (Na_2WO_4) was dissolved in a centrifuge tube using 5-10 mL of deionized H_2O and then acidified using 1-2 mL of concentrated HCl to precipitate tungstic acid (H_2WO_4). The tube was centrifuged at 3000 rpm for 10 minutes and the supernatant was decanted from the tungstic acid. The sample was washed with several aliquots of acetone to remove excess NaCl; this was achieved by vortexing the H_2WO_4 in the acetone, then centrifuging to settle the H_2WO_4, and decanting the acetone. Tungstic acid was then combined with thiourea (1:4 ratio) in a ceramic boat. The mixture was heated to 500° C in a tube furnace under argon gas flow for 3 hours to react the materials together and produce WS_2.

Characterization was not done for this product. The method was based on a literature reference[59]. The only deviation was the 1:4 ratio of tungstic acid: thiourea; the paper used significantly more thiourea (1:48 ratio), which was determined to be excessive.

2.2.1.6 Radiotracer Preparation for Separation Method Developed at LANL and MU

To develop a separation method to isolate rhenium from tungsten, radiotracer samples were prepared to complete a series of batch studies. For studies performed at LANL, a measured mixture of radio-rhenium isotopes ^{183}Re ($t_{1/2}$ = 71 d) and ^{184}Re ($t_{1/2}$ = 38 d) in the form of perrhenate (ReO_4^-) were used as Re tracers, and the activities per batch experiment were 0.38 µCi (14.1 kBq) and 0.07 µCi (2.6 kBq) ± 7.5%, respectively.

Rhenium-183 and ^{184}Re were previously produced at the Los Alamos National Laboratory's Isotope Production Facility (LANL-IPF) via proton beam irradiation via ^{nat}W(p,n) of an encapsulated $^{nat}WO_3$ powder target. The total mass of rhenium in the radiotracer sample was determined as reported previously[46], and amounted to 0.18 ± 0.02 pg Re per measured tracer sample. For studies performed at MU, ^{188}Re ($t_{1/2}$ = 17 h) was used at 0.76 µCi (28.1 kBq) ± 8.0 % per batch experiment. Rhenium-188 was generated from the decay of ^{188}W parent. Tungsten-188 was produced by neutron activation of enriched $^{186}WO_3$ via ^{186}W(2n, γ) using the flux trap at MURR. For studies only involving rhenium, ^{188}Re was isolated from the ^{188}W parent by column chromatography prior to use. The ^{188}W parent activities were calculated indirectly from ^{188}Re in-growth several days post-separation. Tungsten tracer ^{187}W ($t_{1/2}$ = 23.7 h) was produced by neutron activation of enriched $^{186}WO_3$ via ^{186}W(n, γ) using the pneumatic tube system at MURR. The neutron activated WO_3 was dissolved in hot NaOH solution to provide sodium [^{187}W] tungstate solution (0.81 ± 0.06 mCi (30.0 ± 2.2 MBq) ^{187}W/ mg W). The produced radiotracer was utilized as 11.6 ± 0.9 µCi (429 ± 33 kBq) per sample.

Table 2.2.1. Rhenium and tungsten tracer information (per sample)

Isotope	$t_{1/2}$	Gamma Emissions	Activity	Preparation Notes
^{183}Re	70.0	162.3 keV (23.3%)	0.38 µCi (14.1 kBq)	LANL, proton irr.
^{184}Re	38 d	792.1 keV (37.7%)	0.07 µCi (2.6 kBq)	LANL, proton irr.
^{188}Re	17 h	155.0 keV (15.6%)	0.76 µCi (28.1 kBq)	MURR, ^{188}W decay
^{187}W	23.9	479.5 keV (26.6%)	11.6 µCi (0.4 MBq)	MURR, neutron irr.
^{188}W	69.8	155 keV from ^{188}Re	0.76 µCi (28.1 kBq)	MURR, neutron irr.

2.2.1.7 Measurement of distribution coefficients via batch experiments at LANL and MU

Tungsten trioxide dissolved in hot NaOH to yield tungstate (WO_4^{2-}). In the absence of a strong complexing agent, acidifying the sample resulted in re-precipitation of the oxide, so W adsorption studies were only performed in basic solutions, while Re adsorption studies were performed in both acidic and basic media.

Studies were carried out via the batch method, in which the removal of radiorhenium from basic and acidic solutions (and activated tungsten ^{187,188}W from basic solutions) was measured by contacting a weighed amount of resin (50 ± 2 mg) with a definite volume (1.50 ± 0.12 mL) of a ^{183,184,188}Re- (or ^{187,188}W-) spiked aqueous solution. Experiments were performed at three temperatures (20, 40, and 60 °C) using a laboratory shaker. Solutions were shaken for up to 2 minutes and subsequently centrifuged for 1 minute at 7500 rpm. Two 500 μL-aliquots of the resin contacted solution (A_s) were transferred into clean poly collection vials at LANL or clean poly counting vials at MURR. In addition, an aliquot of 500 μL of the original starting solution (A_0) was transferred to a clean poly vial to determine the original activity. For the samples at LANL, the volumes were brought up to 1.5 mL with deionized water for the detector geometry. The distribution coefficient, K_d, was computed according to the following formulation:

$$K_d = \frac{(A_0 - A_s)}{A_s} \cdot \frac{V}{m} \qquad \text{Equation 2.2.1}$$

A_0 is the original radiorhenium or radiotungsten activity of the aqueous solution. A_s is the activity present in the aqueous solution at equilibrium with the resin. ($A_0 - A_s$) is the

amount of activity on the resin. The volume of the aqueous solution (*V*) was measured in mL and the mass of the resin (m) was measured in grams (g).

2.2.1.8 Determination of resin interstitial volume coefficient at LANL

For the conversion of distribution coefficients (ratios), K_d, into column parameters, a study was performed to determine the interstitial volume of a column of a definite volume using AG 1-X8. A known volume (5 mL) of 1.0 M NaOH was measured into a tube and weighed. Approximately 1 mL of resin was added, the volume was recorded, and the sample weighed. Using the following formula, the density, ρ, of the wet resin was determined:

$$\rho_{wet} = \frac{m(resin)}{V\,(resin\ and\ base) - V\,(base)} \qquad \text{Equation 2.2.2}$$

Next, a known volume of AG 1-X8 was measured into a column and weighed. The resin was soaked in 1 cm^3 NaOH and then allowed to completely dry to determine the effect of swelling on resin volume, which was determined to be negligible. The density of the dry resin was calculated. Finally the interstitial volume coefficient, υ_i, was calculated using the following formula:

$$v_i = \frac{\sigma_{wet} - \sigma_{dry}}{\sigma_{wet}} = \frac{V_{solution}}{V_{wet\ resin}} \qquad \text{Equation 2.2.3}$$

The interstitial volume coefficient was determined to be 0.361 mL of solution per 1 mL of AG 1-X8 resin.

2.2.1.9 Separation of Rhenium and Tungsten using AnaLig at MU

Column studies were performed to translate the batch studies to a column application for the AnaLig resin. A poly-prep column was loaded with 0.50 g of AnaLig, washed with deionized water to remove any loose flowing styrene pieces, and then it was conditioned with 1 M NaOH. Tracer ^{188}W (with ^{188}Re daughter in equilibrium) was loaded on the column in 1 mL of 1 M NaOH. The column was washed with additional 10 x 1 mL of 1 M NaOH to rinse any residual tungsten from the column. The columns were eluted with 10 x 1 mL of 70°C DI H_2O. Each fraction was counted on an HPGe detector to determine ^{188}Re. After being allowed to decay for a week, the sample was recounted to determine ^{188}W activity. A column was also performed to examine the effect of macroscale tungsten on rhenium retention. Additional studies were performed under the same conditions with the exception that the heated water was replaced with 1 M HNO_3 or saline (0.9% w/v NaCl).

2.2.1.10 W Metal Target Irradiations at BNL

Three tungsten metal foils were irradiated at BNL. Two of the tungsten foils were irradiated as large foils held in a clam-shell design target holder while the third tungsten target was prepared in a sealed, bolted aluminum can. SRIM-2008 software[56] was used to calculate theoretical proton stopping power for the tungsten metal targets to determine the proton entry energy and exit energy within the target (Appendix A.2.3). A proton energy range of 7 – 16 MeV was chosen for this study to maximize ^{186}Re production (Appendix A.1.2). The targets were prepared to the necessary thickness to achieve this energy deposition.

For the two large tungsten foils in the clam-shell design target holder, either a 0.1 mm or 0.05 mm thick tungsten foil was cut into a 78 mm x 78 mm square and weighed to determine the mass. The foil was laid on the back plate of the target holder and the open front piece closed over the foil. The holder was then placed in the target assembly box. The foils were irradiated for either 5 minutes or 15 minutes using an average proton beam current of 30 μA.

For the third tungsten target, 0.05 mm thick tungsten foil was laser cut into a circle with a 25.4 mm diameter. A well of the same size was cut into the back portion of the aluminum can to hold the foil and provide the optimal thermal conductivity during the irradiation. A silver-plated, Inconel C-ring was used to provide a water tight seal. The target was bolted under helium gas in a glove box. The sealed target was tested for helium gas leaks prior to irradiation. The tungsten target was irradiated for one hour using an average proton beam current of 115 μA.

In all cases, the linac beam was tuned to proton energy of 116.3 MeV. Upstream of the tungsten targets, the target assembly contained two RbCl production targets and selected degraders to ensure the optimum proton energy into each target. A proton entry energy of approximately 12.5 MeV was targeted for all of the tungsten targets.

2.2.1.11 W Metal Target Dissolution and Separation at BNL

The same dissolution method was used for all three foils. The foil was removed from the target holder or target can, cut into smaller pieces to help facilitate dissolution, and transferred to a clean 300 mL beaker. The foils were dissolved in 30% H_2O_2 with gentle heating (60° C) and mechanical stirring. After the foil fully dissolved, the heat was

slowly increased to 100° C to decompose any residual H_2O_2 prior to proceeding with the separation method. Once the peroxide had decomposed, NaOH was added to the solution to create a solution with ~ 1 M NaOH present.

Based on the separation method developed at LANL[60], the first tungsten foil was used to optimize a chromatography column method for this process. Initially, 4 mL of AG 1-X8 resin was added to glass Econo-column and conditioned with 1 M NaOH. An aliquot of the dissolved tungsten foil was loaded on the column. The column was then rinsed with Milli-Q H_2O and eluted with 6 M HNO_3. Subsequent columns utilized a 2 mL bed volume of AG 1-X8 resin instead of 4 mL. Once the column parameters were optimized, the second tungsten foil was used to perform a triplicate study of the separation method to determine the recovery yields for both W and Re. For the final foil irradiated in the target can, the method was adapted for use in a hot cell and the entire target was separated on a single column.

2.2.2 Results and Discussion

2.2.2.1 WO_3 Target Preparation Studies at MU

Samples of $^{nat}WO_3$ were pressed at various pressures to form pressed pellet targets. At all pressures, the WO_3 targets were still brittle and chalky; they would easily crack upon touching and were not suitable for use in the cyclotron. Three additional targets were pressed in the titanium alloy backing and sintered at 1080° C for 6 hours to fuse the grains together and make a more solid target. SEM images were taken of the samples before and after sinter along with visual inspection. Looking at the samples with the naked eye, the pressed $^{nat}WO_3$ was chalky, brittle, and a bright, green-yellow color prior

to sintering. After sintering, the $^{nat}WO_3$ was smoother though still brittle and flaky, and a deeper blue-green color (Figure 2.2.1).

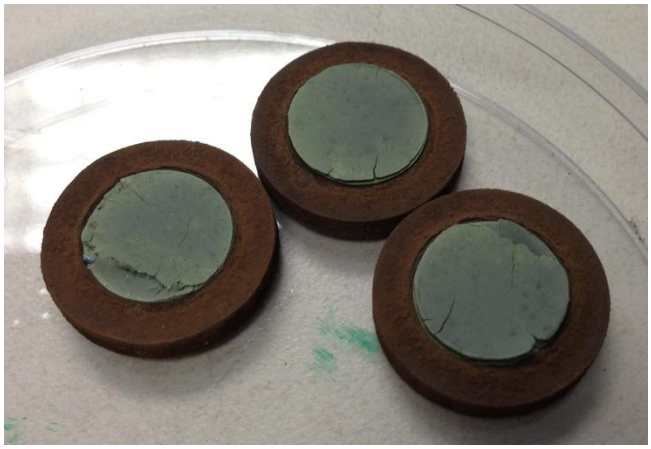

Figure 2.2.1. Pressed $^{nat}WO_3$ disc in tungsten alloy backing (post-sintering)

The blue tint of the material suggests the formation of tungsten blue (WO_{3-x} with x =0.01-0.1). Also visible in Figure 2.2.1, the titanium alloy, originally silvery and smooth, is visibly oxidized and was physically compromised from the high heat of the furnace.

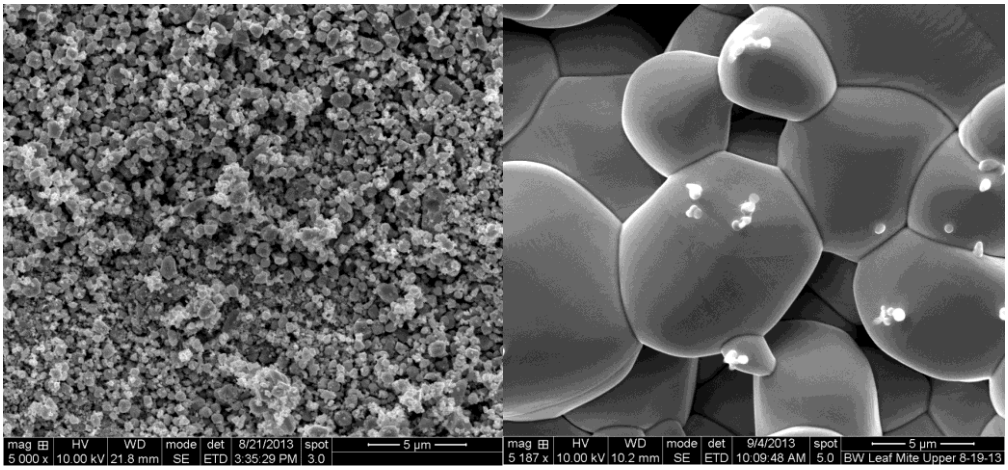

Figure 2.2.2. SEM images of $^{nat}WO_3$ sample prior to sintering (left) and after sintering (right)

Examining the SEM images before and after sintering, grains of WO_3 have fused together into much larger clumps of material proving a more stable target material (Figure 2.2.2).

Though successful to an extent, sintering does not provide the necessary target stability for use in a cyclotron.

2.2.2.2 WS_2 Target Irradiations and Activation Product Analyses at MU

Cross sections for the $^{nat}W(p,x)^{186}Re$ reaction have been reported in the literature[34,45,47,48]. There is some discrepancy on the absolute value of the cross section but there is agreement that the optimal cross section is found at ~10 MeV with the optimal range of production being from 7-16 MeV (Appendix A.1.2). The SRIM calculations showed the experimental targets give a good representation of possible production irradiation parameters (Table A.2.1). With the idea of transitioning to an enriched target, ^{nat}W targets bombarded with both 11 MeV and 14 MeV targets were studied to demonstrate the impurities produced using ^{nat}W at different energies and to determine a cumulative yield over a broad energy range.

Tungsten disulfide forms tight, stable pressed pellets even at lower pressures (Figure 2.2.3). The discs are quite robust to handling. For irradiations, the material was pressed directly into the target backing to minimize material loss and prevent trapping air in the target.

Figure 2.2.3. Pressed disc of tungsten disulfide

Pressed $^{nat}WS_2$ targets were irradiated at 11 and 14 MeV for 10 µAh, and analyzed for radiorhenium. The 16 MeV proton beam from the GE PETtrace was degraded using aluminum degraders in front of the target. For a natural abundance target, 11 MeV is more ideal for a larger production cross section. At this proton energy, radiorhenium was produced in microcurie quantities and the relative amount of radiorhenium contaminants was lower (Table 2.2.2).

Table 2.2.2. Activities of identified rhenium isotopes at the end of bombardment, 581 mg $^{nat}WS_2$ target, 11 MeV protons, 10 µAh

Isotope	$t_{1/2}$	Gamma Energy (Intensity)	Activity at EOB
^{181}Re	20 h	366 (56%)	0.00 µCi
^{182}Re	12.7 h	169 (11.4%), 1121 (22.1%)	19.9 µCi
^{182m}Re	2.67 d	1121 (32%)	144.3 µCi
^{183}Re	70 d	162 (23.3%)	1.7 µCi
^{184}Re	38 d	793 (37.7%)	6.38 µCi
^{186}Re	3.718 d	137 (9.47%)	21.9 µCi

The production rate observed experimentally was compared to the theoretical production rate calculated using data from the TENDL-2014 database (Table 2.2.3). The production rate for ^{186}Re (and ^{182}Re) was slightly biased lower than many of the other production rates. In the literature, there is ambiguity in the absolute value of the cross section for this reaction suggesting the literature cross section may be overestimated for the ^{186}W(p, n)^{186}Re reaction at this energy range. Assuming the lowest cross-section was correct (Lapi *et Al*[45]), the ^{186}Re production rate would increase to closer to 75% of the theoretical production rate.

Table 2.2.3. Comparison of theoretical and experimental production rates for the $^{nat}WS_2$ target irradiated at MURR

Isotope	Production Rate (μCi·μAh^{-1}·g^{-1})		Percentage of Theoretical Produced
	Theoretical	Experimental	
^{181}Re	0.00	0.00	0.00
^{182}Re	18.29	3.43	18.73
^{182m}Re	40.76	24.84	60.93
^{183}Re	0.82	0.29	35.86
^{184}Re	2.16	1.10	50.80
^{186}Re	24.85	3.77	15.17

The irradiation performed using 14 MeV protons produced a comparable activity of ^{186}Re to the 11 MeV irradiation, but the relative production of ^{181,182,182m,183}Re were all increased (Table 2.2.4).

Table 2.2.4. Activities of identified rhenium isotopes at the end of bombardment, 139 mg $^{nat}WS_2$ target, 14 MeV protons, 10 μAh

Isotope	$t_{1/2}$	Gamma Energy (Intensity)	Activity at EOB
^{181}Re	20 h	366 (56%)	13.6 μCi
^{182}Re	12.7 h	169 (11.4%), 1121 (22.1%)	17.3 μCi
^{182m}Re	2.67 d	1121 (32%)	103.0 μCi
^{183}Re	70 d	162 (23.3%)	1.56 μCi
^{184}Re	38 d	793 (37.7%)	1.44 μCi
^{186}Re	3.718 d	137 (9.47%)	5.24 μCi

The production rate observed experimentally was compared to the theoretical production rate calculated using data from the TENDL-2014 database (Table 2.2.5). The observed, experimental production rate for ^{186}Re was a significantly closer to the theoretical value at this energy than for 11 MeV. The literature values for the ^{186}W(p, n)^{186}Re reaction were in closer agreement at this energy as the cross values begin to plateau at higher energy. Some improvements can still be made to increase the production rate.

Table 2.2.5. Comparison of theoretical and experimental production rates for the $^{nat}WS_2$ target irradiated at MURR

Isotope	Production Rate ($\mu Ci \cdot \mu Ah^{-1} \cdot g^{-1}$)		Percentage of Theoretical Produced
	Theoretical	Experimental	
^{181}Re	106.09	2.34	2.21
^{182}Re	27.64	2.98	10.77
^{182m}Re	33.87	17.73	52.33
^{183}Re	1.27	0.27	21.11
^{184}Re	0.22	0.25	114.29
^{186}Re	2.93	0.90	30.82

Enriched ^{186}W should result in a ^{186}Re production rate four-fold higher than ^{nat}W with significant reduction of radiorhenium impurities (Table 2.2.6). Using enriched ^{186}W, the primary isotopes of concern would be ^{182m}Re. The cross section for ^{182m}Re is quite significant at this proton energy and has a 2.67 d half-life; a fair amount will be co-produced. The activity would still be > 99% ^{186}Re.

Table 2.2.6. Comparison of natural abundance tungsten to purchased enriched ^{186}W and the resulted effect to rhenium isotope production rates

Isotope	Natural Abundance	Enriched Target Material	Effective Change
^{180}W	0.12 %	0.01 %	1/12 x original
^{182}W	26.50 %	0.01 %	1/2650 x original
^{183}W	14.31 %	0.01 %	1/1431 x original
^{184}W	30.64 %	0.1 %	1/306 x original
^{186}W	28.43 %	99.9 %	3.5 x original

2.2.2.3 WS_2 Synthesis for Target Recovery and Reuse at MU

Once the production method has been optimized, enriched ^{186}W will be used for the production runs; the cost of the enriched materials necessitates recovery and reuse of the target material. The separation method outlined in Gott *et al.*[60] results in tungsten being recovered as the tungstate ion (WO_4^{2-}) in a 1 M NaOH solution. Acidification of this solution resulted in a quantitative recovery of tungsten as tungstic acid. The NaCl

generated during acidification was rinsed from the tungstic acid using acetone. The tungsten acid was allowed to dry and combined with thiourea. At high temperature, the sulfur group from the thiourea reacted with the tungstate to produce tungsten disulfide, urea, and water. The urea and water were volatilized at the high temperature resulting in a high purity product. Characterization and yield determination were not performed for this production pathway.

2.2.2.4 Rhenium Adsorption Kinetic on AG 1-X8

A kinetic study was performed to ensure that radiorhenium would reach distribution equilibrium quickly enough on AG 1-X8 to function for column chromatography work. The study utilized the subscribed batch method with the modification of varied contact times and a solute matrix of 1 M NaOH for all samples. The radiorhenium extraction maximum was reached at a contact time of 30 seconds or greater (Figure 2.2.4). The resin demonstrated the quick kinetics necessary to perform well in a column chromatography system; the resin must be capable of extracting rhenium in the short time the metal contacts the resin as the mobile phase is passed through the column.

Based on the kinetic study, it was decided to use a contact time of 120 seconds for the remainder of the studies to ensure samples had more than sufficient time to properly reach equilibrium. Thus, acquired distribution coefficients at 120 seconds of contact time were assumed to represent equilibrium distribution coefficients.

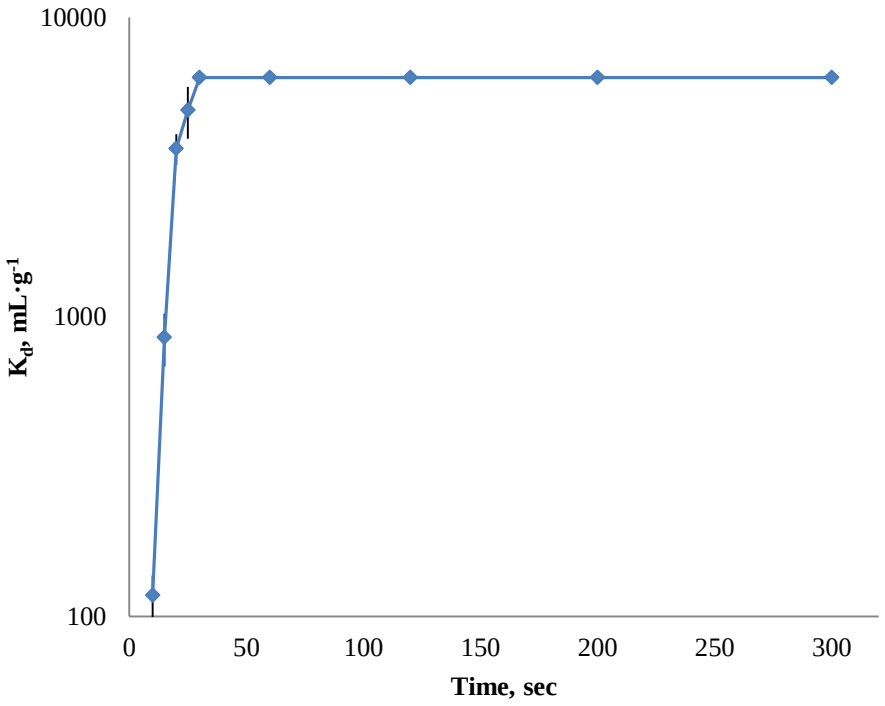

Figure 2.2.4 Rhenium K_d as a function of contact time on AG 1-X8. (n=6)

2.2.2.5 Rhenium Isothermal Kinetics on AG 1-X8

To fully characterize the adsorption characteristics of AG 1-X8 for rhenium, additional kinetic isothermal studies were performed at 40 and 60 °C (Figure 2.2.5). Contact time was limited to 30 seconds for the isotherms since it was previously determined equilibrium was achieved at 20 °C by that time. It was expected that the addition of energy would increase the adsorption rate thereby reducing the amount of time needed to reach equilibrium.

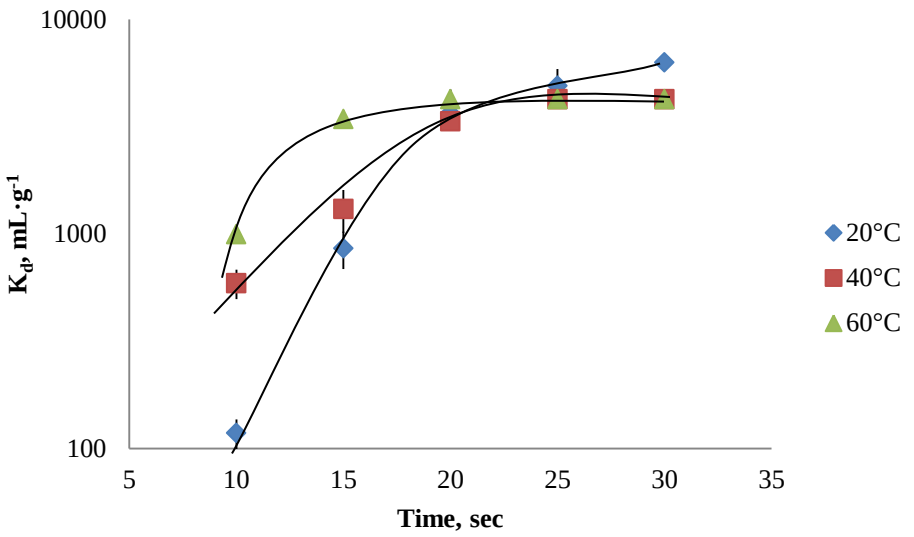

Figure 2.2.5 Rhenium K_d as a function of time and temperature. (n=6)

A simple, pseudo-first order kinetic model[61] was used to describe the kinetics data as the system approached equilibrium.

$$\ln\left(1-\frac{Q_t}{Q_e}\right) = -kt \qquad \text{Equation 2.2.4}$$

Q_t and Q_e are the experimental radiochemical adsorptions (mCi·g^{-1}) at time t and equilibrium, respectively. The rate constant (k, s^{-1}) obtained by the model illustrates the rate of adsorption as the system approached equilibrium. The adsorption rate is directly proportional to the contact time at each temperature and an increase in the adsorption rate is observed with increasing temperature as Figure 2.2.6 illustrates.

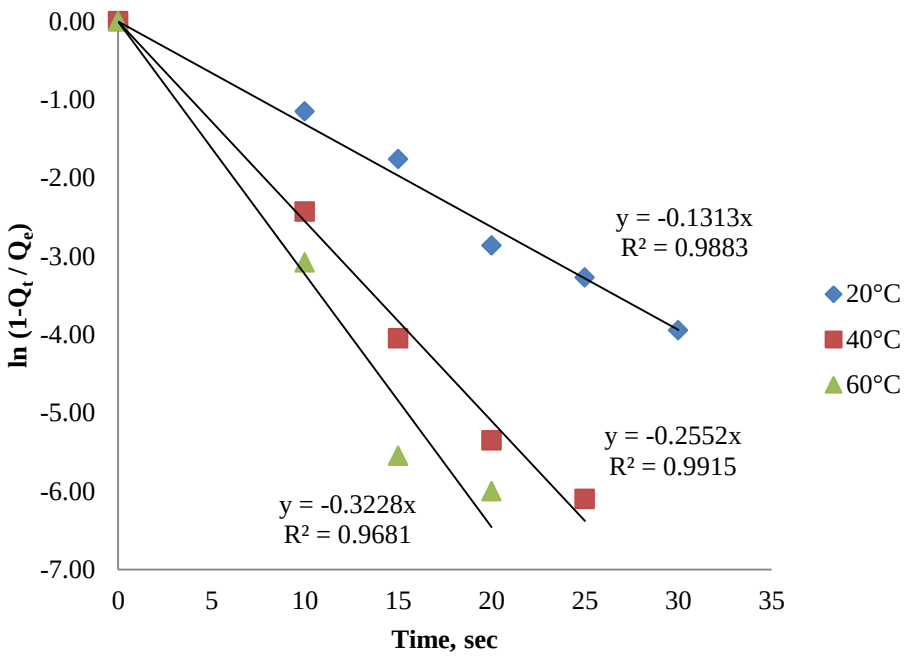

Figure 2.2.6. First-order adsorption rate kinetics as a function of time and temperature (n=6)

Original data points of adsorption rates vs. inverse temperature were linearly regressed and then graphed as illustrated in Figure 2.2.7. From the slope of linear regression the activation energy E_a of the system was calculated by the *Arrhenius* equation[61]:

$$\ln k = -\frac{Ea}{RT} + \ln A \qquad \text{Equation 2.2.5}$$

R represents the universal gas constant (8.314 $J \cdot mol^{-1} \cdot K^{-1}$) and T is temperature in Kelvin (K). The activation energy was determined to be 19 ± 3 $kJ \cdot mol^{-1}$.

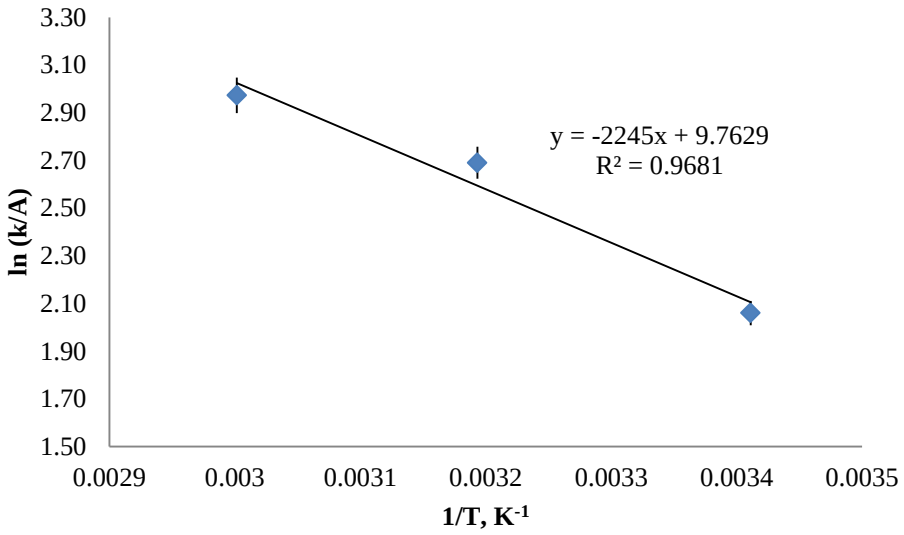

Figure 2.2.7 Linear regression of the reduced adsorption rate constant *k/A* as a function of inverse temperature (n=6)

2.2.2.6 Rhenium Adsorption Thermodynamics on AG 1-X8

Calculations were performed to examine the thermodynamic characteristics of the chromatographic system. The equilibrium distribution coefficient values, K_d, at t = 20 s, were used to determine the changes in enthalpy (ΔH) and in entropy (ΔS) by the following formulation[62]:

$$\ln (K_d \cdot \rho_s) = -\frac{\Delta H}{RT} + \frac{\Delta S}{R} \qquad \text{Equation 2.2.6}$$

R represents the universal gas constant (8.314 J·mol^{-1}·K^{-1}). ρ_s (g· cm^{-3}) is the density of the wet resin. It was decided to use the K_d values at t = 20 s because equilibrium had been reached for the 60 °C samples by this time. By plotting the natural log of the equilibrium distribution coefficient (ln K_d) versus the reciprocal temperature (K^{-1}), ΔH and ΔS were determined from the slope and the intercept of the linear fit equation, respectively (Figure

2.2.8). The enthalpy change (ΔH) was determined to be 11.1 ± 0.5 kJ·mol^{-1}; the positive value indicates that the adsorption of perrhenate on AG 1-X8 is an endothermic reaction. This is an expected outcome since ionic bonds between the support ions and their counter ions must be broken for the perrhenate to bond with the support. The entropy change (ΔS) was determined to be 0.104 ± 0.003 kJ·mol^{-1} K^{-1}.

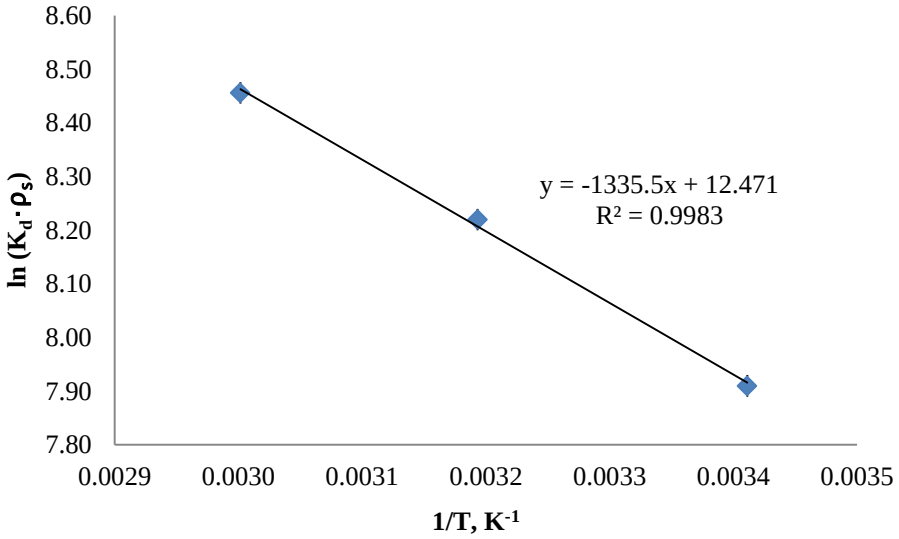

Figure 2.2.8. Linear regression of ln ($K_d \cdot \rho_s$) as a function of inverse temperature (n=6)

Using the enthalpy and entropy changes, it was also possible to calculate the Gibbs free energy (ΔG) of the system using the *Gibbs-Helmholtz* equation (Equation 2.2.7). The results indicated that the thermodynamic potential at 20 °C (ΔG = -19.3 ± 0.8 kJ·mol^{-1}) exceeds the needed activation energy of 19 kJ·mol^{-1} to induce a spontaneous reaction. Additionally, the data for 40 and 60 °C illustrates the increased spontaneity of the system as temperature is increased. The thermodynamic data is summarized in Table 2.2.7.

$$\Delta G = \Delta H - T \cdot \Delta S \qquad \text{Equation 2.2.7}$$

Table 2.2.7. Thermodynamic characteristics of Re adsorption on AG 1-X8 resin

ΔH (kJ·mol^{-1})	ΔS (kJ·mol^{-1}·K^{-1})	ΔG (kJ·mol^{-1}) 293.15 K	313.15 K	333.15 K
11.1 ± 0.5	0.104 ± 0.003	-19.3 ± 0.8	-21.4 ± 0.9	-23 ± 1

2.2.2.7 Rhenium Adsorption Behavior on AG 1-X8 in Aqueous Media

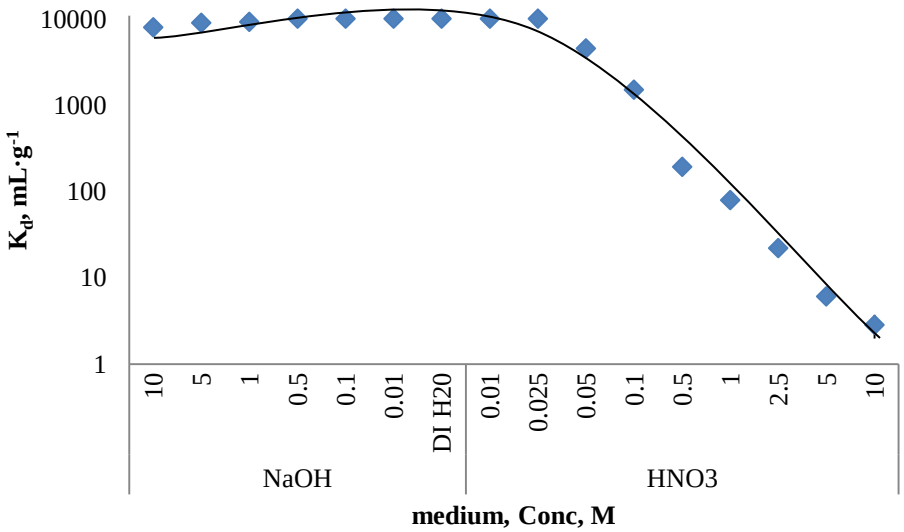

Figure 2.2.9. Rhenium K_d at various acid and base concentrations. (n=6)

Rhenium equilibrium distribution coefficients were acquired as a function of acid or base concentration at 20 °C (Figure 2.2.9). The resin was found to show the best affinity for ReO_4^- in slightly basic conditions and little affinity for rhenium above moderate acid concentrations. At higher concentrations of NaOH, the OH^- ion caused a slight decrease in the amount of perrhenate retained. At higher HNO_3 concentrations, free perrhenic acid was released and stripped from the resin.

2.2.2.8 Tungstate Interference of Perrhenate Adsorption on AG 1-X8

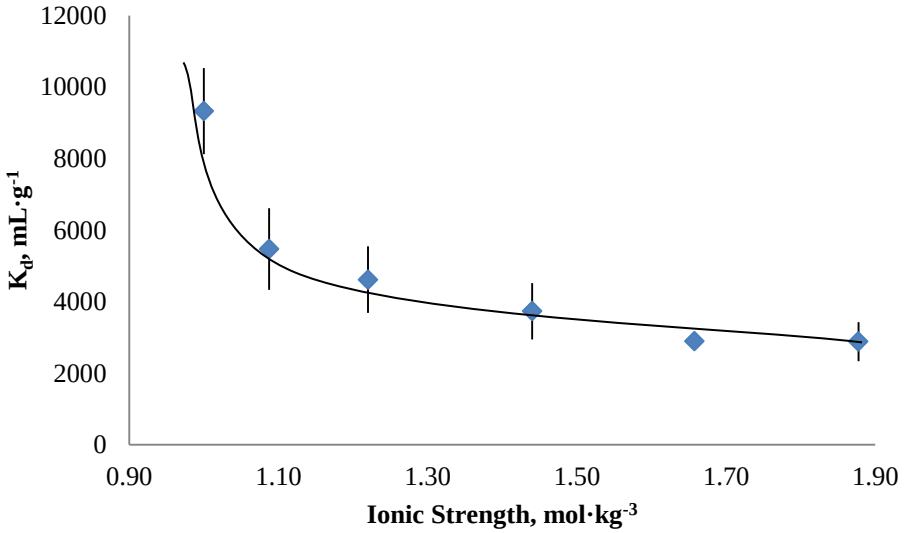

Figure 2.2.10. Rhenium K_d as a function of total ionic strength *I*. (n=6)

A study was performed to examine the effect of tungstate (WO_4^{2-}) mass on the adsorption of no-carrier-added amounts of radiorhenium. The standard batch method described above was applied using varied amounts of tungstate added to 1.0 M NaOH. The total ionic strength *I* of each sample was calculated using Equation 2.2.8. It was found that tungstate does affect the retention of Re but the resin maintained a viable K_d (~3000 mL·g^{-1}) even at the highest expected concentration of tungstate (Figure 2.2.10). The limited interference of tungstate even at higher concentrations may be explained by the large hydration energy of tungstate and relatively low hydration energy of perrhenate. Due to its large hydration energy, the hydrophilic tungstate ion preferentially remains in the aqueous solution while the more lipophilic perrhenate interacts with the organic resin[63].

$$I = \frac{1}{2}\sum[i]\, z_i^2 \qquad \text{Equation 2.2.8}$$

Total ionic strength (I) is a measure of the total amount of ions dissolved in a solution. The variable [i] represents the concentration of a given ion whereas z_i represents the charge of the given ion.

2.2.2.9 Tungsten Adsorption Behavior on AG 1-X8

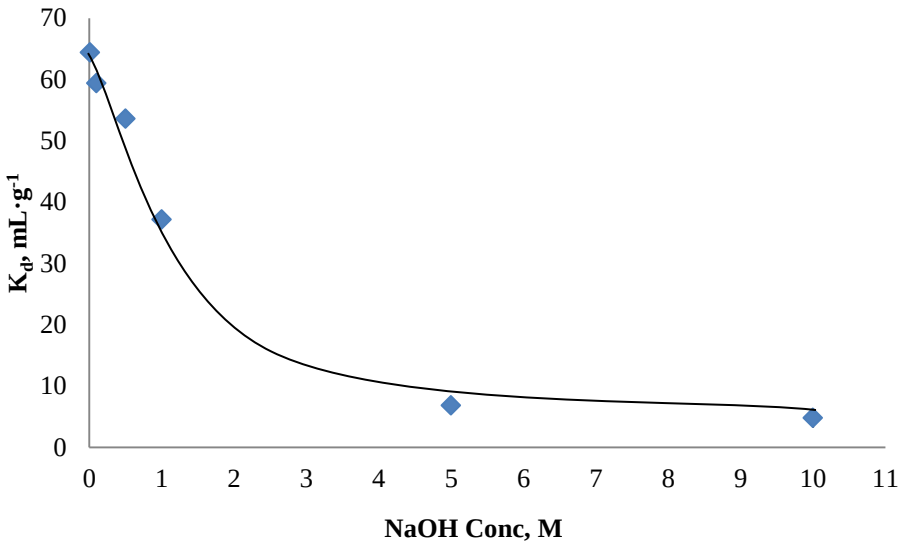

Figure 2.2.11. Tungsten K_d at various base concentrations. (n=6)

Further studies were performed to investigate the retention of tungsten on AG 1-X8 (Figure 2.2.11). Tungstate is not well retained on the column especially above moderate concentrations of base. Tungstate has a large hydration energy, making it hydrophilic and limiting its interaction with the resin[63]. Higher OH^- ion concentrations cause a decrease in the amount of tungsten retained. Tungsten was not tested in acidic solutions owing to WO_3 precipitation in the absence of strong complexing agents.

2.2.2.10 Rhenium/Tungsten Separation Factor on AG 1-X8

Rhenium/tungsten separation factors were calculated from the distribution coefficients obtained for the different base concentrations. The highest separation factors were observed for 10 M and 5 M NaOH matrices due to the very low retention of tungsten at these higher base concentrations (Figure 2.2.12). Large error propagations for the 10 M and 5 M NaOH samples were observed, which was most likely caused by resin flotation effects. At higher NaOH concentrations, the increased density of the solution seems to cause the divinylbenzene-based polystyrene support to float. Favorable separation factors were obtained for all the concentrations of NaOH with the lowest still greater than 150.

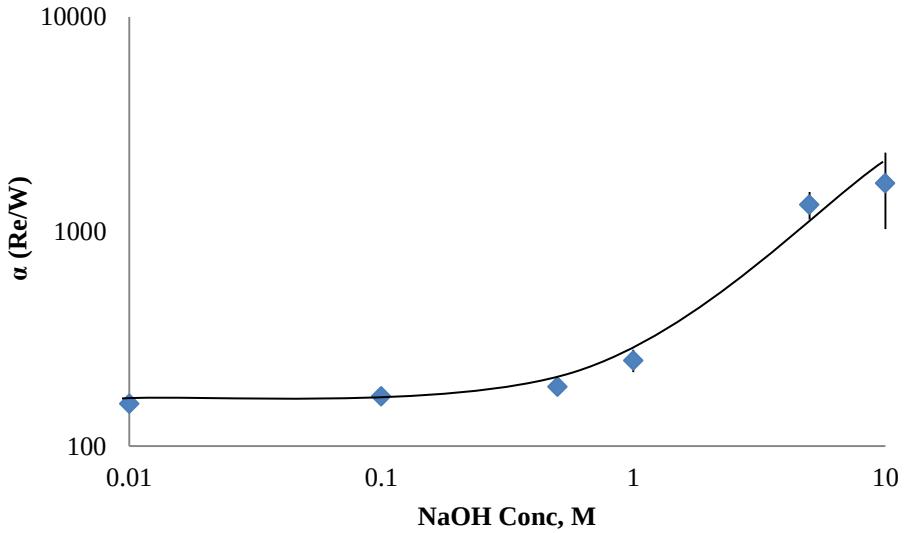

Figure 2.2.12. Rhenium/Tungsten separation factors at various base concentrations. (n=6)

2.2.2.11 Column Retention Volume on AG 1-X8

To put the distribution coefficients, K_d, into a practical application, they were converted to retention factors[64], R_f, to apply the distribution ratio to a column model.

$$R_f = \frac{K_d \cdot m_s}{V_M}$$ Equation 2.2.9

In column chromatography, it is useful to determine the retention volume, V_R, from the retention factor, R_f, and the volume of the mobile phase, V_M:

$$V_R = (R_f + 1) \cdot V_M$$ Equation 2.2.10

The calculated values for the retention factor and retention volume are summarized in Table 2.2.8. The values highlight the efficiency at which Re and W can be separated in basic solutions and subsequently stripping rhenium off the column in acid.

Table 2.2.8. Retention volumes based on K_d. Calculation assumes 1.0 cm^3 bed of resin.

Medium (Conc, M)	Rhenium (n.c.a, 0.18 ± 0.02		Tungsten (14 ± 1 μg of	
	R_f	V_R (cm^3)	R_f	V_R (cm^3)
NaOH (10.0)	1100 ± 200	400 ± 90	1.0 ± 0.3	1.0 ± 0.3
NaOH (5.0)	1300 ± 200	450 ± 60	1.0 ± 0.4	1.00 ± 0.04
NaOH (1.0)	1300 ± 200	470 ± 60	5.0 ± 0.1	2.00 ± 0.04
NaOH (0.5)	1410 ± 10	508 ± 5	7.00 ± 0.07	3.00 ± 0.03
NaOH (0.1)	1410 ± 10	50	8.00 ± 0.08	3.00 ± 0.03
NaOH (0.01)	1410 ± 10	508 ± 5	9.00 ± 0.09	4.00 ± 0.04
DI H_2O	1410 ± 10	508 ± 5	N/A	
HNO_3 (0.01)	1410 ± 10	508 ± 5	N/A	
HNO_3(0.025)	1410 ± 10	508 ± 5	N/A	
HNO_3(0.05)	600 ± 100	230 ± 30	N/A	
HNO_3(0.1)	210 ± 20	76 ± 7	N/A	
HNO_3(0.5)	27 ± 1	10.0 ± 0.5	N/A	
HNO_3(1.0)	11.0 ± 0.3	4.0 ± 0.1	N/A	
HNO_3(2.5)	3.0 ± 0.1	1 .00 ± 0.05	N/A	
HNO_3 (10.0)	1.00 ± 0.05	1.0 ± 0.1	N/A	
HNO_3 (10.0)	0.00 ± 0.00	1.0 ± 0.3	N/A	

2.2.2.12 Rhenium and Tungsten Adsorption Behavior on TEVA Resin

Due to the efficient separation of tungsten and rhenium observed on AG 1-X8, batch studies were performed to test the retention of rhenium on TEVA anion exchange resin.

Like AG 1-X8, TEVA is a quaternary amine anion exchange resin, but TEVA has long, alkyl chains where AG 1-X8 has methanol function groups. For this reason, it was expected that lipophilic perrhenate would have a stronger affinity for TEVA than AG 1-X8. A similar high affinity was observed under basic conditions. Under acidic conditions, TEVA retained this high affinity too well; using TEVA would necessitate very high acid concentrations to recover the perrhenate from the column. Results of this study are illustrated in Figure 2.2.13.

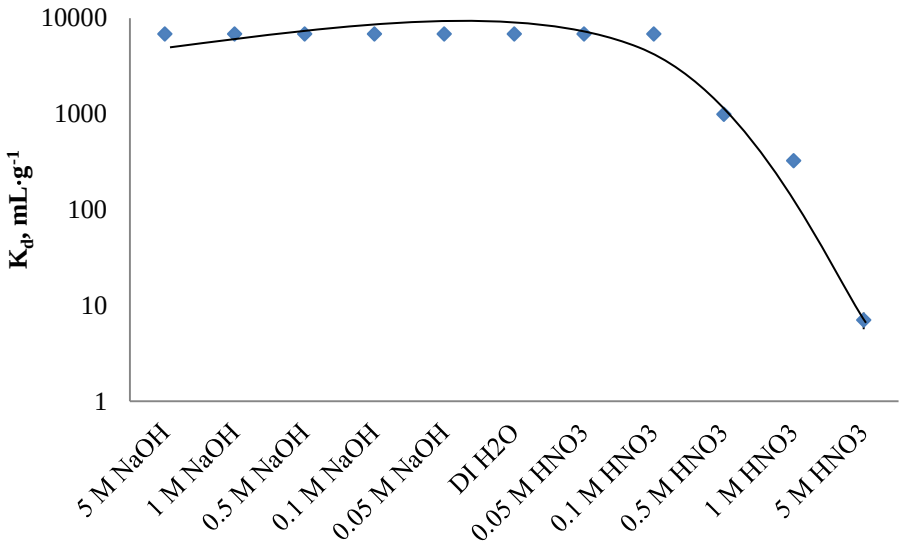

Figure 2.2.13. Rhenium Adsorption Behavior on TEVA resin (n=6)

2.2.2.13 Rhenium and Tungsten Absorption Behavior on AnaLig Resin

A proprietary resin (AnaLig) utilizes a metal selective ligand chemically bonded to a solid support. AnaLig Re-02 PS resin was tested for its ability to selectively extract perrhenate while allowing tungstate to elute. Batch studies were performed to examine the retention of tungsten and rhenium on AnaLig under basic conditions (Figure 2.2.14).

Perrhenate had some affinity for the resin at lower concentrations of NaOH, while tungstate had no affinity at any concentration; this lack of affinity for tungstate makes it possible to cleanly separate the two metals although the affinity for perrhenate is still not strong. To reduce the concentration of base, it was chosen to proceed with column studies using 1 M NaOH since the benefit to increasing the base concentration was minimal.

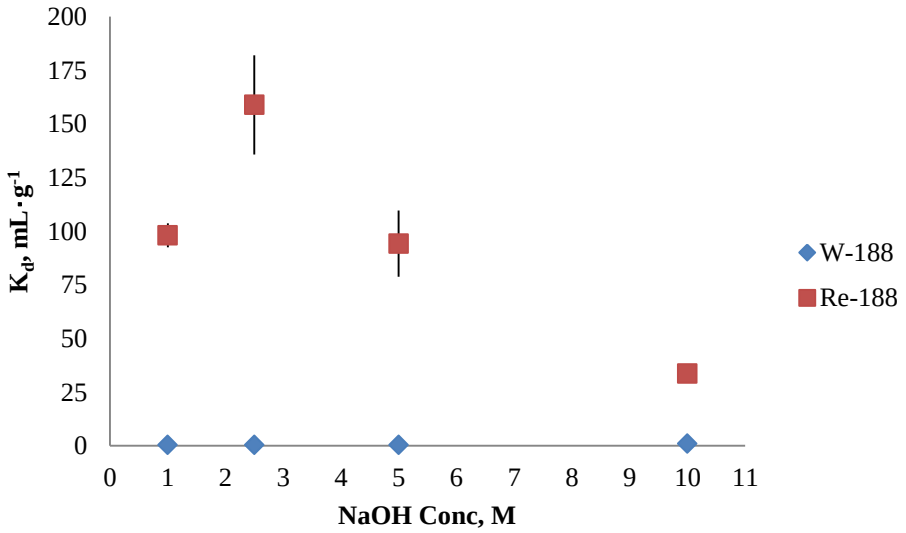

Figure 2.2.14. Rhenium and Tungsten Adsorption Behavior on AnaLig (n=6)

2.2.2.14 Separation of Rhenium and Tungsten using AnaLig Resin

Column studies were performed to separate perrhenate and tungstate using AnaLig Re-02 PS resin. The loading solution (1 M NaOH) was based on batch studies, while the elution conditions (70° C H_2O) were based on a literature source[65] for SuperLig resin (a larger particle size support of the same resin). These conditions proved to be quite effective. The initial tracer studies exhibited separation of perrhenate and tungstate with > 90% of the expected rhenium recovered and isolated from the tungsten.

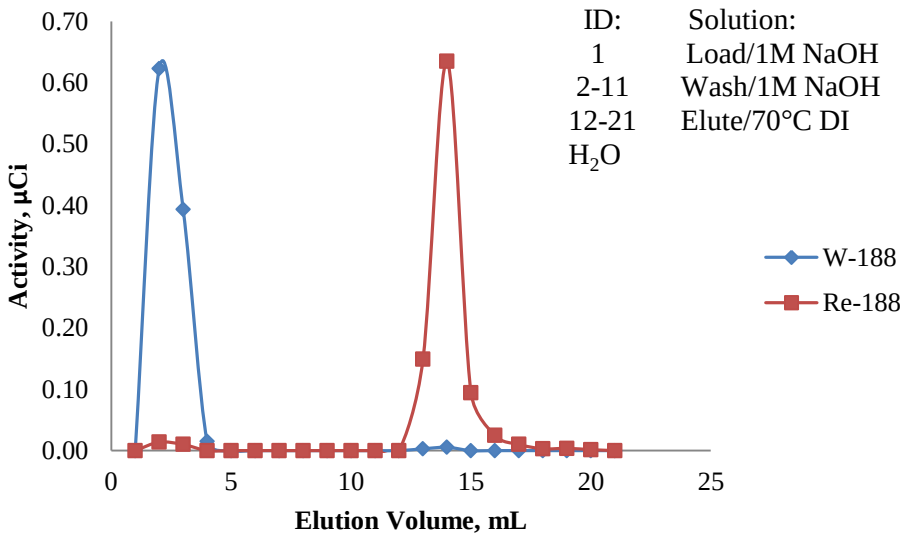

Figure 2.2.15. Separation of rhenium and tungsten using AnaLig resin

For practical application, the column must be robust enough to handle excessive tungsten from the target while retaining the rhenium. With the low distribution coefficients noted in the batch studies, there was concern that rhenium breakthrough would occur easily with increased tungstate concentrations. A column was tested using the same conditions except a large excess of tungstate (1 M concentration) was added to the load solution. Under these conditions, a large fraction of the perrhenate co-eluted with the tungstate in the load volumes and a significantly lower recovery was noted.

Additional studies were performed to alter the elution conditions. The purpose was to eliminate the necessity to heat the solution. 1 M HNO_3 and 0.9% NaCl (saline) were tested as alternate elution solvents. Using 1 M HNO_3 as the eluent necessitated a larger elution volume to strip the rhenium off the column thus making it less effective. Saline did not effectively elute rhenium from the column and thus was ineffective.

2.2.2.15 W Metal Target Irradiations at BNL

^{nat}W metal foils were irradiated at BLIP for various times and currents (Table 2.2.9). The beam was degraded from 116.3 MeV to ~12.5 MeV through various degraders and two RbCl production targets. At this proton energy, several isotopes of rhenium were produced in micro- and millicurie quantities (Table 2.2.10). Additionally, ^{187}W was produced in millicurie quantities; this outcome was unexpected. The secondary neutrons being ejected from the (p, xn) reactions on the RbCl targets produce a strong enough flux of neutrons to produce significant quantities of ^{187}W via the ^{186}W(n, γ)^{187}W reaction. The neutron capture cross section and resonance integral are quite high for this reaction: 38 b and 490 b, respectively.

Table 2.2.9. Tungsten target irradiations at BNL and their respective irradiation parameters

Target	Dimensions	Target Design	Irradiation Time	Integrated Current
1	78 mm x 78 mm x 0.1mm	Clam Shell	5 min	2.53 µAh
2	78 mm x 78 mm x 0.05mm	Clam Shell	15 min	7.57 µAh
3	25.4 mm Ø x 0.05 mm	Bolted Can	60 min	118.38 µAh

Table 2.2.10. Rhenium isotope activities at end of bombardment for tungsten targets irradiated at BLIP

Target	^{181}Re	^{182}Re	^{182m}Re	^{183}Re	^{184}Re	^{186}Re	^{187}W
	mCi	mCi	mCi	µCi	µCi	µCi	mCi
1	0.321	0.728	0.0235	4.83	3.61	5.13	1.13
2	1.62	0.463	0.565	18.9	24.4	22.2	1.98
3	10.2	-	-	223	138	163	3.21

The production rate observed experimentally was compared to the theoretical production rate calculated using data from the TENDL-2014 database (Table 2.2.11). Due to the target array design at BNL, there was some uncertainty in the proton energy entering the

target and the exact current. The presence of ^{181}Re suggest the beam energy was not in 8-10 MeV range as expected but greater than 11.5 MeV; this result lead to the increased production rate of ^{183,184}Re and the reduced production rate of ^{186}Re. Further studies will need to be conducted to better optimize the irradiation parameters.

Table 2.2.11. Comparison of theoretical and experimental production rates for the ^{nat}W metal target irradiated at BNL

Isotope	Production Rate ($\mu Ci \cdot \mu Ah^{-1} \cdot g^{-1}$)		Percentage of Theoretical Produced
	Theoretical	Experimental	
^{181}Re	0.00	181.86	Unexpected
^{182}Re	13.51	N/A	N/A
^{182m}Re	31.93	N/A	N/A
^{183}Re	0.55	3.98	717.04
^{184}Re	2.00	2.46	123.28
^{186}Re	27.83	2.91	10.44

To demonstrate possible production scenarios with enriched ^{186}W, the production rates for ^{186}Re and the largest radiorhenium contaminant (^{181}Re) from the 1 hour irradiation (Target 3) were multiplied by the effective change noted in Table 2.2.4. Additionally, the production schedule at BLIP would allow for significantly longer irradiation periods, so the data was extrapolated to 48 hour irradiations under the same conditions as an example. The results are illustrated in Table 2.2.11. Under these conditions, it would be possible to quickly produce millicurie quantities of ^{186}Re with few radiorhenium impurities.

Table 2.2.11. ^{nat}W irradiation data extrapolated to enriched ^{186}W

Isotope	^{nat}W Production Rate	Enriched ^{186}W Production Rate	Extrapolated Activity (t_{irr} = 48 hours)
	$\mu Ci \cdot \mu Ah^{-1} \cdot g^{-1}$	$\mu Ci \cdot \mu Ah^{-1} \cdot g^{-1}$	μCi
^{181}Re	179.90	0.069	92
^{186}Re	2.85	10.02	22987

2.2.2.16 W Metal Target Dissolution and Separation at BNL

Each of the tungsten targets was dissolved in 30% H_2O_2 with gentle heat. The dissolution took several hours to completely dissolve the foil; this is in comparison to tungsten metal powder that dissolved in ~ 30 minutes for a similar mass. Once dissolved, the heat was increased to decompose any residual peroxide. The peroxide must be completely decomposed or it could cause bubbling and create channels in the column. The solution was made basic to ~ 1 M NaOH prior to loading on the column and it was highly acidic prior to adding base. Slow additions of base with mechanical stirring were necessary to prevent the reaction from becoming too rapid. A vigorous reaction could occur causing the solution to bubble over the sides of the container; this reaction can be exaggerated by the presence of residual peroxide. Once the solution was basic, it was allowed to cool to room temperature prior to loading on the column.

In the initial column study, the 4 mL AG 1-X8 bed volume was too large. The rhenium slowly passed through the column and a large portion (25 %) remained adsorbed on the column. The bed volume was reduced to 2 mL for the next column and recovery rates were quite good (> 95 % for both W and Re). Once the method was optimized, a triplicate study was performed using 1 M NaOH to load, water to wash, and 6 M HNO_3 to elute the column. In the elution volume, 94.6 ± 5.7 % of the rhenium was recovered with no detectable tungsten, while 92.2 ± 5.9 % of the tungsten was recovered in the load and rinse volumes. On the final target, the method was successfully adapted for use in a hot cell. Rhenium was isolated into the elution volume with no detectable tungsten.

2.2.3 Conclusions

Accelerator-based irradiations of $^{nat}WS_2$ and ^{nat}W metal targets established the feasibility of producing rhenium *via* the $^{nat}W(p, xn)^{186}Re$ reaction pathway. The production rates achieved both at MURR and BNL demonstrated that enriched ^{186}W starting material is necessary to produce clinically useful activities of ^{186}Re while reducing the production of other radiorhenium isotopes. The production of ^{186}Re via the $^{186}W(p, n)^{186}Re$ reaction is promising because the optimal cross section occurs at low enough proton energies that small, medical cyclotrons could perform the necessary irradiations.

Several chromatographic resins were evaluated to separate rhenium and tungsten. The results indicate the best resin for the separation scheme appears to be AG 1-X8. AnaLig had a significantly lower distribution coefficient than AG 1-X8, which raises concerns of product loss due to breakthough. Additionally, the AnaLig material received was poorly quality controlled and was the most expensive at ~ $50/gram. TEVA had a slightly reduced distribution coefficient compared to the AG 1-X8 on the basic side but still significantly high. The problems arise on the acidic side. With the large alkyl chains, TEVA had too high of an affinity for the lipophilic perrhenate and rhenium could not be eluted without high concentrations of acid. AG 1-X8 had the best retention of perrhenate in base, stripped well in acid and was the cheapest resin at ~$5/gram.

An in-depth study of the AG 1-X8 separation method was performed. Equilibrium distribution coefficients on AG 1-X8 were measured under various conditions for rhenium and tungsten and found that rhenium can easily be isolated from a large quantity of tungsten. Data on Re isothermal kinetics and adsorption thermodynamics suggests

that Re adsorption follows pseudo-first order kinetics and has a "cut-off" temperature of roughly 20^{o} C, below which spontaneous events are less likely to occur and Re retention would be greater.

A one-step ion exchange column separation method was applied to separate radiorhenium obtained from the proton bombardment of a W metal target. Radiorhenium, in the form of ReO_4^-, is quantitatively retained on the column using basic aqueous media, while allowing WO_4^{2-} to pass through. After acidification, the $^{186}WO_4^{2-}$can be recycled for a more cost effective routine bulk production process design. The retained ReO_4^- can subsequently be removed from the column using acidic media. Although the presence of large quantities of WO_4^{2-} does have a slight effect on the radiorhenium adsorption, it does not impact the quality of the separation method to a significant extent; a high Re distribution ratio still prevails. With its rapid and highly selective adsorption of rhenium from NaOH solutions and its quick release in a small volume with 6 M HNO_3, AG 1-X8 provides the basis for a remote controlled bulk recovery design for high specific activity ^{186}Re.

2.2.4 Future Studies

Future work will include production of clinical activities of ^{186}Re using targets of enriched ^{186}W in a high-current proton beam. Further optimization of the separation method may be necessary. Due to the biocompatibility issues with strong acid, elution with various organic and aqueous media will be tested to provide final form of rhenium easily adapted to radiopharmaceutical kit formation.

Chapter 3: Production of ^{72,77}As

Arsenic has several radioisotopes that may be useful for imaging (^{70,71,72,74}As) and therapy (^{74,76,77}As) making it possible to develop a diagnostic/therapeutic radiopharmaceutical pair[12,42]. The longer half-lives of both ^{72}As and ^{77}As allow for attachment to antibodies and proteins, which require more time to localize at their targeted tissues, thus enabling a wider range of applications[66–70]. Arsenic-72 ($t_{1/2}$ = 26 h, β^+ = 3.34 MeV, 88% abundance) is a longer-lived, positron emitter with suitable nuclear properties for PET imaging. Arsenic-77 ($t_{1/2}$ = 38.8 h, β^- = 0.68 MeV, 100% abundance) is a beta emitter with suitable properties for radioimmunotherapy. The chemistry of arsenic is diverse, enabling the production of a wide variety of radiopharmaceutical drugs. To date, the clinical application of arsenic radiopharmaceuticals has been hindered by the limited availability of radioarsenic and issues with the separation and purification of radioarsenic from the target/parent isotope. In this research, several reaction pathways were investigated for the production of ^{72}As and separation methods were investigated for the purification of ^{72}As and ^{77}As.

3.1 Production of ^{72}As from the Decay of Accelerator Produced ^{72}Se

There is interest in making ^{72}As available from a ^{72}Se generator[42,71]; this would be advantageous in making ^{72}As routinely available for clinical use. Selenium-72 ($t_{1/2}$ = 8.5 d, ε, 100% abundance) is a long-lived radionuclide that can be produced from charged

particle reactions on Ge, Br, and As targets[72–76]. In this research, the proton irradiation of naturally enriched ^{75}As via the ^{75}As(p, 4n)^{72}Se reaction and the alpha particle irradiation of ^{70}Ge or ^{nat}Ge metal via the ^{70}Ge(α, 2n)^{72}Se reaction were studied.

Many methods to produce a ^{72}Se/^{72}As generator have been proposed in the literature, such as distillation[74,77], electroplating[78], solvent extraction[79], and solid phase extraction[75,80]. The primary issues with many of these methods are (1) they require extensive handling, which is prohibitive with a highly radioactive sample, (2) involve the use of harsh chemical solvents, or (3) require special equipment. To simplify this process, a simple, chromatographic selenium/arsenic separation method was developed in an effort to make high-purity, high-specific-activity ^{72}As products readily available from a ^{72}Se generator[81]. The method involves minimal handling of the target material, in an effort to reduce operator dose, and uses mild reagents throughout the separation process.

3.1.1 Materials and Methods

Reagents and solvents were purchased from Alfa Aesar (Ward Hill, MA), Fisher Scientific (Pittsburg, PA), Mallinckrodt (St. Louis, MO), and Sigma-Aldrich (St. Louis, MO). Germanium metal powder was purchased from Alfa Aesar (Ward Hill, MA). Ethylene bis(stearamide) wax was purchased from Fisher Scientific (Pittsburgh, PA). 20 mL HDPE scintillation vials with polyethylene caps (referred to as poly collection vials) were purchased from Fisher Scientific. 1 mL HDPE counting vials (referred to as poly counting vials) were prepared on-site at MURR using HDPE "Finathene 5203" beads from Fina Chemicals (Brussels, Belgium). Titanium and aluminum metal backings were prepared on-site to designed specifications using grade 5 titanium and grade 6061

aluminum purchased from McMaster-Carr (Elmhurst, IL). AG 1-X8 anion exchange resin was obtained from Bio-Rad Corporation (Hercules, CA). All reagents and materials were used as received without any further purification. All water used was purified on-site (deionized water from a Millipore system to >18MΩcm).

3.1.1.1 Instrumental Analysis

Radiochemical assays at MURR for ^{76}As and ^{75}Se were determined by γ-ray spectroscopy using an automated gamma counting system. The automated system was an in-house built unit at MURR. The detector was a Canberra Model GC2018S HPGe detector system with a relative efficiency of 20% at 1.33 MeV. The detector diameter was 60.5 mm, detector length was 30.5 mm, and the distance from the window was 5 mm. The detector's specified FWHM at 1.33 MeV was 1.8 keV. Spectral analyses were performed by a Canberra Model 9660 analyzer. All samples were counted for at least 600 seconds and decay corrected to the time correlating to either the end of contact time for the batch studies or the first column wash for the column studies. The detector dead time was kept to less than 10% for all samples.

Radiochemical assays at BNL for ^{72,73,75}Se were determined by γ-ray spectroscopy using a HPGe detector system. The detector was an Ortec Model GMX-18190-P HPGe detector system with a relative efficiency of 13.4% at 1.33 MeV. The detector diameter was 48.2 mm, detector length was 45.5 mm, and the distance from the window was 3 mm. The detector's specified FWHM at 1.33 MeV was 1.76 keV. Spectral analyses were performed by an Ortec DSPEC Jr. 2.0 multichannel analyzer. All samples were

counted for at least 1200 seconds and decay corrected to the time correlating to the end of target bombardment. The detector dead time was kept to less than 10 % for all samples.

3.1.1.2 Batch Studies for ^{75}Se and ^{76}As Separation on AG 1-X8 Resin at MU

After a target has been irradiated, the ^{72}Se must be isolated from the target material and trapped on a substrate to prepare the generator. Radiotracers of ^{75}Se and ^{76}As were prepared as surrogates for ^{72}Se and ^{72}As. Selenium-75 ($t_{1/2}$ = 119.78 d) was produced at MURR via the ^{74}Se (n, γ) ^{75}Se reaction of an encapsulated ^{74}Se (as SeO_2; 98.85%) target, which was dissolved in 1 M HNO_3. Arsenic-76 ($t_{1/2}$ = 1.0942 d) was produced at the MURR via the ^{75}As (n, γ) ^{76}As reaction of an encapsulated ^{75}As (as $^{nat}As_2O_3$) target, which was dissolved in 1 M $NaHCO_3$.

Table 3.1.1. Evaluated selenium and arsenic isotopes and their associated gamma emissions

Radionuclide	Half-life	Gamma emissions (abundances)	Activity per sample
^{76}As	26.3 h	559.1 keV (45.0%)	3.95 µCi (146 kBq)
^{75}Se	119.78 d	136.0 keV (58.5%), 264.7 keV (58.9%)	3.16 µCi (117 kBq)

Various support media were evaluated to elute arsenate while retaining selenate and AG 1-X8 anion exchange resin was identified for further study. To optimize the elution parameters on AG 1-X8, sorption studies were performed via the batch method for selenite, selenate, and arsenate. Prior to use, samples were verified by Dr. Don Wycoff to contain purely selenate, selenite, or arsenate by comparison to standards using HPLC[81]. All experiments were performed at room temperature (20°C). The removal of selenium and arsenic from varying pH (-1 to 7) solutions was measured by mixing 50 mg of AG 1-X8 resin with 1.5 mL of a ^{75}Se- or ^{76}As-spiked solution. The liquid-solid system was

mixed by vortexing for 2 minutes and immediately centrifuged for 2 minutes at 7500 rpm. Two 500-microliter aliquots of the supernatant (A_s) were transferred into clean poly counting vials. Additionally, a 500-microliter aliquot of the original solution (A_0) was transferred to a clean poly counting vial to determine the original activity. The distribution ratio, K_d, is calculated as follows:

$$K_d = \frac{(A_0 - A_s)}{A_s} * \frac{V}{m} \qquad \text{Equation 3.1.1}$$

A_0 is the original selenium or arsenic activity of the aqueous solution. A_s is the selenium or arsenic activity remaining in solution following contact with the resin. $(A_0 - A_s)$ is the amount of activity adsorbed by the resin. The volume (V) of the aqueous solution is measured in milliliters and the mass (m) is measured in grams resulting in the distribution ratio having units of mL/g. A larger distribution ratio correlates to a more effective removal of selenate, selenite, or arsenate from the aqueous solution.

3.1.1.3 Production of ^{72}As at BNL

SRIM-2008 software[56] was used to calculate theoretical proton stopping power for the arsenide target to determine the proton entry energy and exit energy within the target[82]. A proton energy range of 48 – 50 MeV was chosen for this study to maintain a high ratio of ^{72}Se to ^{73}Se (Appendix A.1.4). The targets were prepared to the necessary thickness to achieve this energy deposition.

Production of ^{72}Se via the ^{75}As(p, 4n)^{72}Se reaction pathway was studied at BNL as one way to produce a ^{72}Se/^{72}As generator. The arsenide target was mounted into an aluminum target can, transferred to a glove box, and sealed under helium gas to ensure a

water tight seal. The target was then irradiated with a 50 µA current of 50 MeV protons for 30 minutes at BLIP. The irradiated target was dissolved and an aliquot was analyzed by gamma spectroscopy using an HPGe detector to determine the radioselenium yields. Separation chemistry was performed by Smith *et al*[82] to isolate selenium and arsenic.

Using data from the batch studies, a $^{72}Se/^{72}As$ generator was developed at the radiotracer scale by Wycoff *et al*[81]. Studies were performed at BNL to translate the published method from the tracer scale to a production scale arsenide target. The solution containing selenium and arsenic was evaporated to dryness and re-dissolved in 30% H_2O_2. The solution was heated to react selenium and arsenic with hydrogen peroxide to ensure they were fully oxidized to selenate and arsenate. A stock solution was prepared by diluting a 500 µL aliquot of this sample to a total volume of 5 mL with Milli-Q water in a clean poly collection vial. A 500 µL aliquot of the stock solution was transferred to a clean vial and diluted to a total volume of 3 mL using Milli-Q H_2O to create a counting sample to determine the original activity. Next, a 4 mL bed volume AG 1-X8 column was prepared and conditioned using 0.03 M HCl followed by Milli-Q water until the pH of the eluent was over pH 5 (the unaltered Milli-Q water tested pH 5.5). A 4 mL aliquot of the stock solution was loaded onto the column. The column washed with 2 x 5 mL of Milli-Q water, and then eluted with 4 x 5 mL of 0.03 M HCl. Each of these fractions were counted on a Na(I) gamma counter. The spectra were compared to a spectrum of the original uncontacted solution to look for a change in ratio of the Se and As peaks.

Additional studies were performed using the method above with some modifications. In the second study, the pH of the Se/As solution was adjusted to between pH 7-8 using sodium bicarbonate. In the third study, the solution was diluted to a total volume of 20

mL using Milli-Q water and pH adjusted to between pH 7-8 to provide a lower total ionic strength solution.

To improve the column performance, a simple method was tested to remove the bulk As target material from the solution prior to loading on the column. A sample of the stock solution was taken to complete dryness and re-dissolved in 10 mL of 30% H_2O_2 and allowed to react with gentle heating. Once no further bubbling was noted, 1 mL of concentrated HCl was added to the sample to ensure it was highly acidic. A 0.75 mL aliquot of the acidic Se/As solution was combined with 0.75 mL of either chloroform, hexane, or toluene in a small centrifuge tube. The samples were allowed to mix on a shaker table for 10 minutes. A 0.5 mL aliquot of each of the organic layers were transferred to a clean poly counting vial and counted on the NaI gamma counter and the spectra compared to a 0.5 mL aliquot of the original uncontacted Se/As solution. The spectra were observed for the presence of activity within the organic layer and a shift in ratio of the Se and As peaks.

3.1.1.4 Germanium Target Development for Irradiation at UW

An alternative target for the production of ^{72}Se *via* the ^{70}Ge(α, 2n)^{72}Se reaction pathway is in development. The behavior of pressed germanium metal was tested at various pressures and temperatures in order to prepare physically stable targets. Germanium metal powder was used in this study because production targets may use enriched ^{70}Ge, which is only available as a powder.

The simplest method by directly pressing the pure germanium metal powder into a backing was tested initially. Germanium metal was dried overnight in an oven heated to

100° C to evaporate any moisture within the material and transferred to a desiccator (placed under vacuum) to cool prior to pressing. A mass of ~240 mg of Ge metal was weighed directly into an aluminum backing. A 13 mm stainless steel anvil was placed on top of the germanium metal powder and given a gentle press by hand to pack the powder; this assembly was then placed inside a 25 mm die. A specially-machined, stainless steel ring was used to help hold the target in place in the center of the die. The 25 mm plunger was placed on top of the assembly and the whole die was transferred to a hydraulic press. The material was pressed three times, incrementally increasing the pressure up to a final pressure of 13.8 MPa. Upon inspection of the first pellet, the pellet was re-pressed to a higher final pressure of 31 MPa.

For the next set of pressed pellets, ethylene bis(stearamide) wax (Figure 3.1.1) was added to the germanium metal powder to work as a binding agent while pressing. Wax-to-metal ratios (by weight) between 1:100 and 1:25 were prepared and shaken on a shaker plate for 15 minutes to ensure homogeneity. The mixture was pressed into an aluminum backings to a final pressure of 31 MPa using the method described above. The targets were then heated to 450° C for 2 hours under argon gas flow to volatilize the wax leaving a pressed germanium pellet.

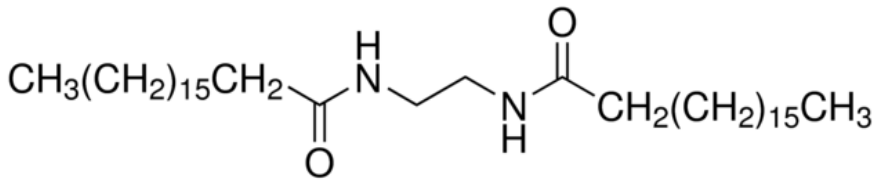

Figure 3.1.1. Ethylene bis(stearamide)

To eliminate the potential contaminates produced from using the wax, studies were conducted to sinter and anneal germanium into a target backing. Germanium has a melting point of 938° C, which is significantly higher than the melting point for aluminum (660° C). For these studies, titanium backings were used for their higher melting point (1668° C). A more appropriate metal will be chosen for the actual production targets. Bombardment of ^{nat}Ti results in the production of ^{48}V, which has two strong gamma emissions at 983.5 keV (99.98%) and 1312.1 keV (98.2%) that create a dose issue even with short irradiations. To sinter the germanium sample, approximately 100 mg of germanium metal was pressed into the titanium backing as previously described and sintered at 800° C for 1.5 hours to allow the germanium to fuse together and form a more firmly packed target. To anneal the germanium sample, approximately 100 mg of germanium metal was pressed into a titanium backing and heated to 940° C for 5 minutes to allow the germanium to melt and anneal as it slowly cooled back to room temperature.

3.1.2 Results and Discussion

3.1.2.1 Batch Studies for Se/As Separation on AG 1-X8

To determine the best pH for selenate retention and arsenate elution, equilibrium distribution ratios were acquired as a function of pH. The retention of selenate, selenite, and arsenate was impeded by the high ionic strength of the pH -1 and 0 solutions. Since selenic acid is a strong acid, selenate was readily retained by the resin and quickly reached its maximum K_d. Maximum K_d is a function of the minimal detectable activity of the detector and the activity of the spike; the maximum K_d in this experiment is 3570

mL/g. Since selenous and arsenic acids are weaker acids, selenite (pK_{a1} = 2.62) and arsenate (pK_{a1} = 2.19) are weakly retained until reaching a solution pH where the anionic species is the primary form. The several orders of magnitude difference in the retention of selenite and selenate highlights the necessity of an oxidation step to prevent loss of selenium from the column. Additionally, the results indicate eluting at pH 2 allows the parent, selenate, to be retained on the column while the arsenate daughter is removed (Figure 3.1.2).

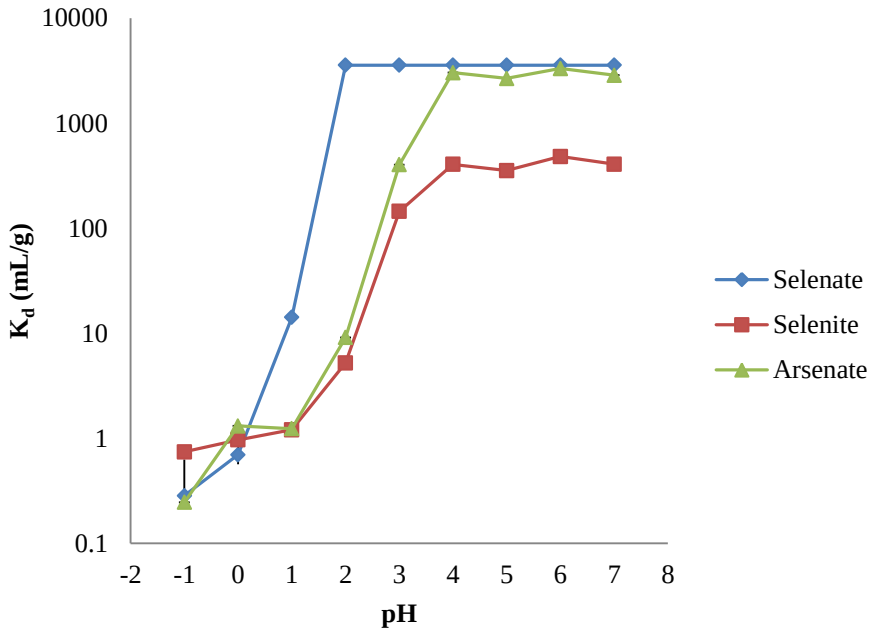

Figure 3.1.2. Distribution coefficient for selenate, selenite, and arsenate as a function of pH (n = 6; the error bars are included)

3.1.2.2 Arsenide Irradiation and $^{72}Se/^{72}As$ Generator Development at BNL

An arsenide target was irradiated for 30 minutes with a 50 µA current of 50 MeV protons. The target was dissolved and an aliquot of the solution was counted on an HPGe detector to qualify and quantify the radioselenium products (Table 3.1.2).

Table 3.1.2. Experimental yield of ^{72,73,75}Se from As target and comparison to theoretical yield

Isotope	Half-Life (d)	Experimental Activity at EOB (mCi)	Theoretical Activity at EOB (mCi)	Percentage of Theoretical Activity Produced
^{72}Se	8.50	0.29	1.49	19.4
^{73}Se	0.30	25.08	36.07	69.5
^{75}Se	119.78	0.01	0.02	62.4

As noted in Table 3.1.2, several hundred microcuries of ^{72}Se were produced in this short irradiation. A longer irradiation could provide enough ^{72}Se to prepare a generator for clinical use. The discrepancy between the production percentages of ^{72}Se and ^{73,75}Se suggest the produced activity of ^{72}Se may be underestimated. Selenium-72 only has one gamma emission at 45.9 keV (57.2% abundance); this gamma emission is in a high background region due to Compton scattering. For this reason, there may be a large error associated with amount of ^{72}Se produced. Once a purified sample of selenium can be obtained, a more accurate representation of the activity can be determined from the ^{72}As daughter in-growth. A significant activity of the short-lived isotope, ^{73}Se, was produced during this irradiation but once this undesired side product decays away the produced ^{72}Se could be utilized to prepare a ^{72}Se/^{72}As generator. The presence of the longer-lived ^{75}Se will affect the specific activity of the product as the generator ages, but ^{75}Se decays to stable ^{75}As so there is no radiation concern from it.

3.1.2.3 Evaluation of Column Separation Method on Production Target at BNL

Initial studies have been performed to transition the ^{72}Se/^{72}As generator developed at the radiotracer scale at MU to a production scale using an irradiated arsenide target at BNL. Initial studies resulted in selenium immediately bleeding through the column in the load solution. An important change from separation performed at the radiotracer scale and the

separation with the arsenide target was the presence of carrier arsenic present in solution resulting from the arsenide target; this excess arsenic seemed to overload the column causing both arsenic and selenium to be eluted during the load aliquot. An additional column was performed with the load solution diluted to reduce the ionic strength of the arsenic loaded on the column. The arsenic concentration was still too high and selenium breakthrough was immediately noted. With this result, it was decided to develop a method to remove the bulk arsenic prior to loading on the column.

A simple liquid-liquid extraction method was tested for its ability to separate arsenic and selenium. As previously mentioned selenic acid is a strong acid, while arsenic acid is a weak acid with pKa_1 = 2.19. In a highly acidic solution, selenium should be in the charged, monoprotic form ($HSeO_4^-$) and arsenic should be fully protonated and neutral (H_3AsO_4); these conditions should allow the arsenic to be extracted into an organic solvent while the selenium remains in the aqueous solution. Chloroform, toluene, and hexane were tested for their ability to extract arsenic. Minimal extraction of arsenic was noted in all cases. It was decided to work on an additional column separation to isolate the selenium from the bulk arsenic prior to loading on the generator.

3.1.2.4 Germanium Target Development for Irradiation at UW

Studies were performed to produce a stable germanium metal pressed pellet for the production of ^{72}Se via the $^{70}Ge(\alpha, 2n)^{72}Se$ reaction pathway. Simply pressing the pure germanium metal into the target backing resulted in an unstable, powdery target that did not hold its form and could easily be disrupted even with gentle handling. The addition of the ethylene bis(stearamide) wax did provide some improvement in the stability of the

target but the pellets were still not robust enough for use in an actual irradiation. The target prepared with the 1:25 wax:metal ratio was too porous and crumbled with handling while the 1:100 ratio appeared more solid but cracked readily with handling.

Sintering the germanium metal at high temperature appears to be the most promising approach. The targets were still slightly crumbly to the touch but did have better overall integrity. A target sintered at 800° C is shown in Figure 3.1.5; the grainy texture of the pressed material is still apparent. Adjusting the sintering temperature to 850° or 900° C could provide a more properly fused pellet while eliminating the grainy texture. A study intended to anneal the metal at 940° C (melting point = 938° C) was unsuccessful. The germanium did not hold its form; surface tension caused the molten metal target to contract into a small sphere (Figure 3.1.3).

Figure 3.1.3. (left) sintered Ge pellet (right) annealed Ge mass

Prior to performing irradiations at the University of Washington, the theoretical cross section data was analyzed from the TENDL-2014 database for alpha bombardment of germanium targets[57,58]. Nineteen reaction pathways were determined to have significant

cross-sections (Appendix A.3.3). Evaluating these reactions, an alpha particle energy of 28 MeV was observed to provide the highest cross section for the $^{70}Ge(\alpha, 2n)^{72}Se$ reaction while reducing the production of many major radionuclidic impurities. Calculations were performed using the cross section data for the $^{70}Ge(\alpha, *)$ reaction pathways and ^{72}As, ^{69}Ge, ^{72}Se, and ^{73}Se are the major activation products expected (Appendix A.3.3). With a significantly shorter half-life, ^{73}Se can be allowed to decay prior to using the ^{72}Se. A method to separate Se from the bulk Ge is under development by Wycoff[83]. Once the germanium is removed, the existing Se/As generator system will remove the co-produced arsenic radiocontaminants in the first elution then the subsequent elutions provide the high purity ^{72}As product.

3.1.3 Conclusions

The development of new drugs utilizing longer-lived positron emitters, such as ^{72}As, will allow for the continued growth and increased application of PET imaging for quantitation, especially radioimmunoimaging. Arsenic-72 can be made available in high specific activity from the decay of its ^{72}Se parent. Clinical scale quantities of ^{72}Se can be produced using the arsenide target developed at BNL. Chemical methods were successfully employed to remove other radionuclides. Distribution coefficient studies showed selenite has greater than an order of magnitude weaker retention on AG 1-X8 than selenate, which would lead to undesired ^{72}Se breakthrough and product loss; this highlights the importance of oxidizing the product prior to loading on the column. Additionally, arsenate retention is over an order of magnitude weaker than selenate at pH 2, which could be used to develop a Se/As generator system. Column studies on an actual arsenide target at BNL showed it was necessary to reduce the bulk arsenic in the

column load solution to prevent overloading the column and causing undesired selenium breakthrough.

Germanium targets could provide viable targets to produce ^{72}Se at UW. The preparation of a physically stable target has been challenging. Pressing the pure metal or using a binder such as ethylene-bis(stearamide) wax did not provide structurally sound targets. While annealing the metal at its melting point, surface tension caused the metal to contract into a small sphere that was unusable. Sintering the metal prepared a more stable target and appears to be the most promising production route.

3.1.4 Future Studies

Further work needs to be performed to isolate selenium from arsenic to simplify the preparation of the ^{72}Se/^{72}As generator. Studies need to be performed to better understand the limitations of the ^{72}Se/^{72}As generator that has been developed. Special consideration needs to be given to the effect of ionic strength on the column and the maximum allowable arsenic concentration without selenium breakthrough. Once this chemistry is verified, a ^{72}Se/^{72}As generator with clinical scale activities should be prepared and evaluated for ^{72}As elution and purity, selenium breakthrough, and radiation resistance.

For the preparation of germanium metal target, sintering studies need to be performed at higher temperatures to balance the results between the sintered sample and annealed sample to get a smoother, fused pellet. Once a stable target form can be prepared, initial irradiation can be performed at UW using natural abundance germanium.

3.2 Production of ^{77}As from the Decay of Reactor Produced ^{77}Ge

Arsenic-77 ($t_{1/2}$ = 38.8 h, β^-, 0.683 MeV) is a beta-emitting radionuclide of interest for therapeutic applications as a matched pair to the diagnostic, positron emitting radionuclide ^{72}As ($t_{1/2}$ = 26.0 h, β^+, 88%, EC, 12%); together these two isotopes would provide an excellent diagnostic/therapeutic pair. High specific activity ^{77}As can be achieved in a reactor by producing ^{77}Ge ($t_{1/2}$ = 11.30 h, β^-) via the ^{76}Ge(n, γ)^{77}Ge reaction, which then decays to the ^{77}As and chemically separated to prepare a high specific activity product.

Availability of high specific activity ^{77}As depends on separation from its ^{76}Ge target and recovery/recycling of the ^{76}Ge for reuse. Many methods to isolate arsenic from germanium have been reported in the literature, such as solvent extraction[84,85], distillation[68,86], ion exchange[68,87,88], solid phase extraction[89], and thin layer chromatography[90]. The primary issues with many of these methods are they require extensive handling, which is prohibitive with a highly radioactive sample, involve the use of harsh chemical solvents, or require special equipment. A simple, chromatographic germanium/arsenic separation method was developed in an effort to make high-purity, high-specific-activity ^{77}As products more readily available. The method involves minimal handling of the target material, in an effort to reduce operator dose, and uses mild reagents throughout the separation process.

3.2.1 Materials and Methods

All reagents and solvents were purchased from Alfa Aesar (Ward Hill, MA) and Fisher Scientific (Pittsburg, PA) and used as received. Enriched $^{76}GeO_2$ (96.2% enrichment)

was purchased from Trace Sciences International (Richmond Hill, ON). Analytical grade silica resin, SilicAR, was purchased from Mallinckrodt, St. Louis, MO. Alumina in the acidic form was purchased from Fisher Scientific. Zirconium oxide resin, HZO-01, and poly-prep columns (0.8 cm ID; 10 mL reservoir) were purchased from Bio-Rad Corporation, Hercules, CA. 20 mL HDPE and glass scintillation vials with polyethylene caps (referred to as poly or glass collection vials) were purchased from Fisher Scientific. 1 mL HDPE counting vials (referred to as poly counting vials) were prepared on-site at MURR using HDPE "Finathene 5203" beads from Fina Chemicals (Brussels, Belgium). All water used was purified on-site (deionized water from a Millipore system to greater than 18 MΩcm).

3.2.1.1 Instrumental Analysis

Radiochemical assays for ^{76,77}As and ^{77}Ge were determined by γ-ray spectroscopy using an automated gamma counting system. The automated system was an in-house built unit at MURR. The detector was a Canberra Model GC2018S HPGe detector system with a relative efficiency of 20% at 1.33 MeV. The detector diameter was 60.5 mm, detector length was 30.5 mm, and the distance from the window was 5 mm. The detector's specified FWHM at 1.33 MeV was 1.8 keV. Spectrum analyses were performed by a Canberra Model 9660 analyzer. All samples were counted for 900 seconds and decay corrected to the time correlating to either the end of contact time for the batch studies or the first column wash for the column studies. The detector dead time was kept to less than 10% for all samples.

3.2.1.2 Irradiation of GeO_2 and production of ^{76}As radiotracer

Germanium-77, used as a Ge tracer in column and batch studies, was produced at MURR via the $^{76}Ge(n, \gamma)^{77}Ge$ reaction of a quartz encapsulated ^{76}Ge (as GeO_2; 96.2% enrichment) target. The quartz capsule was opened and the material transferred to a glass collection vial. The sample was dissolved using 500 µL of 1 M NaOH with gentle heat (35-45° C) and mechanical stirring for 20 minutes. After dissolution, the target was acidified to pH 4-5 using slightly more than 500 µL 1 M HCl and then 100 µL 30% H_2O_2 was added to ensure the sample was fully oxidized. High specific activity ^{77}As, used as an As tracer in column studies, was made available from the decay of ^{77}Ge. Carrier added ^{76}As, used as an As tracer in batch studies, was produced at MURR via the $^{75}As(n, \gamma)^{76}As$ reaction of a poly-vial encapsulated ^{75}As (as $^{nat}As_2O_3$) target. The sample was directly dissolved in the poly counting vial using a needle to create a vent hole and then to add 500 µL of 1 M $NaHCO_3$ to the vial. Once dissolved, the sample was transferred to a clean, glass collection vial. Table 3.2.1 lists the various radionuclides, their nuclear properties, and their activities as used in these studies.

Table 3.2.1. Evaluated germanium and arsenic isotopes and their associated gammas

Radionuclide	Half-life	Gamma emissions (abundances)	Activity per sample
^{76}As	26.3 h	559.1 keV (45.0%)	2.19 µCi (81 kBq)
^{77}As	38.8 h	239 keV (1.59%)	nca
^{77}Ge	11.3 h	211 keV (30.0%), 215.5 keV (27.9%), 264.5 keV (53.3%)	4.17 µCi (154 kBq)

nca = no carrier added; activity calculated.

3.2.1.3 Determination of optimum chromatographic media

For the development of a germanium and arsenic separation method, several support media were evaluated for their ability to retain and elute each element. These studies

were carried out *via* the batch method. All studies were performed at room temperature (20° C). The removal of germanium and arsenic from varying pH (1-13) solutions was measured by mixing 50 mg of each resin with 1.5 mL of a ^{77}Ge- or ^{76}As-spiked solution; the solution pH was adjusted using either HCl or NaOH as necessary. The liquid-solid system was mixed by vortex for 2 mintues and immediately centrifuged for 2 minutes at 7500 rpm. Two 500 µL aliquots of the contacted solution (A_s) were transferred into clean poly counting vials. Additionally, a 500 µL aliquot of the original uncontacted solution (A_0) was transferred to a clean poly counting vial. The activity in each vial was determined by γ-ray spectroscopy and the distribution ratio, K_d, calculated by the following formulation:

$$K_d = \frac{(A_0 - A_s)}{A_s} * \frac{V}{m} \qquad \text{Equation 3.2.1}$$

where A_0 is the original germanium or arsenic activity of the aqueous solution. A_s is the germanium or arsenic activity remaining in the solution following contact with the resin. ($A_0 - A_s$) is the amount of activity absorbed by the resin. The volume (V) of the aqueous solution in measured in milliliters and the mass (m) is measured in grams resulting in a distribution ratio unit of mL/g.

3.2.1.4 Evaluation of the dissolution and solution preparation conditions

While adjusting the pH of the dissolved GeO_2 target, it is suspected that some arsenic is trapped within the Ge, which can re-precipitate as the pH approaches 4-5. To minimize the loss of arsenic to Ge re-precipitation, a study was performed to evaluate the effect of varying the counterions present during the dissolution and pH adjustment of the GeO_2 targets. Several acids (HCl, HNO_3, and H_3PO_4) were used in the previously described

dissolution method to pH adjust the aqueous solution prior to its addition to a column. A poly-prep column packed with a 1 mL bed volume of silica resin was conditioned with methanol (~10 bed volumes). A 50 µL aliquot of the ^{77}Ge (in equilibrium with ^{77}As) solution, which had been oxidized and pH adjusted to 4-5, was loaded on the top of the column. The column was then washed with methanol (5 x 1 mL, then 3 x 5 mL). Arsenic eluted from the column during these methanol washes. The column was washed with DI H_2O (2 x 5 mL) to remove the germanium. Each of these methanol and water fractions was collected in a separate poly collection vial. Then, a 500 µL aliquot of each solution was transferred to a separate poly counting vial. Additionally, A 5 µL aliquot of the original spike solution was diluted into 10 mL and a 500 µL aliquot was transferred to a poly counting vial. The activity in each vial was determined by γ-ray spectroscopy. Percent recovery in each fraction was determined by comparison of the activity in the original spike solution versus the activity in each fraction; any difference between the summed fraction activities and the original spike activity was attributed to loss on the column.

3.2.1.5 Single Silica Column Chromatography

A poly-prep column packed with a 1 mL bed volume of silica resin was conditioned with methanol (~10 bed volumes). A 50 µL aliquot of the ^{77}Ge (in equilibrium with ^{77}As) solution, which had been oxidized and pH adjusted to 4-5, was added to the top of the column followed by methanol washes (20 x 1 mL). Arsenic was eluted from the column during these methanol washes. The column was then washed with DI H_2O (4 x 5 mL) to elute germanium. Each of these fractions was collected in separate poly collection vial, and then a 500 µL aliquot was transferred to a poly counting vial. Additionally, a 5 µL

aliquot of the original spike solution was diluted into 10 mL and a 500 µL aliquot was transferred to a clean poly counting vial. The activity in each vial was determined by γ-ray spectroscopy. The percent recovery in each fraction was determined by comparison of the activity in the original spike solution versus the activity in each fraction; any difference between the summed fraction activities and the original spike activity was attributed to loss on the column.

3.2.1.6 Dual Silica Column Chromatography

Two poly-prep columns were packed with a 1 mL and 0.5 bed volume of silica, respectively. Each column was conditioned with 10 mL of methanol. The separation method described in Section 3.2.1.5 was applied to the 1 mL bed volume column. The first eight 1 mL methanol fractions from this column were combined and added to the 0.5 mL bed volume column. The column was then washed with methanol (20 x 1 mL) and DI H_2O (4 x 5 mL). As before, each fraction was collected in separate vial and a 500 µL aliquot was transferred to a poly counting vial. Additionally, a 5 µL aliquot of the original spike solution was diluted into 10 mL and a 500 µL aliquot was transferred to a clean poly counting vial. The activity in each vial was determined by γ-ray spectroscopy and the percent recovery in each fraction was determined by comparison of the activity of the original spike solution versus the activity in each fraction. An additional study was performed using this method in which the methanol fractions were evaporated to 1 mL to concentrate the sample activity; this step was performed to minimize germanium breakthrough resulting from the larger load volume.

3.2.1.7 Tandem Silica / HZO Column Chromatography

Two poly-prep columns were packed with a 1 mL bed volume of either silica or HZO-01 resin, respectively. The two columns were placed in tandem with the silica column eluting directly onto the HZO-01 column; the columns were conditioned with ~10 mL of methanol. A 50 µL aliquot of ^{77}Ge (in equilibrium with ^{77}As) was added to the top of the silica column followed by methanol washes (10 x 5 mL). During these washes, arsenic was eluted from the silica column and captured on the HZO-01 column while germanium was retained on the silica column; any germanium breakthrough was expected to pass through the HZO-01 column without retention. After the methanol washes, the columns were separated and eluted using a pH 11 NaOH solution (20 x 1 mL). Finally, the columns were completely stripped using a pH 13 NaOH solution (4 x 5 mL). Each of these fractions was collected in a separate poly collection vial and then a 500 µL aliquot was transferred to a poly counting vial. Additionally, a 5 µL aliquot of the original spike solution was diluted into 10 mL and a 500 µL aliquot was transferred to a poly counting vial. The activity in each vial was determined by γ-ray spectroscopy. The percent recovery in each fraction was determined by comparison to the activity of the original spike solution; any difference between the summed fraction activities and the original spike activity was attributed to loss on the column. Although the counting geometries were not optimized for the columns, the columns were counted on the HPGe to determine the approximate activity remaining on each of the two columns.

3.2.2 Results and Discussion

3.2.2.1 Determination of optimum chromatographic media

Several chromatographic materials were evaluated for their ability to retain arsenate and germanate and equilibrium distribution ratios were acquired as a function of pH (1 – 13). Distribution ratios were determined at each pH using a batch method. A larger distribution ratio correlates to a more effective removal of germanium or arsenic from the aqueous solution. For the acidic alumina resin, the retention of arsenate and germanate was too similar to separate one from the other without the use of a large elution volume or risk tailing of one species into the other (Figure 3.2.1). Silica showed promise to recover the bulk of the germanium target material while removing arsenate (Figure 3.2.2). Germanium adsorbed strongly to the silica using methanol and had no retention using any aqueous solution, while arsenate showed little affinity under the conditions evaluated. HZO-01 showed promise for isolating arsenate from germanium (Figure 3.2.3); arsenate was retained by the resin in methanol and had little affinity at high ionic strength (pH $\leq$ 1 or $\geq$ 11), while germanium had little affinity in methanol and greater affinity at high pH. Using the greater affinity at high pH, arsenate could be stripped from the column and any residual germanate not removed by the methanol would remain bound.

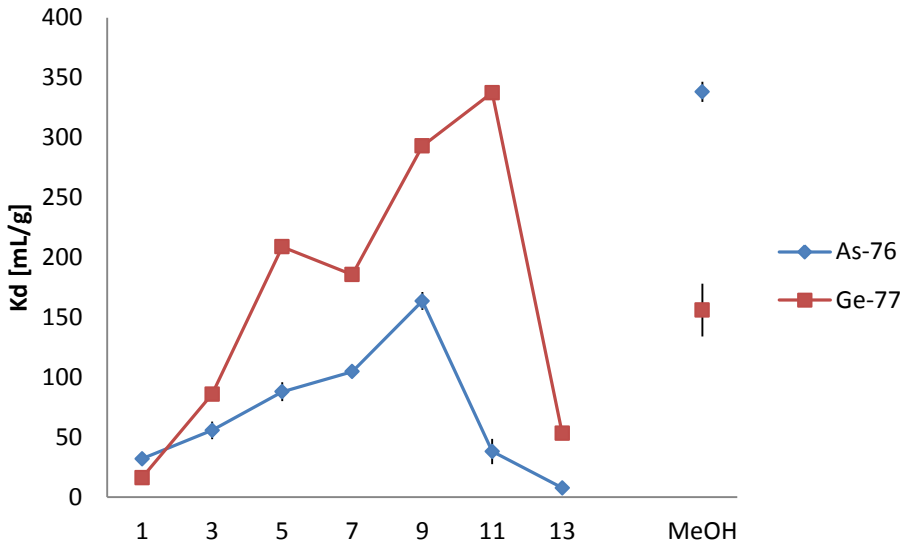

Figure 3.2.1. Distribution coefficient for arsenate and germanate on acidic alumina. (n=6; error bars included)

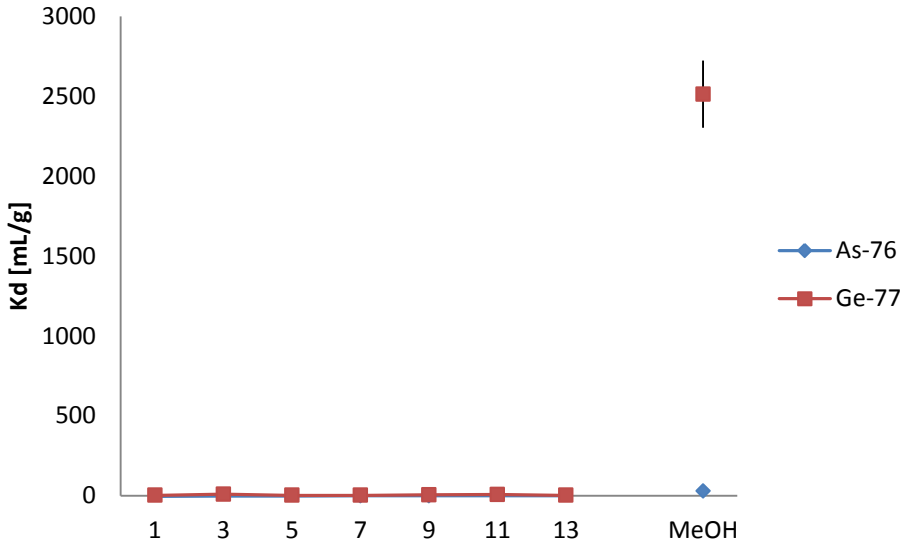

Figure 3.2.2. Distribution coefficient for arsenate and germanate on silica. (n=6; error bars included)

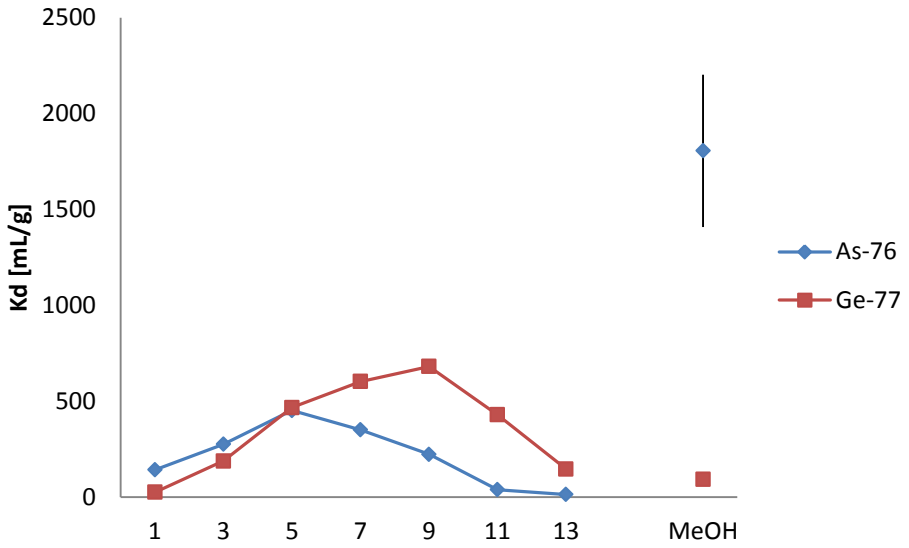

Figure 3.2.3. Distribution coefficient for arsenate and germanate on zirconium oxide. (n=6; error bars included)

3.2.2.2 Evaluation of the dissolution and solution preparation method

Column chromatography studies were performed examining the role of the counterion present from the acid used for the pH adjustment. Initial dissolutions were performed using HCl; HCl was compared to HNO_3 and H_3PO_4. All solutions were adjusted to pH 5 ± 0.5. The first 20 mL of elution volume were methanol and then 10 mL of water was used to strip the column. The results are illustrated in Figures 3.2.4 - 6. Each data set was normalized to the percentage of the recovered material to eliminate variation caused by overall recovery of each solvent system. The HCl-adjusted sample exhibited very small germanium breakthrough in the first 10 mL (0.6 %). However a sizable percentage (12.7%) of the ^{77}As co-elutes with the ^{77}Ge, which could mean it was trapped within the Ge precipitate. Switching to HNO_3 caused the germanium bleed through to lessen (0.04% in the first 10 mL), but it also caused a larger portion of ^{77}As to be trapped within the Ge precipitate (25.7%); this could be a result of a larger portion of Ge precipitating.

Finally, H_3PO_4 was unique compared to the other solvent systems; a much higher percentage of ^{77}As was recovered quickly (67.6% in 1 mL) but the germanium bleed off was more substantial (0.3% with the first mL and 6.1% in the second mL). Additionally, very little ^{77}As co-eluted with germanium (0.4%) suggesting less germanium precipitation occurs with this solvent system. After viewing the results of this study, it was determined to continue using HCl since it successfully removed a large portion of the germanium without sacrificing arsenic recovery.

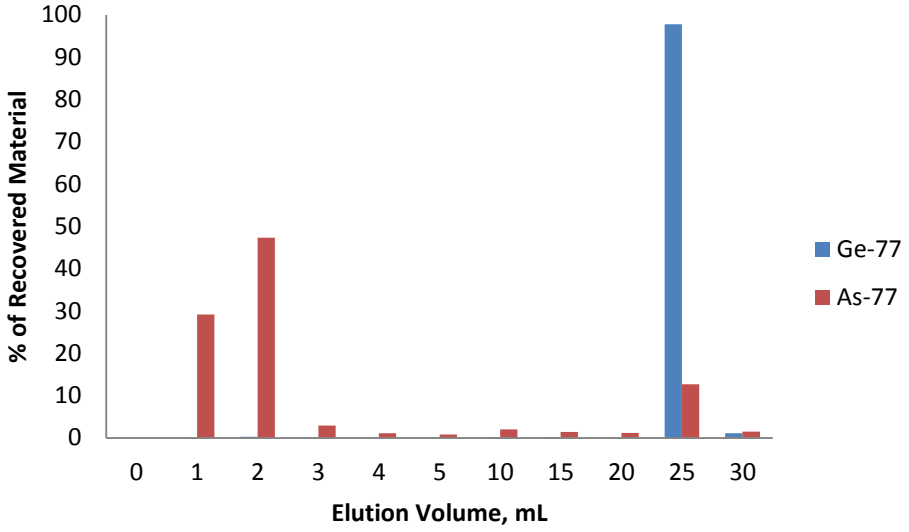

Figure 3.2.4. Elution profile for HCl adjusted Ge sample. (n = 3)

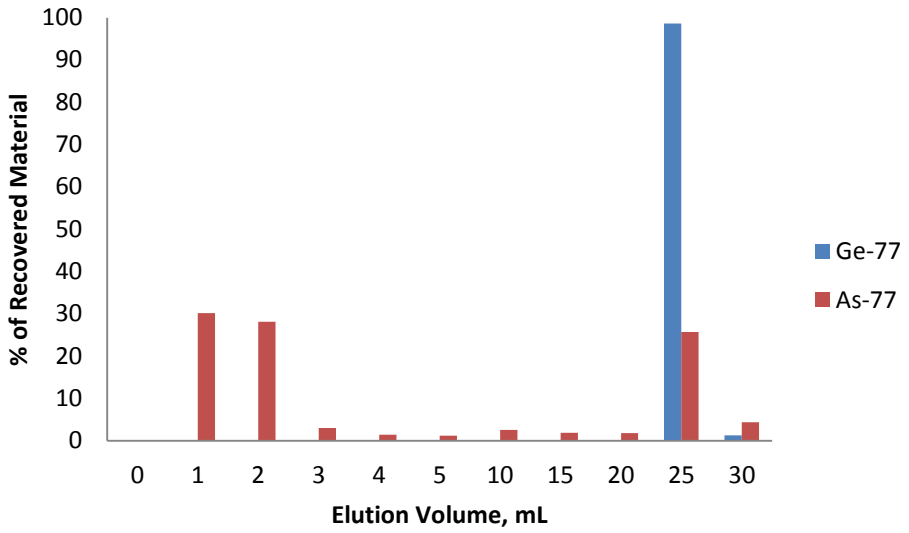

Figure 3.2.5. Elution profile for HNO_3 adjusted Ge sample. (n = 3)

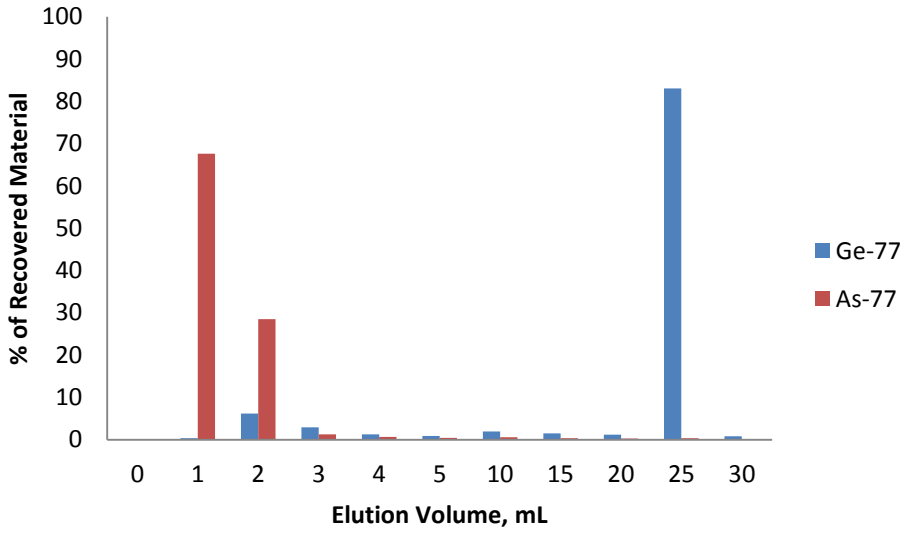

Figure 3.2.6. Elution profile for H_3PO_4 adjusted Ge sample. (n = 3)

3.2.2.3 Single Silica Column

To apply the distribution coefficients in a practical application, column chromatography studies were performed using silica gel. From the distribution coefficients, it was expected that the majority of arsenic would immediately pass through the column with no affinity while the bulk germanium remained adsorbed to the resin. In application, only a fraction of the ^{77}As (33.7 ± 5.5%) quickly passed through and was recovered in a total volume of 2 mL of methanol with a tiny amount of ^{77}Ge (0.09% ± 0.08). After the first few aliquots, germanium slowly began to bleed from the column. Greater than 86% of the Ge-77 was recovered in 5 mL of DI H_2O; this recovery of germanium is critical due to the high cost associated with the enriched $^{76}GeO_2$ starting material, which can be recycled for additional irradiations. The elution profile is illustrated in Figure 3.2.7. It is suspected that the large loss of ^{77}As resulted from the re-precipitation of germanium during pH adjustment with HCl. As the solution approaches pH 4-5, it is possible for a portion of the germanium to precipitate and trap arsenic in the process; this suspicion is further validated by the elution of the germanium. As the elution media is switched to water, effectively increasing the pH to ~7, a large portion of arsenic co-elutes with the germanium.

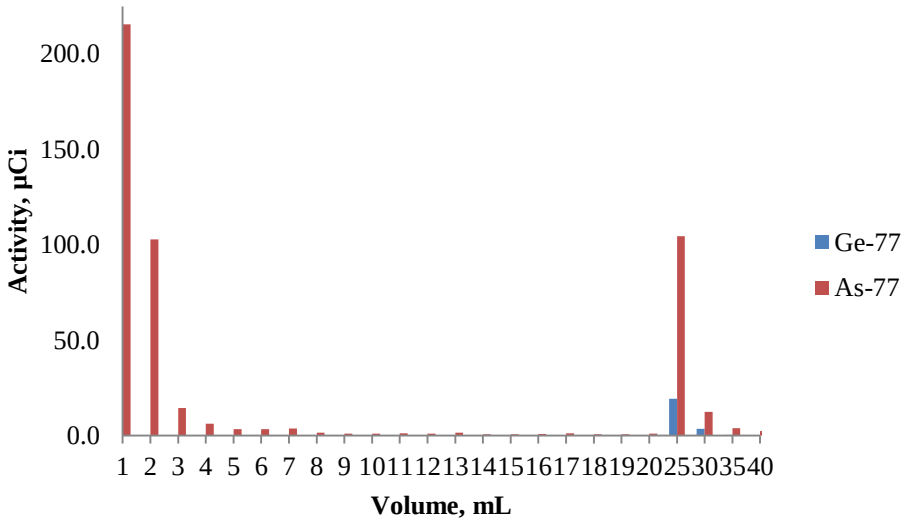

Figure 3.2.7. Column chromatography of Ge-77/As-77 sample. The eluent was changed from methanol to deionized water at 20 mL to recover the Ge target material. (n=6; example graph)

3.2.2.4 Dual Silica Columns

With the slow breakthrough of germanium on the single silica column, a study was performed using two silica columns sequentially to remove the small portion of germanium breakthrough. In the separation process, Ge-77 was reduced to non-detectable quantities but additional As-77 is lost on the column thus reducing the overall yield. Interestingly, greater than 80% of the arsenic loaded onto the second silica column was recovered. If arsenic was merely being lost to the column, the recovery should have been 33.7% as seen on the first column; this result helps to support the loss of arsenic to germanium precipitation. The addition of the dry down step to concentrate the sample prior to loading on the second silica column did not provide any improvement to the method. The overall yield was reduced due to sample loss during transfer from the dry down vial.

3.2.2.5 Tandem Silica / HZO Columns

Due to the increased loss of using two silica columns, a tandem column assembly using silica and HZO-01 was investigated. From the distribution coefficients, it was expected the bulk germanium would be trapped on the silica while the arsenic was trapped on the HZO-01; any germanium breakthrough would pass through the HZO-01 leaving a high purity ^{77}As product behind. In application, the method proved to be no better than the single silica column. Although the sample is free of germanium (Figure 3.2.8), the yield of As-77 is quite reduced by the addition of the HZO-01 column compared to the single silica column.

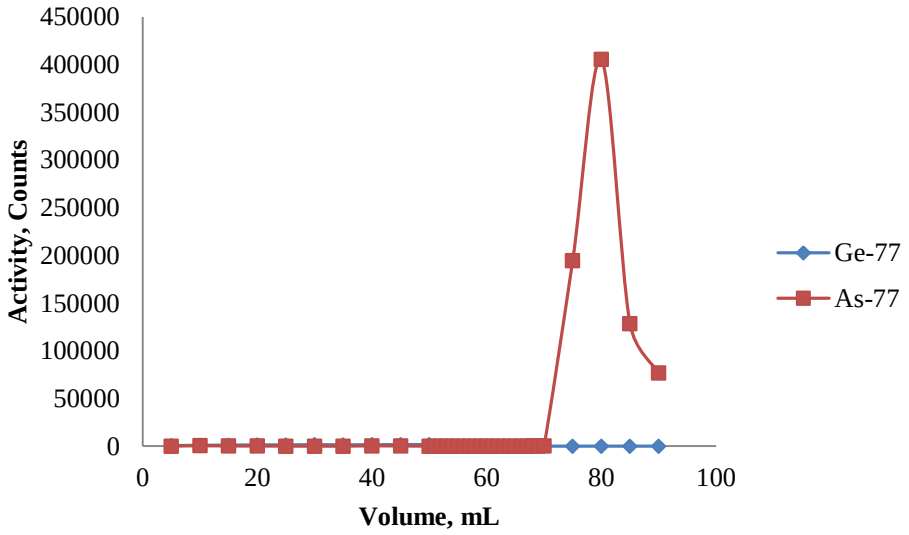

Figure 3.2.8. Ge-77 and As-77 retention on zirconium oxide resin. Volumes: 1-50 methanol, 50-70 pH 11, and 70-90 pH 13.

3.2.3 Conclusions

The availability of high purity radioarsenic, such as ^{72}As and ^{77}As, is highly desirable and would provide a longer-lived, radionuclide pair for radioimmunoimaging and

radioimmunotherapy. The versatile chemistry of arsenic would enable the production of new radiopharmaceutical drugs. A quick, robust method for the separation of no-carrier-added ^{77}As from the GeO_2 target material has been developed to help increase the availability of high purity ^{77}As. Additionally, the enriched ^{76}Ge starting material can be easily recovered for reuse.

Distribution coefficient studies showed germanium has a strong affinity for silica in methanol while arsenic has a limited affinity. In contrast, arsenic has a strong affinity for zirconium oxide in methanol while germanium has a limited affinity. Column chromatography methods were tested based on the results of the distribution coefficient studies. In application to a column, problems were encountered with the tracer level arsenic being trapped inside the bulk germanium precipitate. For this reason, only a fraction of the arsenic was recovered using a single silica column, but most the germanium was removed. Interestingly, most of the arsenic was recovered when passing the eluent of the first column through a second silica column; this further supports the germanium precipitation issue. With some adjustments, this method could quickly separate As from Ge in mild reagents.

3.2.4 Future Studies

Future work will include optimizing the load solution to reduce the loss of arsenic to germanium precipitate. Once this issue is corrected, the method should be applied to the separation of a larger target containing higher activities similar to those used in clinical settings. This would allow for further evaluation of the efficiency of the separation

method. Additionally, the separated ^{77}As would be available for use as a tracer for medical, toxicology, and environmental studies.

Chapter 4: Production of Other Radiopharmaceutical Isotopes

4.1 Production of ^{44,44m}Sc *via* Proton Bombardment of $CaCO_3$

Scandium-44 ($t_{1/2}$ = 3.97 h, $\beta^+_{average}$ = 0.632 MeV, 94.3% abundant) is a positron emitting radiometal with suitable nuclear properties for radiolabeling peptides and other small-molecular-weight biomolecules[12,41]; this radionuclide would provide an excellent imaging agent which could be paired with the beta-emitter ^{47}Sc ($t_{1/2}$ = 3.349 d, β^- = 0.441 MeV, 68.4% abundant, 0.600 MeV, 31.6% abundant) as a diagnostic/therapeutic pair. Additionally, the chemistry of scandium is dominated by Sc^{3+}, which enables the use of well-established chelators such as DOTA or NOTA[91,92]. The production of ^{44}Sc via the ^{44}Ca(p, n)^{44}Sc reaction has been demonstrated on both ^{nat}Ca targets[93] and enriched ^{44}Ca targets[92,94]. These studies demonstrate the feasibility of producing sufficient quantities of high purity ^{44}Sc using a small, medical cyclotron. The purpose of this study was to provide an initial investigation into the feasibility of routinely producing ^{44}Sc using the GE PETtrace cyclotron at MURR.

4.1.1 Methods and Materials

All reagents were purchased from Fisher Scientific (Pittsburgh, PA). Calcium carbonate was purchased from Alfa Aesar (Ward Hill, MA). DGA Resin was purchased from Eichrom Technologies LLC (Lisle, IL). Poly prep columns (0.8 cm ID; 10 mL reservoir and 0.5 cm ID; 2 mL reservoir) were purchased from Bio-Rad (Hercules, CA). 20 mL HDPE scintillation vials with polyethylene caps (referred to as poly collection vials) were

purchased from Fisher Scientific. Aluminum metal backings were prepared on-site to designed specifications using 6061 grade aluminum purchased from McMaster-Carr (Elmhurst, IL). Commercial food-grade aluminum foil was purchased from a local market. Araldite 2011 epoxy adhesive was purchased from Freeman Supply (Avon, Ohio). All reagents and materials were used as received without any further purification. All water used was purified on-site (deionized water fed into a Millipore sytem to > 18 MΩ·cm).

4.1.1.1 Instrumentation

Proton irradiations were performed using a GE PETtrace 800 cyclotron with dual particle capabilities with ion energies up to 16.5 MeV for protons and 8.5 MeV for deuterons and currents up to 80 microamps. Throughout these experiments, the beam was collimated to a 10 mm diameter aperture.

Radiochemical assays for ^{43,44,44m,46,47,48}Sc were performed by γ-ray spectrometry using a Canberra Model GC2018S HPGe detector system (60.5 mm diameter, 30.5 mm length) at a sample distance of 5 mm from the window. The detector has a FWHM at 1.33 MeV of 1.8 keV. Spectral analyses were performed with Canberra Model 9600 multichannel analyzer. All samples were counted for 600 seconds and decay corrected to the time correlating to either the end of contact time for the batch studies or the first column wash for the column studies. The detector dead time was kept to less than 10% for all samples.

4.1.1.2 Target Preparation and Irradiation

SRIM-2008 software[56] was used to calculate theoretical proton stopping power for the $CaCO_3$ targets to determine the proton entry energy and exit energy within the target

(Appendix A.2.7). A proton energy range of 12 – 16 MeV was chosen for this study to maintain a high ratio of ^{44}Sc to ^{44m}Sc (Appendix A.1.5). The targets were prepared to the necessary thickness to achieve this energy deposition.

Calcium carbonate was dried overnight in an oven heated to 100° C to evaporate any moisture within the material and transferred to a desiccator (placed under vacuum) to cool prior to pressing. A mass of 120 – 160 mg of $CaCO_3$ was weighed directly into an aluminum backing. A 13 mm stainless steel anvil was placed on top of the calcium carbonate and given a gentle press by hand to pack the powder; this assembly was then placed inside a 25 mm die. A specially-machined, stainless steel ring was used to help hold the target in place in the center of the die. The 25 mm plunger was placed on top the assembly and the whole die was transferred to a hydraulic press. The material was pressed three times, incrementally increasing the pressure up to a final pressure of 13.8 MPa to ensure a smooth, evenly-distributed pellet. After pressing, the target was sealed in the backing using 16 µm thick aluminum foil, which was epoxied over the face of the target. The epoxy was allowed to cure for a minimum of 15 hours per the manufacturer's specifications. The calcium carbonate targets were irradiated at MURR using 16 MeV protons for a total of 10 µAh. High vacuum was used on the target face while the back side of the target was water cooled to dissipate heat from the proton beam.

4.1.1.3 Target Dissolution and Determination of Activation Products (Initial Irradiation)

After irradiation, calcium carbonate was mechanically separated from the target body and dissolved in 10 mL of 30% H_2O_2 in a poly collection vial. Gentle heating (60° C) was used to help the sample dissolve and completely decompose all of the hydrogen peroxide.

The entire sample was counted on the HPGe detector to qualify and quantify the scandium isotopes produced during the irradiation. The determined activities were decay corrected to the end of bombardment for each isotope present.

4.1.1.4 Target Dissolution and Ca/Sc Separation (H_2O_2 Method)

A second irradiation was performed to test a literature separation method[95]. After irradiation, calcium carbonate was mechanically separated from the target body and dissolved in 10 mL of 30% H_2O_2. A small, 100 µL aliquot was transferred to a poly collection vial and brought up to 10 mL using deionized water; this sample was counted on the HPGe detector to qualify and quantify the scandium isotopes produced during the irradiation. Next, a portion of the sample was combined with 1.0 M HNO_3 in a clean, poly collection vial to create a 0.1 M HNO_3 solution *in situ*. A 0.5 mL bed volume column of DGA resin (0.1625 g) was prepared in a poly-prep column (0.8 cm ID). The column was conditioned with approximately 10 column volumes of 0.1 M HNO_3 and then 5 mL of the Ca/Sc sample was loaded onto the column. The column was washed with 5 mL of 0.1 M HNO_3 and Sc was eluted with 5 mL of 0.1 M HCl. All samples were counted on the HPGe detector to qualify and quantify the scandium radioisotopes present. The activities were compared to the values of the original, untreated aliquot to analyze the sample recovery.

4.1.1.5 Target Dissolution and Ca/Sc Separation (HCl Method)

A third irradiation was performed to test a different literature separation method[92]. After irradiation, calcium carbonate was mechanically separated from the target body and dissolved in 2 mL of 3 M HCl. A small, 50 µL aliquot was transferred to a poly

collection vial and brought up to 10 mL using deionized water; this sample was counted on the HPGe detector to qualify and quantify the scandium isotopes produced during the irradiation. A 0.5 mL bed volume column of DGA resin (0.2038 g) was prepared in a poly-prep column (0.5 cm ID). The column was conditioned with approximately 10 column volumes of 3 M HCl and then 0.5 mL of the Ca/Sc sample was loaded onto the column. The column was washed with 5 x 1 mL of 3 M HCl and Sc was eluted with 5 x 1 mL of 0.1 M HCl. All samples were counted on the HPGe detector to qualify and quantify the Sc isotopes present. The activities were compared to the values of the original, untreated aliquot to analyze the sample recovery.

The study was repeated on an additional $CaCO_3$ target to further test this separation method. The amount of resin was significantly reduced from 0.2038 g to only 0.05377 g. Additionally, a 100 µL aliquot of the original solution was used instead of 50 µL. All other experimental parameters remained the same.

4.1.2 Results and Discussion

4.1.2.1 Target Preparation and Irradiation

Calcium carbonate formed smooth, glossy, firmly-packed pellets at 13.8 MPa. Though the targets are structurally solid, caution was still necessary to not jolt the target as it can easily crack. These thin $^{nat}CaCO_3$ targets were irradiated at 16 MeV for 10 µAh and analyzed for scandium radioisotopes. The scandium radioisotopes, their half-lives, their characteristic gamma used for identification, and activities at the end of bombardment are listed in Table 4.1.1. Under these irradiation conditions, several isotopes of scandium were produced in micro- and millicurie quantities. To produce clean $^{44,44m}Sc$ without the

presence of other scandium radioisotopes, an enriched ^{44}Ca target would be necessary. The ^{47}Sc and ^{48}Sc impurities produced will be severely problematic with their longer half-lives. Though decent cross sections exist for both the ^{43}Ca(p, n)^{43}Sc and ^{46}Ca(p, n)^{46}Sc reactions, neither ^{43}Sc or ^{46}Sc was detected in the irradiated sample; this is most likely due to the low natural abundances of ^{43}Ca (0.135 %) and ^{46}Ca (0.004 %) and the effect of their respective half-lives (^{43}Ca, short-lived, decays significantly prior to counting; ^{46}Ca, long-lived, limited activity build-up in short irradiation.)

Table 4.1.1. Scandium isotopes produced from a 127.8 mg $CaCO_3$ target with their half-lives, utilized gamma energies, and produced activities at the end of bombardment

Isotope	$t_{1/2}$ (h)	Gamma(keV)	Intensity (%)	Activity at EOB (μCi)
^{43}Sc	3.90	373	23	0.0
^{44}Sc	3.93	1157	100	3899.3
^{44m}Sc	58.61	271	87	11.7
^{46}Sc	2011.44	889	100	0.0
^{47}Sc	80.38	159	68	9.3
^{48}Sc	43.70	1038	98	8.5

The production rate observed experimentally was compared to the theoretical production rate calculated using data from the TENDL-2014 database (Table 4.1.2). The production rates for the produced isotopes varied. Though a high production rate was noted for ^{44}Sc, only a small fraction of the theoretical rate was produced. Even with this result, the desired high ratio of ^{44}Sc : ^{44m}Sc was achieved during this irradiation. Using this production rate, clinical quantities of ^{44}Sc could quickly be produced at a small, medical cyclotron.

Table 4.1.2. Comparison of theoretical and experimental production rates for the $^{nat}CaCO_3$ target irradiated at MURR

Isotope	Production Rate ($\mu Ci \cdot \mu Ah^{-1} \cdot g^{-1}$)		Percentage of Theoretical Produced
	Theoretical	Experimental	
^{43}Sc	1010.40	0.00	0.00
^{44}Sc	39015.81	3051.10	7.82
^{44m}Sc	4.17	9.15	219.60
^{46}Sc	0.00	0.00	0.00
^{47}Sc	6.11	7.28	119.05
^{48}Sc	2.09	6.65	317.86

4.1.2.2 Target Dissolution and Ca/Sc Separation

Initial studies utilized 30% H_2O_2 with gentle heating for the dissolution of calcium carbonate; this method proved to be problematic as the dissolution of the sample was incomplete. During irradiation, the normally white colored $CaCO_3$ would slightly discolor and become grey in certain areas; this portion of the sample had greater difficulty dissolving, which was most likely due to radiolysis of the sample. The dissolution media was then switched to 3 M HCl based on a published method[92]; this method fully dissolved the sample quickly without the need of heating. Additionally, this solution could be directly loaded on a column to isolate the scandium from the calcium target.

The column uses a small amount of DGA resin (N,N,N',N'-tetra-n-octyldigylcolamide), which is an extractive chromatography resin that is selective for highly charged cationic species; this allows the separation of Sc^{3+} from Ca^{2+}. Initial studies utilized a column bed volume of approximately 0.5 mL; the scandium readily loaded on the column but was unable to be eluted from the column. The affinity even in the elution mobile phase (0.1 M HCl) was too strong. A significantly smaller column, using only 53.8 mg of resin was

utilized to enable the elution of the scandium. Using this column, approximately 27% of the scandium was eluted from the column with no detectable calcium. The majority of the scandium remained trapped on the column.

4.1.3 Conclusions

Scandium-44 shows great promise as a metallic, positron emitter for radiolabeling peptides and other slower localizing targeting vectors. Small, medical cyclotrons, such as the PETtrace at MURR, can easily produce millicurie quantities of ^{44}Sc using natural abundance calcium; this would be greatly increased using enriched ^{44}Ca. The calcium carbonate targets were easy to produce and irradiate. An extractive chromatography method can quickly provide high purity ^{44}Sc with no detectable calcium. With an optimized separation method, ^{44}Sc could easily be routinely produced at MURR.

4.1.4 Future Studies

The primary issue with the method is the low recovery of the scandium from the column. Studies need to be performed to optimize the elution profile for the scandium while maintaining a good separation from calcium. Once the recovery of scandium has been optimized, samples of the scandium product need to be analyzed by ICP-AES or a calcium tracer introduced into the sample prior to separation to more clearly quantify the presence of calcium. Once testing has been optimized with natural abundance target, the target needs to be switched to enriched $^{44}CaCO_3$ for actual production runs.

4.2 Production of ^{99m}Tc via Proton and Deuteron Bombardment of MoS_2

Diagnostic imaging accounts for about 90% of the nuclear medicine procedures performed with the rest being used for therapeutic applications. Of these diagnostic procedures, approximately 80% of them use a single isotope, ^{99m}Tc[96]. Currently, ^{99m}Tc is available from ^{99}Mo generators which are produced by loading the molybdenum as molybdate (MoO_4^{2-}) onto an alumina column and eluting pertechnetate (TcO_4^-) in saline[39]. At the moment, the United States receives its entire supply of ^{99}Mo from the Chalk River Facility in Canada; this facility is expected to cease operation at the end of 2016 and close in 2018 leaving a huge demand for ^{99m}Tc[97]. Many different setups are being examined to meet the demand for ^{99m}Tc and one option being considered is production in accelerators[96,98–100]. In this research, molybdenum disulfide was evaluated as a novel, easy to use and recovery target form for the direct production of ^{99m}Tc and production of ^{99}Mo as a generator source using a small, medical cyclotron.

4.2.1 Methods and Materials

All reagents were purchased from Fisher Scientific (Pittsburgh, PA). Molybdenum disulfide (99 %) was purchased from Alfa Aesar (Ward Hill, MA). Poly prep columns (0.8 cm ID; 10 mL reservoir) were purchased from Bio-Rad (Hercules, CA). 20 mL HDPE or glass scintillation vials with polyethylene caps (referred to as poly collection vials) were purchased from Fisher Scientific. 1 mL HDPE counting vials (referred to as poly counting vials) were prepared on-site at MURR using HDPE "Finathene 5203" beads from Fina Chemicals (Brussels, Belgium). Aluminum metal backings and thick beam degrader were prepared on-site to designed specifications using 6061 grade

aluminum purchased from McMaster-Carr (Elmhurst, IL). Commercial food-grade aluminum foil was purchased from a local market. Araldite 2011 epoxy adhesive was purchased from Freeman Supply (Avon, Ohio). All reagents and materials were used as received without any further purification. All water used was purified on-site (deionized water fed into a Millipore system to > 18 MΩ·cm).

4.2.1.1 Instrumentation

All irradiations were performed at MURR using a GE PETtrace 800 cyclotron with dual particle capabilities with energies up to 16.5 MeV for protons and 8.5 MeV for deuterons and with currents up to 80 microamps. Throughout these experiments, the beam was collimated to a 10 mm diameter aperture.

Radiochemical assays for ^{99}Mo and ^{94,95,95m,96,99m}Tc were performed by γ-ray spectrometry using a Canberra Model GC2018S HPGe detector system (60.5 mm diameter, 30.5 mm length) at a sample distance of 5 mm from the window. The detector has a FWHM at 1.33 MeV of 1.8 keV. Spectral analyses were performed with Canberra Model 9600 multichannel analyzer. All samples were counted for at least 600 seconds and decay corrected to the time correlating to either the end of contact time for the batch studies or the first column wash for the column studies. The detector dead time was kept to less than 10% for all samples.

4.2.1.2 Target Preparation and Irradiation

SRIM-2008 software[56] was used to calculate theoretical proton and deuteron stopping power for the MoS_2 targets to determine the projectile entry energy and exit energy within each target (Appendix A.2.8 and A.2.9). A proton energy range of 12 – 16 MeV

was chosen for the direct production of ^{99m}Tc via the ^{100}Mo(p, 2n) reaction to minimize the production of $^{96g+m}$Tc as an unwanted impurity. For the deuteron induced reaction, the full energy range of the cyclotron at MURR (0 – 8.5 MeV) will be used to maximize the production of ^{99}Mo via the ^{98}Mo(d, p) reaction. The targets were prepared to the necessary thickness to achieve this energy deposition.

Molybdenum disulfide was dried overnight in an oven heated to 100° C to evaporate any moisture within the material and then transferred to a desiccator (placed under vacuum) to cool prior to pressing. A mass of either approximately 100 or 300 mg of MoS_2 was weighed directly into an aluminum backing. A 13 mm anvil was placed on top of the molybdenum disulfide and given a gentle press by hand to pack the powder then this assembly was placed inside a 25 mm die. A specially-machined, stainless steel ring was used to hold the target in place in the center of the die. The 25 mm plunger was placed on top of the assembly and the whole die was transferred to a hydraulic press. The material was pressed three times at incrementally increased pressure up to a final pressure of 13.8 MPa to ensure a smooth, evenly-distributed pellet. After pressing, the target was sealed in the backing using 16 μm thick aluminum foil, which was epoxied over the face of the target. The epoxy was allowed to cure for a minimum of 15 hours per the manufacturer's specifications. The molybdenum disulfide targets were irradiated at MURR with either 16 MeV protons or 8.5 MeV deuterons without the use of a degrader. All targets were irradiated for a total of 10 μAh. High vacuum was used on the target face while the back side of the target was water cooled to dissipate heat from the proton beam.

4.2.1.3 MoS_2 Target Dissolution and Activation Product Analysis

Several organic and aqueous solvent systems (30% H_2O_2, 12% NaOCl, 6 M HNO_3, acetone, hexane, and ethanol were tested, both at room temperature and with gentle heating (50° C), to dissolve MoS_2. Approximately 100 mg of MoS_2 was combined with 10 mL of each solution. The solutions were observed for any initial reactions and then allowed to continue overnight. The following day, the solutions were gently heated to catalyze any possible reactions. After this initial study, 30% H_2O_2 was further tested alongside acidified H_2O_2, and basified H_2O_2. For each adjusted solution, 1 mL of either 1 M KOH or HNO_3 was combined with 9 mL of 30% H_2O_2. Approximately 100 mg of MoS_2 was combined with 10 mL of each solution and gentle heating was used to catalyze these reactions, which were self-sustaining once the reaction started. To quantify any residual precipitate after the reaction completed, the samples were centrifuged to isolate the precipitate, the solution was decanted, and the vial dried overnight in a vacuum oven. The mass of precipitate was quantified the next day once the vials had cooled. For both the proton and deuteron irradiated target, sample aliquots of MoS_2 were analyzed by gamma spectroscopy using an HPGe detector to quantify and qualify activation products.

4.2.2 Results and Discussion

4.2.2.1 Target Preparation and Irradiation

Molybdenum disulfide forms smooth, firmly-packed pellets at 13.8 MPa of pressure (Figure 4.2.1). To minimize the loss of MoS_2 and WS_2 during target production, it was decided to directly press the material into the aluminum backings. Increased material loss was noted while pressing in a pellet die and then transferring to the aluminum

backing. Additionally, it was necessary for the pellet to snuggly fit inside of the aluminum backing or it could lead to complications during irradiation (Appendix B).

Figure 4.2.1. Thick MoS_2 pellet pressed using the pellet die

Thin, $^{nat}MoS_2$ targets were irradiated with either 16 MeV protons or 8.5 MeV deuterons for a total of 10 µAh and analyzed for activation products. After irradiation, each sample was mechanically disassembled and transferred to a glass collection vial. The samples were then counted as a point source on an HPGe to qualify and quantify the isotope present. The identified activation products for the proton irradiation and the deuteron irradiation are listed in Tables 4.2.1 and 4.2.3, respectively.

Table 4.2.1. Activities of identified technetium isotopes at the end of bombardment, 102.3 mg $^{nat}MoS_2$ target, 16 MeV protons, 10 µAh

Isotope	$t_{1/2}$	Gamma Energy (Intensity)	Activity at EOB
^{99m}Tc	6.0067 h	140.5 (89%)	1059.3 µCi
^{96}Tc	4.3 d	849 (98%), 812.7 (82%)	391.4 µCi
^{95}Tc	20.0 h	766 (93.8%)	1485.4 µCi
^{95m}Tc	61 d	204 (63.2%)	11.2 µCi
^{94}Tc	4.88 h	703 (99.6%)	1572.9 µCi

The production rate observed experimentally was compared to the theoretical production rate calculated using data from the TENDL-2014 database (Table 4.2.2). For all of the produced isotopes, the production rates are biased slightly high. The systematic bias of this result suggests the beam current could have been higher on the target than expected.

In this irradiation, a suitable production rate for the direct production of ^{99m}Tc was observed. Additionally, the significant production rates for ^{94,95m,96}Tc demonstrated the necessity of an enriched ^{100}Mo target.

Table 4.2.2. Comparison of theoretical and experimental production rates for the $^{nat}MoS_2$ target irradiated at MURR

Isotope	Production Rate ($\mu Ci \cdot \mu Ah^{-1} \cdot g^{-1}$)		Percentage of Theoretical Produced
	Theoretical	Experimental	
^{99m}Tc	1261.84	1572.9	124.65
^{96}Tc	1137.65	1485.4	130.57
^{95}Tc	6.73	11.2	166.38
^{95m}Tc	236.32	391.4	165.62
^{94}Tc	6052.70	1059.3	17.50

The purpose of the proton irradiation was to demonstrate the direct production of ^{99m}Tc via the ^{100}Mo(p, 2n)^{99m}Tc reaction using a small, medical cyclotron. As illustrated in Table 4.2.1, several isotopes of technetium were produced using a natural abundance target. Molybdenum has seven naturally occurring isotopes that all have a significant abundance (9.25 – 24.13%). In an actual production scenario, an enriched $^{100}MoS_2$ would be used to increase the production yield of ^{99m}Tc and decrease the production of the other technetium isotopes. Molybdenum-100 is only 9.63% abundant, thus an enriched target could provide 10-fold the ^{99m}Tc over a natural abundance target. An enriched target with similar dimensions to the one used in this irradiation could yield 1.06 mCi/μAh of ^{99m}Tc.

Table 4.2.3. Activities of identified molybdenum and technetium isotopes at the end of bombardment, 284.5 mg $^{nat}MoS_2$ target, 8.5 MeV deuterons, 10 μAh

Isotope	$t_{1/2}$	Gamma Energy (Intensity)	Activity at EOB
^{99}Mo	65.976 h	181 (6.14%), 778 (4.30%)	1.97 nCi
^{99m}Tc	6.0067 h	140.5 (89%)	17.8 μCi
^{96}Tc	4.3 d	778 (99.76%), 849 (98%)	0.20 nCi

The purpose of the deuteron irradiation was to demonstrate the production of ^{99}Mo via the ^{98}Mo(d, p)^{99}Mo reaction to make a ^{99}Mo/^{99m}Tc generator. Counting the sample was delayed by several days; several shorter-lived isotopes may have decayed prior to counting this sample. Additionally, a long count time (12 hours) was necessary to qualify and quantify the activation products. There was some loss of precision with such low count rates over a long period of time. An additional longer irradiation may be needed for verification, but there were no other radio-molybdenum isotopes produced; if this holds true, enriched materials may not be necessary. Since natural abundance molybdenum is only 24.13% ^{98}Mo, an enriched $^{98}MoS_2$ target would increase the production of ^{99}Mo 4-fold but a long irradiation would still be necessary to produce adequate quantities for a production generator.

4.2.2.2 MoS_2 Dissolution

The dissolution of molybdenum disulfide was tested in several different organic and aqueous media. No reaction was noted with acetone, ethanol, hexane, or 6 M HNO_3. Only the strong oxidizing agent, 30% H_2O_2 showed signs of reacting; bubbles began to slowly form at the MoS_2-H_2O_2 interface. Molybdenum disulfide is hydrophobic and stayed suspended on top of the aqueous solutions until enough energy was added to the system to begin oxidizing the contacted surface. Due to the slow progression of the reaction, the sample was gently heated (50° C) to catalyze the reaction. Once a steady reaction rate began, the reaction was fairly self-sustaining (exothermic) by the following reaction[101]:

$$2\,MoS_2 + 7\,O_2 \rightarrow 2\,MoO_3 + 4\,SO_3$$

$$MoO_3 + H_2O_2 \rightarrow {MoO_4}^{2-} + H_2O$$

A small quantity of a dark colored precipitate was observed at the bottom of the vial after the reaction had ceased; a competing reaction occurred alongside the desired reaction, creating the more inert molybdenum species, molybdenum dioxide, by the following reaction[101]:

$$2\,MoS_2 + 7\,O_2 \rightarrow 2\,MoO_3 + 4\,SO_3$$

$$MoS_2 + 6\,MoO_3 \rightarrow 7\,MoO_2 + 2\,SO_2$$

Molybdenum dioxide is a violet color which is perceived as black in solution. Molybdenum dioxide is insoluble in most media requiring hot sulfuric acid to be dissolved.

Further evaluation of the hydrogen peroxide dissolution method was performed. Molybdenum disulfide was reacted with either unaltered 30% H_2O_2, acidified H_2O_2, or basified H_2O_2 with gentle heating to catalyze the reaction. The basified peroxide solution was observed to react more vigorously, bubbling significantly more than the other solutions. The production of MoO_2 was observed in each sample. The mass of MoO_2 and the percentage of molybdenum not dissolved was determined for each glass collection vial. The unaltered 30%H_2O_2 demonstrated the best overall dissolution of MoS_2 with ~92.4% recovered, while both the acidified and basified peroxides only recovered 81.6% and 80.2%, respectively.

4.2.3 Conclusions

Technetium-99m is currently the workhorse radionuclide for nuclear medicine. With the imminent closure of one of the world's major producers, alternative production methods are being analyzed to produce ^{99m}Tc. In this research, molybdenum disulfide was evaluated as a new target form for the production of ^{99m}Tc at small, medical cyclotrons. These initial studies indicate MoS_2 could be used to directly produce ^{99m}Tc, but the deuteron energy capability of most medical cyclotrons is too low to produce viable amounts of ^{99}Mo to prepare a Mo/Tc generator. For processing the sample, it was found that MoS_2 dissolves in 30% H_2O_2 with gentle heating to catalyze the reaction.

4.2.4 Future Studies

The dissolution method needs to be further optimized to fully recover the molybdenum and technetium products. 30% H_2O_2 can be utilized to recover the majority of the molybdenum but nitric acid may be necessary to recover the residual molybdenum. Once the methods have been optimized, studies can be performed with enriched target materials to better analyze production yields and examine the commercial viability of this production pathway. Finally, the target recovery and reuse method needs to be evaluated (the method will be similar to the method evaluated for WS_2 in Section 2.2.1.5)

REFERENCES

1. Stoecklin, G., Qaim, S. M. & Roesch, F. The Impact of Radioactivity on Medicine. *Radiochim. Acta* **70,** 249–272 (1995).

2. Radioisotopes In Medicine. at <http://www.world-nuclear.org/info/Non-Power-Nuclear-Applications/Radioisotopes/Radioisotopes-in-Medicine/>

3. Saha, G. B. in *Fundamentals of Nuclear Pharmacy* 83–113 (Springer New York, 2010).

4. Pagé, M. *Tumor Targeting in Cancer Therapy*. (Springer Science & Business Media, 2002).

5. Khalil, M. M. in *Basic Sciences of Nuclear Medicine* (ed. Khalil, M. M.) 155–178 (Springer Berlin Heidelberg, 2010).

6. Hall, E. J. & Giaccia, A. J. in *Radiobiology for the Radiologist* 3–11 (Lippincott Williams & Wilkins, 2012).

7. Hall, E. J. & Giaccia, A. J. in *Radiobiology for the Radiologist* 303–326 (Lippincott Williams & Wilkins, 2012).

8. Loveland, W. D., Morrissey, D. J. & Seaborg, G. T. in *Modern Nuclear Chemistry* 1–28 (John Wiley & Sons, Inc., 2005).

9. Hall, E. J. & Giaccia, A. J. in *Radiobiology for the Radiologist* 104–113 (Lippincott Williams & Wilkins, 2012).

10. Elgqvist, J., Frost, S., Pouget, J.-P. & Albertsson, P. The potential and hurdles of targeted alpha therapy - clinical trials and beyond. *Front. Oncol.* **3,** 324 (2014).

11. Loveland, W. D., Morrissey, D. J. & Seaborg, G. T. in *Modern Nuclear Chemistry* 177–198 (John Wiley & Sons, Inc., 2005).

12. Cutler, C. S., Hennkens, H. M., Sisay, N., Huclier-Markai, S. & Jurisson, S. S. Radiometals for Combined Imaging and Therapy. *Chem. Rev.* **113,** 858–883 (2013).

13. Xofigo Fact Sheet. *Xofigo Fact Sheet* at <http://www.xofigo-us.com/downloads/PP-600-US-0486-Xofigo-Fact-Sheet.pdf>

14. Cotton, F. A. in *Advanced Inorganic Chemistry* 111–130 (Wiley, 1999).

15. Loveland, W. D., Morrissey, D. J. & Seaborg, G. T. in *Modern Nuclear Chemistry* 199–220 (John Wiley & Sons, Inc., 2005).

16. Knoll, G. F. in *Radiation Detection and Measurement* 415–466 (Wiley, 2010).

17. Hicon (Sodium Iodide I 131) Drug Information: Description, User Reviews, Drug Side Effects, Interactions - Prescribing Information at. *RxList* at <http://www.rxlist.com/hicon-drug.htm>

18. Zevalin (Ibritumomab Tiuxetan) Drug Information: Description, User Reviews, Drug Side Effects, Interactions - Prescribing Information at. *RxList* at <http://www.rxlist.com/zevalin-drug.htm>

19. Quadramet - FDA prescribing information, side effects and uses. at <http://www.drugs.com/pro/quadramet.html>

20. Hall, E. J. & Giaccia, A. J. in *Radiobiology for the Radiologist* 201–221 (Lippincott Williams & Wilkins, 2012).

21. Loveland, W. D., Morrissey, D. J. & Seaborg, G. T. in *Modern Nuclear Chemistry* 221–248 (John Wiley & Sons, Inc., 2005).

22. Kapucu, O. L. *et al.* EANM procedure guideline for brain perfusion SPECT using 99mTc-labelled radiopharmaceuticals, version 2. *Eur. J. Nucl. Med. Mol. Imaging* **36,** 2093–2102 (2009).

23. Baggish, A. L. & Boucher, C. A. Radiopharmaceutical agents for myocardial perfusion imaging. *Circulation* **118,** 1668–1674 (2008).

24. Taylor, A., Ziffer, J. A. & Eshima, D. Comparison of Tc-99m MAG3 and Tc-99m DTPA in renal transplant patients with impaired renal function. *Clin. Nucl. Med.* **15,** 371–378 (1990).

25. Lo, J.-M., Huang, W.-T., Kao, C.-H. & Yang, C.-S. Mechanism of 99mTc-d, l-HMPAO Retention in Brain Cells. *Ann Nucl Med Sci* **14,** 215–222 (2001).

26. FDA-approved Radiopharmaceuticals - Triad Isotopes. at <http://www.triadisotopes.com/downloads/fda-approved.pdf>

27. Florio, T. & Schettini, G. [Somatostatin and its receptors. Role in the control of cell proliferation]. *Minerva Endocrinol.* **26,** 91–102 (2001).

28. Delbeke, D. & Segall, G. M. Status of and Trends in Nuclear Medicine in the United States. *J. Nucl. Med.* **52,** 24S–28S (2011).

29. Cockcroft. Artificial Production of Fast Protons. *Nature* **129,** 242 (1932).

30. Lawrence, E. O. & Livingston, M. S. The Production of High Speed Protons Without the Use of High Voltages. *Phys. Rev.* **38,** 834–834 (1931).

31. Mausner, L. F. & Mirzadeh, S. in *Handbook of Radiopharmaceuticals* (eds. Welch, M. J. & Redvanly, C. S.) 87–117 (John Wiley & Sons, Ltd, 2002).

32. Loveland, W. D., Morrissey, D. J. & Seaborg, G. T. in *Modern Nuclear Chemistry* 383–427 (John Wiley & Sons, Inc., 2005).

33. Tavernier, S. in *Experimental Techniques in Nuclear and Particle Physics* 55–104 (Springer Berlin Heidelberg, 2010).

34. Bonardi, M. L., Groppi, F., Manenti, S., Persico, E. & Gini, L. Production study of high specific activity NCA Re-186g by proton and deuteron cyclotron irradiation. *Appl. Radiat. Isot.* **68,** 1595–1601 (2010).

35. Szelecsényi, F. *et al.* Production possibility of 186Re via the 192Os(p,α3n)186Re nuclear reaction. *J. Radioanal. Nucl. Chem.* **282,** 261–263 (2009).

36. Cotton, S. in *Lanthanide and Actinide Chemistry* 23–33 (John Wiley & Sons, Ltd, 2006).

37. A. Mushtaq, S. M. Q. Production of 73Se via (p, 3n) and (d, 4n) reactions on arsenic. *Int. J. Rad. Appl. Instrum. [A]* **39,** 1085–1091 (1988).

38. Kassis, A. I. & Adelstein, S. J. in *Handbook of Radiopharmaceuticals* (eds. Welch, M. J. & Redvanly, C. S.) 767–793 (John Wiley & Sons, Ltd, 2002).

39. Annex, V. I. I. Production and Supply of Molybdenum-99. *Nucl. Technol. Rev.* 150 (2010).

40. Mirzadeh, S., Rice, D. E. & Knapp, F. F. J. Spontaneous Electrochemical Separation of carrier-free 64Cu and 67Cu from Zn targets. *Radiochim. Acta* **57,** 193–200 (1992).

41. Carroll, V., Demoin, D. W., Hoffman, T. J. & Jurisson, S. S. Inorganic chemistry in nuclear imaging and radiotherapy: current and future directions. *Radiochim. Acta* **100,** 653–667 (2012).

42. Qaim, S. M. The present and future of medical radionuclide production. *Radiochim. Acta* **100,** 635–651 (2012).

43. Ehrhardt, G. J., Blumer, M. E., Su, F. M., Vanderheyden, J. L. & Fritzberg, A. R. Experience with aluminum perrhenate targets for reactor production of high specific activity Re-186. *Appl. Radiat. Isot.* **48,** 1–4 (1997).

44. Moustapha, M. E. *et al.* Preparation of cyclotron-produced 186Re and comparison with reactor-produced 186Re and generator-produced 188Re for the labeling of bombesin. *Nucl. Med. Biol.* **33,** 81–89 (2006).

45. Lapi, S. *et al.* Production cross-sections of 181-186Re isotopes from proton bombardment of natural tungsten. *Appl. Radiat. Isot. Data Instrum. Methods Use Agric. Ind. Med.* **65,** 345–349 (2007).

46. M. E. Fassbender, B. B. Proton irradiation parameters and chemical separation procedure for the bulk production of high-specific-activity 186gRe using WO3 targets. *Radiochim. Acta* **101,** 339 (2013).

47. Tárkányi, F. *et al.* New measurement and evaluation of the excitation function of the 186W(p,n) nuclear reaction for production of the therapeutic radioisotope 186Re. *Nucl. Instrum. Methods Phys. Res. Sect. B Beam Interact. Mater. At.* **264,** 389–394 (2007).

48. Shigeta, N. *et al.* Production method of no-carrier-added186Re. *J. Radioanal. Nucl. Chem.* **205,** 85–92 (1996).

49. Tárkányi, F. *et al.* Excitation functions of deuteron induced nuclear reactions on natural tungsten up to 50 MeV. *Nucl. Instrum. Methods Phys. Res. Sect. B Beam Interact. Mater. At.* **211,** 319–330 (2003).

50. Hilgers, K., Sudár, S. & Qaim, S. M. Experimental study and nuclear model calculations on the 192Os(p,n)192Ir reaction: Comparison of reactor and cyclotron production of the therapeutic radionuclide 192Ir. *Appl. Radiat. Isot. Data Instrum. Methods Use Agric. Ind. Med.* **63,** 93–98 (2005).

51. K Hilgers, H. H. C. Production of the therapeutic radionuclides Pt-193m and Pt-195m with high specific activity via alpha-particle-induced reactions on Os-192. *Appl. Radiat. Isot. Data Instrum. Methods Use Agric. Ind. Med.* **66,** 545–51 (2008).

52. A. Hermanne, R. A. R. Excitation functions of proton induced reactions on natOs up to 65 MeV: Experiments and comparison with results from theoretical codes. *Nucl. Instrum. Methods Phys. Res. Sect. B Beam Interact. Mater. At.* **345,** (2015).

53. F. Szelecsényi, C. V. Excitation functions of 186,187,188,189,190,192Ir formed in proton-induced reactions on highly enriched 192Os up to 66MeV. *Nucl. Instrum. Methods Phys. Res. Sect. B Beam Interact. Mater. At.* **268,** 3306–3314 (2010).

54. L. A. Woodward, H. L. R. The Raman and infra-red absorption spectra of osmium tetroxide. Relation to the structure of the perrhenate and tungstate ions in aqueous solution. *Trans. Faraday Soc.* **52,** (1956).

55. Stingl, T., Müller, B. & Lutz, H. D. Crystal structure refinement of osmium(II) disulfide, OsS2. *Zeitschrift für Kristallographie* **202,** 161–162 (1992).

56. Ziegler, J. SRIM & TRIM. at <http://www.srim.org/>

57. Koning, A. J. *et al.* TENDL-2014: TALYS-based evaluated nuclear data library. at <www.talys.eu/tendl-2014.html>

58. Koning, A. J. & Rochman, D. Modern Nuclear Data Evaluation with the TALYS Code System. *Nucl. Data Sheets* **113,** 2841–2934 (2012).

59. Ramakrishna Matte, H. S. S. *et al.* MoS2 and WS2 Analogues of Graphene. *Angew. Chem. Int. Ed.* **49,** 4059–4062 (2010).

60. Gott, M. D. *et al.* Radiochemical Study of Re/W Adsorption Behavior on a Strongly Basic Anion Exchange Resin. *Radiochim. Acta* **102,** 325–332 (2014).

61. Atkins, P. W., Walters, V. & Paula, J. D. in *Physical Chemistry* 796, 807 (Macmillan Higher Education, 2006).

62. Qiu, T., Zeng, Y., Ye, C. & Tian, H. Adsorption Thermodynamics and Kinetics of p-Xylene on Activated Carbon. *J. Chem. Eng. Data* **57,** 1551–1556 (2012).

63. Abramov, A. A., Dzhigirkhanov, M. S.-A., Iofa, B. Z. & Volkova, S. V. Hydration and Extraction of Oxyanions. *Radiochemistry* **44,** 270–273 (2002).

64. Skoog, D. A., Holler, F. J. & Crouch, S. R. in *Instrumental analysis.* (Cengage Learning, 2007).

65. I E Burgeson, D. L. B. Small Column Testing of SuperLig ® 639 for Removing 99 Tc from Hanford Tank Waste Envelope B (Tank 241-AZ-101).

66. Le Loirec, C. & Champion, C. Track structure simulation for positron emitters of physical interest. Part III: The case of the non-standard radionuclides. *Nucl. Instrum. Methods Phys. Res. Sect. Accel. Spectrometers Detect. Assoc. Equip.* **582,** 665–672 (2007).

67. Jennewein, M., Hermanne, A., Mason, R. P., Thorpe, P. E. & Rösch, F. A new method for the labelling of proteins with radioactive arsenic isotopes. *Nucl. Instrum. Methods Phys. Res. Sect. Accel. Spectrometers Detect. Assoc. Equip.* **569,** 512–517 (2006).

68. Jahn, M. *et al.* Separation and purification of no-carrier-added arsenic from bulk amounts of germanium for use in radiopharmaceutical labelling. *Radiochim. Acta Int. J. Chem. Asp. Nucl. Sci. Technol.* **98,** 807–812 (2010).

69. Nayak, T. K. & Brechbiel, M. W. Radioimmunoimaging with Longer-Lived Positron-Emitting Radionuclides: Potentials and Challenges. *Bioconjug. Chem.* **20,** 825–841 (2009).

70. Palmer, R. B. & Born, J. L. United States Patent: 6106804 - Arsenic-72 labeled compounds for tissue specific medical imaging. (2000).

71. Emran, A. M. & Phillips, D. R. in *New Trends in Radiopharmaceutical Synthesis, Quality Assurance, and Regulatory Control* (ed. Emran, A. M.) 153–168 (Springer US, 1991).

72. Ballard, B. *et al.* Radioarsenic from a portable (72)Se/(72)As generator: a current perspective. *Curr. Radiopharm.* **5,** 264–270 (2012).

73. Al-Kouraishi, S. H. & Boswell, G. G. J. An isotope generator for 72As. *Int. J. Appl. Radiat. Isot.* **29,** 607–609 (1978).

74. Jennewein, M., Schmidt, A., Novgorodov, A. F., Qaim, S. M. & Rösch, F. A no-carrier-added 72Se/72As radionuclide generator based on distillation. *Radiochim. ActaInternational J. Chem. Asp. Nucl. Sci. Technol.* **92,** 245–249 (2004).

75. Jennewein, M. *et al.* A no-carrier-added 72Se/72As radionuclide generator based on solid phase extraction. *Radiochim. Acta* **93,** 579–583 (2005).

76. Mudrová, B., Kopecký, P. & Svoboda, K. The separation of carrier-free 72Se from a germanium oxide target. *Int. J. Appl. Radiat. Isot.* **24,** 610–612 (1973).

77. Phillips, D. R. United States Patent: 5405589 - Production of selenium-72 and arsenic-72. (1995).

78. Phillips, D. R., Moody, D. C., Taylor, W. A., Segura, N. J. & Pate, B. D. Electrolytic separation of selenium isotopes from proton irradiated RbBr targets. *Int. J. Rad. Appl. Instrum. [A]* **38,** 521–525 (1987).

79. Ballard, B. *et al.* Selenium-72 formation via nat Br(p,x) induced by 100 MeV protons: steps towards a novel 72Se/72As generator system. *Appl. Radiat. Isot. Data Instrum. Methods Use Agric. Ind. Med.* **70,** 595–601 (2012).

80. Chajduk, E., Doner, K., Polkowska-Motrenko, H. & Bilewicz, A. Novel radiochemical separation of arsenic from selenium for 72Se/72As generator. *Appl. Radiat. Isot.* **70,** 819–822 (2012).

81. Wycoff, D. E. *et al.* Chromatographic separation of selenium and arsenic: A potential 72Se/72As generator. *J. Chromatogr. A* **1340,** 109–114 (2014).

82. Smith, S. V. Unpublished Work.

83. Wycoff, D. E. Unpublished Work.

84. Chattopadhyay, S., Pal, S., Vimalnath, K. V. & Das, M. K. A versatile technique for radiochemical separation of medically useful no-carrier-added (nca) radioarsenic from irradiated germanium oxide targets. *Appl. Radiat. Isot. Data Instrum. Methods Use Agric. Ind. Med.* **65,** 1202–1207 (2007).

85. Shehata, M. M., Scholten, B., Spahn, I., Coenen, H. H. & Qaim, S. M. Separation of radioarsenic from irradiated germanium oxide targets for the production of 71As and 72As. *J. Radioanal. Nucl. Chem.* **287,** 435–442 (2010).

86. Tolmachev, V. & Lundqvist, H. Separation of arsenic from germanium oxide targets by dry distillation. *J. Radioanal. Nucl. Chem.* **247,** 61–66 (2014).

87. Guin, R., Das, S. K. & Saha, S. K. Separation of carrier-free arsenic from germanium. *J. Radioanal. Nucl. Chem.* **227,** 181–183 (1998).

88. Tanveer Hussain Bokhari, A. M. Separation of no-carrier-added arsenic-77 from neutron irradiated germanium. *Radiochim. Acta* **97,** 503–506 (2009).

89. Jennewein, M. *et al.* A new method for radiochemical separation of arsenic from irradiated germanium oxide. *Appl. Radiat. Isot. Data Instrum. Methods Use Agric. Ind. Med.* **63,** 343–351 (2005).

90. Maki, Y. & Murakami, Y. The separation of arsenic-77 in a carrier-free state from the parent nuclide germanium-77 by a thin-layer chromatographic method. *J. Radioanal. Chem.* **22,** 5–12 (1974).

91. Pniok, M. *et al.* Thermodynamic and kinetic study of scandium(III) complexes of DTPA and DOTA: a step toward scandium radiopharmaceuticals. *Chem. Weinh. Bergstr. Ger.* **20,** 7944–7955 (2014).

92. Müller, C. *et al.* Promises of Cyclotron-Produced 44Sc as a Diagnostic Match for Trivalent β−-Emitters: In Vitro and In Vivo Study of a 44Sc-DOTA-Folate Conjugate. *J. Nucl. Med.* **54,** 2168–2174 (2013).

93. Severin, G. W., Engle, J. W., Valdovinos, H. F., Barnhart, T. E. & Nickles, R. J. Cyclotron Produced 44gSc from Natural Calcium. *Appl. Radiat. Isot.* **70,** 1526–1530 (2012).

94. Krajewski, S. *et al.* Cyclotron production of 44Sc for clinical application. *Radiochim. Acta Int. J. Chem. Asp. Nucl. Sci. Technol.* **101,** 333–338 (2013).

95. Dirks, C., Dirks, T. & Happel, S. On the separation of Sc, Zr and Ga. at <http://www.triskem-international.com/ru/iso_album/4_on_the_separation_of_sc,_zr_and_ga.pdf>

96. Khandaker, M. U., Uddin, M. S., Kim, K. S., Lee, Y. S. & Kim, G. N. Measurement of cross-sections for the (p, xn) reactions in natural molybdenum. *Nucl. Instrum. Methods Phys. Res. Sect. B Beam Interact. Mater. At.* **262,** 171–181 (2007).

97. Chalk River's NRU Reactor closing in 2018. *Pembroke Daily Observer* at <http://www.thedailyobserver.ca/2015/02/06/chalk-rivers-nru-reactor-closing-in-2018>

98. Qaim, S. M., Sudár, S., Scholten, B., Koning, A. J. & Coenen, H. H. Evaluation of excitation functions of 100Mo(p,d+pn)99Mo and 100Mo (p,2n)99mTc reactions: Estimation of long-lived Tc-impurity and its implication on the specific activity of cyclotron-produced 99mTc. *Appl. Radiat. Isot.* **85,** 101–113 (2014).

99. Tárkányi, F. *et al.* Investigation of activation cross-sections of deuteron induced nuclear reactions on natural Mo up to 50 MeV. *Nucl. Instrum. Methods Phys. Res. Sect. B Beam Interact. Mater. At.* **274,** 1–25 (2012).

100. Tárkányi, F., Ditrói, F., Hermanne, A., Takács, S. & Ignatyuk, A. V. Investigation of activation cross-sections of proton induced nuclear reactions on natMo up to 40 MeV: New data and evaluation. *Nucl. Instrum. Methods Phys. Res. Sect. B Beam Interact. Mater. At.* **280,** 45–73 (2012).

101. Shigegaki, Y., Basu, S. K., Wakihara, M. & Taniguchi, M. Thermal analysis and kinetics of oxidation of molybdenum sulfides. *J. Therm. Anal.* **34,** 1427–1440 (1988).

102. Burrage, J. W. *et al.* A simple method to measure proton beam energy in a standard medical cyclotron. *Australas. Phys. Eng. Sci. Med.* **32,** 92–97 (2009).

103. Nozaki, T., Itoh, Y. & Ogawa, K. Yield of 73Se for various reactions and its chemical processing. *Int. J. Appl. Radiat. Isot.* **30,** 595–599 (1979).

104. Bahrami, M. Forced Convection Heat Transfer. at <http://www.sfu.ca/~mbahrami/ENSC%20388/Notes/Forced%20Convection.pdf>

105. Schlyer, D. J. in *Handbook of Radiopharmaceuticals* (eds. Welch, M. J. & Redvanly, C. S.) 1–70 (John Wiley & Sons, Ltd, 2002).

Appendix A: Production Calculations

A.1 Discussion of Target Cross Sections

The reaction cross section of a nuclide is a statistical measure of the probability that a charged particle will interact with a target nucleus. The unit of cross section is typically given in barns, which is equivalent to an area of 10^{-24} cm^2 in SI units. Using the cross section (σ), it is possible to calculate the anticipated product activity (A) of a given nuclide bombarded by a charge particle beam given the following equation:

$$A = n * x * \sigma * I * \left(1 - e^{-\lambda * t_{irr}}\right) * \left(e^{-\lambda * t_{dec}}\right) \qquad \text{Equation A.1.1}$$

n is the number of nuclei in the target material in a given volume (nuclei * cm^{-3}). *x* is the target thickness (cm). *I* is the current of the charged particle beam (charged particle * sec^{-1}). λ is decay constant of the product nuclide (h^{-1}). t_{irr} and t_{dec} are the irradiation time and decay time (h), respectively.

The cross section of a given reaction can be determined experimentally, typically by the stacked foil method[102]. Thin foils of the target material are stacked between thin foils of a material with well characterized cross sections (monitoring foils). The stack of foils is bombarded with protons of a known energy and current. All the foils are analyzed by gamma spectroscopy to qualify and quantify the activation products. The monitoring foil reactions are used to determine the proton entry and exit energy into the target foils and to verify the proton beam current. The equation above can be rearranged and used to solve the cross section for the given target reaction.

Cross sections have been determined either experimentally or theoretically for charge particle bombardment of W[34,45,47–49], Os[35,50–52], Ge[103], As[37,103], Ca[92–94], and Mo[96,98]. In this appendix, a discussion of charged particle energy ranges to maximize the yield of the desired radionuclide while minimizing impurities presented using this known cross sectional data.

A.1.1 Proton Bombardment of Osmium via ^{nat}Os(p, x) reactions

Several reactions on natural abundance osmium produce ^{186}Re. The ^{192}Os(p, α3n)^{186}Re reaction has been previously reported[53]. An optimal proton energy of 24 MeV was noted with a radionuclidic purity twice as high as the ^{186}W(p, n)^{186}Re reaction once the shorter-lived ^{188}Re and ^{189}Re isotopes had decayed. Additionally, it was noted ^{189,190,192}Ir production could create a significant dose depending on the activation time. No cross section data is available from the National Nuclear Database at Brookhaven National Laboratory for the ^{189}Os(p, α)^{186}Re reaction. The TALYS-based evaluated nuclear data library (TENDL-2014) provides cross section calculations utilizing the TALYS nuclear model code system[57,58]. Theoretical cross sections from TENDL-2014 are illustrated in Figure A.1.1 for reactions on ^{189}Os. According to the data, the (p, 2n) and (p, 3n) reactions are significantly more likely to occur and overshadow the (p, α) reaction. Iridium can be separated from rhenium but the increased dose rate from its production could present a processing challenge. The theoretical calculations indicate the maximum cross section for this reaction was close to 24 MeV as well. For this reason, a proton energy range from 20-26 MeV was targeted for this research.

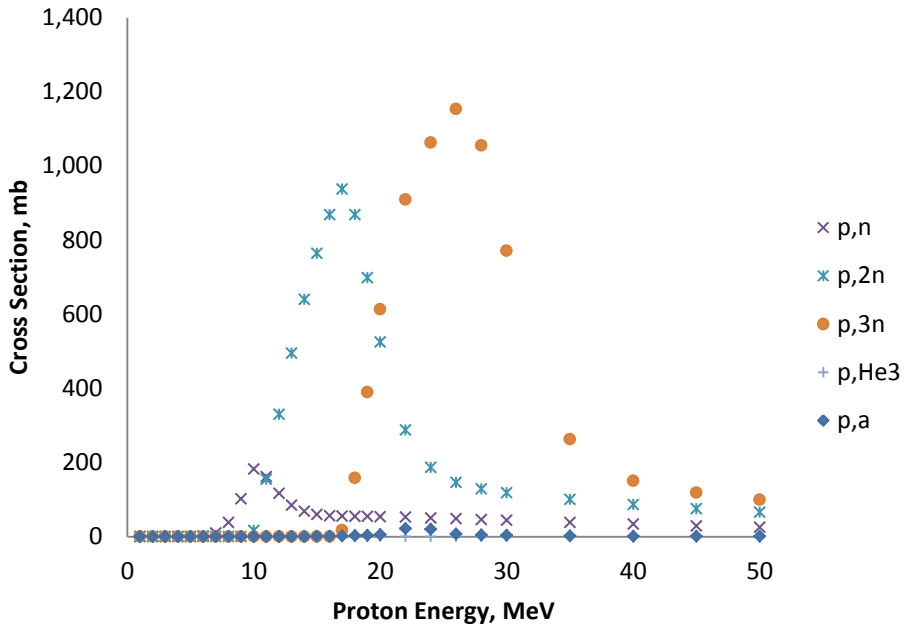

Figure A.1.1. TENDL-2014 theoretical cross sections for select reactions on ^{189}Os

A.1.2 Proton Bombardment of Tungsten via ^{nat}W(p, xn)Re reactions

The ^{186}W(p, n)^{186}Re reaction has been previously reported by several sources[34,45,47,48]. Due to variations in target geometry and calculation parameters, the absolute value for the cross section is inconsistent, but all reports agree the maximum cross section is approximately 10 MeV as illustrated by Figure A.1.2. The benefit of this reaction pathway is any medical cyclotron has the energy capabilities to produce ^{186}Re.

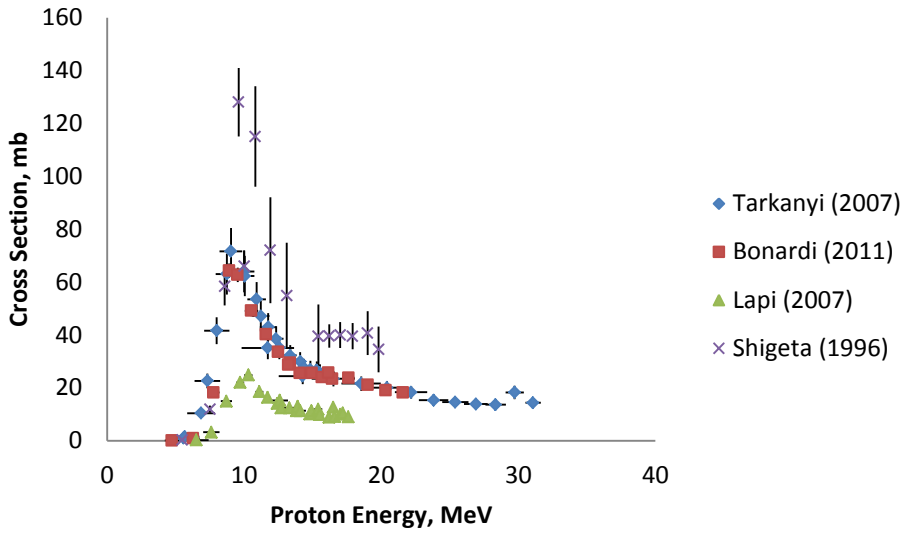

Figure A.1.2. Previously reported cross section data for the $^{186}W(p, n)^{186}Re$ reaction

Lapi *et. Al.*[45] reported the production cross sections for $^{181\text{-}186}Re$ for proton bombardment on natural tungsten foils (Figure A.1.3). Using natural tungsten foils, several isotopes of rhenium are produced alongside ^{186}Re. Using enriched materials, the radiorhenium impurity of greatest concern is ^{184}Re; this is due to the fact that ^{184}W will be the largest expected impurity in enriched ^{186}W. For this reason, a proton energy range from 7 – 16 MeV will be targeted for this research. Above 16 MeV, the cross section for ^{184}Re rapidly increases, while below 7 MeV, there is little return for the use of the expensive, enriched target material.

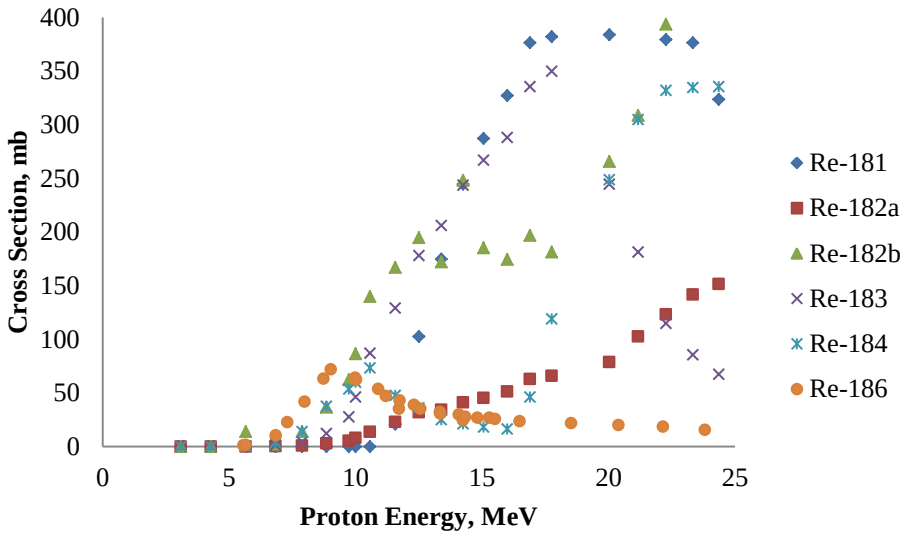

Figure A.1.3. Previously reported cross section data for $^{181\text{-}186}$Re production on a natural W target

A.1.3 Alpha Bombardment of Germanium via ^{nat}Ge(a, x) reactions

No cross section data is available from the National Nuclear Database at Brookhaven National Laboratory for the ^{70}Ge(α, 2n)^{72}Se reaction. Theoretical cross section data from the TENDL-2014 database[57] was used to determine the potential production products for alpha bombardment of germanium metal targets. Using natural abundance germanium, several radioisotopes of arsenic (^{71,72,73,74,76,77}As), gallium (^{72,73,75}Ga), germanium (^{68,69,71,77}Ge), selenium (^{72,73,75,79}Se), and zinc (^{65,69,71,72}Zn) are produced. The use of enriched ^{70}Ge would greatly reduce the radiocontaminants produced. Examining the theoretical cross section data for these reactions, an alpha energy of 28 MeV will be targeted for the initial production runs; this energy provides the highest cross section for the ^{70}Ge(α, 2n)^{72}Se reaction while reducing the production of many major radionuclidic impurities (Figure A.1.4).

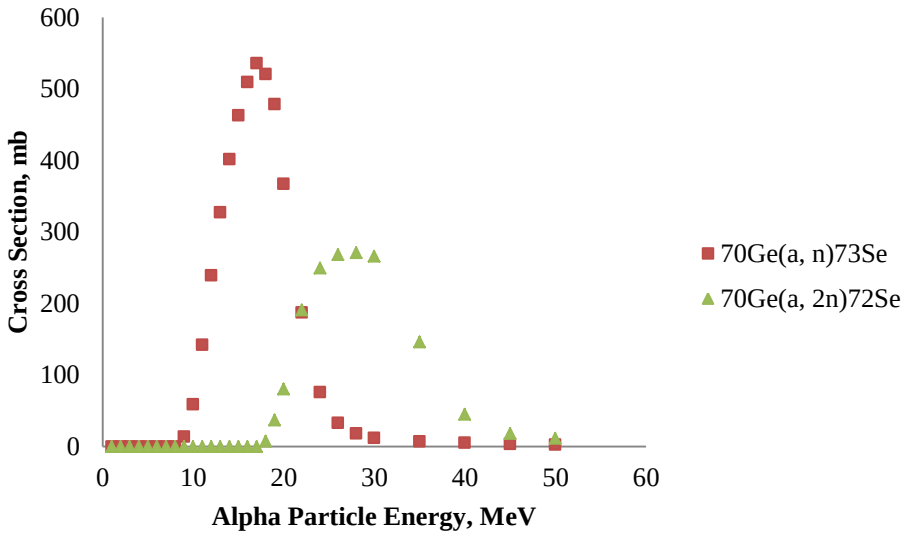

Figure A.1.4. Theoretical cross section for the production of ^{72,73}Se via alpha bombardment of enriched ^{70}Ge

A.1.4 Proton Bombardment of Arsenic via ^{75}As(p, 4n)^{72}Se reactions

Arsenic-75 has potential as a great target source for the production of ^{72}Se. Arsenic is monoisotopic and thus naturally 100% abundant, keeping the cost of the target material cheaper. Additionally, fewer competing reactions occur reducing the production of impurities. The major reactions are illustrated in Figure A.1.5. The maxima for the desired (p, 4n) reaction appears to peak around 50 MeV[37,103]. Additionally, the (p,4n) reaction appears to exceed the (p,3n) reaction at approximately 48 MeV. For this reason, a proton range of 48-50 MeV was targeted for this research.

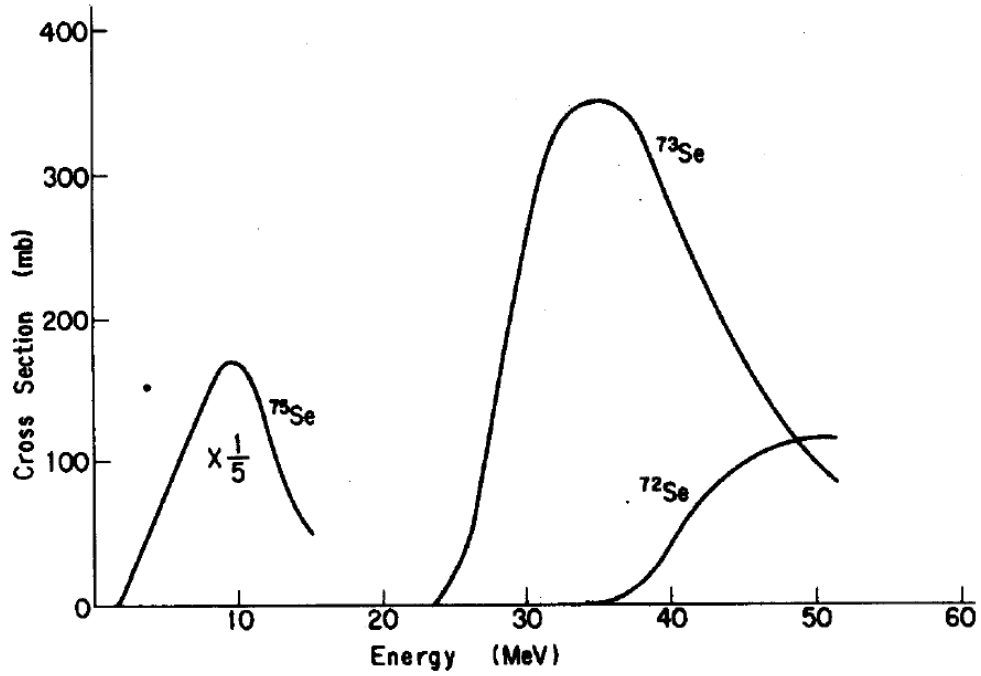

Figure A.1.5. Literature cross section data for select proton bombardment reactions on $^{75}As^{37}$

A.1.5 Proton Bombardment of Calcium via ^{nat}Ca(p, xn)Sc reactions

The cross section data available from the National Nuclear Database at Brookhaven National Laboratory for the ^{44}Ca(p, n)^{44}Sc reaction and the related reactions is limited; the scope of these reactions focus specifically on the production of ^{44}Sc and ^{44m}Sc with little data provided for ^{43,47,48}Sc which could be produced as radionuclidic impurities. The cross section data relevant to this work is illustrated in Figure A.1.6.

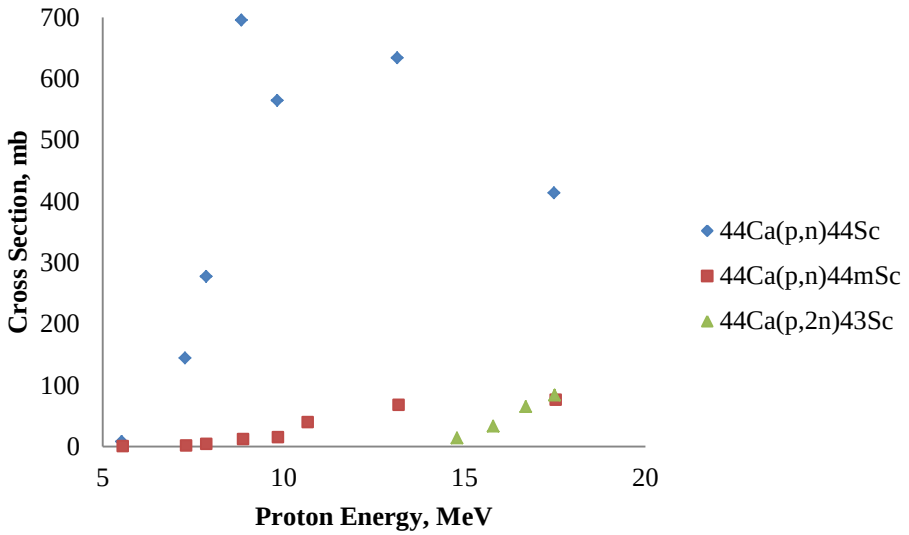

Figure A.1.6. Literature cross section data for proton bombardment of $^{44}CaCO_3$ targets

However, two recent publications[92,94] provide thick target yields for the production of ^{44}Sc by proton bombardment of enriched $^{44}CaCO_3$ targets. The findings of these studies agree well with one another; the production of ^{44}Sc is notably high above 10 MeV, while the in-growth of ^{44m}Sc as a radiocontaminant slowly increases as proton energy is increased. Additionally, ^{47}Sc and ^{48}Sc are noted as very trace contaminants occurring due to the presence of some ^{46}Ca and ^{48}Ca in the enriched ^{44}Ca target. In this study, a proton energy range of 12 – 16 MeV was targeted to maintain a high ratio of ^{44}Sc to ^{44m}Sc. As the production of ^{44}Sc drops at the lower energy, the relative production of ^{44m}Sc is increased.

A.1.6 Proton Bombardment of Molybdenum via $^{nat}Mo(p, xn)$ reactions

Cross sections for the proton bombardment of natural molybdenum targets have been reported[96,98]. Using natural abundance molybdenum, several technetium isotopes are produced as part of the proton and deuteron bombardment of ^{nat}Mo targets (Figure A.1.7).

The production of ^{99m}Tc is the predominant reaction with proton energies ranging from 12 – 21 MeV. For this reason, a proton range of 12 – 16 MeV was targeted for this reseach. The production of ^{99}Mo is possible using protons via the ^{100}Mo(p, pn)^{99}Mo reaction, but this reaction occurs more readily with proton energies above 22 MeV, which exceeds the capability of most medical cyclotrons (Figure A.1.8).

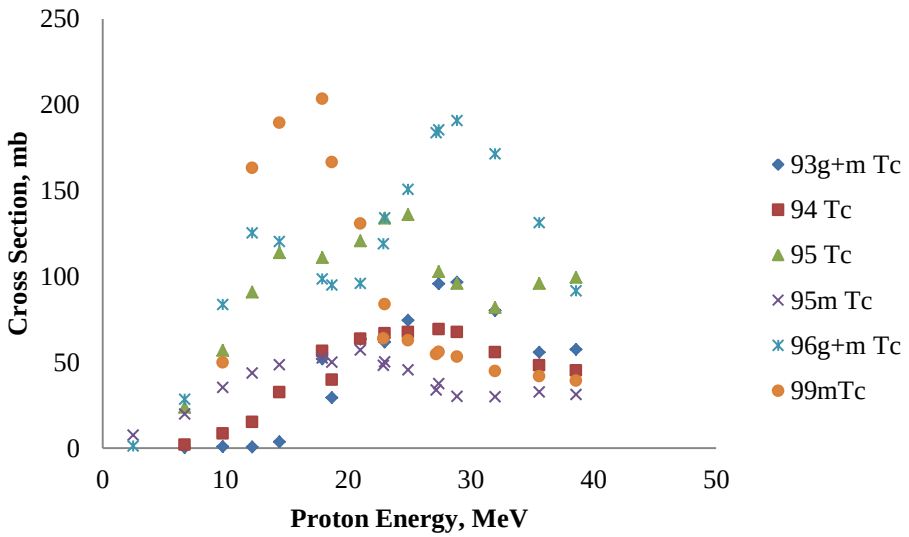

Figure A.1.7. Literature cross sections for technetium radioisotopes production via proton bombardment of natural molybdenum

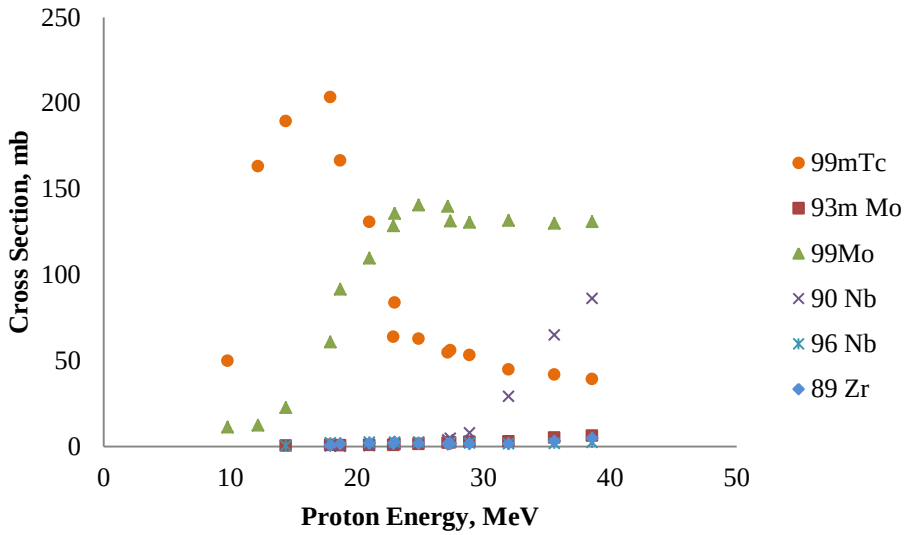

Figure A.1.8. Literature cross sections for other radioisotopes production via proton bombardment of natural molybdenum compared to ^{99m}Tc

A.1.7 Deuteron Bombardment of Molybdenum via ^{nat}Mo(d, xn) reactions

Cross sections for the deuteron bombardment of natural molybdenum targets have been reported[99]. The literature shows that the production of other radio-molybdenum isotopes is minimal for the evaluated deuteron range from 0-10 MeV, which means enriched materials may not be necessary to produce ^{99}Mo for ^{99m}Tc production. The cyclotron at MURR is limited to deuteron energies of 8.5 MeV or below. To evaluate this reaction, the cyclotron's full deuteron energy range (0 – 8.5 MeV) was used for this research.

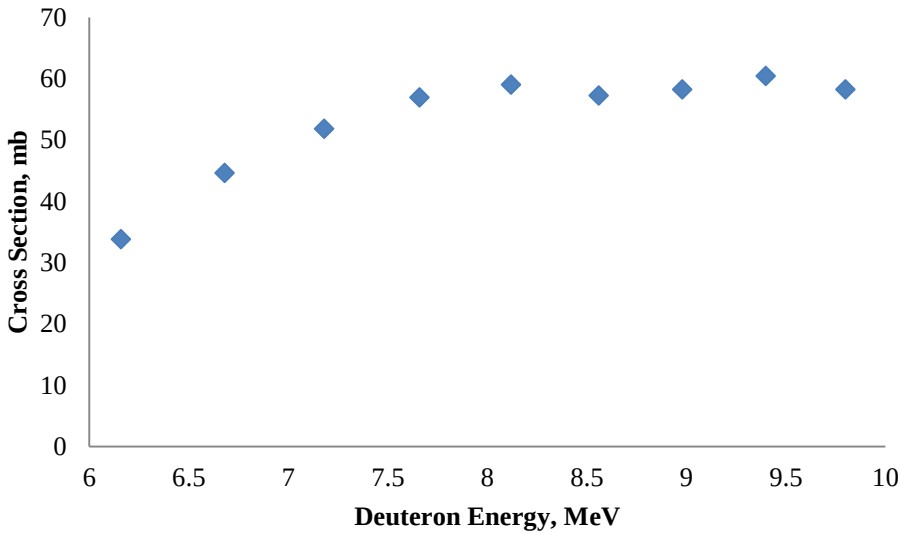

Figure A.1.9. Literature cross section for the production of ^{99}Mo via deuteron bombardment of natural molybdenum

A.2 SRIM Calculations for Targets

The SRIM (Stopping and Range of Ions in Matter) software was developed to calculate many important variables for the transport of ions in matter[56]. In this research, this software was utilized to determine the ion stopping power in a given target material. The molecular formula of the compound (or just the elemental mass for the pure metal) and the density of the bulk material for each target material and the element, its atomic mass, and the range of kinetic energies for the projectile are input into the program. In the simplest operation, the program output a table of the the electronic stopping power, nuclear stopping power, range, and straggling as a function of the projectile energy. Using the electronic and nuclear stopping powers output from SRIM, the total stopping power of the target material was calculated as a function of projectile energy for each target material. The data was plotted as the total stopping power (MeV/mm) as a function of projectile energy (MeV). A power function trend line was fitted to the data to define an equation for each target's stopping power.

Using the defined equation, theoretical predictions of energy deposition into each target were calculated. For the calculations, the target was segmented into smaller layers based on the target thickness (up to 30 layers for each target). The first layer was assigned the desired projectile energy, the equation solved for that layer, and the energy deposition determined over that thickness. The output energy from the first layer was input as the entry energy for the second layer; this process was repeated for the full thickness of the target. The energy deposition in each layer was summed together to determine the energy drop across the whole target.

Using this data, the thickness of the target could be altered to achieve the desired entry and exit energy for each target as described in Appendix A.1 (Table A.2.1). Ensuring the beam enters and exits the targets at the desired energies allows the desired reaction pathways to be maximized and minimize the undesired reaction pathways which may occur with ions of higher or lower kinetic energy. For the cyclotron at the University of Washington, the target must completely stop the ion beam so the full stopping thickness is included in Table A.2.1 for each target.

Table A.2.1. Target materials and the intended irradiation parameters including the desired entry and exit projectile energy, the desired thickness, and the thickness to fully stop the projectile

Target Material	Density ($g*cm^{-1}$)	Projectile	Entry Energy (MeV)	Exit Energy (MeV)	Thickness (µm)	Full Thickness (µm)
Os Metal	22.59	Proton	26	20	249.7	703.4
OsS_2	9.47	Proton	26	20	504.9	1400
W Metal	19.30	Proton	16	7	267.3	362.8
WS_2	7.50	Proton	16	7	572.2	765.0
Ge Metal	5.35	Alpha	28	0	235.6	235.6
$CaCO_3$	2.93	Proton	16	12	475.7	1190
MoS_2	5.06	Proton	16	10	505.7	914.2
		Deuteron	8.5	0	197.7	197.7

The osmium metal, osmium disulfide, tungsten, tungsten disulfide, calcium carbonate, and molybdenum disulfide targets have been irradiated using the 16 MeV PETtrace cyclotron at the University of Missouri Research Reactor. The tungsten metal, osmium metal, and arsenide targets were irradiated using the BLIP accelerator at Brookhaven National Laboratory. Detailed information concerning the arsenide target is not presented in this dissertation for commercial purposes[82]. The osmium disulfide and germanium metal targets have been irradiated using the 50.5 MeV Scanditronix cyclotron at the University of Washington.

A.2.1 Osmium Metal Target

Calculation Conditions: SRIM/TRIM-2008 calculation, hydrogen ion projectile with a mass of 1.008 amu, ion energy range from 1000 keV to 115000 keV, osmium target with a density of 22.59 g*cm^{-3}, MeV/mm for stopping power units, compound correction set to 1.

Table A.2.2. SRIM calculated stopping power for the proton bombardment of osmium metal

Energy	Elec dE/dx	Nuclear dE/dx	Sum dE/dx	Energy	Elec	Nuclear	Sum
MeV	MeV/mm	MeV/mm	MeV/mm	MeV	MeV/mm	MeV/mm	MeV/mm
1.00	1.46E+02	1.37E-01	1.47E+02	**12.0**	3.67E+01	1.74E-02	3.67E+01
1.10	1.41E+02	1.27E-01	1.41E+02	**13.0**	3.48E+01	1.62E-02	3.48E+01
1.20	1.36E+02	1.18E-01	1.36E+02	**14.0**	3.31E+01	1.52E-02	3.31E+01
1.30	1.31E+02	1.11E-01	1.31E+02	**15.0**	3.15E+01	1.44E-02	3.16E+01
1.40	1.26E+02	1.05E-01	1.26E+02	**16.0**	3.02E+01	1.36E-02	3.02E+01
1.50	1.22E+02	9.90E-02	1.22E+02	**17.0**	2.89E+01	1.29E-02	2.90E+01
1.60	1.19E+02	9.40E-02	1.19E+02	**18.0**	2.78E+01	1.23E-02	2.78E+01
1.70	1.15E+02	8.95E-02	1.15E+02	**20.0**	2.59E+01	1.12E-02	2.59E+01
1.80	1.12E+02	8.54E-02	1.12E+02	**22.5**	2.38E+01	1.01E-02	2.38E+01
2.00	1.06E+02	7.84E-02	1.06E+02	**25.0**	2.21E+01	9.20E-03	2.21E+01
2.25	1.00E+02	7.12E-02	1.00E+02	**27.5**	2.07E+01	8.46E-03	2.07E+01
2.50	9.48E+01	6.53E-02	9.48E+01	**30.0**	1.94E+01	7.84E-03	1.94E+01
2.75	9.01E+01	6.04E-02	9.01E+01	**32.5**	1.83E+01	7.31E-03	1.83E+01
3.00	8.59E+01	5.62E-02	8.60E+01	**35.0**	1.74E+01	6.85E-03	1.74E+01
3.25	8.22E+01	5.26E-02	8.22E+01	**37.5**	1.66E+01	6.45E-03	1.66E+01
3.50	7.88E+01	4.95E-02	7.89E+01	**40.0**	1.58E+01	6.09E-03	1.58E+01
3.75	7.58E+01	4.67E-02	7.59E+01	**45.0**	1.45E+01	5.49E-03	1.45E+01
4.00	7.31E+01	4.43E-02	7.31E+01	**50.0**	1.35E+01	5.00E-03	1.35E+01
4.50	6.82E+01	4.01E-02	6.82E+01	**55.0**	1.26E+01	4.60E-03	1.26E+01
5.00	6.41E+01	3.67E-02	6.41E+01	**60.0**	1.18E+01	4.25E-03	1.18E+01
5.50	6.05E+01	3.39E-02	6.05E+01	**65.0**	1.12E+01	3.96E-03	1.12E+01
6.00	5.73E+01	3.15E-02	5.74E+01	**70.0**	1.06E+01	3.71E-03	1.06E+01
6.50	5.46E+01	2.94E-02	5.46E+01	**80.0**	9.65E+00	3.29E-03	9.65E+00
7.00	5.21E+01	2.76E-02	5.21E+01	**90.0**	8.89E+00	2.97E-03	8.89E+00
8.00	4.79E+01	2.46E-02	4.79E+01	**100.**	8.26E+00	2.70E-03	8.26E+00
9.00	4.44E+01	2.23E-02	4.44E+01	**110.**	7.74E+00	2.48E-03	7.74E+00
10.0	4.14E+01	2.04E-02	4.14E+01	**115.**	7.52E+00	2.38E-03	7.52E+00
11.0	3.89E+01	1.88E-02	3.89E+01				

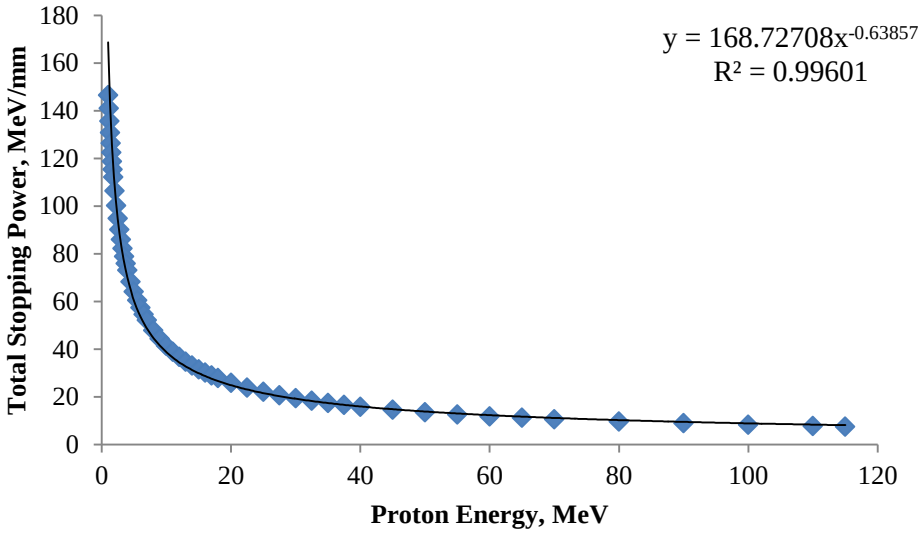

Figure A.2.1. Stopping power as a function of proton energy for the proton bombardment of an osmium target

A.2.2 Osmium Disulfide Target

Calculation Conditions: SRIM/TRIM-2008 calculation, hydrogen ion projectile with a mass of 1.008 amu, ion energy range from 1000 keV to 115000 keV, osmium disulfide target with a density of 9.47 g*cm^{-3}, osmium (x 1) and sulfur (x 2) stoichiometry, MeV/mm for stopping power units, compound correction set to 1.

Table A.2.3. SRIM calculated stopping power for the proton bombardment of osmium disulfide

Energy	Elec dE/dx	Nuclear dE/dx	Sum dE/dx	Energy	Elec	Nuclear	Sum
MeV	MeV/mm	MeV/mm	MeV/mm	MeV	MeV/mm	MeV/mm	MeV/mm
1.00	8.76E+01	7.39E-02	8.76E+01	**12.0**	1.86E+01	9.03E-03	1.86E+01
1.10	8.35E+01	6.84E-02	8.36E+01	**13.0**	1.76E+01	8.42E-03	1.76E+01
1.20	7.96E+01	6.37E-02	7.96E+01	**14.0**	1.67E+01	7.89E-03	1.67E+01
1.30	7.62E+01	5.97E-02	7.62E+01	**15.0**	1.59E+01	7.43E-03	1.59E+01
1.40	7.31E+01	5.61E-02	7.32E+01	**16.0**	1.52E+01	7.02E-03	1.52E+01
1.50	7.04E+01	5.30E-02	7.05E+01	**17.0**	1.45E+01	6.66E-03	1.45E+01
1.60	6.79E+01	5.03E-02	6.80E+01	**18.0**	1.39E+01	6.33E-03	1.39E+01
1.70	6.56E+01	4.78E-02	6.57E+01	**20.0**	1.29E+01	5.77E-03	1.29E+01
1.80	6.35E+01	4.56E-02	6.36E+01	**22.5**	1.18E+01	5.20E-03	1.18E+01
2.00	5.98E+01	4.18E-02	5.98E+01	**25.0**	1.10E+01	4.74E-03	1.10E+01
2.25	5.58E+01	3.79E-02	5.58E+01	**27.5**	1.02E+01	4.36E-03	1.02E+01
2.50	5.24E+01	3.47E-02	5.24E+01	**30.0**	9.57E+00	4.03E-03	9.58E+00
2.75	4.95E+01	3.20E-02	4.95E+01	**32.5**	9.02E+00	3.76E-03	9.03E+00
3.00	4.69E+01	2.97E-02	4.69E+01	**35.0**	8.54E+00	3.52E-03	8.54E+00
3.25	4.46E+01	2.78E-02	4.47E+01	**37.5**	8.12E+00	3.31E-03	8.12E+00
3.50	4.26E+01	2.61E-02	4.26E+01	**40.0**	7.74E+00	3.12E-03	7.74E+00
3.75	4.08E+01	2.46E-02	4.08E+01	**45.0**	7.09E+00	2.81E-03	7.09E+00
4.00	3.92E+01	2.33E-02	3.92E+01	**50.0**	6.56E+00	2.56E-03	6.56E+00
4.50	3.63E+01	2.11E-02	3.63E+01	**55.0**	6.12E+00	2.35E-03	6.12E+00
5.00	3.39E+01	1.93E-02	3.39E+01	**60.0**	5.74E+00	2.18E-03	5.74E+00
5.50	3.18E+01	1.77E-02	3.18E+01	**65.0**	5.41E+00	2.03E-03	5.42E+00
6.00	3.00E+01	1.65E-02	3.01E+01	**70.0**	5.13E+00	1.90E-03	5.13E+00
6.50	2.85E+01	1.54E-02	2.85E+01	**80.0**	4.66E+00	1.68E-03	4.66E+00
7.00	2.71E+01	1.44E-02	2.71E+01	**90.0**	4.28E+00	1.51E-03	4.28E+00
8.00	2.47E+01	1.28E-02	2.47E+01	**100.**	3.98E+00	1.38E-03	3.98E+00
9.00	2.28E+01	1.16E-02	2.28E+01	**110.**	3.72E+00	1.26E-03	3.72E+00
10.0	2.12E+01	1.06E-02	2.12E+01	**115.**	3.61E+00	1.21E-03	3.61E+00
11.0	1.98E+01	9.74E-03	1.98E+01				

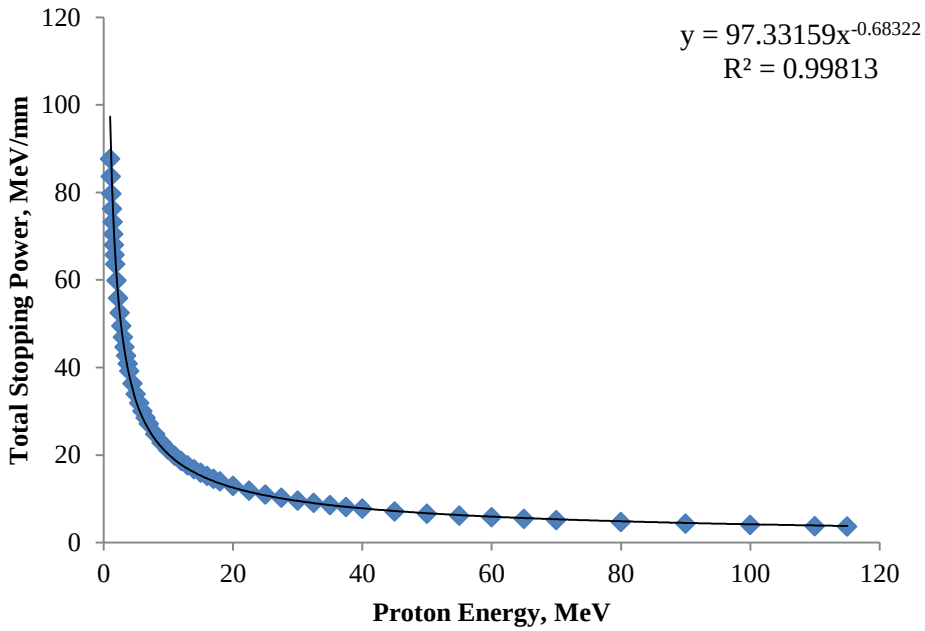

Figure A.2.2. Stopping power as a function of proton energy for the proton bombardment of an osmium disulfide target

A.2.3 Tungsten Metal Target

Calculation Conditions: SRIM/TRIM-2008 calculation, hydrogen ion projectile with a mass of 1.008 amu, ion energy range from 1000 keV to 115000 keV, tungsten target with a density of 19.30 g*cm^{-3}, MeV/mm for stopping power units, compound correction set to 1.

Table A.2.4. SRIM calculated stopping power for the proton bombardment of tungsten metal

Energy	Elec dE/dx	Nuclear dE/dx	Sum dE/dx	Energy	Elec	Nuclear	Sum
MeV	MeV/mm	MeV/mm	MeV/mm	MeV	MeV/mm	MeV/mm	MeV/mm
1.00	1.27E+02	1.20E-01	1.27E+02	**12.0**	3.18E+01	1.52E-02	3.18E+01
1.10	1.22E+02	1.11E-01	1.22E+02	**13.0**	3.01E+01	1.42E-02	3.01E+01
1.20	1.17E+02	1.04E-01	1.17E+02	**14.0**	2.86E+01	1.33E-02	2.87E+01
1.30	1.13E+02	9.71E-02	1.13E+02	**15.0**	2.73E+01	1.25E-02	2.73E+01
1.40	1.09E+02	9.15E-02	1.09E+02	**16.0**	2.61E+01	1.18E-02	2.62E+01
1.50	1.06E+02	8.66E-02	1.06E+02	**17.0**	2.51E+01	1.12E-02	2.51E+01
1.60	1.03E+02	8.22E-02	1.03E+02	**18.0**	2.41E+01	1.07E-02	2.41E+01
1.70	9.98E+01	7.82E-02	9.98E+01	**20.0**	2.24E+01	9.76E-03	2.24E+01
1.80	9.71E+01	7.47E-02	9.72E+01	**22.5**	2.06E+01	8.80E-03	2.06E+01
2.00	9.22E+01	6.86E-02	9.23E+01	**25.0**	1.92E+01	8.03E-03	1.92E+01
2.25	8.69E+01	6.23E-02	8.70E+01	**27.5**	1.79E+01	7.39E-03	1.79E+01
2.50	8.23E+01	5.71E-02	8.24E+01	**30.0**	1.68E+01	6.84E-03	1.68E+01
2.75	7.82E+01	5.28E-02	7.83E+01	**32.5**	1.59E+01	6.38E-03	1.59E+01
3.00	7.46E+01	4.91E-02	7.47E+01	**35.0**	1.51E+01	5.98E-03	1.51E+01
3.25	7.14E+01	4.60E-02	7.14E+01	**37.5**	1.43E+01	5.62E-03	1.43E+01
3.50	6.85E+01	4.32E-02	6.85E+01	**40.0**	1.37E+01	5.31E-03	1.37E+01
3.75	6.59E+01	4.08E-02	6.59E+01	**45.0**	1.26E+01	4.79E-03	1.26E+01
4.00	6.35E+01	3.87E-02	6.35E+01	**50.0**	1.17E+01	4.36E-03	1.17E+01
4.50	5.92E+01	3.50E-02	5.93E+01	**55.0**	1.09E+01	4.01E-03	1.09E+01
5.00	5.56E+01	3.21E-02	5.56E+01	**60.0**	1.02E+01	3.71E-03	1.02E+01
5.50	5.25E+01	2.96E-02	5.25E+01	**65.0**	9.68E+00	3.46E-03	9.68E+00
6.00	4.98E+01	2.75E-02	4.98E+01	**70.0**	9.18E+00	3.24E-03	9.18E+00
6.50	4.73E+01	2.57E-02	4.74E+01	**80.0**	8.36E+00	2.87E-03	8.36E+00
7.00	4.52E+01	2.41E-02	4.52E+01	**90.0**	7.70E+00	2.59E-03	7.70E+00
8.00	4.15E+01	2.15E-02	4.15E+01	**100.**	7.16E+00	2.35E-03	7.16E+00
9.00	3.85E+01	1.95E-02	3.85E+01	**110.**	6.71E+00	2.16E-03	6.71E+00
10.0	3.59E+01	1.78E-02	3.59E+01	**115.**	6.51E+00	2.08E-03	6.52E+00
11.0	3.37E+01	1.64E-02	3.37E+01				

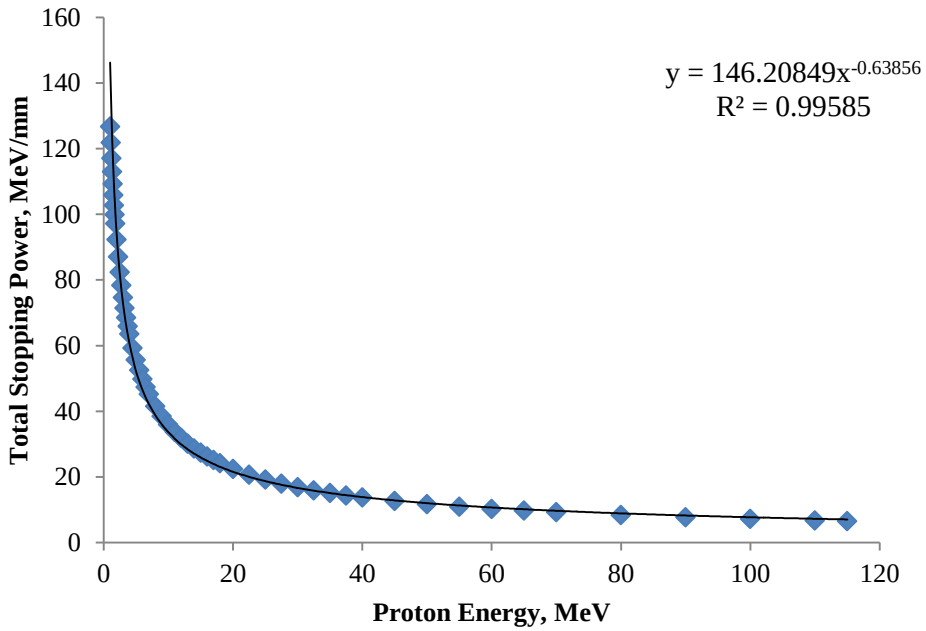

Figure A.2.3. Stopping power as a function of proton energy for the proton bombardment of a tungsten target

A.2.4 Tungsten Disulfide Target

Calculation Conditions: SRIM/TRIM-2008 calculation, hydrogen ion projectile with a mass of 1.008 amu, ion energy range from 1000 keV to 115000 keV, tungsten disulfide target with a density of 7.50 g*cm^{-3}, tungsten (x 1) and sulfur (x 2) stoichiometry, MeV/mm for stopping power units, compound correction set to 1.

Table A.2.5. SRIM calculated stopping power for the proton bombardment of tungsten disulfide

Energy	Elec dE/dx	Nuclear dE/dx	Sum dE/dx	Energy	Elec	Nuclear	Sum
MeV	MeV/mm	MeV/mm	MeV/mm	MeV	MeV/mm	MeV/mm	MeV/mm
1.00	7.02E+01	5.96E-02	7.03E+01	**12.0**	1.49E+01	7.27E-03	1.49E+01
1.10	6.69E+01	5.52E-02	6.70E+01	**13.0**	1.41E+01	6.78E-03	1.41E+01
1.20	6.37E+01	5.14E-02	6.38E+01	**14.0**	1.34E+01	6.35E-03	1.34E+01
1.30	6.10E+01	4.81E-02	6.10E+01	**15.0**	1.27E+01	5.98E-03	1.27E+01
1.40	5.86E+01	4.53E-02	5.86E+01	**16.0**	1.21E+01	5.65E-03	1.21E+01
1.50	5.64E+01	4.27E-02	5.65E+01	**17.0**	1.16E+01	5.36E-03	1.16E+01
1.60	5.45E+01	4.05E-02	5.45E+01	**18.0**	1.12E+01	5.09E-03	1.12E+01
1.70	5.26E+01	3.85E-02	5.27E+01	**20.0**	1.03E+01	4.64E-03	1.03E+01
1.80	5.10E+01	3.68E-02	5.10E+01	**22.5**	9.47E+00	4.19E-03	9.48E+00
2.00	4.80E+01	3.37E-02	4.80E+01	**25.0**	8.77E+00	3.81E-03	8.77E+00
2.25	4.48E+01	3.05E-02	4.48E+01	**27.5**	8.17E+00	3.51E-03	8.18E+00
2.50	4.21E+01	2.79E-02	4.21E+01	**30.0**	7.66E+00	3.25E-03	7.67E+00
2.75	3.97E+01	2.58E-02	3.98E+01	**32.5**	7.22E+00	3.02E-03	7.23E+00
3.00	3.77E+01	2.39E-02	3.77E+01	**35.0**	6.84E+00	2.83E-03	6.84E+00
3.25	3.59E+01	2.24E-02	3.59E+01	**37.5**	6.50E+00	2.66E-03	6.50E+00
3.50	3.42E+01	2.10E-02	3.42E+01	**40.0**	6.19E+00	2.51E-03	6.20E+00
3.75	3.28E+01	1.98E-02	3.28E+01	**45.0**	5.68E+00	2.26E-03	5.68E+00
4.00	3.14E+01	1.88E-02	3.15E+01	**50.0**	5.25E+00	2.06E-03	5.26E+00
4.50	2.91E+01	1.70E-02	2.92E+01	**55.0**	4.90E+00	1.89E-03	4.90E+00
5.00	2.72E+01	1.55E-02	2.72E+01	**60.0**	4.59E+00	1.75E-03	4.60E+00
5.50	2.55E+01	1.43E-02	2.56E+01	**65.0**	4.33E+00	1.63E-03	4.33E+00
6.00	2.41E+01	1.33E-02	2.41E+01	**70.0**	4.11E+00	1.52E-03	4.11E+00
6.50	2.28E+01	1.24E-02	2.28E+01	**80.0**	3.73E+00	1.35E-03	3.73E+00
7.00	2.17E+01	1.16E-02	2.17E+01	**90.0**	3.43E+00	1.22E-03	3.43E+00
8.00	1.98E+01	1.03E-02	1.98E+01	**100.**	3.18E+00	1.11E-03	3.18E+00
9.00	1.83E+01	9.34E-03	1.83E+01	**110.**	2.98E+00	1.02E-03	2.98E+00
10.0	1.70E+01	8.52E-03	1.70E+01	**115.**	2.89E+00	9.75E-04	2.89E+00
11.0	1.59E+01	7.84E-03	1.59E+01				

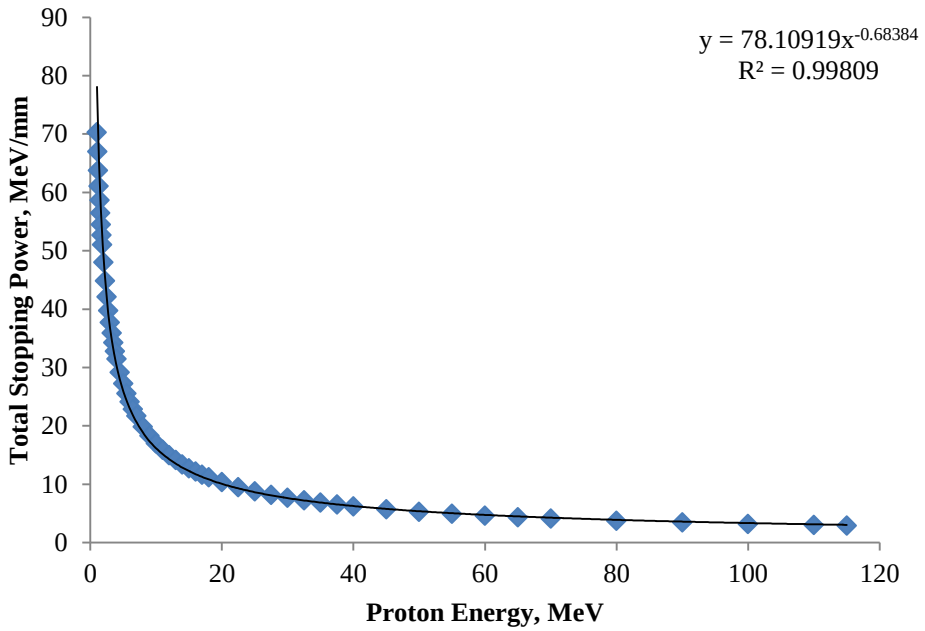

Figure A.2.4. Stopping power as a function of proton energy for the proton bombardment of a tungsten disulfide target

A.2.5 Germanium Target

Calculation Conditions: SRIM/TRIM-2008 calculation, helium ion projectile with a mass of 4.003 amu, ion energy range from 1000 keV to 50000 keV, germanium target with a density of 5.35 g*cm^{-3}, MeV/mm for stopping power units, compound correction set to 1.

Table A.2.6. SRIM calculated stopping power for the alpha particle bombardment of germanium metal

Energy	Elec dE/dx	Nuclear dE/dx	Sum dE/dx	Energy	Elec	Nuclear	Sum
MeV	MeV/mm	MeV/mm	MeV/mm	MeV	MeV/mm	MeV/mm	MeV/mm
1.00	3.62E+02	6.54E-01	3.63E+02	**7.00**	1.79E+02	1.30E-01	1.79E+02
1.10	3.59E+02	6.06E-01	3.60E+02	**8.00**	1.66E+02	1.16E-01	1.66E+02
1.20	3.55E+02	5.65E-01	3.56E+02	**9.00**	1.54E+02	1.05E-01	1.54E+02
1.30	3.51E+02	5.30E-01	3.51E+02	**10.0**	1.44E+02	9.60E-02	1.44E+02
1.40	3.46E+02	4.99E-01	3.47E+02	**11.0**	1.35E+02	8.84E-02	1.35E+02
1.50	3.41E+02	4.72E-01	3.42E+02	**12.0**	1.28E+02	8.20E-02	1.28E+02
1.60	3.36E+02	4.48E-01	3.37E+02	**13.0**	1.22E+02	7.65E-02	1.22E+02
1.70	3.31E+02	4.26E-01	3.32E+02	**14.0**	1.16E+02	7.17E-02	1.16E+02
1.80	3.27E+02	4.07E-01	3.27E+02	**15.0**	1.11E+02	6.76E-02	1.11E+02
2.00	3.17E+02	3.73E-01	3.17E+02	**16.0**	1.06E+02	6.39E-02	1.06E+02
2.25	3.05E+02	3.39E-01	3.05E+02	**17.0**	1.02E+02	6.06E-02	1.02E+02
2.50	2.94E+02	3.10E-01	2.94E+02	**18.0**	9.78E+01	5.76E-02	9.79E+01
2.75	2.83E+02	2.87E-01	2.84E+02	**20.0**	9.11E+01	5.26E-02	9.11E+01
3.00	2.74E+02	2.67E-01	2.74E+02	**22.5**	8.39E+01	4.74E-02	8.40E+01
3.25	2.64E+02	2.49E-01	2.65E+02	**25.0**	7.80E+01	4.32E-02	7.80E+01
3.50	2.56E+02	2.34E-01	2.56E+02	**27.5**	7.29E+01	3.98E-02	7.30E+01
3.75	2.48E+02	2.21E-01	2.48E+02	**30.0**	6.86E+01	3.68E-02	6.86E+01
4.00	2.41E+02	2.10E-01	2.41E+02	**32.5**	6.47E+01	3.43E-02	6.48E+01
4.50	2.27E+02	1.90E-01	2.27E+02	**35.0**	6.14E+01	3.21E-02	6.14E+01
5.00	2.15E+02	1.74E-01	2.15E+02	**37.5**	5.84E+01	3.02E-02	5.84E+01
5.50	2.05E+02	1.60E-01	2.05E+02	**40.0**	5.57E+01	2.86E-02	5.57E+01
6.00	1.95E+02	1.49E-01	1.95E+02	**45.0**	5.11E+01	2.57E-02	5.11E+01
6.50	1.87E+02	1.39E-01	1.87E+02	**50.0**	4.73E+01	2.34E-02	4.73E+01

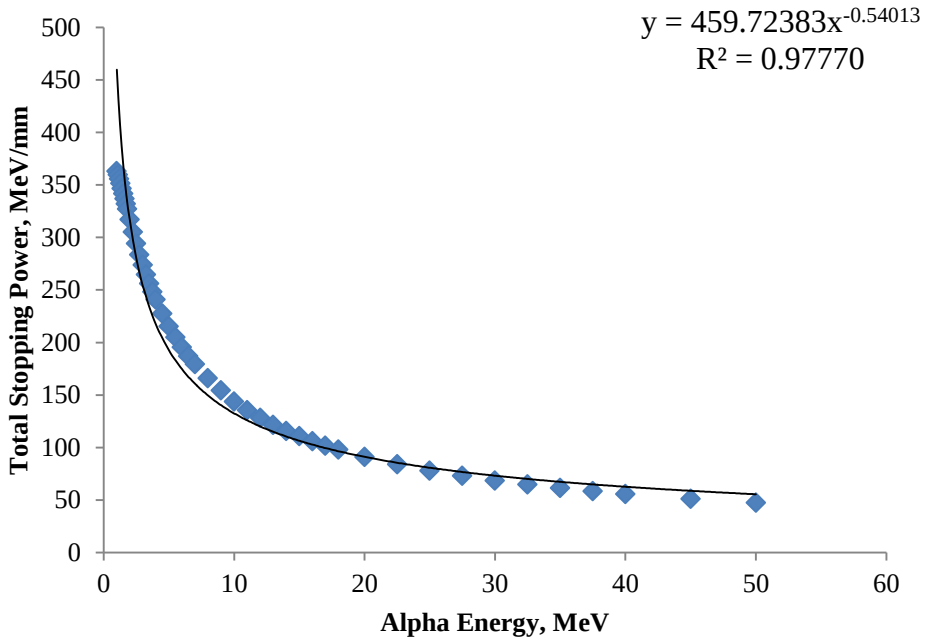

Figure A.2.5. Stopping power as a function of alpha energy for the alpha bombardment of a germanium target

A.2.6 Calcium Carbonate Target

Calculation Conditions: SRIM/TRIM-2008 calculation, hydrogen ion projectile with a mass of 1.008 amu, ion energy range from 1000 keV to 50000 keV, calcium carbonate target with a density of 2.93 g*cm^{-3}, MeV/mm for stopping power units, compound correction set to 1.

Table A.2.7. SRIM calculated stopping power for the proton bombardment of calcium carbonate

Energy	Elec dE/dx	Nuclear dE/dx	Sum dE/dx	Energy	Elec	Nuclear	Sum
MeV	MeV/mm	MeV/mm	MeV/mm	MeV	MeV/mm	MeV/mm	MeV/mm
1.00	5.64E+01	4.05E-02	5.64E+01	**7.00**	1.45E+01	7.42E-03	1.45E+01
1.10	5.38E+01	3.74E-02	5.38E+01	**8.00**	1.30E+01	6.59E-03	1.30E+01
1.20	5.12E+01	3.47E-02	5.12E+01	**9.00**	1.19E+01	5.93E-03	1.19E+01
1.30	4.86E+01	3.24E-02	4.87E+01	**10.0**	1.09E+01	5.40E-03	1.09E+01
1.40	4.64E+01	3.04E-02	4.64E+01	**11.0**	1.02E+01	4.96E-03	1.02E+01
1.50	4.44E+01	2.86E-02	4.44E+01	**12.0**	9.48E+00	4.59E-03	9.49E+00
1.60	4.25E+01	2.71E-02	4.25E+01	**13.0**	8.90E+00	4.27E-03	8.90E+00
1.70	4.08E+01	2.57E-02	4.09E+01	**14.0**	8.39E+00	4.00E-03	8.40E+00
1.80	3.93E+01	2.44E-02	3.93E+01	**15.0**	7.95E+00	3.76E-03	7.95E+00
2.00	3.65E+01	2.23E-02	3.66E+01	**16.0**	7.55E+00	3.55E-03	7.55E+00
2.25	3.36E+01	2.01E-02	3.37E+01	**17.0**	7.19E+00	3.36E-03	7.20E+00
2.50	3.12E+01	1.84E-02	3.12E+01	**18.0**	6.87E+00	3.19E-03	6.88E+00
2.75	2.91E+01	1.69E-02	2.91E+01	**20.0**	6.32E+00	2.90E-03	6.32E+00
3.00	2.73E+01	1.57E-02	2.74E+01	**22.5**	5.75E+00	2.61E-03	5.75E+00
3.25	2.58E+01	1.46E-02	2.58E+01	**25.0**	5.29E+00	2.37E-03	5.29E+00
3.50	2.44E+01	1.37E-02	2.44E+01	**27.5**	4.90E+00	2.18E-03	4.90E+00
3.75	2.32E+01	1.29E-02	2.32E+01	**30.0**	4.57E+00	2.01E-03	4.57E+00
4.00	2.21E+01	1.22E-02	2.21E+01	**32.5**	4.29E+00	1.87E-03	4.29E+00
4.50	2.02E+01	1.10E-02	2.03E+01	**35.0**	4.05E+00	1.75E-03	4.05E+00
5.00	1.87E+01	9.99E-03	1.87E+01	**37.5**	3.83E+00	1.65E-03	3.83E+00
5.50	1.74E+01	9.18E-03	1.74E+01	**40.0**	3.64E+00	1.55E-03	3.64E+00
6.00	1.63E+01	8.50E-03	1.63E+01	**45.0**	3.32E+00	1.39E-03	3.32E+00
6.50	1.53E+01	7.92E-03	1.53E+01	**50.0**	3.05E+00	1.27E-03	3.05E+00

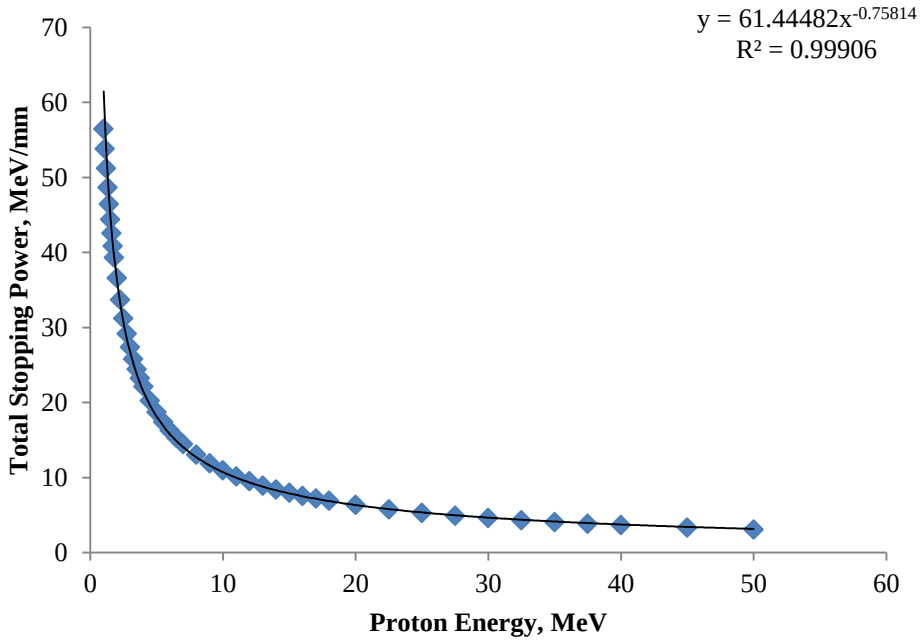

Figure A.2.6. Stopping power as a function of proton energy for the proton bombardment of a calcium carbonate target

A.2.7 Molybdenum Disulfide Target (Proton Bombardment)

Calculation Conditions: SRIM/TRIM-2008 calculation, hydrogen ion projectile with a mass of 1.008 amu, ion energy range from 1000 keV to 50000 keV, molybdenum disulfide target with a density of 5.06 g*cm^{-3}, molybdenum (x 1) and sulfur (x 2) stoichiometry MeV/mm for stopping power units, compound correction set to 1.

Table A.2.8. SRIM calculated stopping power for the proton bombardment of molybdenum disulfide

Energy	Elec dE/dx	Nuclear dE/dx	Sum dE/dx	Energy	Elec	Nuclear	Sum
MeV	MeV/mm	MeV/mm	MeV/mm	MeV	MeV/mm	MeV/mm	MeV/mm
1.00	6.48E+01	5.16E-02	6.48E+01	**7.00**	1.85E+01	9.80E-03	1.85E+01
1.10	6.16E+01	4.77E-02	6.17E+01	**8.00**	1.68E+01	8.72E-03	1.68E+01
1.20	5.86E+01	4.43E-02	5.86E+01	**9.00**	1.54E+01	7.86E-03	1.54E+01
1.30	5.59E+01	4.15E-02	5.59E+01	**10.0**	1.43E+01	7.17E-03	1.43E+01
1.40	5.35E+01	3.90E-02	5.35E+01	**11.0**	1.33E+01	6.59E-03	1.33E+01
1.50	5.13E+01	3.68E-02	5.13E+01	**12.0**	1.25E+01	6.10E-03	1.25E+01
1.60	4.93E+01	3.48E-02	4.94E+01	**13.0**	1.17E+01	5.69E-03	1.17E+01
1.70	4.76E+01	3.31E-02	4.76E+01	**14.0**	1.11E+01	5.33E-03	1.11E+01
1.80	4.59E+01	3.15E-02	4.59E+01	**15.0**	1.06E+01	5.01E-03	1.06E+01
2.00	4.30E+01	2.88E-02	4.30E+01	**16.0**	1.01E+01	4.73E-03	1.01E+01
2.25	3.99E+01	2.61E-02	3.99E+01	**17.0**	9.60E+00	4.49E-03	9.60E+00
2.50	3.73E+01	2.38E-02	3.73E+01	**18.0**	9.19E+00	4.27E-03	9.20E+00
2.75	3.51E+01	2.20E-02	3.51E+01	**20.0**	8.49E+00	3.88E-03	8.49E+00
3.00	3.31E+01	2.04E-02	3.31E+01	**22.5**	7.76E+00	3.50E-03	7.76E+00
3.25	3.14E+01	1.91E-02	3.14E+01	**25.0**	7.16E+00	3.18E-03	7.17E+00
3.50	2.99E+01	1.79E-02	2.99E+01	**27.5**	6.66E+00	2.93E-03	6.66E+00
3.75	2.85E+01	1.68E-02	2.85E+01	**30.0**	6.23E+00	2.71E-03	6.23E+00
4.00	2.73E+01	1.59E-02	2.73E+01	**32.5**	5.86E+00	2.52E-03	5.86E+00
4.50	2.52E+01	1.44E-02	2.52E+01	**35.0**	5.54E+00	2.36E-03	5.54E+00
5.00	2.34E+01	1.31E-02	2.34E+01	**37.5**	5.26E+00	2.22E-03	5.26E+00
5.50	2.19E+01	1.21E-02	2.19E+01	**40.0**	5.00E+00	2.09E-03	5.01E+00
6.00	2.06E+01	1.12E-02	2.06E+01	**45.0**	4.57E+00	1.88E-03	4.58E+00
6.50	1.95E+01	1.05E-02	1.95E+01	**50.0**	4.22E+00	1.71E-03	4.22E+00

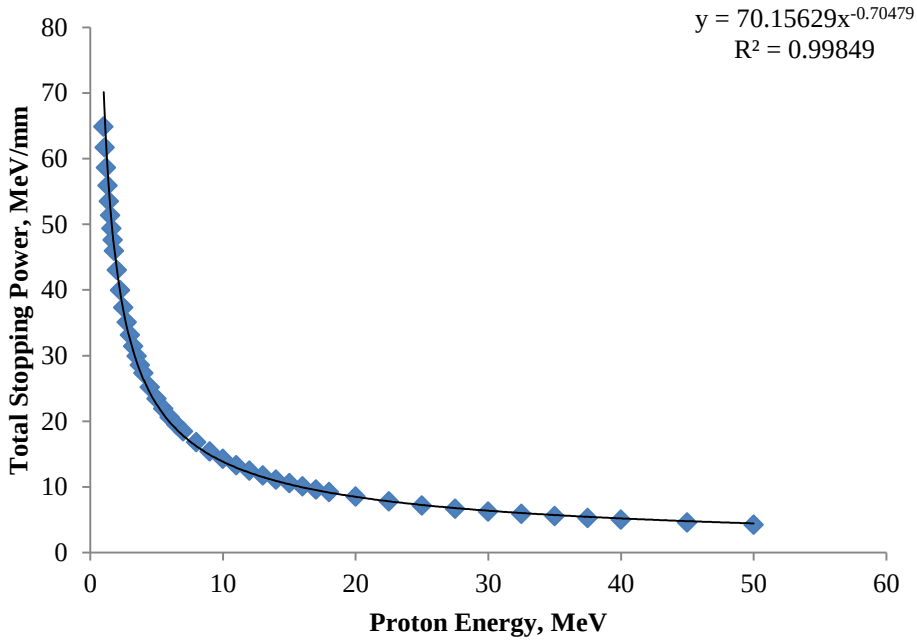

Figure A.2.7. Stopping power as a function of proton energy for the proton bombardment of a molybdenum disulfide target

A.2.8 Molybdenum Disulfide Target (Deuteron Bombardment)

Calculation Conditions: SRIM/TRIM-2008 calculation, deuteron ion projectile with a mass of 2.014 amu, ion energy range from 1000 keV to 115000 keV, molybdenum disulfide target with a density of 5.06 g*cm^{-3}, molybdenum (x 1) and sulfur (x 2) stoichiometry MeV/mm for stopping power units, compound correction set to 1.

Table A.2.9. SRIM calculated stopping power for deuteron bombardment of molybdenum disulfide

Energy	Elec dE/dx	Nuclear dE/dx	Sum dE/dx	Energy	Elec	Nuclear	Sum
MeV	MeV/mm	MeV/mm	MeV/mm	MeV	MeV/mm	MeV/mm	MeV/mm
1.00	6.48E+01	5.16E-02	6.48E+01	**7.00**	1.85E+01	9.80E-03	1.85E+01
1.10	6.16E+01	4.77E-02	6.17E+01	**8.00**	1.68E+01	8.72E-03	1.68E+01
1.20	5.86E+01	4.43E-02	5.86E+01	**9.00**	1.54E+01	7.86E-03	1.54E+01
1.30	5.59E+01	4.15E-02	5.59E+01	**10.0**	1.43E+01	7.17E-03	1.43E+01
1.40	5.35E+01	3.90E-02	5.35E+01	**11.0**	1.33E+01	6.59E-03	1.33E+01
1.50	5.13E+01	3.68E-02	5.13E+01	**12.0**	1.25E+01	6.10E-03	1.25E+01
1.60	4.93E+01	3.48E-02	4.94E+01	**13.0**	1.17E+01	5.69E-03	1.17E+01
1.70	4.76E+01	3.31E-02	4.76E+01	**14.0**	1.11E+01	5.33E-03	1.11E+01
1.80	4.59E+01	3.15E-02	4.59E+01	**15.0**	1.06E+01	5.01E-03	1.06E+01
2.00	4.30E+01	2.88E-02	4.30E+01	**16.0**	1.01E+01	4.73E-03	1.01E+01
2.25	3.99E+01	2.61E-02	3.99E+01	**17.0**	9.60E+00	4.49E-03	9.60E+00
2.50	3.73E+01	2.38E-02	3.73E+01	**18.0**	9.19E+00	4.27E-03	9.20E+00
2.75	3.51E+01	2.20E-02	3.51E+01	**20.0**	8.49E+00	3.88E-03	8.49E+00
3.00	3.31E+01	2.04E-02	3.31E+01	**22.5**	7.76E+00	3.50E-03	7.76E+00
3.25	3.14E+01	1.91E-02	3.14E+01	**25.0**	7.16E+00	3.18E-03	7.17E+00
3.50	2.99E+01	1.79E-02	2.99E+01	**27.5**	6.66E+00	2.93E-03	6.66E+00
3.75	2.85E+01	1.68E-02	2.85E+01	**30.0**	6.23E+00	2.71E-03	6.23E+00
4.00	2.73E+01	1.59E-02	2.73E+01	**32.5**	5.86E+00	2.52E-03	5.86E+00
4.50	2.52E+01	1.44E-02	2.52E+01	**35.0**	5.54E+00	2.36E-03	5.54E+00
5.00	2.34E+01	1.31E-02	2.34E+01	**37.5**	5.26E+00	2.22E-03	5.26E+00
5.50	2.19E+01	1.21E-02	2.19E+01	**40.0**	5.00E+00	2.09E-03	5.01E+00
6.00	2.06E+01	1.12E-02	2.06E+01	**45.0**	4.57E+00	1.88E-03	4.58E+00
6.50	1.95E+01	1.05E-02	1.95E+01	**50.0**	4.22E+00	1.71E-03	4.22E+00

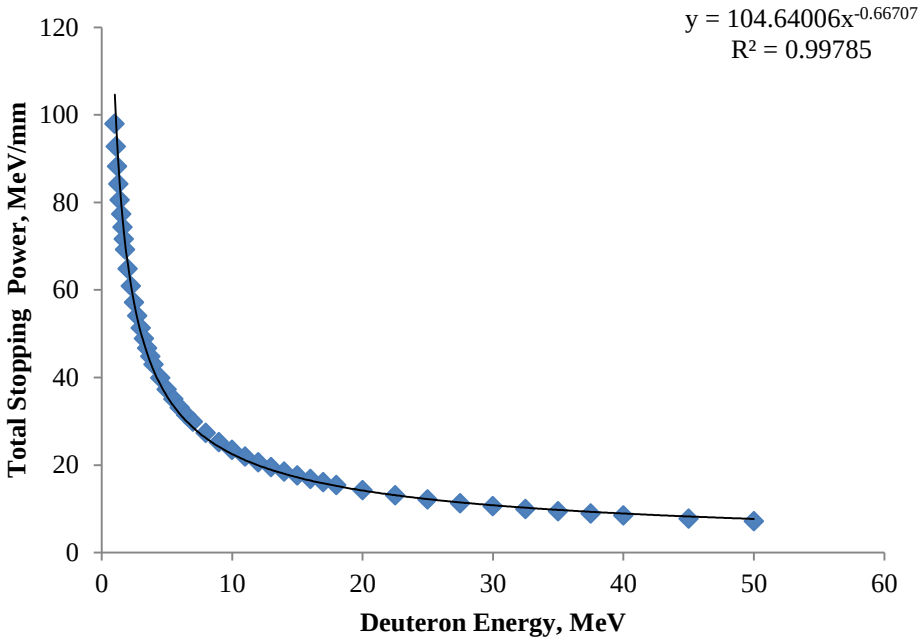

Figure A.2.8. Stopping power as a function of deuteron energy for the deuteron bombardment of a molybdenum disulfide target

A.3 Theoretical Qualification and Quantification of Activation Products

Prior to performing the irradiations, the potential activation products and their theoretical activities were calculated for each of the studied reactions to prevent any radiological dose concerns for the planned irradiation conditions and to compare the experimental production yields to these calculated theoretical yields.

For each target to be studied, the literature or theoretical cross section data was examined to determine the potential reactions for each nuclide present in the target at the desired projectile energy range. If the cross section data was available for the irradiation of a natural abundance target, this data was used in preference to collating the reactions for each individual nuclide. Once the potential reactions had been identified, their potential activities (A) were calculated using the following equation:

$$A = n * x * \sigma * I * \left(1 - e^{-\lambda * t_{irr}}\right) * \left(e^{-\lambda * t_{dec}}\right) \qquad \text{Equation A.3.1}$$

n is the number of target atoms in a given volume (nuclei*cm^{-3}), which was calculated using the density and the atomic mass of the target material. x is the thickness of the target (cm), which was known for the commercially purchased foils and calculated using the target mass for the pressed pellet targets. σ is the reaction cross section (cm^2), which was known from the reported literature or theoretical calculations from the TENDL-2014 database. In the case of thicker foils and targets, the averaged cross section for the projectile energy range deposited in the target was used to give a more accurate approximation. I is the current of the charged particle beam (charged particle*sec^{-1}) and was a known experimental parameter. λ is the decay constant of the product nuclide (h^{-1}). t_{irr} and t_{dec} are the irradiation time (h) and decay time (h), respectively. For these

analyses, all activities were calculated to the end of bombardment so t_{dec} was 0, which cancels out the second exponential term ($e^0 = 1$).

A.3.1 Natural Abundance Osmium Targets

Many of the reaction cross sections for the proton bombardment of natural abundance osmium targets are unknown. For this reason, the theoretical cross sections from the TENDL-2014 database were used in these calculations. There are seven naturally occurring isotopes of osmium, three of which (^{184,186,187}Os) are lower abundance (< 2%) and were not included in these calculations as their effect on overall yield would be minimal. With an intended proton energy range of 20-26 MeV, a large number of reactions are observed (Table A.3.1). The primary reaction of interest is ^{189}Os(p, α)^{186}Re. ^{189}Os is only 16.15% naturally abundant, therefore an enriched target could produce approximately 6-fold the activity of ^{186}Re compared to a natural target.

Table A.3.1. Potential nuclides produced via proton bombardment of a natural abundance osmium target

Parent Nuclide	**^{184}Os**	**^{186}Os**	**^{187}Os**	**^{188}Os**	**^{189}Os**	**^{190}Os**	**^{192}Os**
Abundance	0.0002	0.0159	0.0196	0.1324	0.1615	0.2626	0.4078
Reaction	**Product Nuclide**						
(p,α)	^{181}Re	^{183}Re	^{184}Re	^{185}Re	^{186}Re	^{187}Re	^{189}Re
(p,t)	^{182}Os	^{184}Os	^{185}Os	^{186}Os	^{187}Os	^{188}Os	^{190}Os
(p,d)	^{183}Os	^{185}Os	^{186}Os	^{187}Os	^{188}Os	^{189}Os	^{191}Os
(p,p')	^{184}Os	^{186}Os	^{187}Os	^{188}Os	^{185}Os	^{190}Os	^{192}Os
(p,n)	^{184}Ir	^{186}Ir	^{187}Ir	^{188}Ir	^{189}Ir	^{190}Ir	^{192}Ir
(p,nα)	^{180}Re	^{182}Re	^{183}Re	^{184}Re	^{185}Re	^{186}Re	^{188}Re
(p,nt)	^{181}Os	^{183}Os	^{184}Os	^{185}Os	^{186}Os	^{187}Os	^{189}Os
(p,np)	^{183}Os	^{185}Os	^{186}Os	^{187}Os	^{188}Os	^{189}Os	^{191}Os
(p,2n)	^{183}Ir	^{185}Ir	^{186}Ir	^{187}Ir	^{188}Ir	^{189}Ir	^{190}Ir
(p,2nα)	^{179}Re	^{181}Re	^{182}Re	^{183}Re	^{184}Re	^{185}Re	^{187}Re
(p,2np)	^{182}Os	^{184}Os	^{185}Os	^{186}Os	^{187}Os	^{188}Os	^{190}Os
(p,3n)	^{182}Ir	^{184}Ir	^{185}Ir	^{186}Ir	^{187}Ir	^{188}Ir	^{190}Ir

Though the intended proton range was from 20-26 MeV, the actual experimental ranges used were quite different. At MURR, a 0.04 mm thick OsS_2 target was irradiated for 1 hour with a 10 μA current of protons ranging from 15.4-16 MeV. Since less than 1 MeV of energy was deposited in the target, only the cross section at 16 MeV was used. Additionally, OsS_2 is only 74.8% Os by mass so the calculated activities were corrected to reflect this difference. At BNL, a 0.5 mm thick Os metal target was irradiated for 30 minutes with a 30 μA current of protons ranging from 9-30 MeV. For this target, the average cross section over this range was calculated and used to determine the product nuclides and their activities. The results of these calculations are illustrated in Table A.3.2.

Table A.3.2. Theoretical cross sections and calculated activities for the proton bombardment of natural abundance osmium targets

Activation Products		BNL Target (9-30 MeV)		MURR Target (16 MeV)	
Nuclide	**Half-Life**	**Average σ (mb)**	**Activity (μCi)**	**σ (mb)**	**Activity (μCi)**
^{183}Re	70 d	0.06	0.034	0.00	0.000
^{184}Re	38 d	0.51	5.340	0.00	0.000
^{185}Re	STABLE	1.04	0.000	0.03	0.000
^{186}Re	3.718 d	1.34	143.73	0.07	0.002
^{187}Re	STABLE	0.87	0.000	0.04	0.000
^{188}Re	17.004 h	0.41	230.57	0.004	0.001
^{189}Re	24 h	1.59	628.76	0.06	0.007
^{185}Os	93.6 d	0.03	0.015	0.00	0.000
^{186}Os	STABLE	0.49	0.000	0.00	0.000
^{187}Os	STABLE	4.54	0.000	0.03	0.000
^{188}Os	STABLE	15.19	0.000	3.10	0.000
^{189}Os	STABLE	17.24	0.000	3.69	0.000
^{190}Os	STABLE	17.12	0.000	5.15	0.000
^{191}Os	15.4 d	18.85	487.20	0.15	0.083
^{192}Os	STABLE	19.30	0.000	6.24	0.000
^{186}Ir	16.64 h	50.69	28817.4	0.00	0.000
^{187}Ir	10.5 h	144.16	128023.1	111.66	351.4
^{188}Ir	1.72 d	189.74	43750.4	148.70	124.23
^{189}Ir	13.2 d	134.01	4041.1	242.70	26.61
^{190}Ir	11.8 d	210.75	7108.9	13.14	1.61
^{191}Ir	STABLE	179.78	0.000	372.11	0.000
^{192}Ir	73.83 d	19.28	103.99	7.07	0.809

A.3.2 Natural Abundance Tungsten Targets

The reaction cross sections for the proton bombardment of natural abundance tungsten have been reported in the literature[34,45,47,48]. There are five naturally occurring isotopes of tungsten and four of them have a high natural abundance (14.31-30.64%). With the high abundance of these isotopes, several isotopes of rhenium (^{181,182,182m,183,184,186}Re) and tantalum (^{183}Ta) are produced at the intended proton energy range from 7-16 MeV. The primary reaction of interest is ^{186}W(p, n)^{186}Re. The natural abundance of ^{186}W is only 28.43%, therefore an enriched target could produce approximately 3.5-fold the activity of

^{186}Re compared to a natural target. For these calculations, the literature cross section data from Lapi *et al*[45] and Taranyi *et al*[47] was used.

Though the intended proton range was from 7-16 MeV, the actual experimental ranges used were quite different. Two tungsten disulfide targets were irradiated at MURR. The first target was a 0.05 mm thick WS_2 target that was irradiated for 1 hour with a 10 μA current of protons ranging from 13.4-14 MeV. Since less than 1 MeV of energy was deposited in the target, only the cross section at 14 MeV was used. The second target was a 0.2 mm thick WS_2 target that was irradiated for 1 hour with a 10 μA current of protons ranging from 8-11 MeV. For this target, the average cross section over this range was calculated and used to determine the product radionuclides and their activities. Additionally, WS_2 is only 74.14% W by mass so the calculated activities were corrected to reflect this difference for both targets. At BNL, a 0.05 mm thick W metal foil was irradiated for 1 hour with a either a 30 or 115 μA current of protons ranging from 8-10 MeV. For this target, the average cross section over this range was calculated and used to determine the product nuclides and their activities. The results of these calculations are illustrated in Table A.3.3 and A.3.4.

Table A.3.3. Literature cross sections and calculated activities for the proton bombardment of natural abundance tungsten disulfide targets at MURR

Activation Products		**MURR Target (14 MeV)**		**MURR Target (8-11 MeV)**	
Nuclide	**Half-Life**	**σ (mb)**	**Activity (μCi)**	**Average σ (mb)**	**Activity (μCi)**
^{181}Re	19.9 h	244.54	616.40	0.00	0.00
^{182}Re	64 h	41.05	160.56	6.17	106.26
^{182m}Re	12.7 h	248.12	196.81	67.85	236.81
^{183}Re	70 d	243.46	7.39	35.48	4.74
^{184}Re	35.4 d	20.97	1.26	47.56	12.56
^{186}Re	3.718 d	29.84	17.00	57.59	144.37
^{183}Ta	5.1 d	6.29	2.62	0.88	3.34

Table A.3.4. Literature cross sections and calculated activities for the proton bombardment of a natural abundance tungsten metal targets at BNL

Activation Products		BNL Target (30 µA, 15 min)		BNL Target (115 µA, 60 min)	
Nuclide	**Half-Life**	**Average σ (mb)**	**Activity (µCi)**	**Average σ (mb)**	**Activity (µCi)**
^{181}Re	19.9 h	0.00	0.00	0.00	0.00
^{182}Re	64 h	4.28	92.56	4.28	757.92
^{182m}Re	12.7 h	49.85	215.08	49.85	1790.07
^{183}Re	70 d	22.62	3.72	22.62	31.10
^{184}Re	35.4 d	41.18	13.40	41.18	111.94
^{186}Re	3.718 d	60.50	187.30	60.50	1560.62
^{183}Ta	5.1 d	0.65	1.46	0.65	12.18

A.3.3 Natural Abundance Germanium Metal Target

The reaction cross sections for the alpha particle bombardment of natural abundance germanium metal are unknown. For this reason, the theoretical cross sections from the TENDL-2014 database where used to determine the potential activation products. There are five naturally occurring isotopes of germanium, all of which have a significant natural abundance (7.61-36.28%). With an intended alpha particle energy range of 0-28 MeV, a large number of reactions are observed (Table A.3.5). The primary reaction of interest is ^{70}Ge(α, 2n)^{72}Se. The natural abundance of ^{70}Ge is only 20.84%, therefore an enriched target could provide approximately 5-fold the activity of ^{72}Se compared to a natural target. The alpha particle beam must be fully stopped in the target due to the clinical operations at the University of Washington cyclotron facility. Due to the large number of observed reactions, the theoretical activities were only calculated for the reactions on ^{70}Ge.

Table A.3.5. Potential nuclides produced via proton bombardment of a natural germanium target

Parent Nuclide	**^{70}Ge**	**^{72}Ge**	**^{73}Ge**	**^{74}Ge**	**^{76}Ge**
Abundance	0.2084	0.2754	0.0773	0.3628	0.0761
Reaction	**Product Nuclide**				
(α, g)	^{74}Se	^{76}Se	^{77}Se	^{78}Se	^{80}Se
(α, α')	^{70}Ge	^{72}Ge	^{73}Ge	^{74}Ge	^{76}Ge
(α, 2α)	^{66}Zn	^{68}Zn	^{69}Zn	^{70}Zn	^{72}Zn
(α, ^{3}He)	^{71}Ge	^{73}Ge	^{74}Ge	^{75}Ge	^{77}Ge
(α, t)	^{71}As	^{73}As	^{74}As	^{75}As	^{77}As
(α, d)	^{72}As	^{74}As	^{75}As	^{76}As	^{78}As
(α, p)	^{73}As	^{75}As	^{76}As	^{77}As	^{79}As
(α, pα)	^{69}Ga	^{71}Ga	^{72}Ga	^{73}Ga	^{75}Ga
(α, 2p)	^{72}Ge	^{74}Ge	^{75}Ge	^{76}Ge	^{78}Ge
(α, n)	^{73}Se	^{75}Se	^{76}Se	^{77}Se	^{79}Se
(α, nα)	^{69}Ge	^{71}Ge	^{72}Ge	^{73}Ge	^{75}Ge
(α, n2α)	^{65}Zn	^{67}Zn	^{68}Zn	^{69}Zn	^{71}Zn
(α, nd)	^{71}As	^{73}As	^{74}As	^{75}As	^{77}As
(α, np)	^{72}As	^{74}As	^{75}As	^{76}As	^{78}As
(α, npα)	^{68}Ga	^{70}Ga	^{71}Ga	^{72}Ga	^{74}Ga
(α, n2p)	^{71}Ge	^{73}Ge	^{74}Ge	^{75}Ge	^{77}Ge
(α, 2n)	^{72}Se	^{74}Se	^{75}Se	^{76}Se	^{78}Se
(α, 2nα)	^{68}Ge	^{70}Ge	^{71}Ge	^{72}Ge	^{74}Ge
(α, 2np)	^{71}As	^{73}As	^{74}As	^{75}As	^{77}As
(α, 3n)	^{71}Se	^{73}Se	^{74}Se	^{75}Se	^{77}Se

At the time of these calculations the irradiation was still theoretical and the intended irradiation parameters were used for these calculations; a 0.24 mm thick germanium metal target will be irradiated for 4 hours with a 20 μA current of alpha particle energy ranging from 0-28 MeV. For this target, the average cross section over this range was calculated and used to determine the product nuclides and their activities. The results of these calculations are illustrated in Table A.3.6.

Table A.3.6. Theoretical cross sections and calculated activities for the alpha particle bombardment of a natural abundance germanium metal target at UW

Activation Products		UW Target (0-28 MeV)	
Nuclide	**Half-Life**	**Average σ (mb)**	**Activity (μCi)**
^{71}As	2.72 d	0.11	257.64
^{72}As	26.0 h	105.78	226010.00
^{73}As	80.3 d	83.47	82.32
^{68}Ga	1.130 h	0.00001	0.49
^{69}Ga	STABLE	0.99	0.00
^{68}Ge	270.8 d	0.01	0.30
^{69}Ge	1.63 d	10.19	20933.75
^{70}Ge	STABLE	61.54	0.00
^{71}Ge	11.4 d	0.05	31.81
^{72}Ge	STABLE	9.44	0.00
^{71}Se	4.7 m	0.00	0.00
^{72}Se	8.5 d	46.01	10656.27
^{73}Se	7.1 h	182.11	17177.68
^{74}Se	STABLE	0.43	0.00
^{65}Zn	243.8 d	0.00	0.00
^{66}Zn	STABLE	0.47	0.00

A.3.4 Natural Abundance Calcium Carbonate Targets

The reaction cross sections for the proton bombardment of natural abundance calcium targets have been reported in the literature but is limited[92,93]. These reports primarily focus on the production of ^{44,44m}Sc with little data provided for the production of ^{43,47,48}Sc, which could be produced as radionuclidic impurities. There are six naturally occurring isotopes of calcium, but ^{40}Ca is the predominant isotope (96.941 %). For this reason, several isotope of scandium (^{43,44,44m,46,47,48}Sc) are produced as a result of irradiating natural abundance calcium targets using the intended proton energy range from 12-16 MeV. The primary reaction of interest is ^{44}Ca(p, n)^{44}Sc. The natural abundance of ^{44}Ca is only 2.086%, therefore the use of an enriched target could provide

48-fold the activity of ^{44}Sc compared to a natural target. For these calculations, the literature cross section data from Muller[92] was used.

The calculations were performed for the intended proton range from 12-16 MeV. A 0.42 mm thick calcium carbonate target was irradiated at MURR for 1 hour with a 10 μA current of protons ranging from 12.6-16 MeV. Due to the limited literature data, the cross section at 14.9 MeV was used to calculate the activities for ^{43,44,44m,48}Sc production. The theoretical cross section for the ^{48}Ca(p, 2n)^{47}Sc and ^{48}Ca(p, 3n)^{46}Sc reactions were used to determine the ^{46,47}Sc production; these values were abundance corrected for the natural abundance of ^{48}Ca (0.187%). Additionally, $CaCO_3$ is only 40.04% Ca by mass so the calculated activities were corrected to reflect this difference. The results of these calculations are illustrated in Table A.3.7.

Table A.3.7. Theoretical cross section and activities for the proton bombardment of a natural abundance calcium carbonate target at MURR

Activation Products		MURR Target (14.9 MeV)	
Nuclide	**Half-Life**	**σ (mb)**	**Activity (μCi)**
^{43}Sc	3.90 h	14.0	1291.29
^{44}Sc	3.93 h	544.4	49862.20
^{44m}Sc	2.442 d	0.8	5.33
^{46}Sc	83.81 d	0	0.00
^{47}Sc	3.349 d	1.6	7.81
^{48}Sc	43.7 h	0.3	2.67

A.3.5 Natural Abundance Molybdenum Disulfide Targets

The reaction cross sections for the proton and deuteron bombardment of natural abundance molybdenum have been reported in the literature[96,98,99]. There are seven naturally occurring isotopes of molybdenum and they all have a significant natural abundance (9.25-24.13%). For the proton irradiation, the primary reaction of interest is

^{100}Mo(p, 2n)^{99m}Tc; ^{100}Mo is only 9.63% abundant therefore an enriched target would product 10 fold the activity of ^{99m}Tc compared to the natural target. For the deuteron irradiation, the primary reaction of interest is ^{98}Mo(p, d)^{99}Mo; ^{98}Mo has the highest natural abundance (24.13%) of all the molybdenum isotopes, but an enriched target would still yield 4-fold the activity of ^{99}Mo compared to a natural target. In these studies, natural abundance molybdenum was used. With the high abundance of each isotope, several isotopes of technetium (^{94,95,95m,96,96m,99m}Tc) and molybdenum (^{93,99}Mo) are produced at the intended proton energy range from 10-16 MeV and the intended deuteron energy range from 0-8.5 MeV. For these calculations, the literature cross section data was used from Khandaker *et al*[96] for the proton irradiation and Tarkanyi *et al*[99] for the deuteron irradiation.

Though the intended proton range was from 12-16 MeV, the actual experimental range used was quite different. A 0.15 mm thick molybdenum disulfide targets was irradiated at MURR for 1 hour with a 10 μA current of protons ranging from 14.5-16 MeV. Due to the limited literature data, the cross section at 14.4 MeV was used to determine the product radionuclides and their activities for this target. MoS_2 is only 59.94% Mo by mass so the calculated activities were corrected to reflect this difference. The results of these calculations are illustrated in Table A.3.8.

Table A.3.8. Literature cross sections and calculated activities for the proton bombardment of a natural abundance molybdenum disulfide target at MURR

Activation Products		MURR Target (14.4 MeV)	
Nuclide	**Half-Life**	**σ (mb)**	**Activity (μCi)**
$^{93g+m}$**Tc**	2.73 h	3.6	233.09
^{94}**Tc**	4.88 h	32.5	1242.64
^{95}**Tc**	20.0 h	113.9	1120.34
^{95m}**Tc**	61 d	48.5	6.63
$^{96g+m}$**Tc**	4.3 d	120.4	232.73
^{99m}**Tc**	6.01 h	189.5	5960.63
^{93m}**Mo**	6.9 h	0.5	13.80
^{99}**Mo**	2.7476 d	22.6	68.24
^{96}**Nb**	23.4 h	0.5	4.21

Calculations were performed for the intended deuteron range from 0-8.5 MeV for the deuteron bombardment of a natural molybdenum target. A 0.42 mm thick molybdenum disulfide targets was irradiated at MURR for 1 hour with a 10 μA current of deuterons ranging from 0-8.5 MeV. Due to the limited literature data, the average cross section from 6.2-8.5 MeV was used to determine the product radionuclides and their activities for this target. MoS_2 is only 59.94% Mo by mass so the calculated activities were corrected to reflect this difference. The results of these calculations are illustrated in Table A.3.9.

Table A.3.9. Literature cross section and calculated activities for the deuteron bombardment of a natural abundance molybdenum disulfide target at MURR

Activation Products		MURR Target (6.2-8.5 MeV)	
Nuclide	**Half-Life**	**Average σ (mb)**	**Activity (μCi)**
$^{93g+m}$**Tc**	2.73 h	27.98	5072.66
^{94}**Tc**	4.88 h	0.37	39.61
^{94m}**Tc**	52 m	0.95	422.90
^{95}**Tc**	20.0 h	45.5	1253.13
^{96}**Tc**	4.3 d	57.95	313.64
^{96m}**Tc**	52 m	34.4	15313.26
^{99m}**Tc**	6.01 h	10.62	935.33
^{99}**Mo**	2.7476 d	50.55	427.36
^{92m}**Nb**	10.13 d	0.52	1.20
^{95}**Nb**	34.99 d	0.64	0.43
^{95m}**Nb**	3.61 d	0.07	0.45
^{96}**Nb**	23.4 h	0.64	15.10

A.4 Steady State Thermal Analysis of Irradiated Targets

ANSYS® is a software suite developed to perform computer-based engineering simulations. In this research, the software was utilized to model the steady state heat generation within the designed research targets. For each target design, an axisymmetric model was prepared using Creo Parametric 3.0® computer aided drafting software. The axisymmetric model has symmetry around center axis of the cylindrical target design (Figure A.4.1).

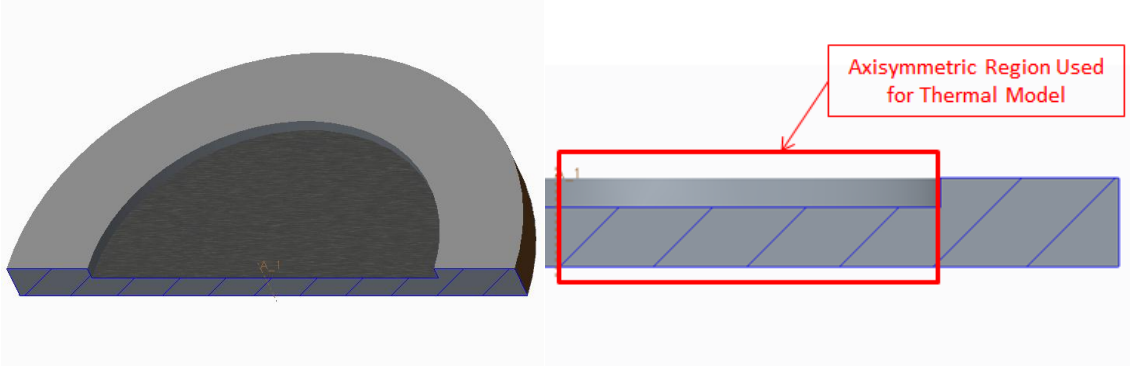

Figure A.4.1. Illustration of an axisymmetric modeled target region. (left) cross section of an example target (right) axisymmetric region used for the thermal analysis

The axisymmetric model is imported into the ANSYS software and the thermal load is applied to the system. Several important parameters must be input into the software to properly model the thermal environment inside of the charged particle beam. Firstly, the thermal conductivity for each material must be applied to each layer of the target. Next, contact between each layer must be defined. In this study, the layers are treated as though bonded together with specified thermal contact resistance of 2000 $W*m^{-2}*K^{-1}$; this represents a reduced heat transfer between the contacted layer to provide a conservative thermal model. Before the thermal load can be input into the system, a map

face meshing is applied the model to provide a defined grid to apply the load. In this research, edge sizing was applied to divide the target into 0.005" divisions (Figure A.4.2).

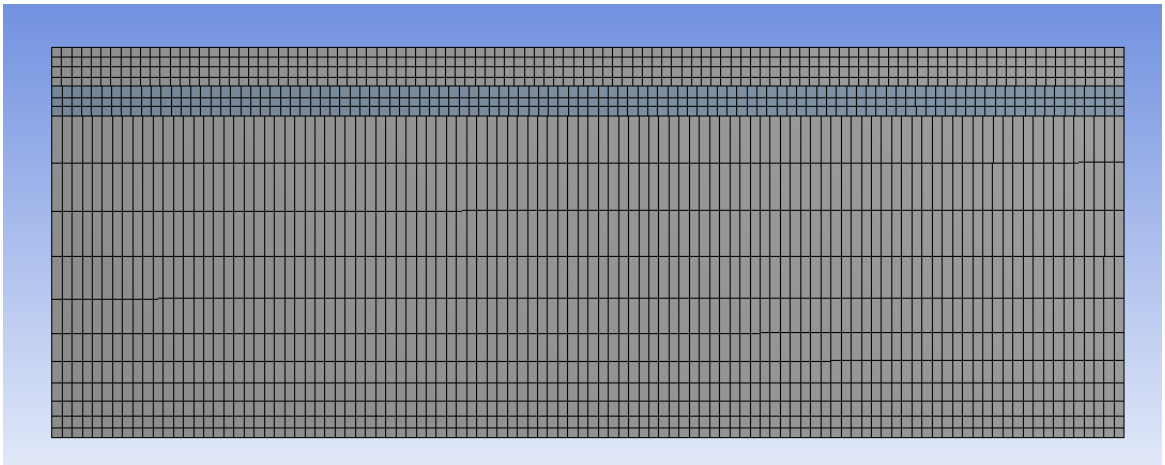

Figure A.4.2. Illustration of map faced meshing with edge sizing

A Gaussian heat generation distribution is created in excel and imported into ANSYS for each layer of the target. The highest heat generation is applied to the center of the target with no heat generation applied at the edge of the target. The initial values for heat generation are later scaled in the program to apply the correct heat load in each layer. Next, thermal convection is applied to target faces being cooled with water while thermal radiation is applied to target faces under vacuum. The forced convection heat transfer coefficient was calculated using the Nussett (Nu), Reynolds (Re), and Prandtl (Pr) Numbers by the following equations[104]:

$$Nu = \frac{h*D}{k} = 0.664 * Re^{1/2} * Pr^{1/3} \qquad \text{Equation A.4.1}$$

h is the convective heat transfer coefficient ($W*m^{-2}*K^{-1}$), which was the variable being calculated. D is the length of the convective surface (m). k is the thermal conductivity of the fluid ($W*m^{-1}*K^{-1}$).

$$Re = \frac{D*V*p}{u}$$ Equation A.4.2

V is the velocity of the fluid ($m*s^{-1}$). p is the density of the fluid ($kg*m^{3}$). u is the viscosity of the fluid ($N*s*m^{-2}$).

$$Pr = \frac{u*C_p}{k}$$ Equation A.4.3

C_p is the heat capacity of the fluid ($J*kg^{-1}*K^{-1}$).

Thermal radiation was calculated by the program using the emissivity (unitless) of radiating material. Prior to solving the system, the thermal loads must be scaled for each layer of the target. The thermal load (P, watts) is calculated using the energy deposition for each layer (ΔE, MeV) that was calculated using SRIM and the current of the charged particle beam (I, μA), by the following equation[105]:

$$P = I * \Delta E$$ Equation A.4.4

For the targets at MURR and UW, it is assumed that 100% of the beam current will be on the target. For the BNL target, it is assumed that 60% of the beam current will be on the target; this is due to the large beam profile available at BLIP. Once the thermal load is scaled, the system solves the temperature of the whole target and the temperature for each layer within the target.

A.4.1 Osmium Metal Target at MURR

Steady state thermal analysis was performed for a 0.010" thick osmium metal pressed pellet in an aluminum backing with an epoxied aluminum front window. The experimental conditions used for this calculation are illustrated in Table A.4.1.

Table A.4.1. Experimental conditions used for steady state thermal analysis of an osmium metal target

Target Density:	22.59	$g*cm^{-3}$	**Target Radius:**	0.256	inches	
Thermal Conductivity:	88	$W*m^{-1}*K^{-1}$	**Mesh Divisions:**	51	total	
Thermal Contact Resistance:	2000	$W*m^{-2}*K^{-1}$	**Beam Current:**	10	uA	Proton

	Thickness	**ΔE**	**Power Deposited**	**Target Depth of Gaussian Distribution**			**Convection / *Radiation***
Layers	**(inches)**	**(MeV)**	**(Watts)**	**(inches)**			**($W*m^{-2}*K^{-1}$) *(unitless)***
Aluminum	0.001	0.1	1	0.031	0.030		0.09 (rad)
Osmium	0.010	7.9	79	0.030	0.025	0.020	
Aluminum	0.020	6.7	67	0.020	0.010	0.000	2152 (conv)

Analysis shows the maximum achievable temperature for the osmium pellet and the aluminum housing were found to be 418° C and 415° C, respectively. These values are below the respective melting points of each material. Increasing the beam current could lead to target failure by melting the front aluminum foil.

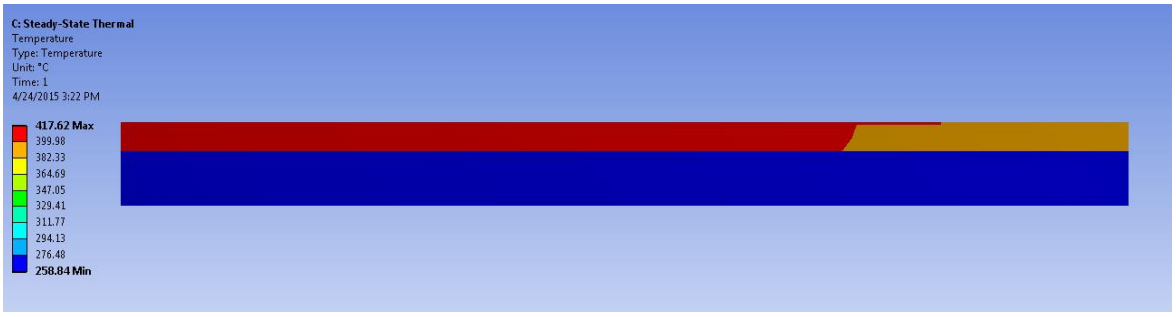

Figure A.4.3. Steady state thermal analysis of osmium metal target irradiated at MURR

A.4.2 Osmium Disulfide Target at MURR

Steady state thermal analysis was performed for a 0.020" thick osmium disulfide pressed pellet in an aluminum backing with an epoxied aluminum front window. The experimental conditions used for this calculation are illustrated in Table A.4.2.

Table A.4.2. Experimental conditions used for steady state thermal analysis of an osmium disulfide target

Target Density:	9.47	$g*cm^{-3}$	**Target Radius:**	0.256	inches	
Thermal Conductivity:	0.75	$W*m^{-1}*K^{-1}$	**Mesh Divisions:**	51	total	
Thermal Contact Resistance:	2000	$W*m^{-2}*K^{-1}$	**Beam Current:**	10	uA	Proton

	Thickness	**ΔE**	**Power Deposited**	**Target Depth of Gaussian Distribution**			**Convection / *Radiation***
Layers	**(inches)**	**(MeV)**	**(Watts)**	**(inches)**			**($W*m^{-2}*K^{-1}$) *(unitless)***
Aluminum	0.001	0.1	1	0.041	0.040		0.09 (rad)
OsS_2	0.020	8.5	85	0.040	0.030	0.020	
Aluminum	0.020	7.6	76	0.020	0.010	0.000	2152 (conv)

Analysis shows the maximum achievable temperature for the osmium disulfide pellet and the aluminum housing were found to be 586° C and 573° C, respectively. The elevated temperature at the center of the OsS_2 target material could lead the target to sublime creating issues during irradiation.

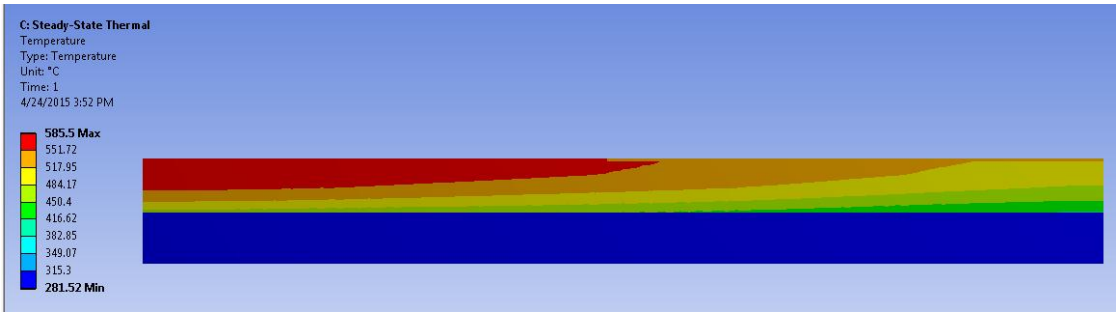

Figure A.4.4. Steady state thermal analysis of osmium disulfide target irradiated at MURR

A.4.3 Osmium Metal Target at BNL

Steady state thermal analysis was performed for a 0.020" thick osmium metal disc sealed in a bolted aluminum can. The experimental conditions used for this calculation are illustrated in Table A.4.3.

Table A.4.3. Experimental conditions used for steady state thermal analysis of an osmium metal target

Target Density:	22.59	$g*cm^{-3}$	**Target Radius:**	0.5	inches	
Thermal Conductivity:	88	$W*m^{-1}*K^{-1}$	**Mesh Divisions:**	100	total	
Thermal Contact Resistance:	2000	$W*m^{-2}*K^{-1}$	**Beam Current:**	30	uA	Proton

	Thickness	**ΔE**	**Power Deposited**	**Target Depth of Gaussian Distribution**			**Convection**
Layers	**(inches)**	**(MeV)**	**(Watts)**	**(inches)**			**($W*m^{-2}*K^{-1}$)**
Aluminum	0.020	2.2	40	0.200	0.190	0.180	7054 (conv)
Osmium	0.020	12.7	229	0.180	0.170	0.160	
Aluminum	0.160	11.4	205	0.160	0.080	0.000	5177 (conv)

Analysis shows the maximum achievable temperature for the osmium disc and the aluminum can were found to be 408° C and 224° C, respectively. These values are well below the respective melting points.

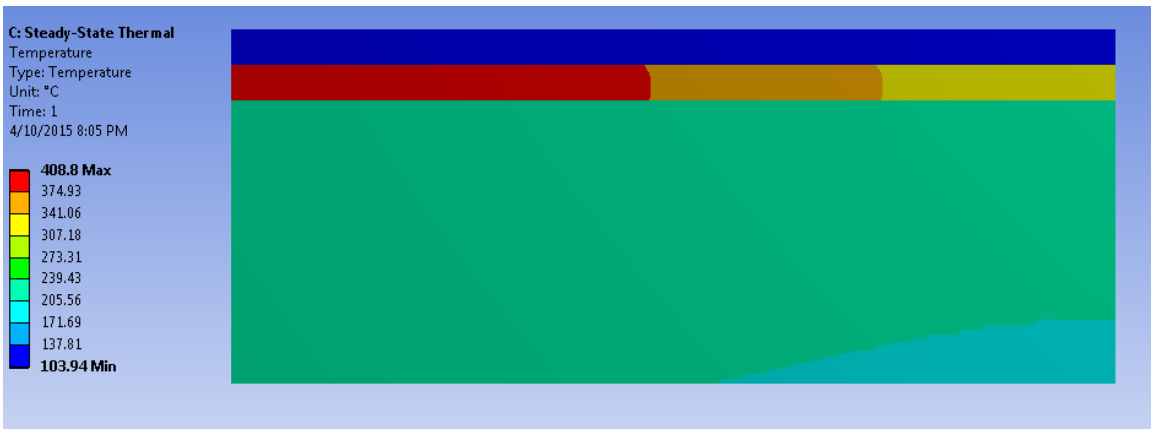

Figure A.4.5. Steady state thermal analysis of osmium metal target irradiated at BNL

A.4.4 Tungsten Metal Target at MURR

Steady state thermal analysis was performed for a 0.010" thick tungsten metal pressed pellet in an aluminum backing with an epoxied aluminum front window. The experimental conditions used for this calculation are illustrated in Table A.4.4.

Table A.4.4. Experimental conditions used for steady state thermal analysis of a tungsten metal target

Target Density:	19.3	$g*cm^{-3}$	**Target Radius:**	0.256	inches	
Thermal Conductivity:	173	$W*m^{-1}*K^{-1}$	**Mesh Divisions:**	51	total	
Thermal Contact Resistance:	2000	$W*m^{-2}*K^{-1}$	**Beam Current:**	10	uA	Proton

	Thickness	**ΔE**	**Power Deposited**	**Target Depth of Gaussian Distribution**			**Convection / *Radiation***
Layers	**(inches)**	**(MeV)**	**(Watts)**	**(inches)**			**($W*m^{-2}*K^{-1}$) *(unitless)***
Aluminum	0.001	0.1	1	0.031	0.030		0.09 (rad)
Tungsten	0.010	7.2	72	0.030	0.025	0.020	
Aluminum	0.020	6.0	60	0.020	0.010	0.000	2152 (conv)

Analysis shows the maximum achievable temperature for the tungsten pressed pellet and the aluminum housing were found to be 376° C and 375° C, respectively. These values are well below the respective melting points.

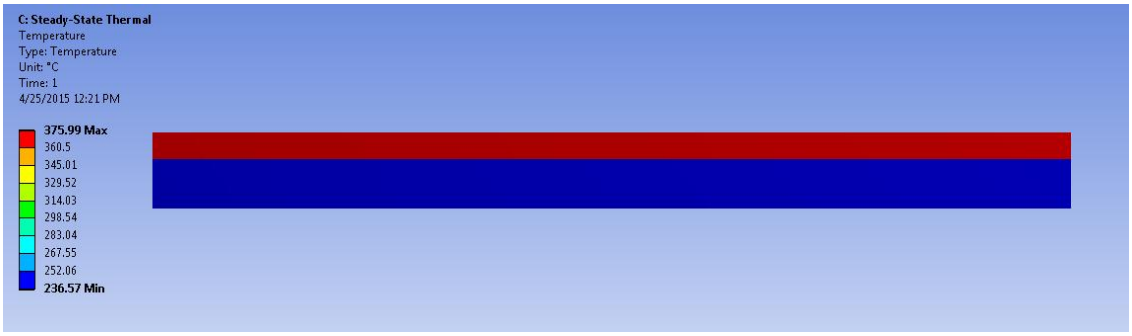

Figure A.4.6. Steady state thermal analysis of tungsten metal target irradiated at MURR

A.4.5 Tungsten Disulfide Target at MURR

Steady state thermal analysis was performed for a 0.020" thick tungsten disulfide pressed pellet in an aluminum backing with an epoxied aluminum front window. The experimental conditions used for this calculation are illustrated in Table A.4.5.

Table A.4.5. Experimental conditions used for steady state thermal analysis of a tungsten disulfide target

Target Density:	7.5	$g*cm^{-3}$	**Target Radius:**	0.256	inches	
Thermal Conductivity:	0.8	$W*m^{-1}*K^{-1}$	**Mesh Divisions:**	51	total	
Thermal Contact Resistance:	2000	$W*m^{-2}*K^{-1}$	**Beam Current:**	10	uA	Proton

	Thickness	**ΔE**	**Power Deposited**	**Target Depth of Gaussian Distribution**			**Convection / *Radiation***
Layers	**(inches)**	**(MeV)**	**(Watts)**	**(inches)**			**($W*m^{-2}*K^{-1}$) *(unitless)***
Aluminum	0.001	0.1	1	0.041	0.040		0.09 (rad)
WS_2	0.020	7.8	78	0.040	0.030	0.020	
Aluminum	0.020	6.5	65	0.020	0.010	0.000	2152 (conv)

Analysis shows the maximum achievable temperature for the tungsten foil and the aluminum housing were found to be 526° C and 515° C, respectively. The elevated temperature of the aluminum could lead the front foil to soften at the hottest portion of the beam.

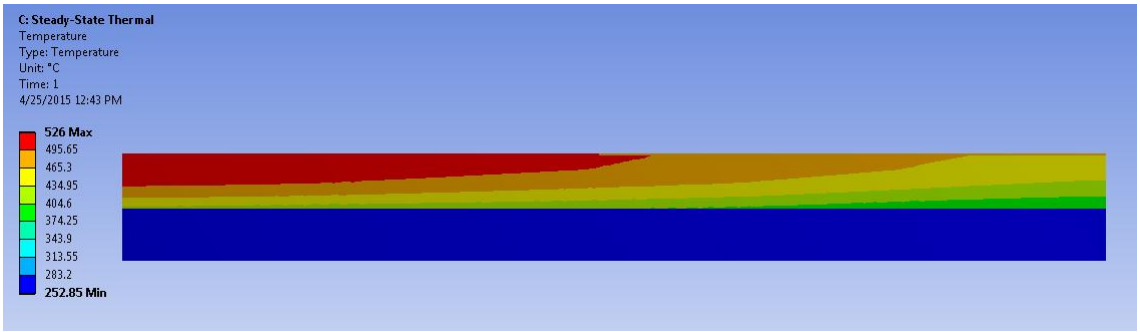

Figure A.4.7. Steady state thermal analysis of tungsten disulfide target irradiated at MURR

A.4.6 Tungsten Metal Target at BNL

Steady state thermal analysis was performed for a 0.002" thick tungsten metal foil sealed in a bolted aluminum can. The experimental conditions used for this calculation are illustrated in Table A.4.6.

Table A.4.6. Experimental conditions used for steady state thermal analysis of a tungsten metal target

Target Density:	19.3	$g*cm^{-3}$	**Target Radius:**	0.5	inches	
Thermal Conductivity:	173	$W*m^{-1}*K^{-1}$	**Mesh Divisions:**	100	total	
Thermal Contact Resistance:	2000	$W*m^{-2}*K^{-1}$	**Beam Current:**	115	uA	Proton

	Thickness	**ΔE**	**Power Deposited**	**Target Depth of Gaussian Distribution**			**Convection**
Layers	**(inches)**	**(MeV)**	**(Watts)**	**(inches)**			**($W*m^{-2}*K^{-1}$)**
Aluminum	0.020	5.4	373	0.031	0.030		5000 (conv)
Tungsten	0.002	2.8	193	0.030	0.025	0.020	
Aluminum	0.178	1.6	110	0.020	0.010	0.000	5000 (conv)

Analysis shows the maximum achievable temperature for the tungsten foil and the aluminum can were found to be 316° C and 228° C, respectively. These values are well below the respective melting points.

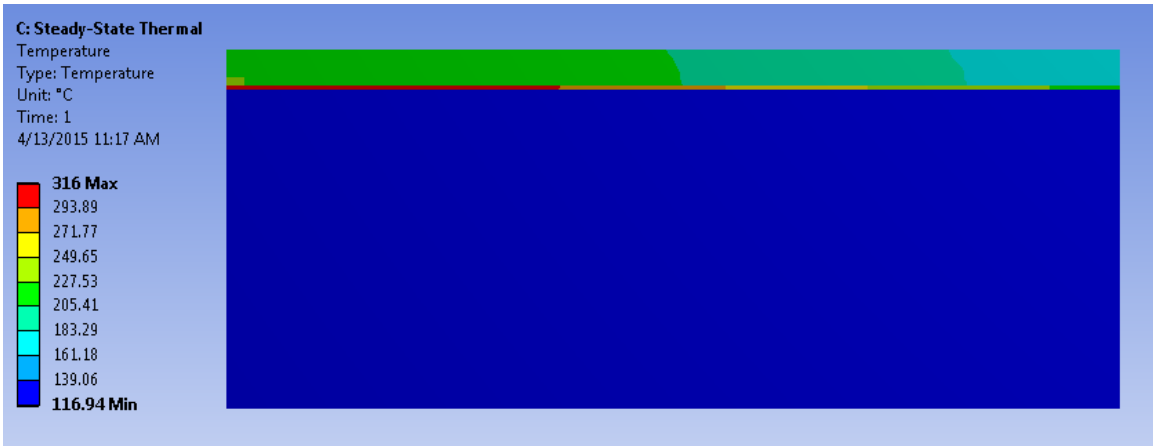

Figure A.4.8. Steady state thermal analysis of tungsten metal target irradiated at BNL

A.4.7 Germanium Metal Target at UW

Steady state thermal analysis was performed for a 0.010" thick germanium metal pressed pellet in an aluminum backing. The experimental conditions used for this calculation are illustrated in Table A.4.7.

Table A.4.7. Experimental conditions used for steady state thermal analysis of a germanium metal target

Target Density:	5.35	$g*cm^{-3}$	**Target Radius:**	0.49	inches	
Thermal Conductivity:	60.2	$W*m^{-1}*K^{-1}$	**Mesh Divisions:**	98	total	
Thermal Contact Resistance:	2000	$W*m^{-2}*K^{-1}$	**Beam Current:**	20	uA	Alpha

	Thickness	**ΔE**	**Power Deposited**	**Target Depth of Gaussian Distribution**			**Convection / *Radiation***
Layers	**(inches)**	**(MeV)**	**(Watts)**	**(inches)**			**($W*m^{-2}*K^{-1}$) *(unitless)***
Germanium	0.010	20.0	400	0.070	0.065	0.060	0.26 (rad)
Aluminum	0.060	8.0	160	0.060	0.030	0.000	3657 (conv)

Analysis shows the maximum achievable temperature for the germanium metal pressed pellet and the aluminum backing were found to be 876° C and 353° C, respectively; these irradiation parameters approach the melting point of the germanium metal target. Increasing the current too much beyond this point could result in the target melting.

Figure A.4.9. Steady state thermal analysis of germanium metal target irradiated at UW

A.4.8 Calcium Carbonate Target at MURR

Steady state thermal analysis was performed for a 0.020" thick calcium carbonate pressed pellet in an aluminum backing with an epoxied aluminum front window. The experimental conditions used for this calculation are illustrated in Table A.4.9.

Table A.4.8. Experimental conditions used for steady state thermal analysis of a calcium carbonate target

Target Density:	2.93	$g*cm^{-3}$	**Target Radius:**	0.256	inches	
Thermal Conductivity:	4.65	$W*m^{-1}*K^{-1}$	**Mesh Divisions:**	51	total	
Thermal Contact Resistance:	2000	$W*m^{-2}*K^{-1}$	**Beam Current:**	10	uA	Proton

	Thickness	**ΔE**	**Power Deposited**	**Target Depth of Gaussian Distribution**			**Convection / *Radiation***
Layers	**(inches)**	**(MeV)**	**(Watts)**	**(inches)**			**($W*m^{-2}*K^{-1}$) *(unitless)***
Aluminum	0.001	0.1	1	0.041	0.040		0.09 (rad)
$CaCO_3$	0.020	3.8	38	0.040	0.030	0.020	
Aluminum	0.020	4.3	43	0.020	0.010	0.000	2152 (conv)

Analysis shows the maximum achievable temperature for the calcium carbonate pressed pellet and the aluminum housing were found to be 249° C and 246° C, respectively. These values are well below the respective melting points.

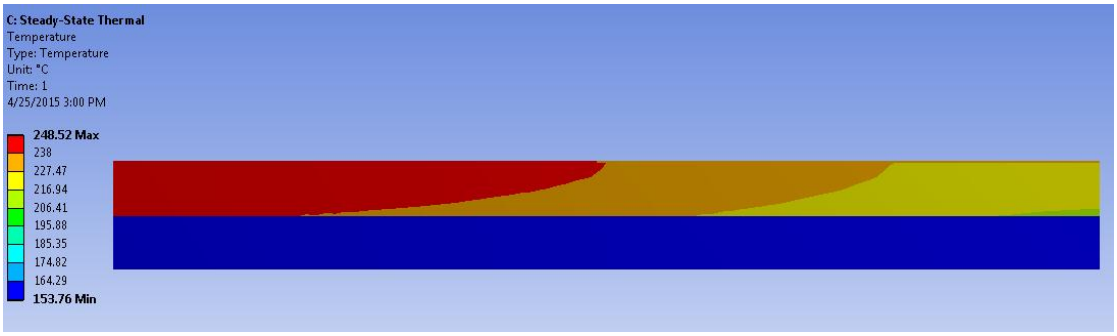

Figure A.4.10. Steady state thermal analysis of calcium carbonate target irradiated at MURR

A.4.9 Molybdenum Disulfide Target at MURR (Proton Bombardment)

Steady state thermal analysis was performed for a 0.020" thick molybdenum disulfide pressed pellet in an aluminum backing with an epoxied aluminum front window. The experimental conditions used for this calculation are illustrated in Table A.4.10.

Table A.4.9. Experimental conditions used for steady state thermal analysis of a molybdenum disulfide target

Target Density:	5.06	$g*cm^{-3}$	**Target Radius:**	0.256	inches	
Thermal Conductivity:	0.75	$W*m^{-1}*K^{-1}$	**Mesh Divisions:**	51	total	
Thermal Contact Resistance:	2000	$W*m^{-2}*K^{-1}$	**Beam Current:**	10	uA	Proton

	Thickness	**ΔE**	**Power Deposited**	**Target Depth of Gaussian Distribution**			**Convection / *Radiation***
Layers	**(inches)**	**(MeV)**	**(Watts)**	**(inches)**			**($W*m^{-2}*K^{-1}$) *(unitless)***
Aluminum	0.001	0.1	1	0.041	0.040		0.09 (rad)
MoS_2	0.020	5.5	55	0.040	0.030	0.020	
Aluminum	0.020	4.9	49	0.020	0.010	0.000	2152 (conv)

Analysis shows the maximum achievable temperature for the molybdenum disulfide pressed pellet and the aluminum housing were found to be 390° C and 382° C, respectively. These values are well below the respective melting points.

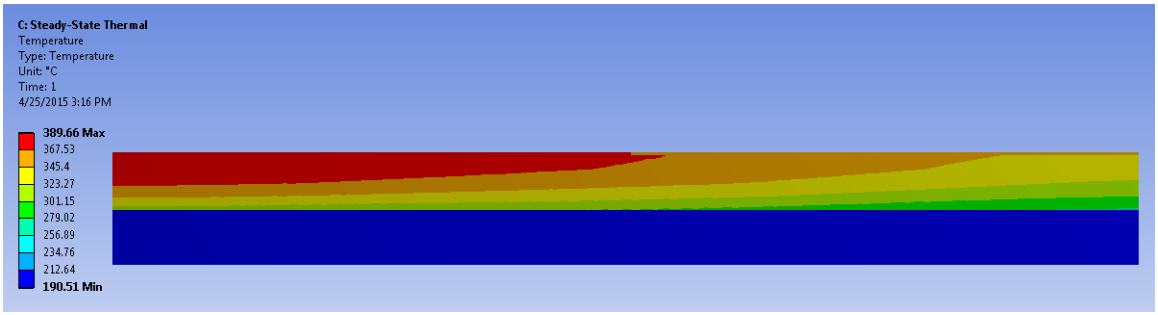

Figure A.4.11. Steady state thermal analysis of molybdenum disulfide target irradiated at MURR

A.4.10 Molybdenum Disulfide Target at MURR (Deuteron Bombardment)

Steady state thermal analysis was performed for a 0.010" thick molybdenum disulfide pressed pellet in an aluminum backing with an epoxied aluminum front window. The experimental conditions used for this calculation are illustrated in Table A.4.11.

Table A.4.10. Experimental conditions used for steady state thermal analysis of a molybdenum disulfide target

Target Density:	5.06	$g*cm^{-3}$	**Target Radius:**	0.256	inches	
Thermal Conductivity:	0.75	$W*m^{-1}*K^{-1}$	**Mesh Divisions:**	51	total	
Thermal Contact Resistance:	2000	$W*m^{-2}*K^{-1}$	**Beam Current:**	10	uA	Deuteron

	Thickness	**ΔE**	**Power Deposited**	**Target Depth of Gaussian Distribution**			**Convection / *Radiation***
Layers	**(inches)**	**(MeV)**	**(Watts)**	**(inches)**			**($W*m^{-2}*K^{-1}$) *(unitless)***
Aluminum	0.001	0.3	3	0.031	0.030		0.09 (rad)
MoS_2	0.010	4.9	49	0.030	0.025	0.020	
Aluminum	0.020	3.3	33	0.020	0.010	0.000	2152 (conv)

Analysis shows the maximum achievable temperature for the molybdenum disulfide pressed pellet and the aluminum housing were found to be 311° C and 309° C, respectively. These values are well below the respective melting points.

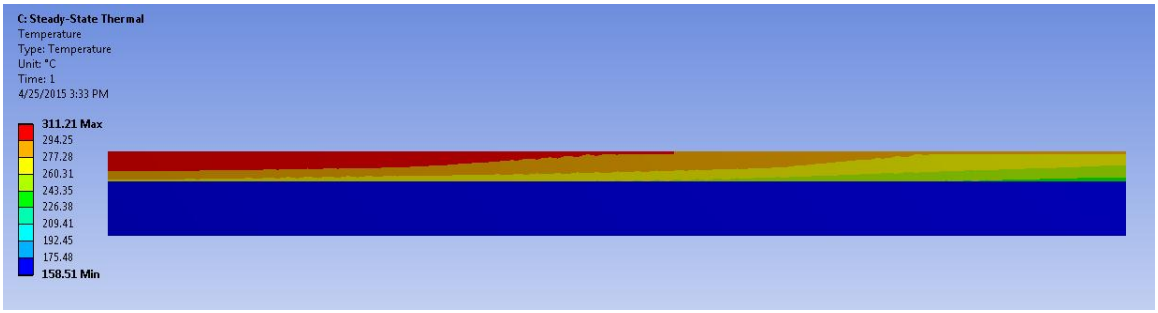

Figure A.4.12. Steady state thermal analysis of molybdenum disulfide target irradiated at MURR

Appendix B: Considerations in the Target Assembly Design

Lessons Learned through Experimentation using the MURR Cyclotron

B.1 Determination of Target Assembly Materials

In initial studies, the choice of target backing material was driven by the need for a high melting point material; experiments were attempting to sinter tungsten trioxide (MP: 1473° C) at 1100° C prior to irradiation. A titanium metal alloy (grade 5 titanium) was chosen for its high melting point, compression strength, and corrosion resistance. The backings served the purpose of high temperature studies well, but issues arose with proton irradiation. The primary isotope of natural titanium is ^{48}Ti (73.72 % abundance). Proton bombardment resulted in significant activation of the titanium backing via the ^{48}Ti(p, n)^{48}V reaction pathway. Vanadium-48 is a positron-emitter (Mean β^+ = 290 keV, 49.9% abundance) with several high energy, high intensity gamma emissions (983.5 kev, 99.98%; 1312 keV, 98.2%) that create a dose issue and necessitate thick shielding. Due to this outcome, target development with titanium was ceased and studies were adapted to use more customary target assembly materials.

Aluminum was the primary metal used for these studies. Aluminum (grade 6061) is widely available, easily machined, and produces few activation products. The primary concern with using aluminum is its lower melting point (MP: 660° C). With the cooling capabilities of the cyclotron at MURR, current must be restricted to prevent target overheating, potentially leading to melting the target assembly. In this research, current

was typically 10 μA and did not cause concern for melting the target assembly. At the proton energy used in these studies, aluminum will not produce any activation products with substantial half-lives. Any dose from the backing results from the activation of the trace metals in the aluminum alloy.

B.2 Design of the Target Assembly

The MURR cyclotron has a solid-state target port (Figure B.2.1). The port is designed to accommodate small, circular targets (**A**) with a diameter of 0.75" (19.05 mm) and a thickness of 1-4 mm. The target holder (**B**) screws together to hold the target body in position. An O-ring is compressed against the back side of the target body to form a water tight seal to prevent the leak of cooling water. Position (**C**) is the proton beam inlet. It is possible to put degraders or foils into the beam line prior to reaching the target (**D**). There are inlet and outlet ports (**E**) to either pull vacuum or flow helium gas over the front of the target. The target holder is placed into the assembly at position (**F**). The piston (**I**) pushes the water cooling assembly in place behind the target holder. Water is flowed over the back of the target (**G**) from the inlet and outlet ports (**H**).

Figure B.2.1. Solid-state target port for MURR GE PETtrace Cyclotron

The design used to produce targets at MURR is a basic disc design with a well bored into the center for the target (Figure B.2.2). The 13.1 mm diameter for the well was chosen from the commercial availability of 13 mm diameter pressed pellet dies. Initially, the design utilized a thinner target (1.5 mm) with a shallower well (0.5mm); the purpose of this initial design was prepared with the intention to having the pressed target flush with the side walls of the backing. With the flush target design, the front foil could be laid directly on top of the target without the need to press foil into the well. The design was changed due to the difficulty of making the target flush with the backing and the thicker 1 mm portion behind the target would not disperse heat as well.

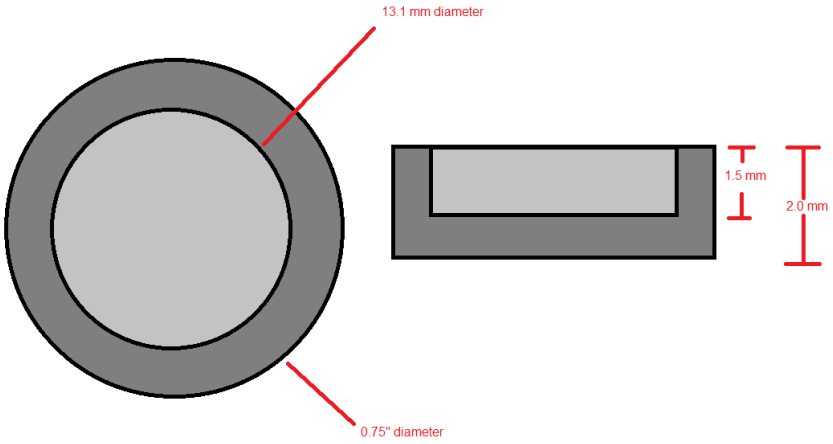

Figure B.2.2. Target specifications used to produce targets at MURR

B.3 Failed Target (Case Study #1)

A target of $^{nat}OsS_2$ was irradiated for 30 minutes with a 20µA current of 16 MeV protons. Using a hydraulic press, the OsS_2 was directly pressed into the aluminum metal backing. The target was then covered with a 75 µm thick Kapton foil which was sealed using Araldite2011 epoxy adhesive (Figure B.3.1). Kapton foil is a polyimide foil that was chosen for its compositions and relatively high melting point (500° C). Being composed of C, N, and H, the Kapton foil would present minimal dose issues upon irradiation.

Figure B.3.1. (Left) empty aluminum backing (Middle) OsS_2 pressed into aluminum backing (Right) Target coated with Kapton foil epoxyed to the surface

Two issues occurred during this irradiation. First, a hole was burned through the Kapton foil by the proton beam, even though we had previously tested the foil without issue. Secondly, the O-ring on the back side of the target was not properly sealed and cooling water was allowed to come into contact with the target face causing a loss of materials.

Figure B.3.2. OsS_2 target with burnt foil and wet target material

The most likely cause of the foil burn-up was the inability of the foil to dissipate heat. When the foil tested was initially tested in beam, it was mounted on a solid aluminum backing, which gave it a pathway to dissipate heat and thus the foil survived a 20 μA current for 1 hour. Kapton foil is quite rigid and was not able to be pressed down into the well and directly contact the target material. The actual target had a gap between the

target material and the foil, giving the foil no means to dissipate heat and it was burned up by the proton beam. To mediate this issue, the Kapton foil was replaced by aluminum foil. The aluminum foil is more malleable and able to be pressed into well to contact the target material.

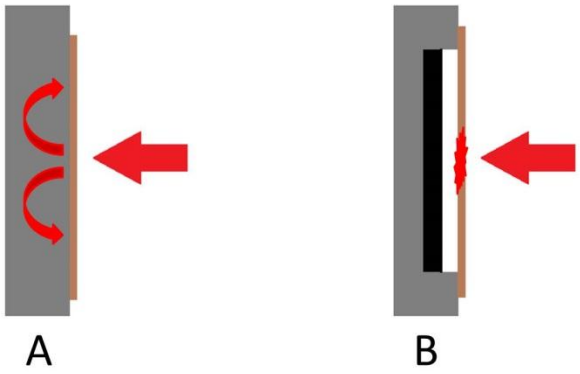

Figure B.3.3. (A) Represents the kapton foil being able to dissipate heat through the aluminum backing. (B) Represents the OsS_2 target which was not able to dissipate heat and burned through

The solid-state target port design required the target to be screwed together to compress the O-ring against the target backing. It is possible that as it was being screwed into place that the target shifted slightly causing a loose seal with O-ring. To account for this issue, a new solid-state target port was designed that hydraulically presses the target holder in place reducing the chance of the target slipping off the O-ring.

B.4 Failed Targets (Case Study #2)

Several targets failed in a similar manner. The front foils appear to have puffed up and blew small hole in the foil to release pressure. The mechanism of this failure was unclear as several possibilities existed could have accounted for this release of pressure. Initially, it was believed that issue was moisture trapped in the target material. Upon irradiation, the intense heat would cause the water to evaporate and steam would create the necessary pressure to blow a hole in the foil. To resolve this issue, the target materials were dried in an oven overnight before preparing the target to minimize the amount of water present in the target; this resolution was not enough to fix the issue.

The foil puffing continued to be an inconsistent issue until a correlation was noted. The foil was more likely to puff with targets that were pressed in the pressed pellet die and transferred to the aluminum backing than for targets pressed directly into the backing. It was speculated that this could be a contributing issue. The 13 mm pellet die produced targets that were just slightly smaller than 13 mm in diameter and the well within the backing was 13.1 mm; this leaves a small gap between the side of the pellet and the well, which would be filled with air. Upon irradiating, this air would get heated and expand, leading the front foil to puff and puncture. To mitigate this issue, studies will focus on targets pressed directly into the backing.

B.5 Conclusion

There are many considerations that need to be considered when irradiating a target in the intense environment present in a proton beam. Several lessons were learned experimentally during the course of this research. In addition to ensuring the physical properties are suitable for cyclotron irradiations, it is very important to thoroughly check all the possible isotopes that could be produced during an irradiation including the target assembly not just the target. The thermal load deposited in the target and target assembly generates an intense amount of heat. Proper cooling of all layers of the target are necessary as complications can arise during irradiation.

Appendix C: Data from Batch Studies

Table C.1 Rhenium Contact Kinetics Study on AG 1-X8 Resin

Time (seconds)	Distribution Coefficient	Standard Deviation
15	856	170
20	3646	423
25	4897	963
30	6294	62.9
60	6294	62.9
120	6294	62.9
200	6294	62.9
300	6294	62.9

Table C.2 Rhenium Isothermal Kinetics Study on AG 1-X8 Resin

	20°C		40°C		60°C	
Time (seconds)	**Initial Counts**	**Final Counts**	**Initial Counts**	**Final Counts**	**Initial Counts**	**Final Counts**
10	19517	6255	60090	5566	77553	3922
15	14316	2516	14130	312	14030	121
20	20859	1285	13759	130	13593	98
25	19091	812	14043	98	13658	98
30	14316	343	14127	98	13906	98

Table C.3 Rhenium Adsorption Behavior on AG 1-X8 in Aqueous Media

Media	Distribution Coefficient	Standard Deviation
10 M NaOH	8059	1773
5 M NaOH	9077	1279
1 M NaOH	9324	1107
0.5 M NaOH	10146	101
0.1 M NaOH	10146	101
0.01 M NaOH	10146	101
DI H_20	10146	101
0.01 M HNO_3	10146	101
0.025 M HNO_3	10146	101
0.05 M HNO_3	4564	692
0.1 M HNO_3	1519	143
0.5 M HNO_3	194	10
1 M HNO_3	80	2
2.5 M HNO_3	22	1
5 M HNO_3	6	1
10 M HNO_3	3	1

Table C.4 Rhenium Adsorption Behavior on AG 1-X8 with Varied Tungsten Concentrations

Ionic Strength (molarity)	Distribution Coefficient	Standard Deviation
1.00	9326	1201
1.09	5471	1144
1.22	4616	927
1.44	3732	787
1.66	2896	158
1.88	2883	546

Table C.5 Tungsten Adsorption Behavior on AG 1-X8 in Aqueous Media

NaOH (Molarity)	Distribution Coefficient	Standard Deviation
10	5	1.5
5	7	0.3
1	37	0.7
0.5	54	0.5
0.1	59	0.5
0.01	64	0.5

Table C.6 Rhenium and Tungsten Adsorption Behavior on TEVA in Aqueous Media

Media	Distribution Coefficient	Standard Deviation
5 M NaOH	6810	68.1
1 M NaOH	6810	68.1
0.5 M NaOH	6810	68.1
0.1 M NaOH	6810	68.1
0.05 M NaOH	6810	68.1
DI H2O	6810	68.1
0.05 M HNO3	6810	68.1
0.1 M HNO3	6810	68.1
0.5 M HNO3	991	141.9
1 M HNO3	325	6.67
5 M HNO3	7.05	1.4

Table C.7 Rhenium Contact Kinetics Study on AnaLig

Time (seconds)	Distribution Coefficient	Standard Deviation
15	26	0.5
30	31	0.9
45	34	1.3
60	35	0.5
120	35	0.1

Table C.8 Rhenium Isothermal Kinetics Study on AnaLig

Temperature (Celsius)	Distribution Coefficient	Standard Deviation
30	28	2
40	24	2
50	19	3
60	23	2
70	29	1

Table C.9 Rhenium and Tungsten Absorption Behavior on AnaLig in Aqueous Media

	Rhenium		Tungsten	
NaOH (molarity)	Distribution Coefficient	Standard Deviation	Distribution Coefficient	Standard Deviation
0.1	40	0.3	-	-
0.5	80	1.6	-	-
1	98	6	0.36	0.02
2.5	159	23	0.45	0.03
5	94	15	0.37	0.84
10	34	3	1.04	0.03

Table C.10 Arsenate Adsorption Behavior on AG 1-X8 in Aqueous Media

Solution pH	Distribution Coefficient	Standard Deviation
-1	0.1	0.1
0	1	0.1
1	1	0.0
2	9	0.0
3	403	39.9
4	3021	61.5
5	2668	70.6
6	3313	437.2
7	2965	81.9

Table C.11 Selenate Adsorption Behavior on AG 1-X8 in Aqueous Media

Solution pH	Distribution Coefficient	Standard Deviation
-1	0.3	0.3
0	1	0.1
1	14	0.2
2	3569	36
3	3569	36
4	3569	36
5	3569	36
6	3569	36
7	3569	36

Table C.12 Selenite Adsorption Behavior on AG 1-X8 in Aqueous Media

Solution pH	Distribution Coefficient	Standard Deviation
-1	0.7	0.08
0	1.0	0.11
1	1.2	0.08
2	5.2	0.47
3	144.6	3.76
4	405.2	6.17
5	353.62	6.70
6	480.51	9.56
7	406.04	14.09

Table C.13 Arsenic Adsorption Behavior on Alumina in Various Media

Solution pH	Distribution Coefficient	Standard Deviation
1	32.05	0.90
3	55.75	0.90
5	87.98	0.76
7	104.70	0.43
9	163.63	3.47
11	38.13	4.21
13	7.78	0.17
MeOH	338.1	22.1

Table C.14 Arsenic Adsorption Behavior on Silica in Various Media

Solution pH	Distribution Coefficient	Standard Deviation
1	-4.46	3.84
3	-1.99	2.72
5	-0.55	0.22
7	0.27	0.07
9	0.04	0.17
11	-0.24	0.04
13	-0.18	0.28
MeOH	30.5	19.8

Table C.15 Arsenic Adsorption Behavior on HZO in Various Media

Solution pH	Distribution Coefficient	Standard Deviation
1	142.38	3.26
3	276.07	8.49
5	452.03	6.41
7	351.21	14.48
9	223.72	14.13
11	39.10	1.36
13	14.36	0.18
MeOH	1805	397

Table C.16 Arsenic Adsorption Behavior on AG 1-X8 in Various Media

Solution pH	Distribution Coefficient	Standard Deviation
1	4	0
3	36	3
5	318	7
7	156	2
9	5098	51
11	5098	51
13	949	8
MeOH	42	1

Table C.17 Germanium Adsorption Behavior on Alumina in Various Media

Solution pH	Distribution Coefficient	Standard Deviation
1	16.30	0.64
3	85.93	7.40
5	208.90	7.82
7	185.67	1.78
9	292.92	7.49
11	337.33	10.54
13	53.24	1.27
MeOH	156.05	8.40

Table C.18 Germanium Adsorption Behavior on Silica in Various Media

Solution pH	Distribution Coefficient	Standard Deviation
1	3.33	0.29
3	10.25	0.51
5	3.06	0.14
7	3.43	0.35
9	6.14	0.98
11	7.56	0.32
13	3.41	0.09
MeOH	2512.26	210.56

Table C.19 Germanium Adsorption Behavior on HZO in Various Media

Solution pH	Distribution Coefficient	Standard Deviation
1	26.07	3.29
3	188.35	24.10
5	467.12	20.78
7	602.75	10.85
9	681.41	22.44
11	429.37	18.14
13	146.52	5.24
MeOH	92.80	14.39

Table C.20 Germanium Adsorption Behavior on AG 1-X8 in Various Media

Solution pH	Distribution Coefficient	Standard Deviation
1	0.49	0.23
3	0.28	0.11
5	-0.71	2.81
7	0.41	0.18
9	43.63	1.15
11	52.84	1.01
13	24.62	0.61

Table C.21 Arsenic Contact Kinetics Study on HZO

Time (seconds)	Distribution Coefficient	Standard Deviation
15	460	4
30	1584	171
45	1723	191
60	2391	395
90	2304	178
120	2422	290

Table C.22 Germanium Contact Kinetics Study on Silica

Time (seconds)	Distribution Coefficient	Standard Deviation
15	144	20
30	157	8
45	193	14
60	123	4
90	153	11
120	196	15

Appendix D: Data from Column Chromatography Studies

Table D.1 Separation of Rhenium and Tungsten on a 4 mL AG 1-X8 Column

Fraction	Media	Volume	*Re-181*	*W-187*
		mL	*µCi*	*µCi*
Load 1	1 M NaOH	10	0.0	21.7
Load 2	1 M NaOH	10	0.0	46.3
Load 3	1 M NaOH	10	0.8	53.7
Wash 1	H_2O	10	0.0	31.5
Wash 2	H_2O	10	0.2	5.7
Elute 1	6 M HNO_3	5	0.0	1.1
Elute 2	6 M HNO_3	5	1.0	0.2
Elute 3	6 M HNO_3	5	10.1	0.0
Elute 4	6 M HNO_3	5	13.8	0.0
Stock	1 M NaOH	30	32.2	173.0

Table D.2 Separation of Rhenium and Tungsten on a 2 mL AG 1-X8 Column

Fraction	Media	Volume	13-Apr-15		14-Apr-15		15-Apr-15	
			Re-181	W-187	Re-181	W-187	Re-181	W-187
		mL	*µCi*	*µCi*	*µCi*	*µCi*	*µCi*	*µCi*
Load 1	1 M NaOH	10	0.0	93.4	0.0	87.7	0.0	52.9
Load 2	1 M NaOH	10	0.0	129.0	0.0	145.1	0.0	129.2
Load 3	1 M NaOH	10	0.0	135.8	0.0	136.7	0.0	144.4
Wash 1	H_2O	10	0.0	45.1	0.0	52.9	0.0	51.4
Wash 2	H_2O	10	0.0	0.0	0.0	0.2	0.0	0.0
Elute 1	6 M HNO_3	5	19.4	0.0	22.9	0.0	21.1	0.0
Elute 2	6 M HNO_3	5	98.9	0.0	109.7	0.0	103.8	0.0
Elute 3	6 M HNO_3	5	71.8	0.0	70.1	0.0	72.0	0.0
Elute 4	6 M HNO_3	5	24.6	0.0	16.3	0.0	20.8	0.0
Stock	1 M NaOH	30	247.5	407.4	225.2	455.4	217.7	445.9

Table D.3 Separation of Rhenium and Tungsten on a 0.5 g AnaLig Column with H_2O Eluent

Fraction	Media	Volume	8-Nov-12		29-Nov-12	
			W-188	Re-188	W-188	Re-188
		mL	*µCi*	*µCi*	*µCi*	*µCi*
Load	1 M NaOH	1	0.000	0.000	0.000	0.000
Wash 1	1 M NaOH	1	0.623	0.013	4.367	0.029
Wash 2	1 M NaOH	1	0.393	0.010	3.833	0.035
Wash 3	1 M NaOH	1	0.015	0.000	0.063	0.001
Wash 4	1 M NaOH	1	0.000	0.000	0.002	0.000
Wash 5	1 M NaOH	1	0.000	0.000	0.000	0.000
Wash 6	1 M NaOH	1	0.000	0.000	0.000	0.000
Wash 7	1 M NaOH	1	0.000	0.000	0.000	0.000
Wash 8	1 M NaOH	1	0.000	0.000	0.000	0.000
Wash 9	1 M NaOH	1	0.000	0.000	0.000	0.000
Wash 10	1 M NaOH	1	0.000	0.000	0.000	0.000
Elute 1	70° C H_2O	1	0.000	0.000	0.000	0.000
Elute 2	70° C H_2O	1	0.003	0.149	0.001	0.269
Elute 3	70° C H_2O	1	0.005	0.635	0.023	5.196
Elute 4	70° C H_2O	1	0.000	0.095	0.002	0.636
Elute 5	70° C H_2O	1	0.000	0.025	0.000	0.172
Elute 6	70° C H_2O	1	0.000	0.010	0.000	0.040
Elute 7	70° C H_2O	1	0.000	0.003	0.000	0.035
Elute 8	70° C H_2O	1	0.000	0.004	0.000	0.029
Elute 9	70° C H_2O	1	0.000	0.002	0.000	0.010
Elute 10	70° C H_2O	1	0.000	0.000	0.000	0.013
Column	-	-	0.000	0.006	0.000	0.024
Stock	1 M NaOH	1	1.040	0.944	8.291	6.466

Table D.4 Separation of Rhenium and Tungsten on a 0.5 g AnaLig Column with NaCl Eluent

Fraction	Media	Volume	W-188	Re-188
		mL	*µCi*	*µCi*
Load	1 M NaOH	1	0.000	0.000
Wash 1	1 M NaOH	1	3.259	0.408
Wash 2	1 M NaOH	1	2.313	0.287
Wash 3	1 M NaOH	1	0.038	0.004
Wash 4	1 M NaOH	1	0.002	0.000
Wash 5	1 M NaOH	1	0.000	0.000
Wash 6	1 M NaOH	1	0.000	0.000
Wash 7	1 M NaOH	1	0.000	0.000
Wash 8	1 M NaOH	1	0.000	0.000
Wash 9	1 M NaOH	1	0.000	0.000
Wash 10	1 M NaOH	1	0.000	0.000
Elute 1	0.9 M NaCl	1	0.000	0.000
Elute 2	0.9 M NaCl	1	0.000	0.000
Elute 3	0.9 M NaCl	1	0.000	0.000
Elute 4	0.9 M NaCl	1	0.000	0.001
Elute 5	0.9 M NaCl	1	0.000	0.005
Elute 6	0.9 M NaCl	1	0.000	0.039
Elute 7	0.9 M NaCl	1	0.000	0.016
Elute 8	0.9 M NaCl	1	0.000	0.027
Elute 9	0.9 M NaCl	1	0.000	0.038
Elute 10	0.9 M NaCl	1	0.000	0.054
Column	-	-	0.015	1.120
Stock	1 M NaOH	1	5.627	1.999

Table D.5 Separation of Rhenium and Tungsten on a 0.5 g AnaLig Column with HNO_3 Eluent

Fraction	Media	Volume	W-188	Re-188
		mL	*µCi*	*µCi*
Load	1 M NaOH	1	0.000	0.000
Wash 1	1 M NaOH	1	4.005	0.231
Wash 2	1 M NaOH	1	3.395	0.196
Wash 3	1 M NaOH	1	9.674	0.000
Wash 4	1 M NaOH	1	0.003	0.000
Wash 5	1 M NaOH	1	0.000	0.000
Wash 6	1 M NaOH	1	0.000	0.000
Wash 7	1 M NaOH	1	0.000	0.000
Wash 8	1 M NaOH	1	0.000	0.000
Wash 9	1 M NaOH	1	0.000	0.000
Wash 10	1 M NaOH	1	0.000	0.000
Elute 1	0.9 M NaCl	1	0.000	0.000
Elute 2	0.9 M NaCl	1	0.000	0.007
Elute 3	0.9 M NaCl	1	0.000	0.164
Elute 4	0.9 M NaCl	1	0.000	0.640
Elute 5	0.9 M NaCl	1	0.001	1.033
Elute 6	0.9 M NaCl	1	0.002	1.234
Elute 7	0.9 M NaCl	1	0.000	1.113
Elute 8	0.9 M NaCl	1	0.000	0.870
Elute 9	0.9 M NaCl	1	0.000	0.587
Elute 10	0.9 M NaCl	1	0.000	0.390
Column	-	-	0.000	0.220
Stock	1 M NaOH	1	17.080	6.440

Table D.6 Separation of Arsenic and Germanium on a Single 1 mL Silica Column

			23-Sep-14						12-Nov-14					
			Column A		Column B		Column C		Column A		Column B		Column C	
Fraction	**Media**	**Volume**	**Ge-77**	**As-77**	**Ge-77**	**As-77**	**Ge-77**	**As-77**	**Ge-77**	**As-77**	**Ge-77**	**As-77**	**Ge-77**	**As-77**
		mL	*µCi*	*µCi*	*µCi*	*µCi*	*µCi*	*µCi*	*µCi*	*µCi*	*µCi*	*µCi*	*µCi*	*µCi*
Load	pH 5	0.05	0.00	0.00	0.00	0.00	0.00	0.00	0.00	0.00	0.00	0.00	0.00	0.00
Wash 1	MeOH	1	0.00	42.51	0.0	72.6	0.00	39.12	0.00	222.68	0.03	239.35	0.02	215.59
Wash 2	MeOH	1	0.02	96.87	0.0	130.1	0.00	162.01	0.06	134.49	0.02	107.02	0.00	102.85
Wash 3	MeOH	1	0.03	6.10	0.0	11.1	0.02	23.93	0.05	18.66	0.03	13.48	0.04	14.44
Wash 4	MeOH	1	0.02	2.61	0.0	3.7	0.01	3.38	0.05	7.15	0.01	4.93	0.02	6.20
Wash 5	MeOH	1	0.03	3.03	0.0	2.6	0.01	1.82	0.02	2.72	0.01	2.70	0.02	3.38
Wash 6	MeOH	1	0.01	1.58	0.0	1.5	0.01	2.19	0.02	3.14	0.00	2.28	0.02	3.32
Wash 7	MeOH	1	0.01	1.29	0.0	2.1	0.01	1.13	0.01	2.17	0.01	1.75	0.02	3.72
Wash 8	MeOH	1	0.02	1.82	0.0	1.4	0.01	1.31	0.00	1.29	0.01	1.64	0.01	1.55
Wash 9	MeOH	1	0.02	1.59	0.0	1.7	0.01	1.34	0.00	0.91	0.00	1.06	0.01	1.12
Wash 10	MeOH	1	0.00	0.46	0.0	1.1	0.01	1.02	0.00	0.99	0.01	1.37	0.01	1.06
Wash 11	MeOH	1	0.01	0.89	0.0	0.7	0.01	0.84	0.01	0.99	0.01	1.17	0.01	1.26
Wash 12	MeOH	1	0.01	0.90	0.0	122.2	0.00	0.58	0.00	0.92	0.00	1.00	0.01	1.00
Wash 13	MeOH	1	0.02	1.12	0.0	0.8	0.00	0.62	0.00	1.10	0.00	1.30	0.00	1.48
Wash 14	MeOH	1	0.01	0.77	0.0	1.0	0.00	0.51	0.00	0.77	0.01	5.38	0.00	0.78
Wash 15	MeOH	1	0.01	0.72	0.0	0.7	0.02	1.35	0.00	0.70	0.00	0.74	0.00	0.69
Wash 16	MeOH	1	0.01	0.79	0.0	0.6	0.00	0.53	0.01	0.92	0.00	0.75	0.00	0.79
Wash 17	MeOH	1	0.01	0.72	0.0	0.5	0.00	0.47	0.01	0.86	0.01	1.12	0.01	1.25
Wash 18	MeOH	1	0.01	0.55	0.0	0.8	0.00	0.29	0.00	0.61	0.00	0.61	0.01	0.74
Wash 19	MeOH	1	0.01	0.51	0.0	0.7	0.00	0.33	0.00	0.63	0.00	0.65	0.00	0.75
Wash 20	MeOH	1	0.01	0.55	0.0	0.5	0.00	0.27	0.00	0.65	0.00	0.66	0.01	1.07
Elute 1	H_2O	5	25.33	110.77	32.9	70.2	46.35	49.67	20.35	116.39	22.30	96.90	19.39	104.48
Elute 2	H_2O	5	8.19	38.65	12.0	30.9	0.32	9.70	2.98	9.78	4.31	12.76	3.57	12.46
Elute 3	H_2O	5	0.38	9.10	2.1	11.1	0.17	7.77	0.21	3.34	0.32	4.58	0.29	3.96
Elute 4	H_2O	5	0.09	5.62	0.8	11.4	0.10	4.37	0.09	3.46	0.12	4.46	0.06	2.38
Stock	pH 5	0.05	54.1	736.4	54.6	741.9	53.60	730.99	29.85	967.31	30.63	979.60	26.04	770.49

Table D.7 Separation of Arsenic and Germanium on Dual 1 mL Silica Column

			24-Jun-14 First Columns						25-Jun-14 Second Columns					
			Column A		Column B		Column C		Column A		Column B		Column C	
Fraction	**Media**	**Volume**	**Ge-77**	**As-77**	**Ge-77**	**As-77**	**Ge-77**	**As-77**	**Ge-77**	**As-77**	**Ge-77**	**As-77**	**Ge-77**	**As-77**
		mL	µCi	µCi	µCi	µCi	µCi	µCi	µCi	µCi	µCi	µCi	µCi	µCi
Load	pH 5	0.05	0.00	0.00	0.0	0.0	0.00	0.00	0.00	100.32	0.00	61.13	0.00	42.62
Wash 1	MeOH	1	0.00	76.21	0.0	144.4	0.00	123.74	0.00	29.91	0.00	32.58	0.00	33.98
Wash 2	MeOH	1	0.00	494.83	0.0	278.4	0.00	425.75	0.00	3.33	0.00	5.69	0.00	38.45
Wash 3	MeOH	1	0.01	22.94	0.0	15.8	0.02	13.48	0.00	1.52	0.00	1.75	0.00	12.66
Wash 4	MeOH	1	0.00	8.01	0.0	6.8	0.02	4.65	0.00	1.64	0.00	1.09	0.00	2.94
Wash 5	MeOH	1	0.01	7.11	0.0	6.1	0.01	4.90	0.00	0.65	0.00	0.90	0.00	1.61
Wash 6	MeOH	1	0.00	6.45	0.0	4.8	0.01	2.97	0.00	0.33	0.00	0.61	0.00	1.20
Wash 7	MeOH	1	0.00	4.52	0.0	3.2	0.00	2.89	0.00	0.23	0.00	0.50	0.00	0.83
Wash 8	MeOH	1	0.00	2.81	0.0	2.2	0.01	2.38	0.00	0.35	0.00	0.41	0.00	0.79
Wash 9	MeOH	1	0.00	2.36	0.0	2.3	0.00	2.18	0.00	0.33	0.00	0.31	0.00	0.61
Wash 10	MeOH	1	0.00	1.06	0.0	1.5	0.01	1.52	0.00	0.24	0.00	0.30	0.00	0.55
Wash 11	MeOH	1	0.00	1.32	0.0	0.9	0.00	1.27	0.00	0.22	0.00	0.22	0.00	0.50
Wash 12	MeOH	1	0.00	0.88	0.0	1.4	0.01	1.00	0.00	0.31	0.00	0.26	0.00	0.50
Wash 13	MeOH	1	0.00	0.83	0.0	1.0	0.00	0.86	0.00	0.21	0.00	0.25	0.00	0.19
Wash 14	MeOH	1	0.00	0.64	0.0	1.1	0.00	1.00	0.00	0.16	0.00	0.21	0.00	0.16
Wash 15	MeOH	1	0.00	0.77	0.0	1.4	0.00	0.98	0.00	0.23	0.00	0.21	0.00	0.14
Wash 16	MeOH	1	0.00	0.82	0.0	1.0	0.00	0.99	0.00	0.19	0.00	0.18	0.00	0.16
Wash 17	MeOH	1	0.00	0.85	0.0	0.9	0.00	0.72	0.00	1.95	0.00	0.21	0.00	0.09
Wash 18	MeOH	1	0.00	1.49	0.0	1.4	0.00	0.70	0.00	3.14	0.00	0.20	0.00	0.12
Wash 19	MeOH	1	0.00	1.63	0.0	1.7	0.01	0.84	0.00	0.62	0.00	0.15	0.00	0.09
Wash 20	MeOH	1	0.00	1.79	0.0	1.3	0.00	0.65	0.00	0.23	0.00	0.19	0.00	0.15
Elute 1	H_2O	5	68.56	21.68	74.4	47.6	57.75	31.96	0.00	5.52	0.01	9.57	0.00	10.63
Elute 2	H_2O	5	0.89	7.57	0.8	10.1	17.50	2.15	0.00	0.39	0.00	0.70	0.00	2.67
Elute 3	H_2O	5	0.19	3.26	0.1	3.9	2.32	2.96	0.00	0.14	0.00	0.26	0.00	0.72
Elute 4	H_2O	5	0.09	2.09	0.1	2.5	0.00	1.21	0.00	0.08	0.00	0.12	0.00	0.31
Stock	MeOH	8	-	-	-	-	-	-	0.00	135.07	0.01	100.14	0.00	126.97

Table D.8 Separation of Arsenic and Germanium on Tandem 1 mL Silica and HZO Columns

Table D.8.1 Tandem Loading of Arsenic and Germanium on Silica and HZO

			4-Feb-14		15-Apr-14	
Fraction	**Media**	**Volume**	**Ge-77**	**As-77**	**Ge-77**	**As-77**
		mL	*µCi*	*µCi*	*µCi*	*µCi*
1	MeOH	5	0.01	0.00	0.04	0.00
2	MeOH	5	0.02	0.14	0.05	0.00
3	MeOH	5	0.02	0.05	0.05	0.00
4	MeOH	5	0.02	0.05	0.04	0.00
5	MeOH	5	0.02	0.00	0.11	0.00
6	MeOH	5	0.03	0.00	0.10	0.00
7	MeOH	5	0.02	0.00	0.08	0.00
8	MeOH	5	0.03	0.11	0.06	0.05
9	MeOH	5	0.03	0.05	0.09	0.19
10	MeOH	5	0.03	0.01	0.07	0.08

Table D.8.2 Separated Washing and Elution of Silica Column

			4-Feb-14		15-Apr-14	
Fraction	**Media**	**Volume**	**Ge-77**	**As-77**	**Ge-77**	**As-77**
		mL	*µCi*	*µCi*	*µCi*	*µCi*
1	pH 11	1	11.18	27.21	13.95	0.00
2	pH 11	1	7.81	0.00	12.98	0.00
3	pH 11	1	0.68	0.00	1.12	0.00
4	pH 11	1	0.08	0.41	0.22	0.72
5	pH 11	1	0.03	0.28	0.08	0.49
6	pH 11	1	0.02	0.24	0.09	0.33
7	pH 11	1	0.02	0.16	0.08	0.50
8	pH 11	1	0.01	0.14	0.12	0.84
9	pH 11	1	0.01	0.12	0.13	1.08
10	pH 11	1	0.01	0.08	0.08	0.61
11	pH 11	1	0.01	0.09	0.04	0.27
12	pH 11	1	0.01	0.06	0.02	0.16
13	pH 11	1	0.00	0.06	0.02	0.14
14	pH 11	1	0.00	0.01	0.02	0.22
15	pH 11	1	0.00	0.06	0.06	0.50
16	pH 11	1	0.00	0.05	0.03	0.26
17	pH 11	1	0.00	0.03	0.02	0.18
18	pH 11	1	0.00	0.04	0.13	0.96
19	pH 11	1	0.00	0.05	0.03	0.26
20	pH 11	1	0.00	0.03	0.03	0.26
21	pH 13	5	0.01	0.53	0.02	0.69
22	pH 13	5	0.00	0.29	0.02	0.39
23	pH 13	5	0.00	0.13	0.02	0.16
24	pH 13	5	0.00	0.13	0.01	0.15

Table D.8.3 Separated Washing and Elution of HZO Column

			4-Feb-14		15-Apr-14	
Fraction	**Media**	**Volume**	**Ge-77**	**As-77**	**Ge-77**	**As-77**
		mL	*µCi*	*µCi*	*µCi*	*µCi*
1	pH 11	1	0.00	0.01	0.01	0.00
2	pH 11	1	0.00	0.00	0.00	0.03
3	pH 11	1	0.00	0.00	0.00	0.02
4	pH 11	1	0.00	0.00	0.00	0.02
5	pH 11	1	0.00	0.00	0.00	0.01
6	pH 11	1	0.00	0.00	0.00	0.02
7	pH 11	1	0.00	0.00	0.01	0.03
8	pH 11	1	0.00	0.00	0.01	0.04
9	pH 11	1	0.00	0.02	0.01	0.03
10	pH 11	1	0.00	0.00	0.01	0.04
11	pH 11	1	0.00	0.00	0.01	0.05
12	pH 11	1	0.00	0.00	0.01	0.04
13	pH 11	1	0.00	0.02	0.01	0.08
14	pH 11	1	0.00	0.01	0.01	0.07
15	pH 11	1	0.00	0.00	0.02	0.07
16	pH 11	1	0.00	0.00	0.02	0.12
17	pH 11	1	0.00	0.02	0.02	0.10
18	pH 11	1	0.00	0.05	0.02	0.15
19	pH 11	1	0.00	0.05	0.02	0.19
20	pH 11	1	0.00	0.06	0.02	0.10
21	pH 13	5	0.00	60.21	0.07	103.91
22	pH 13	5	0.00	125.49	0.00	222.28
23	pH 13	5	0.00	39.70	0.00	67.72
24	pH 13	5	0.00	23.79	0.00	16.02

Table D.8.4 Residual Activity Remaining on the Columns

	4-Feb-14		15-Apr-14	
Column	**Ge-77**	**As-77**	**Ge-77**	**As-77**
	µCi	*µCi*	*µCi*	*µCi*
Silica	0.27	4.36	0.15	1.36
HZO	6.39	89.79	6.61	41.09

Table D.9 Separation of Arsenic and Germanium on a Single 1 mL Silica Column with Varied Load Conditions

Table D.9.1 Stock Solution Adjusted with HCl

			Column A		Column B		Column C	
Fraction	**Media**	**Volume**	**Ge-77**	**As-77**	**Ge-77**	**As-77**	**Ge-77**	**As-77**
		mL	*µCi*	*µCi*	*µCi*	*µCi*	*µCi*	*µCi*
Load	pH 5	0.05	0.0	0.0	0.0	0.0	0.0	0.0
Wash 1	MeOH	1	0.0	36.0	0.0	45.6	0.0	50.0
Wash 2	MeOH	1	0.0	93.9	0.0	74.0	0.0	53.2
Wash 3	MeOH	1	0.0	7.0	0.0	3.8	0.0	2.9
Wash 4	MeOH	1	0.0	1.9	0.0	1.5	0.0	1.5
Wash 5	MeOH	1	0.0	1.7	0.0	1.2	0.0	1.0
Wash 6	MeOH	5	0.0	3.3	0.0	3.0	0.0	2.8
Wash 7	MeOH	5	0.0	2.1	0.0	2.3	0.0	2.0
Wash 8	MeOH	5	0.0	1.8	0.0	1.9	0.0	1.6
Elute 1	H_2O	5	7.0	19.2	8.3	24.6	6.6	15.1
Elute 2	H_2O	5	0.1	2.2	0.1	2.7	0.1	1.8
Stock	pH 5	0.05	14.9	434.7	14.4	415.7	16.1	465.3

Table D.9.2 Stock Solution Adjusted with H_3PO_4

			Column A		Column B		Column C	
Fraction	**Media**	**Volume**	**Ge-77**	**As-77**	**Ge-77**	**As-77**	**Ge-77**	**As-77**
		mL	*µCi*	*µCi*	*µCi*	*µCi*	*µCi*	*µCi*
Load	pH 5	0.05	0.0	0.0	0.0	0.0	0.0	0.0
Wash 1	MeOH	1	0.0	167.4	0.0	180.1	0.0	170.3
Wash 2	MeOH	1	0.3	59.6	0.3	70.2	0.5	90.5
Wash 3	MeOH	1	0.2	2.9	0.2	3.2	0.2	3.4
Wash 4	MeOH	1	0.1	1.3	0.1	1.6	0.1	1.8
Wash 5	MeOH	1	0.1	1.1	0.0	1.2	0.1	1.2
Wash 6	MeOH	5	0.2	1.4	0.1	1.5	0.1	1.4
Wash 7	MeOH	5	0.1	0.9	0.1	1.0	0.1	1.0
Wash 8	MeOH	5	0.1	0.7	0.1	0.6	0.1	0.6
Elute 1	H_2O	5	5.1	1.2	6.5	1.0	5.1	0.7
Elute 2	H_2O	5	0.1	0.3	0.0	0.1	0.1	0.3
Stock	pH 5	0.05	7.2	244.5	7.0	236.7	6.9	239.7

Table D.9.3 Stock Solution Adjusted with HNO_3

			Column A		Column B		Column C	
Fraction	**Media**	**Volume**	**Ge-77**	**As-77**	**Ge-77**	**As-77**	**Ge-77**	**As-77**
		mL	*µCi*	*µCi*	*µCi*	*µCi*	*µCi*	*µCi*
Load	pH 5	0.05	0.0	0.0	0.0	0.0	0.0	0.0
Wash 1	MeOH	1	0.0	66.6	0.0	57.4	0.0	70.0
Wash 2	MeOH	1	0.0	40.1	0.0	49.5	0.0	92.0
Wash 3	MeOH	1	0.0	5.5	0.0	5.8	0.0	7.7
Wash 4	MeOH	1	0.0	3.0	0.0	3.3	0.0	2.6
Wash 5	MeOH	1	0.0	2.6	0.0	2.7	0.0	2.3
Wash 6	MeOH	5	0.0	6.0	0.0	6.1	0.0	4.0
Wash 7	MeOH	5	0.0	4.1	0.0	4.0	0.0	3.8
Wash 8	MeOH	5	0.0	4.5	0.0	4.0	0.0	3.0
Elute 1	H_2O	5	17.5	81.6	11.0	49.4	13.4	34.3
Elute 2	H_2O	5	0.2	12.6	0.1	8.9	0.2	6.5
Stock	pH 5	0.05	6.2	342.6	6.1	321.6	6.5	377.7

Table D.10 Separation of Scandium and Calcium on a 50 mg DGA Column

Fraction	**Media**	**Volume**	**Sc-44**
		mL	*µCi*
Load	3 M HCl	0.5	0.00
Wash	3 M HCl	3	0.00
Elute 1	0.1 M HCl	1	3.19
Elute 2	0.1 M HCl	1	10.94
Elute 3	0.1 M HCl	1	12.32
Elute 4	0.1 M HCl	1	14.15
Elute 5	0.1 M HCl	1	16.32
Elute 6	0.1 M HCl	5	9.76
Stock	3 M HCl	0.5	205.35

VITA

Matthew David Gott was born in Kingsport, Tennessee on July 8th, 1987 to Larry David and Mary Catherine Gott. He graduated from Sullivan South High School in May of 2005. He matriculated at Tennessee Technological University in Cookeville, Tennessee in August of 2005 and earned his Bachelors of Science in Chemistry in December of 2009. He continued his education at Tennessee Technological University enrolling in a fast-track program and earned his Master of Science in Chemistry in December of 2010. Matthew joined the doctoral program in Chemistry at the University of Missouri (Columbia, MO) in August of 2011. He will receive his Doctorate of Philosophy in Chemistry in July of 2015. Matthew has accepted a postdoctoral research position at the Institute of Radiopharmaceutical Cancer Research at Helmholtz Zentrum Dresden Rossendorf in Dresden, Germany.